State-selected and state-to-state dynamics of chemical reactions

A Thesis

Submitted for the Degree of

Doctor of Philosophy

by

SUGATA GOSWAMI

SCHOOL OF CHEMISTRY

UNIVERSITY OF HYDERABAD

HYDERABAD 500 046

INDIA

JUNE 2017

Dedicated

To
My Parents

STATEMENT

I hereby declare that the matter embodied in this thesis is the result of investigations carried out by me in the School of Chemistry, University of Hyderabad, Hyderabad, under the supervision of **Prof. Susanta Mahapatra**.

In keeping with the general practice of reporting scientific observations, due acknowledgment has been made wherever the work described is based on the findings of other investigators.

June 2017 (**Sugata Goswami**)

Hyderabad - 500 046

School Of Chemistry
University Of Hyderabad
Hyderabad-500 046
India

CERTIFICATE

This is to certify that the thesis entitled "**State-selected and state-to-state dynamics of chemical reactions**" submitted by **Mr. Sugata Goswami** bearing registration number **11CHPH08** in partial fulfilment of the requirements for award of Doctor of Philosophy in the School of chemistry is a bonafide work carried out by him under my supervision and guidance.

This thesis is free from plagiarism and has not been submitted previously in part or in full to this or any other University or Institution for award of any degree or diploma.

Parts of this thesis have been:

A. published in the following publications :

1. Sugata Goswami, T. Rajagopala Rao, S. Mahapatra, B. Bussery-Honvault, and P. Honvault, J. Phys. Chem. A **118**, 5915 (2014) (ISSN Number 1089-5639 (print), 1520-5215 (web)), **Chapter 3**

2. Sugata Goswami, B. Bussery-Honvault, P. Honvault, and S. Mahapatra, Mol. Phys. (in press), DOI: 10.1080/00268976.2017.1296195 (ISSN Number 0026-8976 (Print) 1362-3028 (Online)), **Chapter 4**

and

B. presented in following conferences :

1. DAE BRNS Symposium on Current Trends in Theoretical Chemistry (CTTC-2013), 26-28 September, 2013, at Bhabha Atomic Research Centre, Mumbai, India (National).
2. The First Indo-Taiwan Symposium on Recent Trends in Chemical Sciences (RTCS-2014), 17-18 November, 2014, at University of Hyderabad, Hyderabad, India (International).
3. Theoretical Chemistry Symposium (2014), 18-21 December, 2014, at CSIR - National Chemical Laboratory in association with Indian Institute of Science Education and Research, Pune (National).
4. A Tributary Symposium on 100 Years of Chemical Bonding-2016, 4-5 August, 2016, at CSIR-Indian Institute of Chemical Technology, Hyderabad (National).
5. 15^{th} Indian Theoretical Chemistry Symposium (TCS-2016), 14-17 December, 2016, at University of Hyderabad, Hyderabad (National)

Further, the student has passed the following courses towards fulfillment of course-work requirement for Ph. D

Course code	Name	Credits	Pass/Fail
1. CY-801	Research Proposal	3	Pass
2. CY-802	Chemistry Pedagogy	3	Pass
3. CY-806	Instrumental Methods	3	Pass
4. CY-822	Symmetry and Spectroscopy	3	Pass

(Prof. Susanta Mahapatra) Head of Department Dean of School
Supervisor

Acknowledgement

It is very difficult for me now to remember the names of all people without whose help it could be impossible for me to carry out my research work and stay in Hyderabad. Hence, I beg pardon if I miss to acknowledge someone. I thank all of them who assisted me in various ways at different time.

At first I like to thank my Ph. D supervisor, Prof. Susanta Mahapatra for his continuous guidance and encouragement. I still wonder about his art of scientific writing. I strongly believe that the experience I have got from his suggestions and comments will help me in future.

I extend my thanks to Prof. M. Durga Prasad and Prof. T. P. Radhakrishnan for their excellent teaching techniques and some fruitful discussions. I also thank Prof. K. D. Sen for allowing me to be a teaching assistant of him. I am thankful to Prof. P. Honvault and Dr. B. Bussery-Honvault for all scientific discussions.

I thank present and former deans, all faculty members and all other colleagues of School of Chemistry, University of Hyderabad.

I thank all my present and former lab mates with whom I had an opportunity to work. Thanks to all of them to provide me a friendly atmosphere. I am very thankful to Dr. T. Rajagopala Rao who helped me a lot to learn computer programing, various other techniques and of course reaction dynamics. It is worthwhile to mention here that still he assists me in various occasions to solve a problem whenever I need his help. I can still remember that *Subbu* (Mr. Subrahmanyam Sappati) and I used to learn from him with sleepy and red eyes in my early days of Ph. D. I believe that I am fortunate to come to know a person

with the name Dr. Tanmoy Kumar Roy. I never heard the word "no" from him. He always came forward to solve a problem. I thank Dr. S. Rajagopala Reddy for many fruitful discussions on quantum mechanics. I extend my thanks to Dr. Nagaprasad Reddy to offer me a handful of memorable incidents. I thank Mr. Rudraditya Sarkar to be a classmate, lab mate, roommate for a year and finally a great teammate. He used to call me over telephone before half an hour of every match but in many occasions I reached at the ground when the match is about to start. I do not have enough words to thank Arpita. She helped me a lot from various aspects throughout my stay in Hyderabad. I feel I am lucky to interact with someone like Dr. K. Rajak at latter part of my Ph. D days. I do not know how to thank him, but still thanks *Karunamoy Da* for all the memories. I thank Mr. Krishna Reddy for all the academic discussions and I respect his knowledge in quantum mechanics. I extend my thanks to Mr. Arun Kumar Kanakati and Mr. Jayakrushna Sahoo for their immense help. I also thank Mr. Satyendra Gupta. I thank Manjusha, Varun, Suranjan, Deepak and Sruthi for being colleagues of mine at different time.

I am very much thankful to *Sanghamitra Di* (Dr. Sanghamitra Banerjee). She was the only person I knew when I came to this university and a huge amount of assistance I received from her. I must not miss the opportunity to thank *Tulika Di* (Dr. Tulika Ghosh). She was always like an elder sister to me. I thank Mehboob Da and Mrinmoy Da for their support. I feel I am very fortunate to know people like Rishi Da, Santanu Da, Arpita Di, Maity Da, Anup Da, Satya Da, Pati Da, Dinu Da, Nayan Da, Avijit Da and Sanatan Da. I must thank Olivia, Sinjini and Saheli. It will be unjustified if I forget to thank Monojit, Pradip, Suman Da, Kaijer Da, Dibya Da and of course, Raju. A group of boys made my stay in university

campus very colourful and I must not forget to acknowledge them. Hence, I extend my acknowledgement to Soumen, Koushik, Kallol, Sudipto, Shuvo, Arijit, Bappa, Kuntal, Saddam, Apurbo, Arindam, Debojyoti Das, Debojyoti Chetterjee, Tausif, Rajib, Deepan, Suman, Nilanjan, Shuvam, Soutrick, Aleem, Anupam, Souvik, Atindra ,Azhar, Sourav, Sayantan, Ujjal, Saptarshi, and Kalyan. I specially thank Arup and Sritam for all the memories they have built. I thanks Soumen, Tathagata, Ranjan, Pratik and Kalishankar in this occasion. I do not know how to thank Debaparna as we are being friends for almost two decades. I thank Sneha, Sabari, Suchana and Tasnim for all the assistance I received from them. I am also thankful to Sharmistha, Parijat, Mou and Sarada. I am grateful to *Gupta anna*, *Chandu anna*, *Kishore anna*, *Ashoke anna*, *Sashi anna*, *Vikranth anna*, *Sridhar anna*, Keshava, Anil, Amala, K. S. Sruthi and Srujana.

I am always and always will be grateful to two excellent personalities. They are none other than *Paromita Di* (Dr. Paromita Bose) and *Raja Da* (Dr. Raja Kumar Rit). I really do not know how to thank them. Thanks *Paromiata Di* and *Raja Da* for countless reasons. On the other hand, I can never forget the memories I have with Suman Ghosh and Navendu Mondal. I will always feel guilty if I miss the opportunity to acknowledge *Subrata Da* (Dr. Subrata Banik) for his immense help and guidance. I must not forget to thank *Lalitha Di* also.

I thank Madam (Mrs. Mahapatra), Papai and Diya for providing me a homely atmosphere and for their delightful company on various occasions.

I acknowledge **Council of Scientific and Industrial Research (CSIR), New Delhi** for the doctoral fellowship and Center for Modelling Simulation and Design (CMSD) for the computational facility. I also thank DST-SERB, New

Delhi for funding. I am grateful to School of Chemistry, University of Hyderabad.

I thank my parents, my cousin *Avi Da* and *Daliya Di*, my maternal uncle (Mr. A. K. Bhattacharya) and all my family members for their huge support. I am grateful to all my teachers since my childhood.

Sugata Goswami

List of Abbreviations

ACCSA	Adiabatic capture in the centrifugal sudden approximation method
AVTZ	aug-cc-pVTZ
BF	Body-fixed
BO	Born-Oppenheimer
CM	Center-of-mass
CS	Centrifugal sudden or Coupled states
DCS	Differential cross section
DMBE-SEC	Double many body expansion-scaled external correlation
FFT	Fast Fourier Transform
FVCAS	Full velance complete active space
GWP	Gaussian wave packet
ICS	Integral cross section
MEP	Minimum energy path
MRCI	Multireference configuration interaction
MR-SDCI	Multireference single and double configuration interaction
NAC	Nonadiabatic coupling
PES	Potential energy surface
QCT	Quasi classical trajectory
R. H. S.	Right hand side
RKHS	Reproducing kernel Hilbert space
RRKM	Rice-Ramsperger-Kassel-Marcus
RWP	Real wave packet
SF	Space-fixed
SIL	Short iterative Lanczos
SO	Split operator
SOD	Second order differencing
SQM	Statistical quantum method
SVP	Sudden vector projection
TDQM	Time-dependent quantum mechanical
TDWP	Time-dependent wave packet
TIQM	Time-independent quantum mechanical
WP	Wave packet

Contents

Chapter 1

Introduction

To begin with let me focus on a question that often went into the mind and addressed in the book of Raphael D. Levine, "What is molecular reaction dynamics?" [1] This can be answered in different ways and one of them is the following -
"Molecular reaction dynamics is the study of elementary processes and the means of probing them, understanding them and controlling them". In bulk kinetic studies rate constant of a reaction is measured at thermal equilibrium conditions and hence such studies are incapable of finding out the exact factors for which the reaction proceeds. On the contrary, molecular reaction dynamics provides a molecular level understanding of reactivity and it can predict the factors upon which the reactivity depends.

It has always been one of the greatest challenges of all time in chemistry is to design experiments to find the real picture of molecular transformations which are hidden behind thermal averaging of states and to develop theoretical methodologies to explain, understand experimental observations and to predict outcomes of molecular encounters. The introduction of lasers in experiments and

the immense improvement of computational techniques during last few decades helped chemists to accept the challenge and involve themselves in the process of overcoming this.

An elementary reaction can be visualized as a result of collision among the species where the chemical identities of these are altered through the cleavage of old bonds and the formation of new bonds. Every such collision is unique in terms of the relative translational energy, angular distribution and the internal motion of the newly generated product molecules [2]. In addition, the outcome of a chemical encounter not only depends upon the structure and chemical identity of the reactants but also on their relative orientation, velocity, electronic and internal states [2]. For an example, the reaction between a H atom and the HOD molecule can be considered. The products are H_2 + OD when the OH bond is vibrationally excited, whereas, the encounter results the formation of HO + HD when the OD bond of HOD molecule is vibrationally excited [1]. The dependence of the outcome of a chemical encounter on a wide range of factors has made the field of molecular reaction dynamics highly interesting and also very challenging too.

One may ask a second question at this point. How the "state-selected"and "state-to-state"dynamics can be defined? If the final results of a molecular encounter are resolved into the internal states of the product, it is known as state-to-state dynamics study. Whereas, in a state-selected study the final result is summed over the internal states of the product. It is obvious that a state-to-state study is always superior than state-selected studies, but technically the former is always more difficult to be carried out.

The link between experimental measurements and theoretical calculations are found to be very strong in molecular reaction dynamics studies. The electronic

potential energy surface (PES) serves as the bridge between theory and experiment. The construction of PES starts with the invocation of the well known Born-Oppenheimer (BO) adiabatic approximation [3]. The BO approximation simplifies the theoretical calculations by decoupling the electronic and the nuclear motion from each other and consequently they can be treated separately. A huge number of nuclear configurations are chosen by clamping the nuclei at different geometries at space. The electronic Schrödinger equation is solved at these configurations to obtain electronic energies and corresponding eigenfunctions. The electronic energies become a function of nuclear coordinates, whereas, electronic eigenfunctions depend parametrically on the same. Interpolation of the energy values obtained at different nuclear configurations generate a smooth function of nuclear coordinates which is commonly known as adiabatic PES. The PES behaves as the landscape for the motion of the nuclei and hence the construction of PES is the first step for a theoretical treatment of nuclear dynamics.

Calculated electronic eigenfunctions at different nuclear geometries form a complete set of functions and hence the total molecular wavefunction can be expressed as linear combination of them. The coefficients for this expansion are nuclear wavefunctions which depend on the nuclear coordinates. Substitution of the total molecular wavefunction in the molecular Schrödinger equation and the integration over the electronic coordinates afterwards produce the coupled channel eigenvalue equation for the nuclear wavefunction in adiabatic representation. In an adiabatic representation different electronic states are coupled through nuclear kinetic coupling terms and they are called as nonadiabatic coupling (NAC) elements. All these NAC elements are completely ignored when a strict BO approximation is followed [3], whereas, few diagonal NAC elements are considered under Born-Huang (BH) approximation [4]. In both the cases, the coupled chan-

nel nuclear eigenvalue equation is reduced to an equation of single electronic state and hence the nuclear motion is confined on a single adiabatic PES (all relevant mathematical equations are given and discussed in Chapter 2). This BO adiabatic approximation can be justified by considering the fact that the nuclei are ~ 1800 times heavier than the electrons and the electrons move much faster than the nuclei. In fact the nuclei behave as spectators during electronic motion. Nevertheless, there are certain circumstances where the BO approximation breaks down and the nuclear motion is no longer confined on a single adiabatic PES. When two adiabatic potential energy surfaces come very close to each other or in case of electronic degeneracy, the NAC elements can not be ignored and nonadiabatic transitions take place between coupled electronic adiabatic states. At nonadiabatic situation, the use of adiabatic electronic representation is limited in nuclear dynamics treatment and a non unique representation called diabatic [5] is commonly used to circumvent the difficulty. All molecular dynamics studies mentioned in this thesis were done within BO limit and hence the discussion about nonadibatic nuclear dynamics is restricted here.

Eventually, the nuclear Schrödinger equation has to be solved numerically to study a reactive scattering process quantum mechanically. Either the time-dependent wave packet (TDWP) propagation approach or the time-independent quantum mechanical (TIQM) method can be followed for this. Both the approaches have advantages and demerits. These two methods do not conflict with each other, rather they are complementary. TIQM methods are best suited for cold and ultracold reaction dynamics study where the calculations are carried out at very low collision energies. At such low collision energies, the wave packet used in a TDWP propagation approach has a large de Broglie wave length and consequently a huge absorbing range is required for the removal of spurious reflections

at grid boundaries which makes the approach impractical and computationally unfeasible. On the other hand, time-dependent methods scale better than the TIQM methods and the dynamics can be pictorially visualized in the former approach if one records the snapshots of the wave-packet at regular time intervals. The studies reported here in the thesis correspond to thermal conditions and the TDWP propagation approach has been followed to carry out the nuclear dynamics. The theoretical methodologies and computational details are given in detail in chapter 2.

The mechanism and the characteristics of a bimolecular reaction are described by the knowledge of some dynamical observables. The common observables are briefly described here in order to better understand the results reported and remarks made for a few bimolecular reactions in latter chapters.

a) **Reaction probability** : Most commonly reaction probability is expressed as a function of energy, either total or collision energy, and it shows the probability for a reaction to occur at a particular energy.

b) **Opacity function** : When the probability of a particular process of interest is expressed as a function of the impact parameter (in classical mechanical studies) or total angular momentum quantum number, J (in quantum mechanical studies) at a particular energy, it is known as opacity function. The pattern of the opacity function at a fixed energy gives the idea about the number of partial waves required to obtain converged cross section and rate constant.

c) **Cross section** : Often this is termed as integral cross section (ICS) also. It can be defined as the area of target within which the colliding particles must approach to each other for a particular process to occur.

d) **Differential cross section** : This quantity is directly related to the angular distribution of the product which provides a clear idea about the mechanism of

the reaction and the topography of the underlying PES. The differential cross section (DCS) is the effective target area for the colliding particles which leads to the scattering of the products towards a particular angular range. Hence, the integration of DCSs over the scattering angle results into integral cross sections. The pattern of the DCSs indicates a lot about the mechanism of the reaction. A preferential forward scattering is found in DCSs when the reaction is dominated by long range attractive forces and the collisions are glancing blow type with high impact parameters. Whereas, backward scattering is observed for the reactions dominated by repulsive short range forces. The magnitudes of the cross section is more in the former case than the latter as in the former case collisions with high impact parameter predominates the reaction [2]. On the other hand, when the reaction takes place on a PES having deep wells on it leading to the formation of stable intermediate collision complexes, the DCS appears to be symmetric in forward and backward direction.

e) **Product internal state distribution** : The distribution of vibrational and rotational levels of the product diatom at different energies provides the idea about the energy disposal of the process and the mechanism of it. The distribution can be represented in terms of either probability or cross section. A non-statistical distribution of the vibrational levels of product diatom predicts a direct type reaction, whereas, a statistical distribution supports an insertion type of reaction mechanism with the formation of stable intermediate collision complexes.

f) **Rate constant** : The rate constant of a reaction is calculated from ICSs and it is a highly averaged quantity compared to the other dynamical observables noted here. Hence, less mechanistic details of a reaction is available from rate constant data, rather it introduces the dependence of temperature on the process.

These observables are calculated for different bimolecular reactions and are

reported here in this thesis in latter chapters in order to find the mechanistic details of these reactions.

1.1 Description of the potential energy surfaces

The essential features of the underlying PESs of various reactive system whose dynamics have been studied are noted in this section. The topographical features of the surfaces help to better understand the dynamics results as the nature of the PES largely controls the outcome of a chemical encounter.

1.1.1 Electronic ground PES of HSO/SOH reactive system

The S(^{3}P) + OH ($X^2\Pi$) $\rightarrow$ SO($X^3\Sigma^-$) + H(^{2}S) (say R1) reaction takes place on the electronic ground state ($\tilde{X}^2A''$) of the HSO reactive system. The latter molecule, HSO, plays an important role in the atmospheric chemistry as it takes part in the catalytic cycle [6–8] of the ozone destruction process in the following way -

$HS + O_3 \rightarrow HSO + O_2$

$HSO + O_3 \rightarrow HS + 2O_2$.

Martínez-Núñez and Varandas have constructed a global PES for the electronic ground state of the HSO reactive system where the S + OH, SH + O and SO +H are considered as the asymptotes [9]. The authors carried out full valence complete active space (FVCAS) and multireference configuration interaction (MRCI) calculations over 500 geometries of the triatomic HSO system followed by the correction of these energy values by using double many-body expansion-scaled external correlation (DMBE-SEC) method [10]. The calculated energies were

subsequently used to calibrate the PES based on the DMBE formalism [11–14]. The aug-cc-pVTZ (AVTZ) basis set of Dunning [15–17] and the MOLPRO [18] computational package were used for the calculations. Important topographical features of this PES are discussed below and this PES is designated as the DMBE PES in the rest of the text.

The potential energy curves of the OH, SO and SH diatoms are generated from the DMBE PES [9] by keeping the third atom far away from the other two atoms in each case and they are shown in different colours in Figure 1.1. The energy of the OH diatom is set to zero at its equilibrium bond length [$\sim$ 1.88 (a_0)]. From Figure 1.1 it can be found that the, S + OH $\rightarrow$ SO + H, reaction is exoergic and value of exoergicity is $\sim$ 0.8 eV. Whereas, the, S + OH $\rightarrow$ SH + O, has endoergicity of $\sim$ 0.84 eV. The values of the exoergicity and the endoergicity calculated here agree well with the reported values in Ref. [9] (see the description below table 10 of Ref. [9]). The DMBE PES contains four minima and four saddle points on it [9]. The geometries of the triatomic HSO system in terms of inter atomic distances at these eight stationary points and corresponding energy values are given in Table 1.1. The energy values mentioned in the last column of Table 1.1 are calculated by using a computer program and the DMBE PES [9]. Moreover, these values are reported with respect to the energy of S + OH asymptote which is set to $\sim$0.0 eV. All these values agree well with the energies given in Table 10 of Ref. [9] when they are converted into eV unit except for TS4. From Table 1.1 it can be seen that there exist two deep potential wells of energy $\sim$-3.43 eV and $\sim$-3.38 eV on the surface which correspond to the HSO and HOS conformers, respectively. The DMBE PES [9] predicts HSO as the most stable isomer which confirms the previous theoretical prediction of Goumri *et al.* [19]. Two van der Walls minima located $\sim$0.14 eV and $\sim$0.06 eV below the S

+ OH and SH + O asymptotes, respectively, correspond to the S...OH and SH..O complexes. Among the four saddle points, TS1 connects the two deep potential wells corresponding the HSO and HOS isomers. TS1 lies ∼2.03 eV energy above the global HSO minimum and hence the barrier for the conversion between these two isomers is very high. Though HSO and HOS complexes are energetically very close but only the HSO isomer is found experimentally due to this high barrier between them. The second transition state, TS2 is the small barrier for the dissociation of HOS complex into SO + H and it is located at ∼-0.7 eV. This saddle point acts as a late barrier along the minimum energy path (MEP) for the S + OH → SO + H reaction [see Figure 12(b) of Ref. [9]]. The other two saddle points, TS3 and TS4 connect the HSO and SOH isomers with the two van der Walls minima. We reiterate here that all energies given above are with respect to the S + OH reagent channel unless it is mentioned otherwise.

A 2-D contour plot of the DMBE PES [9] is shown in Figure 1.2 as a function of the OH and SH bond distances. The distance between S and O atoms, R_{SO} is kept fixed at ∼2.8569 a_0. In Figure 1.2 the HSO potential well appears perfectly and it can be found at R_{OH}=∼4.48 a_0, and R_{SH}=∼2.59 a_0 [R_{OH} and R_{SH} are the OH and SH bond distance, respectively]. Whereas, the less deeper HOS potential well is closely reproduced in this figure. Moreover, it can be seen from the figure that the system has to overcome a barrier to migrate from one well to the other. Hence, in Figure 1.2 the two potential wells and the saddle point between them on the DMBE PES have been shown almost perfectly.

From Figure 12(b) of Ref. [9] it can be seen that the reaction R1 is barrierless and hence it can be anticipated that the reactive system can easily slides down to the HOS minima present at the entrance channel. The system can then move to the SO + H product asymptote directly by overcoming the small late barrier

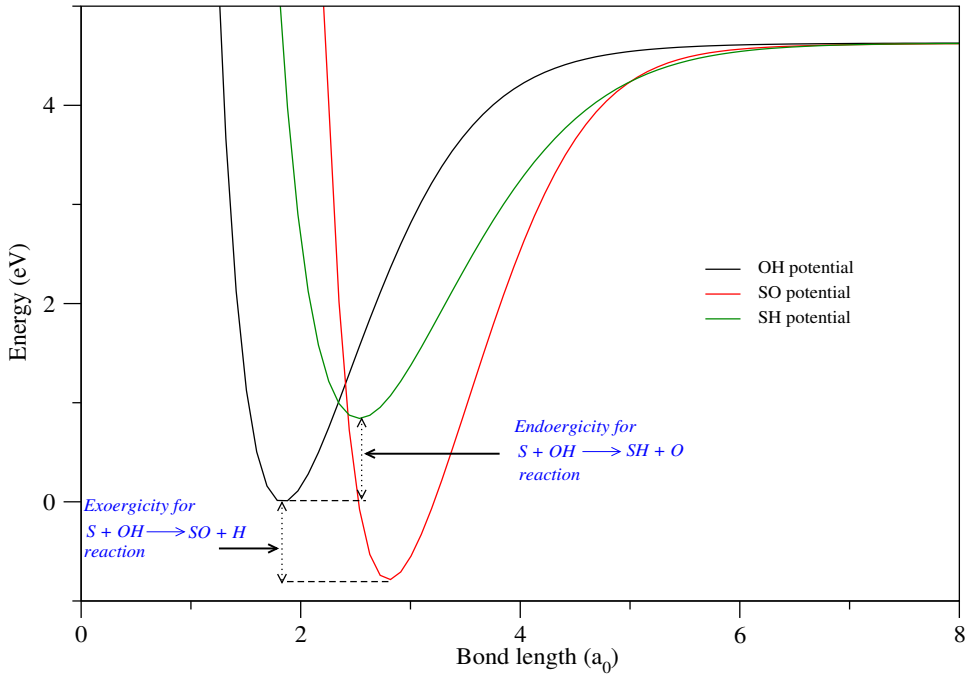

Figure 1.1: Potential energy curves of OH, SO and SH diatoms calculated by using the electronic ground DMBE PES [9] of the HSO reactive system. The third atom is kept infinitely separated from the other two atoms in each case.

Table 1.1: Geometries and the energies of the stationary points of the triatomic HSO system on its electronic ground DMBE PES

Stationary point description	$R_{OH}/R_{SH}/R_{SO}$ (a_0)	calculated energy value (eV)
HSO minima	4.4857/2.6190/2.8569	∼-3.43
HOS minima	1.8233/4.0819/3.0983	∼-3.38
S...HO minima	1.8360/5.2513/7.0873	∼-0.14
SH...O minima	5.4670/2.5142/7.9812	∼0.78
TS1	2.5679/2.7084/3.1668	∼-1.41
TS2	4.0509/6.0086/2.8296	∼-0.71
TS3	7.1363/2.5335/6.3778	∼0.83
TS4	1.8379/5.4132/6.5254	∼-0.12

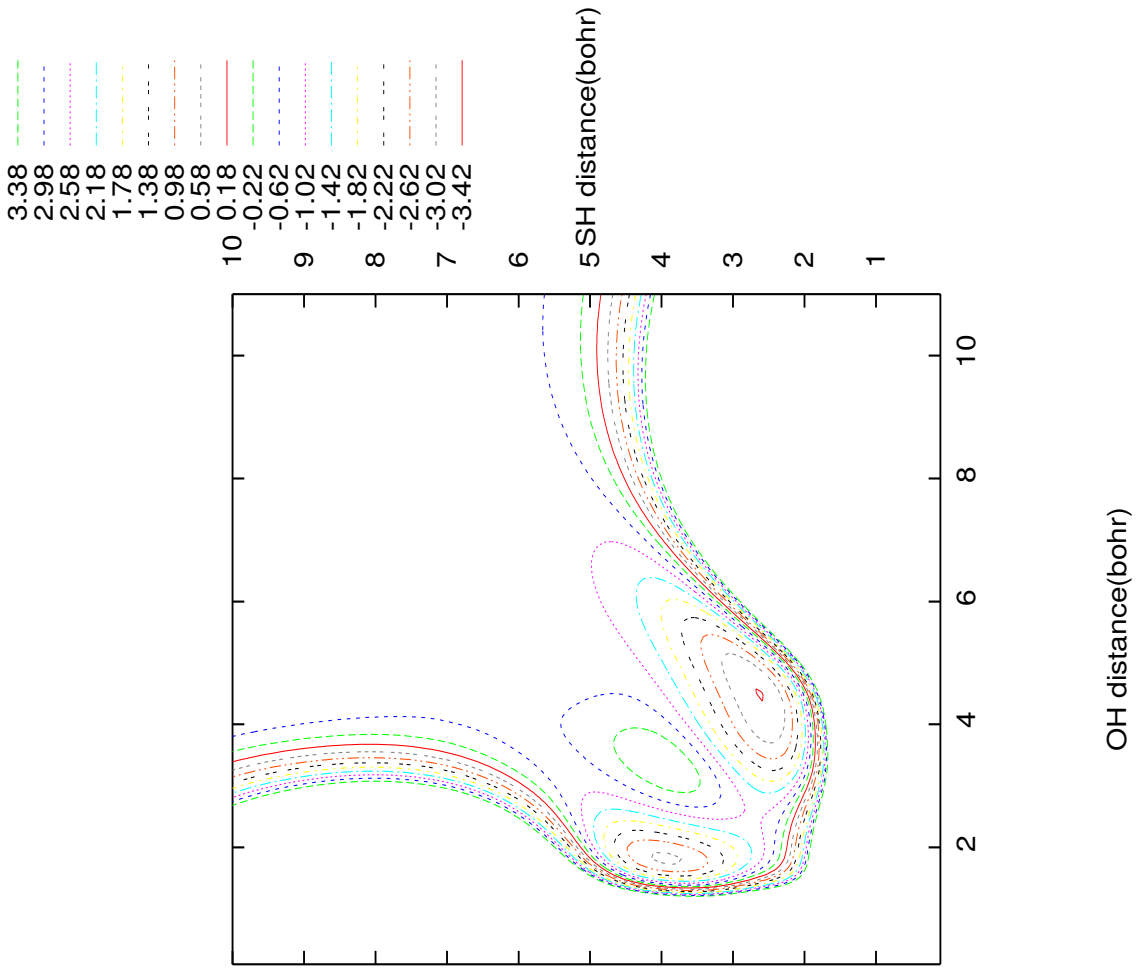

Figure 1.2: Potential energy contours for the DMBE PES of the SOH reactive system on its electronic ground state as a function of OH and SH bond distances. The SO bond distance is fixed at ∼2.8569 a_0 and the energies are given in eV.

or it can reach to the more stable HSO well by crossing the isomerization barrier (TS1) followed by proceeding to the SO + H product valley [20]. The minimum energy paths (MEPs) for R1 at different approach angles of S atom are shown and discussed in detail in Chapter 3.

1.1.2 Electronic ground, First excited and second excited PESs of the COH/HCO reactive system

The $C(^3P) + OH(X^2\Pi) \rightarrow CO(X^1\Sigma_g^+) + H(^2S)$ reaction (say R2) takes place on the electronic ground (X^2A') PES of the HCO reactive system, whereas, the four excited electronic states, $1^2A''$, $1^4A''$, $1^4A'$ and $2^2A'$ correlate to the, $C(^3P) + OH(X^2\Pi) \rightarrow CO(a^3\Pi) + H(^2S)$, reaction (say R3) [21, 22]. Zanchet *et. al.* have constructed global *ab initio* PESs for the electronic ground (X^2A'), first excited ($1^2A''$) and second excited ($1^4A''$) electronic states. The essential features of these PESs are discussed in the following paragraphs.

1.1.2.1 Electronic ground PES

A global *ab initio* PES for R2 taking place on the electronic ground state (X^2A') of the HCO reactive system is constructed by Zanchet *et al.* by using the internally contracted multireference singles and doubles configuration interaction (MR-SDCI) method followed by Davidson correction [21]. The authors used Dunning's aug-cc-pVQZ basis set for the calculation and the surface has been constructed by fitting ∼2000 geometries analytically by means of reproducing kernel Hilbert space (RKHS) method.

The reaction R2 is found to be highly exoergic (∼6.4 eV) and barrierless (with respect to the reagent asymptote) on the electronic ground X^2A' PES, whereas,

five potential barriers are found on it [21]. Among these five saddle points, two correspond to the inversion barriers for the HCO and COH complexes, while the isomerization barrier between these two conformers represents third saddle point. The barriers for the dissociation of HCO and COH complexes into product CO + H channel correspond to the other two saddle points. In addition to these saddle points, three potential minima are located on this surface and these correspond to the HCO, COH collisional complexes and CO + H product asymptote, respectively. The structures and energies of the HCO and COH minima and five saddle points are given in Table 4 and Table 5 of Ref. [21], whereas, the same have been reproduced here in Table 1.2 and Table 1.3 for a ready reference to the readers. From Table 1.2 it can be seen that the COH minima is being metastable with respect to the product channel. These topographical features will be revisited during the discussion of the dynamics on the excited states in latter chapters in conjunction with the same on the electronic ground state of the HCO reactive system.

1.1.2.2 First ($1^2A''$) and second ($1^4A''$) excited PESs

Unlike R2 reaction on the X^2A' state, the R3 reaction on both first and second excited electronic states of HCO reactive system is less exoergic ($\sim$0.41 eV). Zanchet *et al.* have constructed *ab initio* global PESs [22] for both first ($1^2A''$) and second ($1^4A''$) excited states by MR-SDCI method including Davidson correction. Though the exoergicity of R3 reaction is $\sim$0.41 eV on both excited PESs, but their topographical features are largely different from each other.

The R3 reaction is barrierless on the $1^2A''$ PES for a wide range of favorable approaches of the attacking atom and the surface contains two potential wells and two saddle points on it [22]. The two minima correspond to the HCO ($\sim$-

Table 1.2: Structure and relative energies of the HCO and COH minima on the electronic ground (X^2A') PES of C + OH collisional system, (Reproduced from Ref. [21]).

Parameter description	Parameter value
HCO *Minimum*	
Energy relative to reagent asymptote (C + OH)	-7.26 eV
R_{CH}	2.10 a_0
R_{CO}	2.24 a_0
$\angle$HCO	126^o
R/r/θ	2.03 a_0/3.87 a_0/151^o
COH *Minimum*	
Energy relative to reagent asymptote (C + OH)	-5.50 eV
R_{OH}	1.85 a_0
R_{CO}	2.44 a_0
$\angle$COH	111^o
R/r/θ	2.48 a_0/1.85 a_0/67^o

Table 1.3: Structure and relative energies of the saddle points on the electronic ground (X^2A') PES of C + OH collisional system, (Reproduced from Ref. [21]).

Parameter description	Parameter value
Saddle point - I (H-CO saddle point)	
Energy relative to	
reagent asymptote (C + OH)	-6.34 eV
R_{CH}	3.46 a_0
R_{CO}	2.15 a_0
$\angle$HCO	115^o
R/r/θ	1.95 a_0/4.79 a_0/134^o
Saddle point - II (HCO inversion saddle point)	
Energy relative to	
reagent asymptote (C + OH)	-6.18 eV
R_{CH}	2.01 a_0
R_{CO}	2.30 a_0
$\angle$HCO	180^o
R/r/θ	2.04 a_0/4.31 a_0/180^o
Saddle point - III (CO-H saddle point)	
Energy relative to	
reagent asymptote (C + OH)	-5.03 eV
R_{OH}	2.32 a_0
R_{CO}	2.26 a_0
$\angle$COH	120^o
R/r/θ	2.33 a_0/2.32 a_0/57^o
Saddle point - IV (COH inversion saddle point)	
Energy relative to	
reagent asymptote (C + OH)	-4.23 eV
R_{OH}	1.95 a_0
R_{CO}	2.46 a_0
$\angle$COH	180^o
R/r/θ	2.58 a_0/1.95 a_0/0 ^{o}
Saddle point - V (isomerization saddle point)	
Energy relative to	
reagent asymptote (C + OH)	-4.44 eV
R_{CH}	2.48 a_0
R_{CO}	2.40 a_0
$\angle$HCO	52.8^o
R/r/θ	2.35 a_0/2.17 a_0/ 112^o

Table 1.4: Geometrical structure and relative energies of the two minima on the first excited ($1^2A''$) PES of C + OH collisional system, (Reproduced from Ref. [22]).

Parameter description	Parameter value
HCO *Minimum*	
Energy relative to reagent asymptote (C + OH)	-6.16 eV
R_{CH}	2.01 a_0
R_{CO}	2.25 a_0
$\angle$HCO	180^o
R/r/θ	2.00 a_0/4.26 a_0/180^o
COH *Minimum*	
Energy relative to reagent asymptote (C + OH)	-4.63 eV
R_{OH}	1.82 a_0
R_{CO}	2.49 a_0
$\angle$COH	116^o
R/r/θ	2.54 a_0/1.82 a_0/61^o

6.16 eV) and COH (∼-4.63 eV) collision complexes, respectively. The first saddle point is the isomerization barrier between these two isomers and the second one correspond to the inversion barrier of COH complex. The energies of the isomerization and inversion saddle points are ~ -3.11 eV and ~ -4.34 eV, respectively. It is better to mention that the energies of the stationary points given here are relative to the energy of the reagent asymptote which is set to be equal to 0.0 eV. The structures and relative energies of these stationary points are given in Table 1 and Table 2 of Ref. [22] and they are reproduced here in Table 1.4 and Table 1.5 for a ready reference. From Table 1.5 it can be seen that unlike electronic ground state, the isomerization barrier is energetically lower than the product channel on the $1^2A''$ state and hence the HCO complex is predicted to play a major role in the dynamics on the latter state [22].

The OH, CO and CH diatomic potentials calculated by using both the $1^2A''$

Table 1.5: Geometrical structure and relative energies of the saddle points on the first excited ($1^2A''$) PES of C + OH collisional system, (Reproduced from Ref. [22]).

Parameter description	Parameter value
Saddle point - I (isomerisation saddle point)	
Energy relative to reagent asymptote (C + OH)	-3.11 eV
R_{CH}	2.34 a_0
R_{CO}	2.37 a_0
$\angle$HCO	68^o
R/r/θ	2.82 a_0/2.64 a_0/121^o
Saddle point - II (COH inversion saddle point)	
Energy relative to reagent asymptote (C + OH)	-4.34 eV
R_{OH}	1.79 a_0
R_{CO}	2.41 a_0
$\angle$COH	180^o
R/r/θ	2.52 a_0/1.79 a_0/0^o

and $1^4A''$ PESs and by keeping the third atom far away from the diatom in each case are presented here in Figure 1.3 in different colours. The potentials calculated by using $1^4A''$ PES are shown in solid lines, whereas, the same calculated from $1^2A''$ PES are shown in dashed lines. From Figure 1.3 it can be seen that the diatomic potentials calculated from both the excited states are almost identical and the R3 reaction is exoergic on these states with an energy value $\sim$0.41 eV as it is reported in Ref. [22] and the other product channel, CH + O is highly exoergic ($\sim$1.0 eV).

Like electronic ground state, the second excited PES ($1^4A''$) [22] has eight stationary points on it. The two deep potential wells correspond to the HCO and COH complexes with energy $\sim$-2.25 eV and $\sim$-1.85 eV (the energy of the C + OH reagent asymptote is considered as zero), respectively, and the, CO($a^3\Pi$) + H(^{2}S), product asymptote contains three minima. On the other hand, among

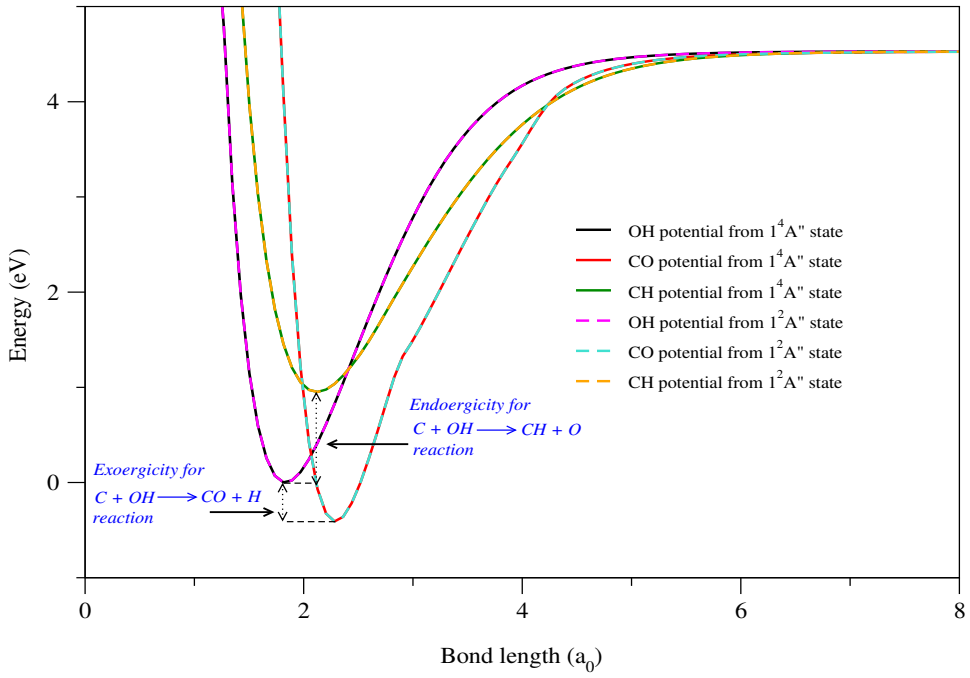

Figure 1.3: Potential energy curves of OH, CO and CH diatoms calculated by using the first ($1^2A''$) and second ($1^4A''$) excited PESs of HCO reactive system are presented as a function of the bond length in different colours. The potential energy curves calculated from the first and second excited states are shown in dashed and solid lines, respectively.

five saddle points, two correspond to the barrier for the dissociation of HCO and COH complexes into the, CO + H, products. The isomerization barrier between the HCO and COH complexes, and the inversion barriers of the latter two collisional complexes characterize the other three saddle points on the surface. A 2-D contour plot of the $1^4A''$ PES is presented in Figure 1.4 as a function of the R and γ (Jacobi coordinates are discussed in detail in chapter 2). The CO distance is fixed at 2.60 a_0 here. The two potential wells corresponding to the HCO and COH complexes and the saddle point between them are clearly visible in Figure 1.4. The energies of the HCO and COH wells and the five saddle points are computed on the $1^4A''$ PES. The set of Jacobi coordinates taken from Table 1 and Table 2 of Ref. [22] are used as inputs in the calculations. The values of the Jacobi coordinates, and calculated internuclear distances and energies (relative to the C + OH reagent asymptote) of the seven stationary points are given in Table 1.6. The numbers presented in the fourth column of Table 1.6 agree well with the energies given in the second column of Table 1 and Table 2 of Ref. [22]. A careful examination of the energies of the stationary points given in Table 1.6 suggests that R3 reaction can follow two major paths on the $1^4A''$ PES once the COH minimum is accessed by the reactive system at the entrance channel : (i) The COH complex can dissociate into the products directly by crossing the barrier of energy $\sim$ 0.03 eV (Path I). This path is classically forbidden at low energies. (ii) The COH complex can isomerize to HCO by overcoming the barrier of energy $\sim$ -0.33 eV followed by the dissociation of the latter into products by crossing the barrier of energy $\sim$ -0.11 eV (Path II). As both the barriers have energy less than reagent channel, Path II is feasible at any value of collision energy, whereas, the other path is possible only at higher collision energies unless significant tunneling takes place. Moreover, unlike electronic ground [21] and

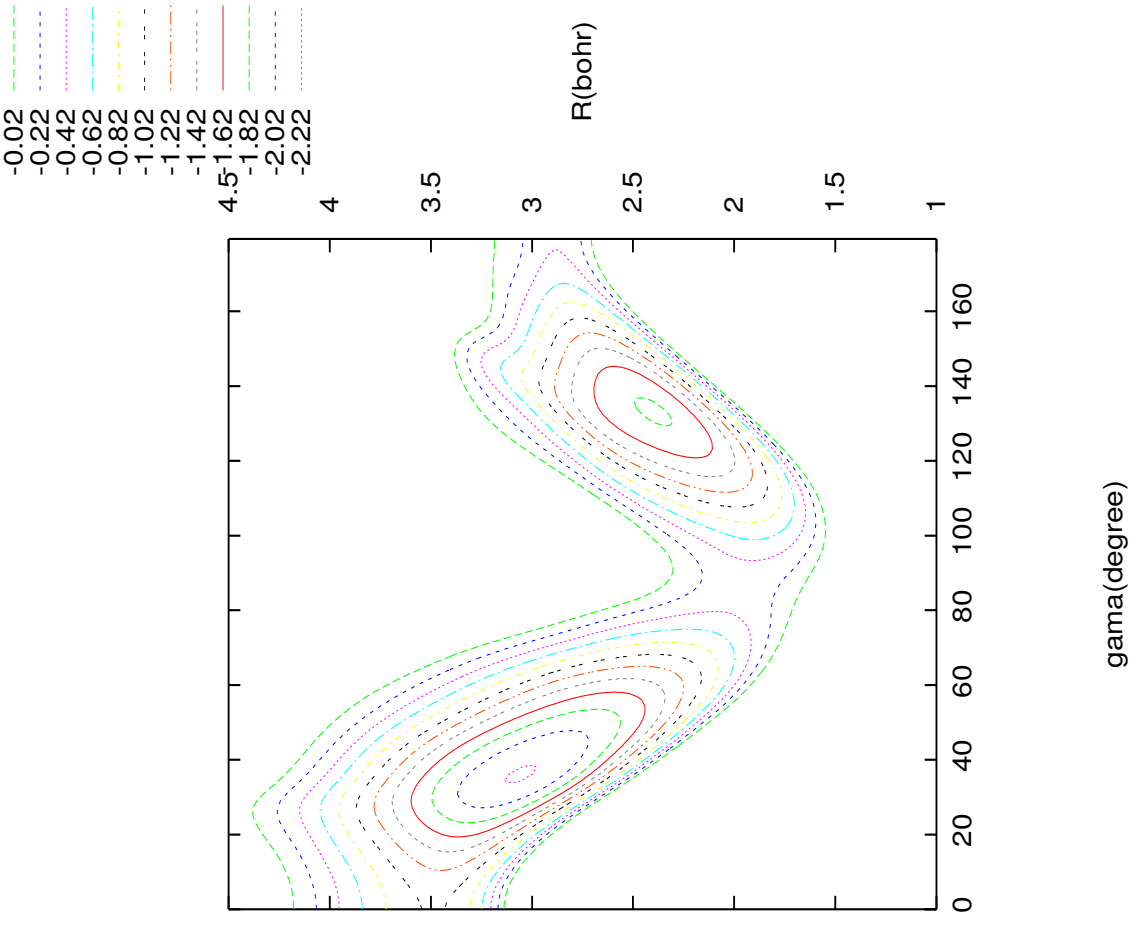

Figure 1.4: 2-D contour plot of the second excited ($1^4A''$) PES of HCO reactive system as a function of the R and γ Jacobi coordinates. The CO distance is kept at 2.60 (a_0) here and energies are given in eV.

Table 1.6: The geometries in terms of the Jacobi and internal coordinates and the energies of various stationary states on the second excited ($1^4A''$) PES of the HCO reactive system

Stationary point description	$R(a_0)/r(a_0)/\gamma$(degree)	$R_{CO}/R_{OH}/R_{CH}$ (a_0)	Energy (eV)
HCO minima	2.38/4.06/151	2.593/4.060/2.085	∼-2.22
COH minima	2.66/1.83/72	2.628/1.830/3.587	∼-1.85
Isomerization saddle point	2.58/2.34/121	2.654/2.340/2.377	∼-0.33
COH inversion saddle point	2.68/1.77/0.0	2.575/1.770/4.345	∼-0.41
HCO inversion saddle point	2.39/4.67/180	2.666/4.670/2.003	∼-1.05
CO-H saddle point	2.43/2.86/56	2.339/2.860/4.522	∼0.03
H-CO saddle point	2.20/4.24/121	2.339/4.24/3.422	∼-0.11

first excited [22] states, the reagents approach along a barrierless path for a very narrow angular approach on the second excited state [22]. Consequently, it can be anticipated that the narrow angular approach and the presence of a late barrier at the exit channel may reduce the reactivity on the $1^4A''$ state compared to the same on the electronic ground and first excited states of HCO reactive system [23].

1.1.3 Electronic ground BKMP2 PES of the H_3 reactive system

Numerous of PESs [24–31] have been developed for the description of the benchmark H-exchange reaction, $H_A + H_BH_C \rightarrow H_AH_B + H_C$, occurring on its electronic ground state. The BKMP2 PES developed by Boothroyd *et al.* [28] is used here to study the state-to-state dynamics (see chapter 6) of this reaction as the surface is fairly accurate to reproduce experimentally measured dynamical attributes [32, 33]. The BKMP2 surface is an improvement over an earlier

surface, the BKMP PES developed by the same authors [27]. The refined surface is constructed on the basis of 8701 *ab initio* energies and posses the same functional form as the previous BKMP PES [27]. In BKMP2 PES, the zero of energy corresponds to the fully dissociated H + H + H conformation and the relative energy of the minimum of H_2 diatomic potential is ∼-0.1745 E_h [28]. Contour diagrams of BKMP2 PES for γ_c' [angle between r1(=H_AH_B internuclear distance) and r2(=H_BH_C internuclear distance)]= 180^0, 90^0 and 45^0 are shown in Figure 1.5, 1.6 and 1.7, respectively. From Figure 1.5, the barrier height along the collinear approach, γ_c'=180^0 is found to be ∼0.42 eV (∼9.613 kcal/mol) [28]. Similar contour plot is also shown by Jankunas *et al.* [34]. Though the features of the contour plot is similar for the perpendicular approach, γ_c'=90^0 the barrier height increase noticeably to ∼1.2 eV (see Figure 1.6). Whereas, the reaction is energetically infeasible for the sideways approach, γ_c'=45^0 (see Figure 1.7). Thus, it can be concluded that the collinear approach is most favorable and it posses a barrier of height ∼0.42 eV for the H-exchange reaction.

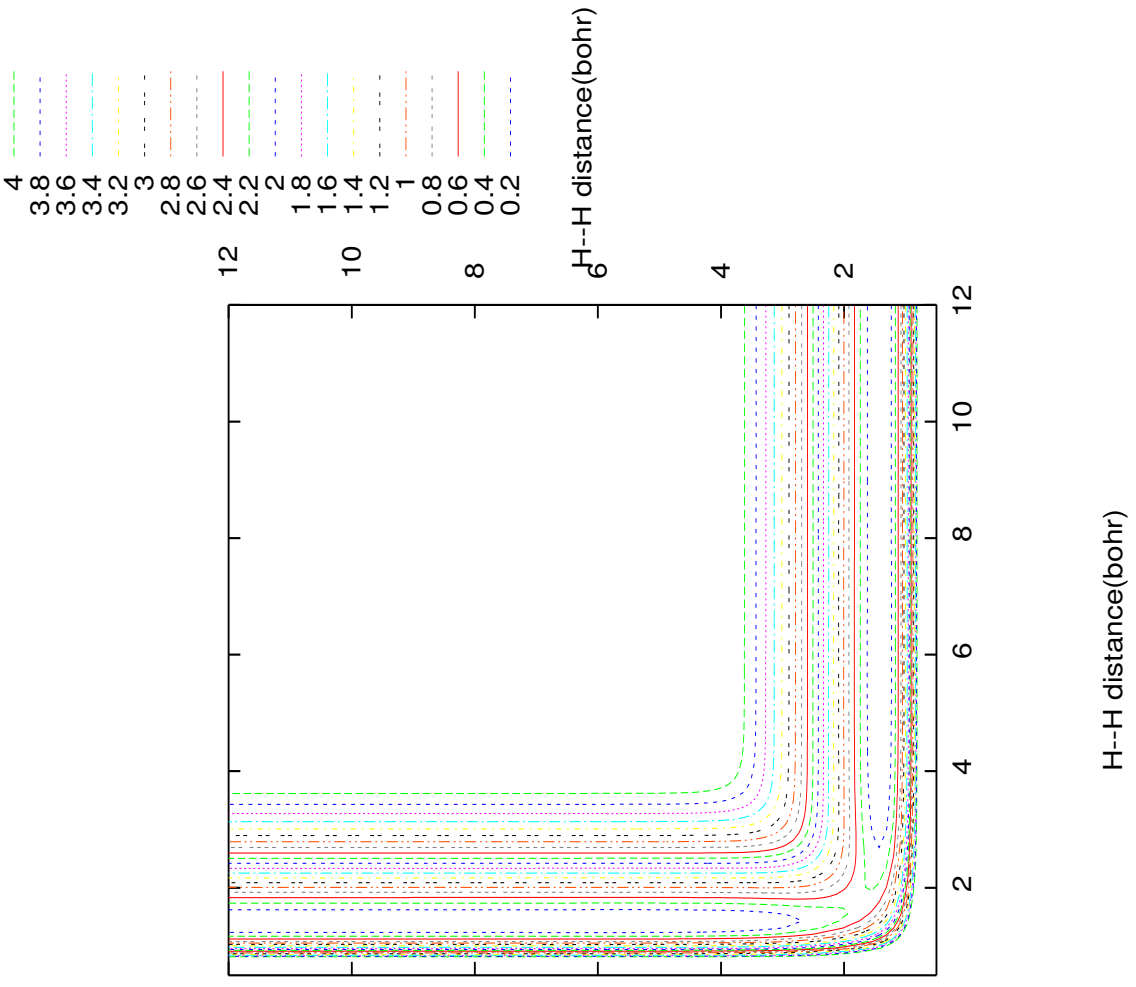

Figure 1.5: 2-D contour plot of the BKMP2 PES for γ_c'=180^0. Energies are given in eV and see text for further details.

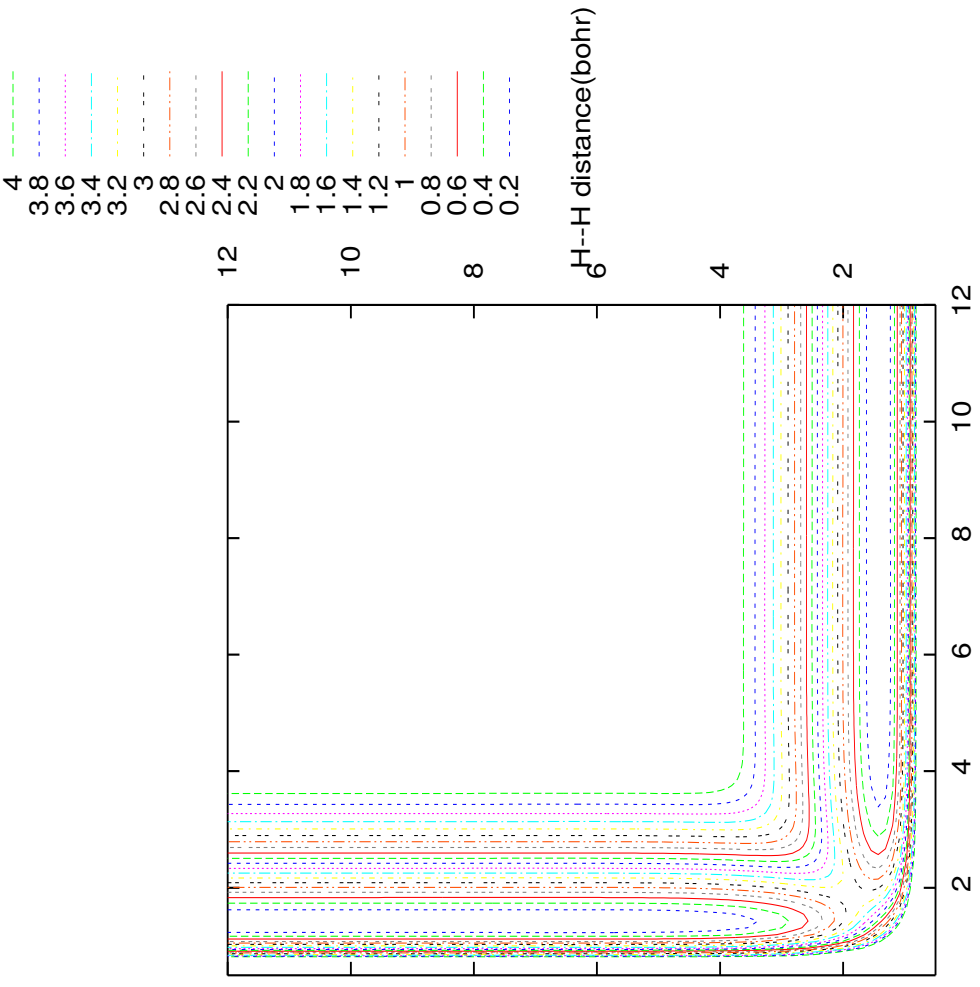

Figure 1.6: 2-D contour plot of the BKMP2 PES for γ_c'=90^0. Energies are given in eV and see text for further details.

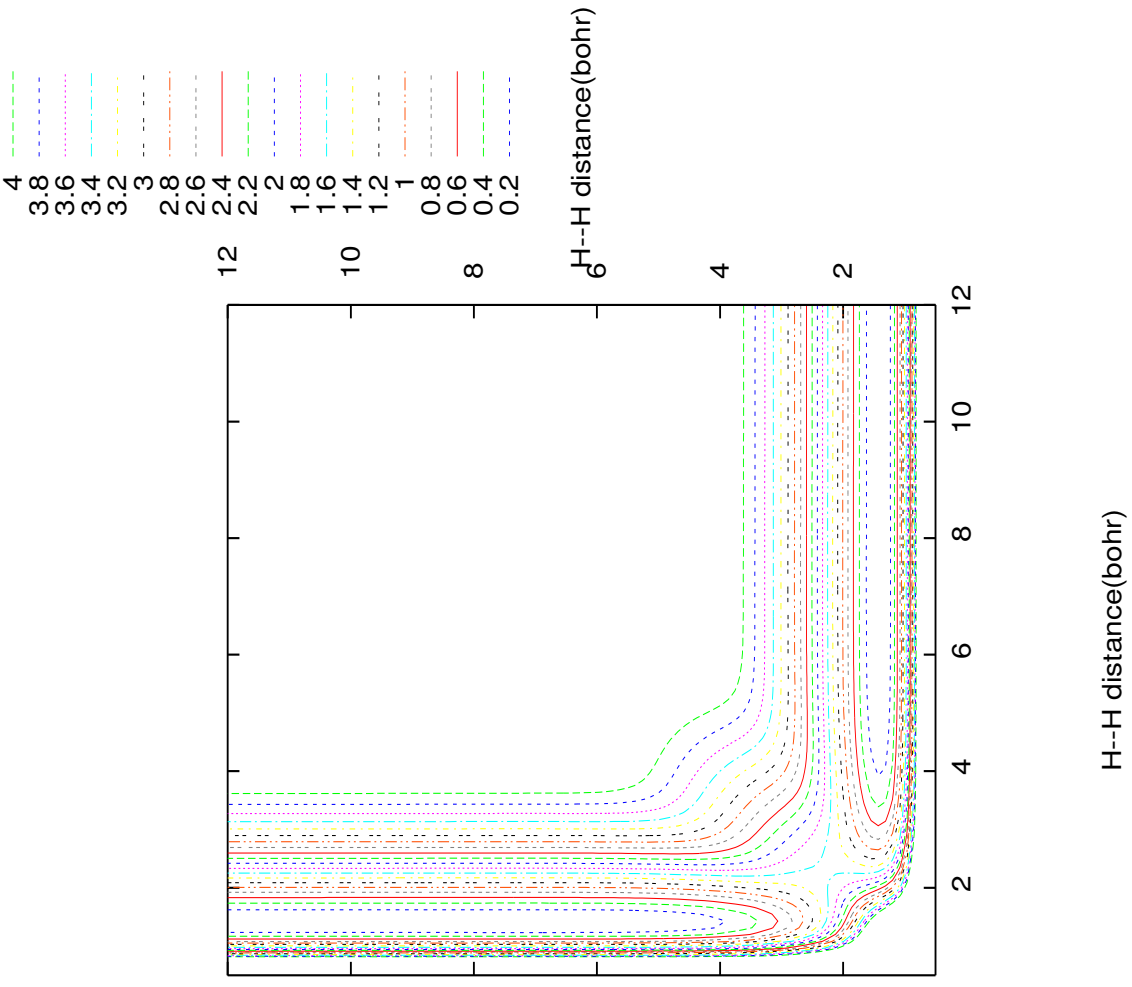

Figure 1.7: 2-D contour plot of the BKMP2 PES for γ_c'=45^0. Energies are given in eV and see text for further details.

1.2 Current state of research and the objective of the present work

In the following, an overview of the current state of research and the objective behind the present work is discussed.

1.2.1 Quantum dynamics of S + OH reaction on its electronic ground state

The S + OH → SO + H reaction plays an important role in the formation of SO in interstellar dust clouds [35]. This reaction occurs between an open shell atom and a free radical and it is known that theoretical and experimental studies are difficult to be carried out for such reactions. Experimentally, it is a challenging task to make this reaction pseudo-first-order by the generation of one of the reactants in large excess compared to the other and also it is very cumbersome to measure the concentrations to calculate the rate constant because of high reactivity of the reagents. On the other hand, from theoretical point of view the presence of wells on corresponding PES [9] makes it difficult to obtain converged dynamics results. Nevertheless, various attempts are made to study this reactive system [36–46].

The S (^{3}P) + OH ($X^2\Pi$) → SO ($X^3\Sigma^-$) + H (^{2}S) (R1 as defined in section 1.1.1) reaction occurs on the electronic ground ($\tilde{X}^2A''$) PES [9] of HSO reactive system and it progresses through the formation of two stable collision complexes, HSO and SOH, respectively. The essential features of the electronic ground ($\tilde{X}^2A''$) PES are discussed already in section 1.1.1.

The MEPs for the formation of HSO and HOS isomers are computed by Xantheas and Dunning [40]. They found a barrier of ∼2.4 kcal/mol along the

MEP leading to HOS, whereas, no barrier is found along the path leading to the other isomer. Later, Martínez-Nunez *et al.* carried out an unimolecular reaction dynamics study for HSO [42] by using the DMBE PES [9]. These authors predicted that at low energies the system favors the isomerization path, whereas, with the increase of energy the dissociation path leading to the formation of SO + H becomes more important. Jourdain and co-workers measured the rate constant for R1 and a value of $(6.6\pm1.4)\times10^{-11}$ $cm^3s^{-1}molecule^{-1}$ at 298 K is reported by them [43]. It is the only experimentally measured rate constant value available till date. On the other hand, Sendt and Haynes have calculated the rate constant [44] by using Rice-Ramsperger-Kassel-Marcus (RRKM) theory and a value of 6.6×10^{-10} $cm^3s^{-1}molecule^{-1}$ is found which is 10 times larger than the experimentally measured value of Jourdain *et al.* [43]. Jorfi and Honvault studied the dynamics of the S + OH $\rightarrow$ SO + H reaction quantum mechanically for the first time [45] by using TIQM method and the DMBE PES [9]. They reported total, product vibrationally and rotationally state-resolved reaction probabilities as a function of collision energy for the total angular momentum, J=0. They have also calculated a temperature dependent state-specific rate constant where reaction probabilities for $J>0$ were obtained by using J-shifting approximation. Later, these authors employed the quasi classical trajectory (QCT) method to calculate ICS, DCS, rate constant, rotational and vibrational product energy distribution, and the the average lifetime of the intermediate collision complexes [46]. Though the rate constants calculated by TIQM and QCT methods are in good accord with each other, they are not in agreement with the experimental estimate at 298 K. Moreover, the results of QCT study suggest the formation of intermediate collision complex of life time more than a rotational period.

The objective of the work presented in chapter 3 is to study the initial state-

selected dynamics of R1 reaction and calculate total reaction probabilities, ICSs, state-specific rate constants by using the electronic ground DMBE PES [9] and a TDWP propagation approach. As the time-dependent approach followed here is computationally less expensive than TIQM method, probabilities for $J > 0$ are also calculated within coupled-states (CS) (or centrifugal sudden) approximation [47,48]. ICSs (upto 0.5 eV collision energy) are calculated by including all partial wave contributions of J=0-138, J=0-158, J=0-175 and J=0-180 for reagent OH in its v=0, 1, 2 and 3 vibrational levels, respectively. State-specific rate constants are calculated only for OH(v=0). The effect of rotational and vibrational excitations of reagent OH on the dynamics is also investigated. The results of the present study are compared with those available in the literature.

1.2.2 Quantum dynamics of the C + OH reaction on its excited states

As discussed earlier in section 1.1.2, the C (^{3}P) + OH ($X^2\Pi$) $\rightarrow$ CO ($X^1\Sigma^+$) + H (^{2}S), reaction (R2) occurs on the electronic ground (X^2A') [21] PES of HCO reactive system. The dynamics of R2, including the effects of internal excitations of reagent diatom is studied by various theoretical methods [49–54]. ICSs calculated by QCT study are found to be insensitive to internal excitations of reagent OH [49], whereas, slight dependence of DCSs on reagent rotational excitation is found in a latter QCT study [51]. Furthermore, decrease in reactivity at low collision energies with vibrationally hot reagent OH is obtained by quantum mechanical calculations [54] which is in contrast to the results of QCT study. The results of all these studies suggest a predominate direct mechanism for R2 on its electronic ground state, X^2A'. Several stereodynamical studies are also carried out for R2 in the recent past [55–59]. According to the stereodynamical study

of Huang, an abstraction path which involves the formation of short-lived COH collisional complex is followed by R2 at low collision energies. Whereas, the reaction proceeds through an insertion path via the formation of long-lived HCO intermediate at higher energies [59].

The, C (^{3}P) + OH ($X^2\Pi$) $\rightarrow$ CO ($a^3\Pi$) + H(^{2}S), reaction (R3) occurs on the first ($1^2A''$) and second ($1^4A''$) excited states of HCO reactive system [22]. A detail discussion of the topographical features of these two PESs is given in section 1.1.2.2. Jorfi *et al.* have studied the dynamics of R3 on its first excited ($1^2A''$) PES by employing a TIQM method. They have calculated total and state-to-state reaction probabilities for J=0 upto 0.9 eV collision energy [60]. Dense resonance oscillations are found in probabilities of R3 on its $1^2A''$ state for J=0 [60] which is in strong contrast to the probability profile of R2 [54] on its X^2A' PES. Jorfi *et al.* have also calculated a state-specific rate constant of R3 by using J-shifting approximation for $J >$0 and compared this with QCT results. A relatively good agreement is found between the rate constants obtained by QCT and TIQM methods. The reagent diatom was kept in its ground ro-vibrational level, OH (v=0, j=0) in this TIQM study [60]. Rao *et al.* employed a TDWP propagation approach to investigate the dynamics of R3 on its $1^2A''$ PES in more detail [61]. They have calculated initial state-selected total reaction probabilities for $J \geq$0, converged ICSs upto 1.0 eV collision energy and state-specific thermal rate constants. CS approximation [47, 48] is used for the calculation of probabilities for $J >$0. Effect of internal excitations of reagent OH on the reactivity of R3 is also studied by Rao *et al.* [61]. Reactivity is found to decrease with reagent rotational excitation, whereas, no such noticeable impact of vibrationally hot reagent OH on the dynamics is found. TDWP results of Rao *et al.* [61] are in good agreement with those obtained by Jorfi *et al.* [60]. Later, Jorfi *et al.*

employed statistical quantum method (SQM) to study the dynamics of R3 on its $1^2A''$ PES further [62]. Though not very prominent, decrease of reactivity with reagent rotational excitation is also found in this study similar to the findings of Rao *et al.* [61].

Jorfi *et al.* have investigated the dynamics of R3 on its second excited ($1^4A''$) PES at the state-to-state level by a TIQM formalism [22,63]. They have reported total and state-to-state reaction probabilities for J=0, rotational and vibrational distributions of the product diatom at some selected collision energies and an approximate state-specific rate constant by employing J-shifting approximation for J >0 probabilities. The dynamics is investigated by keeping the reagent OH in its ground ro-vibrational level, OH (v=0, j=0). The rate constant calculated by TIQM method [63] is in good accord with the same obtained by using QCT method below 60 K. However, significant disagreement is noticed at higher temperatures. This is quite surprising as quantum effects are usually less important with the increase of temperature. The difference is ascribed to the use of J-shifting approximation in TIQM study and the intrinsic shortcomings of the QCT approach [63]. Zanchet *et al.* employed a time-dependent quantum mechanical (TDQM) approach [64, 65] for carrying out the dynamics of R3 on its $1^4A''$ PES in a subsequent study [66]. Reaction probabilities, ICSs and DCSs are reported for reagent OH (v=0, j=0) where all partial wave contributions for J=0-50 are considered to obtain cross sections. Coriolis coupling terms present in the Hamiltonian are also considered in the dynamics study. Moreover, in addition to the time-dependent approach, they also carried out QCT and statistical calculations and compared the results. Dense resonance oscillations in probabilities, statistical product vibrational distributions and forward-backward symmetry in DCSs are found in these studies [63, 66]. An indirect mechanism via the forma-

tion of long lived intermediate collisional complexes of R3 on its $1^4A''$ PES is suggested [63, 66].

It emerges from the above discussion that there is lack of investigation involving internal excitations of reagent OH on the dynamics of R3 on its $1^4A''$ state. Moreover, it is reiterated here that despite same exoergicity of R3 occurring on its two excited states, the topographies of corresponding PESs are largely different. This can be seen from the schematic energy diagram presenting the important stationary points on the three lowest lying states of HCO reactive system given by Jorfi *et al.* [63]. It is also believed that the fate of an exothermic barrierless reaction occurring on a PES possessing wells on it largely depends on three factors - the mass combinations of the participating atoms, exoergicity and the topographical details [20]. The first two factors remain identical for R3 on its $1^2A''$ and $1^4A''$ states and hence it is worthwhile to investigate how the topographical difference of these two PESs can solely affect the dynamics.

The aim of the work presented in chapter 4 is to investigate the initial state-selected dynamics of R3 on its second excited ($1^4A''$) state involving the effects of internal excitations of reagent OH by employing a TDWP propagation approach. Initial state-selected total reaction probabilities for $J \geq 0$ and ICSs are reported as a function of collision energy. Reaction probabilities for $J > 0$ are calculated within the CS approximation [47, 48] and converged ICSs upto 0.25 eV collision energy are obtained by including partial wave contributions for J=0-48 for OH (v=0, j=0). The results are compared with those obtained by using other theoretical methods [63, 66]. Finally, the mechanistic details of the, C + OH $\rightarrow$ CO + H, reaction occurring on its $1^2A''$ and $1^4A''$ PESs are discussed by comparing present results with those of Rao *et al.* [61] in relation to the topographical features of these PESs.

The comparison of the dynamics of R3 on its $1^2A''$ and $1^4A''$ PESs has been further extended at the state-to-state level in chapter 5. The objective of the work presented in chapter 5 is to study the effect of vibrational excitations of reagent OH on the state-to-state dynamics of R3 occurring on its excited states by using a TDQM approach [64, 65, 67]. Total and state-to-state reaction probabilities are calculated for the total angular momentum, J=0. Moreover, product vibrational level distributions are also calculated at some selected values of collision energy.

1.2.3 Effect of vibrationally hot reagent H_2 on the state-to-state dynamics of the benchmark H-exchange reaction

The collision between a H_2 molecule and an incoming H atom to produce a new H_2 molecule and a recoil H atom, $H_A + H_BH_C \rightarrow H_BH_C + H_A$ (atoms are labeled here to better understand the exchange), is commonly known as the H-exchange reaction. It is one of the most important elementary reactions which is used as a benchmark for major theoretical advances in the field of reaction dynamics and the concepts of PES, transition-state emerged from the study of this reaction [32, 68–71]. In a review article [32] Aoiz *et al.* discussed the sequential progress in the study of this reaction, the convergence between theoretical calculations and experimental measurements, the relation between forward scattering and reaction time, presence of resonances in dynamical observables, effect of geometric phase on the dynamics and the rotational distribution in reactive and inelastic scattering. In a later review article [72], Yang has also addressed different aspects of this reaction. Though kinetic studies started in way back in 1920-1930 [32], still this H-exchange reaction with its isotopic variants is used for the development of

new concepts and methodologies.

On the theoretical front, the presence of only three electrons and three light nuclei has made the electronic structure and dynamics calculations computationally easier. Several PESs such as LSTH [24, 25], DMBE [26], BKMP [27] and BKMP2 [28], surface of Wu *et al.* [29] and Meilke *et al.* [30] are constructed to investigate the dynamics of the H-exchange reaction by different theoretical methods. Abrol and Kuppermann have developed a diabatic potential matrix [31] which is recently used to study the nonadiabatic effects on the H-exchange reaction at the state-to-state level [73].

On the other hand, experiments were difficult to carry out due to lack of permanent dipole moment of H_2 molecule and the position of electronic absorption spectra in vacuum UV [32, 71]. The availability of advance experimental methods [72] and substitution of H atom(s) with its heavier isotopes to distinguish products from reactants have made the measurement of state-resolved DCSs possible. Theoretical predictions are precisely compared with experimentally measured DCSs and good agreement between them has been reported [32].

Recently Jankunas *et al.* have modeled the H-exchange reaction as molecular billiards [34] within the BO approximation when the nuclei are treated as classical particles. They expected backward scattering with little rotational excitation of product diatom from nearly head-on collisions, whereas, sideways scattering is likely to occur with rotationally excited product from glancing collisions. They carried out experiments for, H + D_2 $\rightarrow$ HD + D, reaction to validate their anticipation. DCSs are measured at few collision energies for product HD in different ro-vibrational levels and these are compared with available quantum mechanical results [34]. Their expectation is fulfilled for HD (v'=1,2) but it failed for HD (v'=4) and a trend opposite to negative $j' - \theta$ [74] correlation is

found in the latter case [34].

In reaction dynamics, a reaction is commonly described by its MEP and for H-exchange reaction, the collinear approach of three nuclei is the lowest energy configuration [34]. The barrier of ∼0.42 eV (see Figure 1.5) along the purely repulsive MEP must be surmounted by the reacting particles to proceed (see Figure 2 of Ref. [34]). Such purely repulsive MEP with a central barrier is inadequate to explain the unexpected behavior of DCSs [34]. The barrier height and the topography of reaction path largely depend on the vibrational levels of reagent and product diatoms and the path constructed by considering the energies of internal modes of triatomic species is known as vibrationally adiabatic potential/path [34, 75]. For H-exchange reaction attractive wells are found along its vibrationally adiabatic potentials [34, 75]. The surprising behavior of DCSs observed by Jankunas *et al.* [34] is attributed to the complex topography of vibrationally adiabatic potentials, formation of highly internally excited products with higher j' values from nearly collinear collisions with low impact parameters and the negligible contribution from the time-delayed mechanism for the formation of rotationally excited products. Highly internally excited product diatoms are lack of enough recoil energy to overcome high centrifugal barrier originating from collisions with high impact parameter. These findings suggest that the H-exchange reaction is not as simple as it is thought and it is only the beginning of detail understanding of this seemingly simple reactive system. Jankunas *et al.* suggested that the situation would be more complicated with an increase of translational energy of H-atom or if reagent diatom is internally excited to higher levels. In a subsequent investigation, Sneha *et al.* presented the angular distribution of, H + $D_2 \rightarrow$ HD (v'=4, j') + D, reaction at 3.26 eV collision energy [74]. They found that at such high collision energy, the expected negative $j' - \theta$ trend is followed

for v'=4 manifold and thus it supports the justification that the opposite trend followed earlier at 1.97 eV collision energy [34, 76] is due to the lack of enough recoil energy of the products.

The investigations carried out for the H-exchange reaction with internally excited reagent diatom are briefly outlined here. Kendrick *et al.* found significant geometric phase effects in total and state-to-state rate coefficients for the H + H_2 (v=4, j=0) → H_2 (v', j') + H reaction at ultracold conditions [77]. In another study, Kendrick showed the effect of geometric phase on the state-to-state probabilities for H + H_2 (v=1, j=0) → H_2 (v'=2, j') reaction upto 2.4 eV total energy [78]. Juanes-Marcos *et al.* also investigated the geometric phase effect for H + H_2 (v=0-1, j=0) reaction and they reported reaction probabilities, ICSs, DCSs and product distributions upto ∼2.5 eV total energy [79, 80]. Jiang and Guo calculated excitation functions for the H + H_2 (v=0-1, j=0) reaction to re-examine the well known Polanyi's rule and proposed a new model called sudden vector projection (SVP) as an alternative [81]. All these investigations employed the electronic ground BKMP2 PES of H_3 reactive system [28]. On the other hand Rao *et al.* studied the effects of rotational and vibrational excitations of reagent H_2 comprehensively for the first time by employing a TDWP propagation approach and the DMBE PES [26, 82, 83]. They investigated the effects of NAC on initial state-selected reaction probabilities and ICSs for, H + H_2 (v=0-10, j=0-10) → H_2 ($\sum v'$, $\sum j'$) + H, reaction [83] within CS approximation. Significant nonadiabatic effects are found for rotationally excited reagent H_2, whereas, vibrationally hot reagent H_2 could not bring such effects in the dynamics. Moreover, way back in 1981, Barg *et al.* studied the effects of internal excitations of reagent H_2 on the state-to-state dynamics of H-exchange reaction [84] by employing QCT method and Porter-Karplus [85] and LSTH PESs [24, 25]. They restricted the vi-

brational excitation of reagent H_2 upto v=2 and at a given translational energy, initial vibration was found to enhance the reactivity and also broaden the distribution in DCSs.

Hence, a comprehensive quantum mechanical investigation for the effects of internal excitations of reagent H_2 on the state-to-state dynamics of H-exchange reaction is in high demand at present in order to understand the mechanism of this seemingly simple reaction in more detail. The work presented in chapter 6 is aimed towards this goal. The effect of vibrational excitations of reagent H_2 on the, H + H_2 (v=0-5, j=0) $\rightarrow$ H_2 (v', j') + H, reaction is carried out by using the BKMP2 [28] PES and a TDQM [64, 65, 67] formalism. Total and state-to-state reaction probabilities, product vibrational level distribution, ICSs and state-to-state DCSs are reported here. To the best of our knowledge, the work presented in chapter 6 is going to be the first of its kind to include the effects of vibrational excitations of reagent H_2 on the state-to-state dynamics of the benchmark H-exchange reaction at length in a comprehensive manner.

1.3 Overview of the thesis

In chapter 2, the theoretical methodology and computational details to study the nuclear dynamics on adiabatic PESs are described in detail. The methods employed to investigate the initial state-selected and state-to-state dynamics are described in two separate sections, section 2.2 and 2.3, respectively. A brief discussion of the procedure for the construction of MEPs is given in section 2.4 of this chapter.

In chapter 3, the findings of the initial state-selected dynamics study of, S + OH $\rightarrow$ SO + H, reaction on its electronic ground state is presented. Total

reaction probabilities, ICSs and state-specific rate constants calculated by using the DMBE PES [9] and a TDWP propagation approach are shown. The effects of rotational and vibrational excitations of reagent OH on the dynamics are also presented in this chapter. Finally, the results are compared with those available in the literature.

Chapter 4 contains the results of the investigation of the initial state-selected dynamics of the C + OH → CO + H reaction on its second excited ($1^4A''$) [22] electronic state. Initial state-selected total reaction probabilities for $J \geq 0$ and ICSs calculated by employing a TDWP propagation approach are shown in this chapter as a function of collision energy. The results are compared with those available in the literature [63, 66]. The mechanistic details of the, C + OH, reaction on its excited states [22] are discussed in this chapter by comparing the results of the present study with an earlier investigation of Rao *et al.* [61].

The effects of vibrational excitations of reagent OH on the state-to-state dynamics of the, C + OH → CO + H, reaction on its first and second excited states [22] are presented in chapter 5. A TDQM approach [64, 65] is employed to calculate total and state-to-state reaction probabilities as a function of collision energy for total angular momentum, J=0. Product vibrational level distribution is also shown at a few selected collision energies in terms of probabilities for J=0 in order to reveal the mechanism for the reaction primarily.

Chapter 6 includes a comprehensive quantum mechanical investigation for the effects of vibrationally hot reagent H_2 on the state-to-state dynamics of the benchmark H-exchange reaction on its electronic ground state. The investigation is carried out by employing a TDQM approach [64, 65] and the BKMP2 [28] PES of H_3 reactive system to understand the mechanistic details of the, $H_A + H_BH_C \rightarrow H_BH_C + H_A$, reaction. Total and state-to-state reaction probabilities, product

vibrational level distribution, ICSs and DCSs are reported for the H-exchange reaction in this chapter.

Finally, in chapter 7 a summary of all works presented in different chapters is presented in addition to the concluding remarks and a brief outlook.

References

[1] R. D. Levine, *Molecular reaction dynamics*, Cambridge university press, 2005.

[2] M. Brouard and C. Vallence (Editors) *Tutorials in molecular reaction dynamics*, RSC Publishing, 2010.

[3] M. Born and E. Oppenheimer, Ann. Phys. **84**, 457 (1927).

[4] M. Born and K. Huang, in The Dynamical Theory of Crystal Lattices, Oxford University Press, 1954.

[5] F. T. Smith, Phys. Rev. **179**, 111 (1969).

[6] J. G. Black, J. Chem. Phys. **80**, 1103 (1984).

[7] R. R. Friedl, W. H. Brune, J. G. Anderson, J. Phys. Chem. **89**, 5505 (1985).

[8] G. S. Tyndal and A. R. Ravishankara, Int. J. Chem. Kinet. **23**, 483 (1991).

[9] E. Martínez-Núñez and A. J. C. Varandas, J. Phys. Chem. A **105**, 5923 (2001).

[10] A. J. C. Varandas, J. Chem. Phys. **90**, 4379 (1989).

[11] A. J. C. Varandas, THEOCHEM **120**, 401 (1985).

[12] A. J. C. Varandas, Adv. Chem. Phys. **74**, 255 (1988).

[13] A. J. C. Varandas, Chem. Phys. Lett. **194**, 333 (1992).

[14] A. J. C. Varandas, In dynamical Processes in Molecular Physics; G. Delgado-Barrio, Ed; IOP Publishing: Bristol, U. K., 1993; p 3.

[15] T. H. Dunning Jr., J. Chem. Phys. **90**, 1007 (1989).

[16] R. Kendell, T. H. Dunning Jr., and R. Harrison, J. Chem. Phys. **96**, 6769 (1992).

[17] D. Woon and T. H. Dunning Jr., J. Chem. Phys. **98**, 1358 (1993).

[18] H.-J. Werner, P. J. Knowles, MOLPRO is a package of ab initio programs written by H.-J. Werner and P. J. Knowles, with contributions from J. Almlöf, R D. Amos, M. J. O. Deegan, S. T. Elbert, C. Hampel, W. Meyer, K. A. Peterson, R. Pitzer, A. J. Stone, P. R Taylor, and R. Lindh, 1998.

[19] A. Goumri, D. Laakso, J.-D. R. Rocha, C. E. Smith, and P. Marshal, J. Chem. Phys. **102**, 161 (1995).

[20] S. Goswami, T. R. Rao, S. Mahapatra, B. Bussery-Honvault, and P. Honvault, J. Phys. Chem. A **118**, 5915 (2014).

[21] A. Zanchet, B. Bussery-Honvault, and P. Honvault, J. Phys. Chem. A **110**, 12017 (2006).

[22] A. Zanchet, B. Bussery-Honvault, M. Jorfi, and P. Honvault, Phys. Chem. Chem. Phys. **11**, 6182 (2009).

[23] S. Goswami, B. Bussery-Honvault, P. Honvault, and S. Mahapatra, Mol. Phys. DOI: 10.1080/00268976.2017.1296195 (in press).

[24] D. G. Trauhlar and C. J. Horowitz, J. Chem. Phys. **68**, 2466 (1978).

[25] D. G. Trauhlar and C. J. Horowitz, J. Chem. Phys. **71**, 1514 (1979).

[26] A. J. C. Varandas, F. B. Brown, C. A. Mead, D. G. Trauhlar, and N. C. Blais, J. Chem. Phys. **86**, 6258 (1987).

[27] A. I. Boothroyd, W. J. Keogh, P. G. Martin, and M. R. Peterson, J. Chem. Phys. **95**, 4343 (1991)

[28] A. I. Boothroyd, W. J. Keogh, P. G. Martin, and M. R. Peterson, J. Phys. Chem. **104**, 7139 (1996).

[29] Y.-S. M. Wu, A. Kuppermann, and J. B. Anderson, Phys. Chem. Chem. Phys. **1**, 929 (1999).

[30] S. L. Mielke, B. C. Garrett, and K. A. Peterson, J. Chem. Phys. **116**, 4142 (2002).

[31] R. Abrol and A. Kuppermann, J. Chem. Phys. **116**, 1035 (2002).

[32] F. J. Aoiz, L. Bañares, and V. J. Herrero, Int. Rev. Phys. Chem. **24**, 119 (2005).

[33] L. Bañares, F. J. Aoiz, V. J. Herrero, M. J. DMello, B. Niederjohann, K. Seekamp-Rahn, E. Wrede, and L. Schnieder, J. Chem. Phys. **108**, 6160 (1998)

[34] J. Jankunas, M. Sneha, R. N. Zare, F. Bouakline, S. C. Althorpe, D. Herrez-Aguilar, and F. J. Aoiz, PNAS, **111**, 15 (2014).

[35] S. S. Prasad and W. H. Huntress, Jr., **260**, 590 (1982).

[36] A. K. Wilson and T. H. Dunning, Jr., J. Phys. Chem. A **108**, 3129 (2004).

[37] B. T. Luke and A. D. McLean, J. Phys. Chem. **89**, 4592 (1985).

[38] P. L. M. Plummer, J. Chem. Phys. **92**, 6627 (1990).

[39] S. S. Xantheas and T. H. Dunning, Jr., J. Phys. Chem. **97**, 18 (1993).

[40] S. S. Xantheas and T. H. Dunning, Jr., J. Phys. Chem. **97**, 6616 (1993).

[41] M. Kawasaki, K. Kasatani, S. Tanahasi, H. Sato, and Y. Fujimura, J. Chem. Phys. **78**, 7146 (1983).

[42] E. Martínez-Nũñez, S. A. Vázquez, and A. J. C. Varandas, Phys. Chem. Chem. Phys. **4**, 279 (2002).

[43] J. L. Jourdain, G. L. Bras, and J. Combourieu, Int. J. Chem. Kinet. **11**, 569 (1979).

[44] K. Sendt and B. S. Haynes, Proc. Combust. Inst. **31**, 257 (2007).

[45] M. Jorfi and P. Honvault, J. Chem. Phys. **133**, 144315 (2010).

[46] M. Jorfi and P. Honvault, Phys. Chem. Chem. Phys. **13**, 8414 (2011).

[47] R. T. Pack, J. Chem. Phys. **60**, 633 (1974).

[48] P. McGuire and D. J. Kouri, J. Chem. Phys. **60**, 2488 (1974).

[49] A. Zanchet, P. Halvick, J.-C. Rayez, B. Bussery-Honvault, and P. Honvault, J. Chem. Phys. **126**, 184308 (2007).

[50] A. Zanchet, P. Honvault, B. Bussery-Honvault, P. Halvick, J.-C. Rayez, S. Y. Lin, and H. Guo, in *Molecules in space and Laboratory Conference Proceedings*, edited by J. L. Lemaire and F. Combes (S. Diana, Paris, 2007), p. 118.

[51] A. Zanchet, P. Halvick, B. Bussery-Honvault, and P. Honvault, J. Chem. Phys. **128**, 204301 (2008).

[52] M. Jorfi, B. Bussery-Honvault, P. Honvault, T. Stoecklin, P. Larrégaray, and P. Halvick, J. Phys. Chem. A **114**, 7494 (2010).

[53] S. Ying Lin, H. Guo, and P. Honvault, Chem. Phys. Lett. **453**, 140 (2008).

[54] N. Bullut, A. Zanchet, P. Honvault, B. Bussery-Honvault, and L. Bañares, J. Chem. Phys. **130**, 194303 (2009).

[55] P. Song, Y.-H. Zhu, J.-Y. Liu, and F.-C. Ma, J. Theor. Comput. Chem. **9**, 935 (2010).

[56] Y. Ding and Y. Shi, Comput. Theor. Chem. **963**, 306 (2011).

[57] Q. wei, J. Theor. Comput. Chem. **11**, 811 (2012).

[58] W. Yuan-Peng, Z. Mei-Yu, Y. Shun-Huai, S. Peng, and M. Feng-Cai, Chin. Phys. B **22**, 128201 (2013).

[59] Y. Huang, J. Mol. Model, **21**, 103 (2015).

[60] M. Jorfi and P. Honvault, J. Phys. Chem. A **114**, 4742 (2010).

[61] T. R. Rao, S. Goswami, S. Mahapatra, B. Bussery-Honvault, and P. Honvault, J. Chem. Phys. **138**, 094318 (2013).

[62] M. Jorfi, T. González Lezana, A. Zanchet, P. Honvault, and B. Bussery-Honvault, J. Phys. Chem. A **117**, 1872 (2013).

[63] M. Jorfi and P. Honvault, J. Phys. Chem. A **115**, 8791 (2011).

[64] M. Hankel, S. C. Smith, R. J. Allan, S. K. Gray, and G. G. Balint-Kurti, J. Chem. Phys. **125**, 164303 (2006).

[65] M. Hankel, S. C. Smith, S. K. Gray, and G. G. Balint-Kurti, Comp. Phys. Commun. **179**, 569 (2008).

[66] A. Zanchet, T. González Lezana, O. Roncero, M. Jorfi, P. Honvault, and M. Hankel, J. Chem. Phys. **136**, 164309 (2012).

[67] S. K. Gray and G. G. Balint-Kurti, J. Chem. Phys. **108**, 950 (1998).

[68] F. London, Z. Electrochem **35**, 552 (1929).

[69] H. Erying, J. Chem. Phys. **3**, 107 (1935).

[70] M. G. Evans and M. Polanyi, Trans Faraday Soc. **31**, 875 (1935).

[71] R. N. Zare, Ann. Rev. Phys. Chem. **64** 1 (2013).

[72] X. Yang, Ann. Rev. Phys. Chem. **58**, 433 (2007).

[73] T.-S. Chu, K.-L. Han, M. Hankel, G. G. Balint-Kurti, A. Kuppermann, and R. Abrol, J. Chem. Phys. **130**, 144301 (2009).

[74] M. Sneha, H. Gao, R. N. Zare, P. G. Jambrina, M. Menéndez, and F. J. Aoiz, J. Chem. Phys. **145**, 024308 (2016).

[75] F. Fernández-Alonso and R. N. Zare, Ann. Rev. Phys. Chem. **53**, 67 (2002).

[76] J. Jankunas, R. N. Zare, F. Bouakline, S. C. Althorpe, D. Herráez-Aguiler, and F. J. Aoiz, Science **336**, 1687 (2012).

[77] B. K. Kendrick, J. Hazra, and N. Balakrishnan, Phys. Rev. Lett. **115**, 153201 (2015).

[78] B. K. Kendrick, J. Phys. Chem. A **107**, 6739 (2003).

[79] J. C. Juanes-Marcos and S. C. Althorpe, J. Chem. Phys. **122**, 204324 (2005).

[80] J. C. Juanes-Marcos and S. C. Althorpe, and E. Wrede, Science **309**, 1227 (2005).

[81] B. Jiang and H. Guo, J. Chem. Phys. **138**, 234104 (2013).

[82] B. J. Rao, R. Padmanaban, and S. Mahapatra, Chem. Phys. **333**, 135 (2007).

[83] B. J. Rao and S. Mahapatra, Ind. J. Phys. **81**, 1003 (2007).

[84] G.-D. Barg, H. R. Mayne, and J. P. Toennis, J. Chem. Phys. **74**, 1017 (1981).

[85] R. N. Porter and M. Karplus, J. Chem. Phys. **40**, 1105 (1964).

Chapter 2

Theoretical methodology and computational details

2.1 Introduction

Theoretical methods employed to study the dynamics of different bimolecular reactions on single adiabatic PESs are discussed in detail in this chapter. Spatial grids are constructed on suitable Jacobi coordinate system (reagent or product) to solve the nuclear Schrödinger equation numerically by means of time-dependent quantum mechanical (TDQM) methods. An initial wave packet (WP) pertinent to the reagent channel is allowed to evolve in time over the PES and finally it is analyzed at the product asymptote to calculate the dynamical attributes. The methodologies behind the initial state-selected and state-to-state dynamics studies are discussed in detail in two separate sections of the present chapter. Finally, at the end of this chapter, a brief discussion on the procedure followed for the construction of MEPs is presented. To start with the nuclear Schrödinger equation separated from the molecular Schrödinger equation as the former is the

fundamental equation for the dynamical evolution of a reactive system.

2.1.1 From molecular Schrödinger equation to nuclear Schrödinger equation

The motion of a molecular system involves composite motion of electrons and nuclei can be completely described by means of the time-dependent molecular Schrödinger equation,

$$i\hbar\frac{\partial\Psi_M(q,Q,t)}{\partial t} = \hat{H}_M\Psi_M(q,Q,t). \tag{2.1}$$

In equation 2.1, $\Psi_M(q,Q,t)$ and $\hat{H}_M$ are the molecular wavefunction and the molecular Hamiltonian, whereas, $\{q\}$ and $\{Q\}$ collectively represent coordinates of electrons and nuclei, respectively. The non-relativistic molecular Hamiltonian, $\hat{H}_M$, can be symbolically written as-

$$\hat{H}_M = \hat{T}_N + \hat{T}_e + \hat{V}_{eN} + \hat{V}_{NN} + \hat{V}_{ee} \tag{2.2}$$

The operators on the R. H. S of equation 2.2, $\hat{T}_N$, $\hat{T}_e$, $\hat{V}_{eV}$, $\hat{V}_{NN}$ and $\hat{V}_{ee}$ represent the nuclear kinetic energy, electron kinetic energy, electron-nuclei attraction potential, nuclei-nuclei repulsion potential and electron-electron repulsion potential, respectively. Explicit expressions of these operators in atomic unit are given

below.

$$\hat{T}_N = \sum_{\alpha} -\frac{1}{2M_\alpha}\nabla_\alpha^2,$$
$$\hat{T}_e = \sum_{i} -\frac{1}{2}\nabla_i^2,$$
$$\hat{V}_{eN} = \sum_{\alpha}\sum_{i} -\frac{Z_\alpha}{R_{i\alpha}},$$
$$\hat{V}_{NN} = \sum_{\alpha}\sum_{\beta<\alpha} \frac{Z_\alpha Z_\beta}{R_{\alpha\beta}},$$
$$\hat{V}_{ee} = \sum_{i}\sum_{j<i} \frac{1}{r_{ij}}.$$

In the above i/j and α/β represent the electronic and nuclear indices, respectively. The quantities M_α and Z_α represent mass and charge of the nucleus, respectively. $R_{\alpha\beta}$ and r_{ij} are the inter nuclear and inter electronic distances, respectively. The total molecular energy and the wavefunction can be calculated by solving the time-independent molecular Schrödinger equation,

$$\hat{H}_M \Psi_M(q, Q) = E\Psi_M(q, Q). \tag{2.3}$$

Here E is the total energy of the system. Unfortunately, an accurate solution of equation 2.3 is practically cumbersome and consequently approximation is made to solve it. Let us first pick out the electronic Hamiltonian, $\hat{H}_e$, from the molecular Hamiltonian, $\hat{H}_M$, as

$$\hat{H}_e = \hat{T}_e + \hat{V}_{eN} + \hat{V}_{NN} + \hat{V}_{ee} \tag{2.4}$$

and thus, $\hat{H}_M = \hat{T}_N + \hat{H}_e$. Due to the heavier mass of nuclei compared to the electrons, nuclei can be treated as spectators during electronic motion and the

$\hat{T}_N$ term can be ignored to have the electronic Schrödinger equation,

$$\hat{H}_e\phi_i(q;Q) = \epsilon_i(Q)\phi_i(q;Q). \tag{2.5}$$

In equation 2.5, $\phi_i(q;Q)$ represents the electronic wavefunction in its i^{th} state and it depends parametrically on nuclear coordinates. On the other hand, $\epsilon_i(Q)$, represents the electronic energy and it is an explicit function of nuclear coordinates, Q. The set of functions obtained by solving equation 2.5 forms a complete set and the set can be used as a basis for the expansion of the molecular wavefunction as

$$\Psi_M(q,Q) = \sum_i \chi_i(Q)\phi_i(q;Q). \tag{2.6}$$

In this equation, χ_i, represent the coefficients of expansion and these are explicit functions of the nuclear coordinates. In order to find these coefficients, the expression of $\Psi_M(q,Q)$ in equation 2.6 is substituted into equation 2.3 as

$$\hat{H}_M \sum_i \chi_i(Q)\phi_i(q;Q) = E\sum_i \chi_i(Q)\phi_i(q;Q)$$

Taking the operator, $\hat{H}_M$, inside the sum over i on the left hand side, we obtain

$$\sum_i (\hat{T}_N + \hat{H}_e)\chi_i(Q)\phi_i(q;Q) = E\sum_i \chi_i(Q)\phi_i(q;Q)$$

$$\sum_i \left[\sum_\alpha -\frac{1}{2M_\alpha}\nabla^2_\alpha[\chi_i(Q)\phi_i(q;Q)] + \hat{H}_e\chi_i(Q)\phi_i(q;Q)\right] = E\sum_i \chi_i(Q)\phi_i(q;Q)$$

Using equation 2.5, the above expression is reduced to

$$\sum_i \left[\sum_\alpha -\frac{1}{2M_\alpha} \nabla_\alpha^2 [\chi_i(Q)\phi_i(q;Q)] + \chi_i(Q)\epsilon_i(Q)\phi_i(q;Q) \right] = E \sum_i \chi_i(Q)\phi_i(q;Q)$$

By using the product rule of differentiation for the nuclear kinetic energy operator, we obtain

$$\begin{gathered} \textstyle\sum_i \sum_\alpha -\frac{1}{2M_\alpha} [2(\nabla_\alpha \chi_i(Q))(\nabla_\alpha \phi_i(q;Q)) + \chi_i(Q)\nabla_\alpha^2 \phi_i(q;Q) + \phi_i(q;Q)\nabla_\alpha^2 \chi_i(Q)] \\ + \textstyle\sum_i \chi_i(Q)\epsilon_i(Q)\phi_i(q;Q) = E \sum_i \chi_i(Q)\phi_i(q;Q) \end{gathered}$$

After taking a projection on ϕ_j^* and integration over electronic coordinates, the above equation reduces to

$$\begin{gathered} \textstyle\sum_i \left[\sum_\alpha -\frac{1}{2M_\alpha} [2(\nabla_\alpha \chi_i(Q)) \langle \phi_j(q;Q) | \nabla_\alpha | \phi_i(q;Q) \rangle + \langle \phi_j(q;Q) | \nabla_\alpha^2 | \phi_i(q;Q) \rangle \chi_i(Q)] \right] \\ + \textstyle\sum_\alpha -\frac{1}{2M_\alpha} \nabla_\alpha^2 \chi_j(Q) + \epsilon_j(Q)\chi_j(Q) = E\chi_j(Q) \end{gathered}$$

The terms present inside the brackets are known as nonadiabatic coupling (NAC) terms. These are neglected within BO approximation and the approximation is fairly accurate unless the electronic energy, $\epsilon_j(Q)$, is very close to the energy of other electronic states. Thus within BO approximation, the above equation reduces to

$$\sum_\alpha -\frac{1}{2M_\alpha} \nabla_\alpha^2 \chi_j(Q) + \epsilon_j(Q)\chi_j(Q) = E\chi_j(Q) \tag{2.7}$$

or

$$\hat{H}_{nuc}\chi_j(Q) = E\chi_j(Q) \tag{2.8}$$

Thus, within BO approximation, the nuclear Hamiltonian, $\hat{H}_{nuc}$, contains only the nuclear kinetic energy operator and the potential energy which is the total electronic energy of the given electronic state. Furthermore, it appears that within the BO approximation, the nuclear motion is confined to a single electronic state. It is also reiterated here that the potential energy, $\epsilon_j(Q)$, is a function of the nuclear coordinates and except for a diatomic molecule, it represents a hypersurface which is commonly known as the PES. Hence, the electrons of a molecular system provide the potential for the movement of the nuclei. Finally, the nuclear movement is followed by means of equation 2.8 or its time-dependent form,

$$i\hbar\frac{\partial\chi(Q,t)}{\partial t} = \hat{H}_{nuc}\chi(Q,t). \tag{2.9}$$

This equation is known as the time-dependent nuclear Schrödinger equation and the subscript j has been removed here for the sake of clarity.

2.2 Methodology for initial state-selected study

Initial state-selected dynamics of the S + OH and C + OH reactions on the electronic ground and second excited states (see chapter 3 and 4), are investigated by solving the time-dependent nuclear Schrödinger equation numerically on a grid. If the Hamiltonian of the reactive system is explicitly time-independent, the solution of equation 2.9 reads as

$$|\chi(Q,t)\rangle = exp\left[\frac{-i\hat{H}_{nuc}t}{\hbar}\right]|\chi(Q,t=0)\rangle \tag{2.10}$$

In equation 2.10, $|\chi(Q,t)\rangle$ and $|\chi(Q,t=0)\rangle$ represent the propagated wave packet at time t and the initial wave packet (WP), respectively. For a numerical solution

of equation 2.10, discrete grid points are constructed along reagent Jacobi coordinates. The reagent Jacobi coordinate system in body-fixed (BF) frame used for the study of atom-diatom collisions is defined by three variables, R [the distance between the approaching atom and the center-of-mass of the reagent diatom], r [reagent diatom internuclear distance] and γ [the angle between R and r]. The z axis is defined to be parallel to R, while the molecular plane corresponds to the xy plane. In this coordinate system, the reagent asymptote is defined by making R very large, whereas, the product asymptote is defined by making r relatively larger. The reagent Jacobi coordinate system is schematically shown in Figure 2.1.

The coordinate space, x is divided into a set of N discrete regular grid points with uniform grid spacing, Δx, between two successive grid points. Hence, the eigenvalues of the position operator, $\hat{x}$ at these grid points are given by [1],

$$x_i = (i-1)\Delta x \tag{2.11}$$

The eigenvector, $|x_i\rangle$, corresponding to each eigenvalue is obtained by the orthogonality and completeness relations and wavefunctions for an arbitrary physical state is given by

$$\phi'(x_i) = \langle x_i|\phi'\rangle. \tag{2.12}$$

The maximum length along the spatial coordinate, $L = N\Delta x$, determines the spacing between two successive points on its conjugate momentum space (k) by the relation,

$$\Delta k = \frac{2\pi}{N\Delta x}. \tag{2.13}$$

Unlike in coordinate space, in momentum space, the center of the grid is kept at zero and other points are symmetrically distributed on both sides of it. Hence, if

the maximum value of momentum is $p_{max}(=\hbar k_{max})$, the momentum then ranges from $-p_{max}$ to $+p_{max}$. Furthermore, the number of grid points in the coordinate space for a fixed value of grid length (L) determines the value of p_{max}. A dense grid in the coordinate space always increases the maximum value of the momentum in its conjugate space, which is evident from the following relations.

$$p_{max} = \frac{N\Delta k}{2}, \tag{2.14}$$

by putting the expression of Δk from equation 2.13, it is obtained that

$$p_{max} = \frac{N}{2}\frac{2\pi}{N\Delta x} = \frac{\pi}{\Delta x}. \tag{2.15}$$

As for a fixed value of L, the magnitude of Δx decrease with the increase of N which makes the grid more dense, the magnitude of maximum momentum increases consequently. Here x is used as a representative for a particular nuclear coordinate.

Once the construction of grids along Jacobi coordinates is done, the potential energy at each set of grid points is calculated and thus the construction of potential energy grid is also done to consider the action of potential energy operator on the wave packet. In most applications the PES of a molecular system is constructed as a function of its internal coordinates. Hence, a transformation between Jacobi coordinates and internal coordinates is required to construct the potential energy grid. A set of Jacobi coordinates corresponds to an unique set of internal coordinates and the relation between them is given by the following equations, (in relation to the nuclear arrangement and definition of coordinates

given in Figure 2.1)

$$r_{ac} = \sqrt{R^2 + (\frac{w_B}{w_B + w_C})^2 r^2 + 2(\frac{w_B}{w_B + w_C}) r R cos(\gamma)},$$

$$r_{ab} = \sqrt{R^2 + (\frac{w_C}{w_B + w_C})^2 r^2 - 2(\frac{w_C}{w_B + w_C}) r R cos(\gamma)}$$

and

$$r_{bc} = r$$

In the above three equations, r_{ab}, r_{bc} and r_{ac} correspond to the internuclear distances between A and B, B and C, A and C atoms. Whereas, w_B and w_C represent the masses of B and C atoms, respectively.

An initial WP, $|\chi(R, r, \gamma, t = 0)\rangle$, is prepared in the reagent asymptote (representing the zero of the interaction potential) as a product of three functions as

$$|\chi(R, r, \gamma, t = 0)\rangle = \sqrt{\omega_n} F(R) \phi''_{vj}(r) \tilde{P}^{\Omega}_{j}(\cos\gamma). \tag{2.16}$$

In this equation $F(R)$ is the minimum uncertainty Gaussian wave packet (GWP) that defines the translation of the atom towards the center-of-mass of the molecule

$$F(R) = \left(\frac{1}{2\pi\delta^2}\right)^{\frac{1}{4}} \exp\left[-\frac{(R - R_0)^2}{4\delta^2} - ik_0(R - R_0)\right]. \tag{2.17}$$

In equation 2.17, δ, R_0 and $\hbar k_0$ represent the width of the GWP, location of the center of the wave packet in coordinate and momentum space, respectively. Among the other two functions present in equation 2.16, $\phi''_{vj}(r)$ represents the rovibrational eigenfunction of the reagent diatom. This eigenfunction is obtained

by solving the following eigenvalue equation,

$$\left[-\frac{\hbar^2}{2\mu_r}\frac{d^2}{dr^2} + V(r) + \frac{j(j+1)\hbar^2}{2\mu_r r^2}\right]\phi''_{vj}(r) = \epsilon'_{vj}\phi''_{vj}(r). \tag{2.18}$$

In this equation μ_r, $V(r)$ and ϵ'_{vj} are the diatom reduced mass, diatom potential and ro-vibrational energy of the diatom at its v^{th} vibrational and j^{th} rotational quantum levels, respectively. The diatomic potential is calculated from the underlying PES for $R \to \infty$. Equation 2.18 is solved to find the ϵ'_{vj} and $\phi''_{vj}(r)$ by following sine discrete variable representation method of Colbert and Miller [2]. The third function, $\tilde{P}_j^{\Omega}(cos\gamma)$ in equation 2.16 corresponds to the associated Legendre polynomials and they are given by

$$\tilde{P}_j^{\Omega} = \sqrt{\frac{2j+1}{2}\frac{(j-\Omega)!}{(j+\Omega)!}}P_j^{\Omega}(cos\gamma). \tag{2.19}$$

Here Ω represents the quantum number for the projection of both two-body rotational (j) and total (three-body) angular momentum (J) on the body-fixed z axis. Hence, from equation 2.16 it is quite obvious that the initial WP contains the preselected quantum state of the reagent molecule.

The term, $\hat{H}_{nuc}$, present in equation 2.10 represents the nuclear Hamiltonian operator of the reactive system. For a A + BC reaction represented in a body-fixed Jacobi coordinate system, it is given by [3]

$$\begin{aligned}\hat{H}_{nuc} &= -\frac{\hbar^2}{2\mu_R}\frac{\partial^2}{\partial R^2} - \frac{\hbar^2}{2\mu_r}\frac{\partial^2}{\partial r^2} - \frac{\hbar^2}{2I}\left[\frac{1}{\sin\gamma}\frac{\partial}{\partial\gamma}\sin\gamma\frac{\partial}{\partial\gamma} - \frac{j_z^2}{sin^2\gamma}\right] \\ &+ \frac{1}{2\mu_R R^2}\left[J^2 - 2J_z j_z\right] - \frac{1}{2\mu_R R^2}\left[J_+ j_- + J_- j_+\right] + \hat{V}(R,r,\gamma).\end{aligned} \tag{2.20}$$

Out of the six terms in equation 2.20, the first five collectively represent the

nuclear kinetic energy operator, $\hat{T}_{nuc}$, whereas $\hat{V}(R, r, \gamma)$ describes the electronic potential energy. The first two terms in equation 2.20 represent the radial kinetic energy operators ($\hat{T}_{radial}$) along R and r Jacobi coordinates, respectively. Whereas, the third and fourth terms are the angular kinetic energy operators $\hat{T}_{angular}$ for the reagent diatom, AB, and the triatomic system, ABC. The fifth term which includes a combination of raising and lowering operators ($J_{\pm}$ and $j_{\pm}$) represents the Coriolis interactions. The raising and lowering operators are defined as $J_{\pm} = J_x \pm iJ_y$ and $j_{\pm} = j_x \pm ij_y$, respectively. Furthermore, in equation 2.20, J represents the operator for the total angular momentum quantum number. The other two quantities, $\mu_R \left(= \frac{w_A(w_B+w_C)}{(w_A+w_B+w_C)}\right)$ and $\mu_r \left(= \frac{w_B w_C}{w_B+w_C}\right)$ are the three-body (A + BC) and reagent diatom (BC) reduced masses, respectively. Here w_A, w_B and w_C are the masses of A, B, and C atoms, respectively. Lastly, $I = \frac{\mu_R \mu_r R^2 r^2}{\mu_R R^2 + \mu_r r^2}$, represents the moment of inertia of the collisional system.

The action of the kinetic ($\hat{T}_{nuc}$) and potential ($\hat{V}$) energy parts on the WP needs to be carried out separately in order to have a numerical solution of equation 2.10. The potential energy operator, is local in coordinate space and consequently the action of the operator which includes $\hat{V}$ on the wave packet is simply multiplicative at each grid point, such as

$$\hat{V}(Q_i)\chi(Q_i) = V(Q_i)\chi(Q_i). \tag{2.21}$$

Here in equation 2.21, Q_i represents a particular nuclear coordinate. On the other hand, the kinetic energy operator, $\hat{T}_{nuc}$ is non-local in coordinate space and the evaluation of the term, $\hat{T}_{nuc}\chi(Q)$ is not simply multiplicative, rather it becomes a key step in the dynamics study. Thus, the action of the operator containing $\hat{T}_{nuc}$ on the WP can be carried out by following a suitable collocation technique [4, 5]

utilizing the concept of the discrete Hilbert space.

In a collocation method, a function is presented in two different representations. Firstly, a grid representation where the value of the function is known at the grid points. On the other hand, in a basis set representation, at each grid point continuous functions are approximated as a sum of finite basis functions. These basis functions are connected with the function through expansion coefficients at different grid points by the equation

$$\chi(Q_i) = \sum_{n=0}^{N-1} a_n g_n(Q_i). \tag{2.22}$$

In equation 2.22 a_n and N are the expansion coefficient of the n^{th} basis function g_n and the size of the basis, respectively. This technique is utilized to evaluate the action of non-local operators on the function such as

$$\hat{T}_{radial}\chi(Q) = \frac{\hbar^2 k^2}{2\mu}\chi(Q) = \frac{\hbar^2 k^2}{2\mu}a_k. \tag{2.23}$$

The Fourier method [4–7] is a special case of the collocation technique. In Fourier transformation method, one can move back and forth between two reciprocal Hilbert spaces. Position-momentum and time-energy are the examples of reciprocal spaces. Fourier method becomes very useful to evaluate the action of a non-local operator on a function and it is utilized here for the operator involving $\hat{T}_{radial}$. In this method, the function, $\chi(Q)$ is expressed as a sum of the orthogonal plane wave basis functions.

$$\chi(Q) \approx \sum_{k=-(\frac{N}{2}-1)}^{\frac{N}{2}} a_k exp[i2\pi kQ/L] \tag{2.24}$$

Here a_k is the coefficient in the expansion and it represents the amplitude of the function in momentum space.

The fast Fourier transform (FFT) method is conveniently used in numerical calculations rather than the use of simple Fourier transform method. The use of FFT to evaluate the action of the kinetic energy part of the Hamiltonian was introduced by Feit *et al.* [8] and Kosloff and Kosloff [6]. In this method, the wave packet is transformed into momentum space by employing forward FFT, followed by its multiplication with the operator in momentum space. In the latter space, the operator involving the kinetic energy part is local. Finally the evolved wave packet is transformed back to the coordinate space by inverse FFT. The transformation of the wave packet between coordinate and momentum space can be schematically represented as

$$FT[\chi(Q)] = \chi(k) = \frac{1}{\sqrt{2\pi}} \int_{-\infty}^{\infty} \chi(Q) exp(-ikQ) dQ. \tag{2.25}$$

and

$$FT^{-1}[\chi(k)] = \chi(Q) = \frac{1}{\sqrt{2\pi}} \int_{-\infty}^{\infty} \chi(k) exp(ikQ) dk. \tag{2.26}$$

FT and FT^{-1} in equation 2.25 and 2.26 designates the forward and inverse FFT, respectively.

The application of this method is limited to the functions which satisfy periodic boundary conditions and such transformation turns out to be exact for band limited functions [6]. Functions following these conditions are localized in the phase space box and the amplitude of the function is zero at the boundary of the box. If the latter criteria is not fulfilled by the WP, with the progress of time the WP reaches to the grid edges and introduces a spurious reflection which results an interference between the outgoing and reflected components. But un-

fortunately except semilocalized functions, others are not band limited and they can not be confined both in momentum and coordinate space simultaneously. However, multiplication of the wave packet with a suitable damping function at grid edges helps to meet the boundary condition of the WP. The following sine type damping function [9] is used at the grid edges to remove artificial reflection at the boundaries.

$$f(X_i') = sin\left[\frac{\pi}{2}\frac{(X'_{mask}) + \Delta X'_{mask} - X_i'}{\Delta X'_{mask}}\right], X_i' \geq X'_{mask} \tag{2.27}$$

In this equation, X' represents a nuclear coordinate along which this function is employed. Here X'_{mask} is the starting point of the damping function and $\Delta X'_{mask} = X'_{max} - X'_{mask}$ represents the width of the coordinate over which the function is employed and its magnitude decays from 1 to 0. X'_{max} is the maximum grid value of the coordinate. This kind of sine type damping function efficiently reduces the amplitude of the function to zero at the grid edges and consequently eliminates the spurious reflections as mentioned above.

Another important aspect of the FFT scheme is its efficient scaling property [10]. The FFT method scales the problem as $O(NlogN)$ where N is the number of grid points. Such scaling makes this method highly suitable for larger problems as the computational overhead rises slowly with the increase of the grid size.

This FFT method is incapable of evaluating the action of the portion of the operator which involves the angular part ($\hat{T}_{angular}$) of kinetic energy. This incapability arises due to the presence of the ($\frac{1}{sin^2\gamma}$) term in the operator which leads to a singularity for angles γ= 0 and π. The situation can be tackled by using another orthogonal collocation technique known as discrete variable representation (DVR) - finite basis representation (FBR) transformation. Specific basis

functions and points along the grid are used in the DVR-FBR transformation method [11, 12]. The DVR basis is composed of N discrete points, whereas the FBR basis contains N square integrable functions which are appropriate to the coordinates of DVR. Light and coworkers showed that in a DVR framework, the collocation technique is more effective when some quadrature scheme relates the two representations [13–15]. Furthermore, the use of orthogonal polynomial basis functions corresponding to Gaussian quadrature was proposed by Haris *et al.* [11] and Dickinson and Certain [12]. In this method, an orthogonal transformation between the quadrature points and basis functions are carried out. For the calculations reported in chapter 3 and 4, the nodes of a Gauss-Legendre quadrature are considered as the grid points along the Jacobi angle, γ. This is followed as the angular part of the kinetic energy operator is diagonal in the associated Legendre polynomial basis set, $P_l^{\Omega}(cos\gamma)$. If the function of the angular coordinate is represented as $\psi_j^{\Omega}(\gamma)$ and it is expanded in associated Legendre polynomial basis, the action of the $\hat{T}_{angular}$ (third and fourth term of the nuclear Hamiltonian shown in equation 2.20) can be evaluated as [16]

$$\hat{T}_{angular}\psi_j^{\Omega}(\gamma_k) = \sum_{l=1}^{N_\gamma} L_{lk} \left(\frac{\hbar^2}{2I}\right) \psi_j^{\Omega}(\gamma_l) \tag{2.28}$$

where, $\mathbf{L} = \mathbf{U}\Lambda\mathbf{U}^t$, and N_γ is the number of angular grid points. Here Λ and $\mathbf{U}$ are the diagonal and unitary matrices with the matrix elements $\Lambda_{l,l} = l(l+1) + J(J+1) - 2\Omega^2$ and $U_{kl}^{\Omega} = \sqrt{w_k}\tilde{P}_l^{\Omega}(cos\gamma_k)$, respectively. The action of the operator including Coriolis interactions (the fifth term of equation 2.20) can also be evaluated similarly. But the procedure is not discussed here as coupled states (CS) approximation [3, 17] is used in the state-selected dynamics studies. This discussion is defered to section 2.3 where the methodology outlined for the state-

to-states dynamics study.

The discussion so far on the action of different operators present in nuclear Hamiltonian on the function can be considered as the prelude for following up the time-evolution of the WP. Hence, in the next part of this section we discuss on the methods to calculate the time-evolution of the wave packet over the underlying PES. The exponential operator, present on the R. H. S. of equation 2.10 is known as the time-evolution operator and it is denoted here as $\hat{U}'(t, t_0)$. For $t_0 = 0$, the operator is given by

$$\hat{U}'(t, t_0) = exp(\frac{-i\hat{H}_{nuc}t}{\hbar}). \tag{2.29}$$

The total time of propagation, t is divided into a certain number of smaller time steps of length Δt and the time-evolution is carried out through $\hat{U}'(t) = \Pi_{n=0}^{N_t-1}\hat{U}'[(n+1)\Delta t, n\Delta t]$. Here N_t is the total number of time steps used for the entire propagation. It is reiterated here that the exponential operator, $e^{-i\hat{H}_{nuc}t/\hbar}$ contains the kinetic and potential energy operators and their action on the wave-function must be treated separately. The kinetic energy operator ($\hat{T}_{nuc}$) is a function of momentum, whereas, the potential energy operator ($\hat{V}$) is a function of position. Consequently, these two operators, $\hat{T}_{nuc}$ and $\hat{V}$ do not commute with each other and due to this non-commutability an error is introduced when the exponential operator is split simply in a straight forward manner as

$$\begin{aligned} exp\left(\frac{-i\hat{H}_{nuc}\Delta t}{\hbar}\right) &= exp\left(\frac{-i(\hat{T}_{nuc}+\hat{V})\Delta t}{\hbar}\right) \\ &= exp\left(\frac{-i\hat{T}_{nuc}\Delta t}{\hbar}\right) \times exp\left(\frac{-i\hat{V}\Delta t}{\hbar}\right) \\ &+ O(\Delta t) \end{aligned} \tag{2.30}$$

In equation 2.30 the last term on the R. H. S., $O(\Delta t)$ represents the error and

it is of the first order in time. Hence the exponential operator must be approximated appropriately which can efficiently reduce this error. The operator is approximated in various ways in literature such as the second-order differencing (SOD) scheme [18], the split operator (SO) method [19], the chebyshev polynomial scheme [20] and the short iterative Lanczos (SIL) scheme [21]. Among all these procedures, the SO method is employed for the work presented in chapter 3 and chapter 4 and hence this method is discussed in detail in the next section.

2.2.1 Split operator (SO) method

In this method, the kinetic energy part of the exponential operator present in equation 2.10 is symmetrically split around the potential energy part as

$$e^{-i\hat{H}_{nuc}\Delta t/\hbar} = e^{-i\hat{T}_{nuc}\Delta t/2\hbar}e^{-i\hat{V}\Delta t/\hbar}e^{-i\hat{T}_{nuc}\Delta t/2\hbar} + O(\Delta t^3). \tag{2.31}$$

Due to the symmetrical splitting, the error due to the non-commutability of $\hat{T}_{nuc}$ and $\hat{V}$ becomes Δt^3 [19]. Hence, the time evolution of the wave packet is done by the relation,

$$\chi(Q, t+\Delta t) = e^{-i\hat{T}_{nuc}\Delta t/2\hbar}e^{-i\hat{V}\Delta t/\hbar}e^{-i\hat{T}_{nuc}\Delta t/2\hbar}\chi(Q,t). \tag{2.32}$$

Such split operator scheme shown in equation 2.31 and 2.32 is known as the potential-referenced split operator scheme. In this scheme, the action of the kinetic energy part of the operator is carried out twice. An equivalent scheme, known as the kinetic-referenced split operator scheme is also possible and frequently used in dynamics calculations. In the latter scheme, the potential energy part of the operator is split symmetrically into two parts keeping the kinetic

energy part sandwitched in between. It is to be mention here that the kinetic-referenced and potential-referenced schemes produce same results. The kinetic-referenced scheme is quite advantageous as the computationally expensive non-local kinetic energy operator part is evaluated only once. The kinetic energy part is further split symmetrically for the state-selected dynamics study reported in this thesis and hence finally the time evolution of the wave packet is done by the following relation,

$$\begin{aligned}\chi(Q,t+\Delta t) &= e^{-i\hat{V}\Delta t/2\hbar}e^{-i\hat{T}_{nuc,R}\Delta t/2\hbar}e^{-i\hat{T}_{nuc,r}\Delta t/2\hbar}e^{-i\hat{T}_{nuc,\gamma}\Delta t/\hbar} \\ & e^{-i\hat{T}_{nuc,r}\Delta t/2\hbar}e^{-i\hat{T}_{nuc,R}\Delta t/2\hbar}e^{-i\hat{V}\Delta t/2\hbar}\chi(Q,t)+O(\Delta t^3). \quad (2.33)\end{aligned}$$

In equation 2.33, $\hat{T}_{nuc,R}, \hat{T}_{nuc,r}$ and $\hat{T}_{nuc,\gamma}$ are the nuclear kinetic energy operators along R, r and γ Jacobi coordinates. The action of each exponential operator present in equation 2.33 is evaluated in a local representation as discussed earlier. Hence, for the second, third, fifth and sixth operators from the left of the R. H. S. of equation 2.33, the wave packet was transformed in momentum space by forward Fourier transformation followed by multiplication with corresponding operator in momentum space and finally the operated wave packet was taken back to the coordinate space by inverse Fourier transformation. The action of the exponential operator involving $\hat{T}_{nuc,\gamma}$ is carried out by DVR-FBR transformation. The effect of the operators present at the two terminals involving $\hat{V}$ term is carried out by simple multiplication. Finally, it should be mentioned that the operator remains linear and unitary and thus the norm is always conserved. Furthermore, to obtain accurate results a restriction over the length of the time step is imposed by the following relation and an optimum time step, Δt has been selected depending

upon the maximum potential energy value on the grid [8, 22].

$$\Delta t < \frac{\pi}{3\Delta V_{max}}, \Delta V_{max} = V_{max} - V_{min} \tag{2.34}$$

In the above equation, V_{max} and V_{min} are maximum and minimum values of the potential and hence ΔV_{max} is the difference between them.

2.2.2 Analysis of the propagated wave packet, calculation of probabilities and integral reaction cross sections

At each time step the propagated wave packet is analyzed at a dividing surface which separates the products from reactants and the flux operator approach developed by Neuhauser *et al.* [23] is used for the calculation of initial state-selected total reaction probabilities and integral cross sections (ICSs). The latter approach allows the entire dynamics calculation to be carried out solely on reagent Jacobi coordinate system. Initial state-selected and energy resolved total reaction probabilities are calculated from the expectation value of the flux operator [23–25], $\hat{F} = -\frac{i\hbar}{2\mu}[\frac{\partial}{\partial r}\delta(r - r_d) + \delta(r - r_d)\frac{\partial}{\partial r}]$ at the dividing surface kept at $r = r_d$ as

$$\begin{aligned} P_i^R(E) &= \langle\chi'(R, r_d, \gamma, E)|\hat{F}|\chi'(R, r_d, \gamma, E)\rangle \\ &= \frac{\hbar}{\mu_r} Im\left[\langle\chi'(R, r_d, \gamma, E)|\frac{\partial\chi'(R, r_d, \gamma, E)}{\partial r}\right]|r = r_d. \end{aligned} \tag{2.35}$$

Integration over R and γ coordinates are carried out on the R. H. S of equation 2.35. The energy-normalized and time-independent function, $|\chi'(R, r_d, \gamma, E)\rangle$ is calculated at the dividing surface as

$$|\chi'(R, r_d, \gamma, E)\rangle = |\chi(R, r_d, \gamma, E)\rangle/\kappa_E. \tag{2.36}$$

The function, $|\chi(R, r_d, \gamma, E)\rangle$ present at the numerator on the R. H. S. of equation 2.36 is obtained through Fourier transformation of the time-evolved wave packet at the dividing surface as

$$|\chi(R, r_d, \gamma, E)\rangle = \frac{1}{\sqrt{2\pi}} \int_{-\infty}^{\infty} e^{iEt/\hbar} |\chi(R, r_d, \gamma, t)\rangle dt. \tag{2.37}$$

On the other hand, the term κ_E present at the denominator of equation 2.36 is the weight of the translational energy component of the initial WP and it is calculated by the relation,

$$\kappa_E = \left(\frac{\mu_R}{2\pi\hbar|\mathbf{k}|}\right)^{1/2} \int_{-\infty}^{\infty} F(R) e^{i|\mathbf{k}|R} dR. \tag{2.38}$$

In equation 2.38, $|\mathbf{k}| = \sqrt{2\mu_R(E - \epsilon'_{vj})}/\hbar$ and ϵ'_{vj} represents the ro-vibrational energy of the reagent diatom. It is to be noted here that the reaction probabilities of the two possible product channels are approximately distinguished by comparing the internuclear distances of the product diatoms.

Energy resolved total reaction probabilities calculated by equation 2.35 depend on the two quantum numbers, J and Ω. It is reiterated here that J represents the total angular momentum, whereas Ω is the projection of J and j. Initial state-selected and energy resolved total ICSs are calculated by summing up the probabilities over these two quantum numbers at a given energy, E.

$$\sigma_{vj}(E) = \frac{\pi}{|\mathbf{k}|^2} \sum_{\Omega=0}^{j} \frac{g_\Omega}{(2j+1)} \sum_{J \geq \Omega}^{J_{max}} (2J+1) P_{vj}^{J\Omega}(E). \tag{2.39}$$

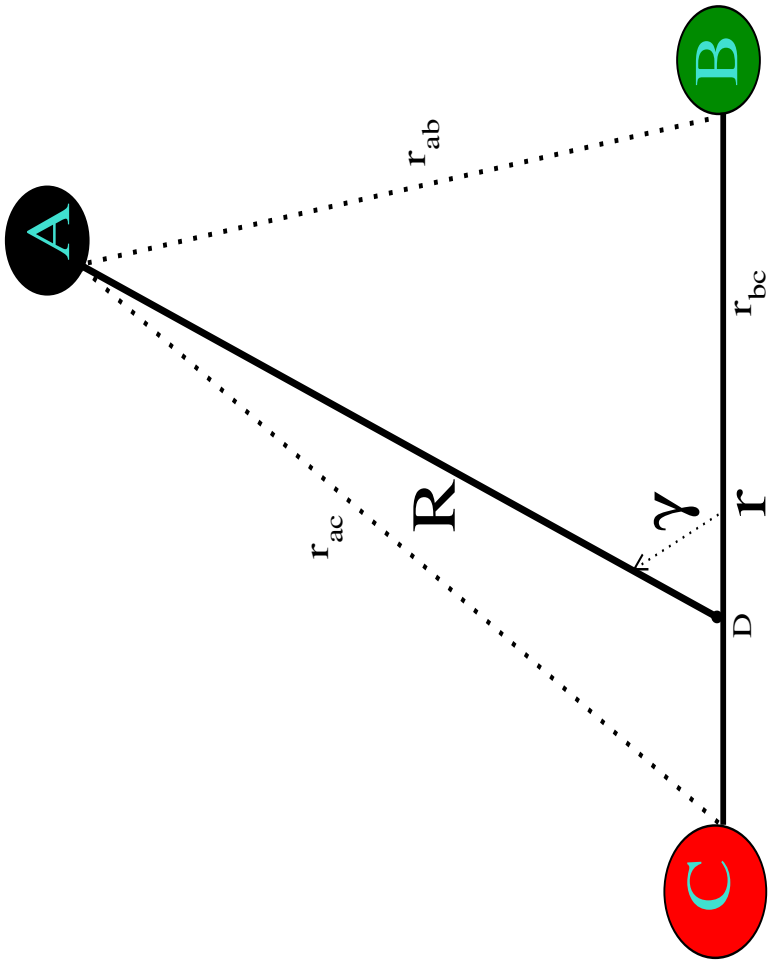

Figure 2.1: Schematic representation of the body-fixed reagent Jacobi coordinate system. See text for details.

2.3 Methodology for state-to-state study

The entire methodology for carrying out the state-to-state dynamics study of the C + OH reaction on its excited states and the benchmark H-exchange reaction on its degenerate electronic state reported in chapter 5 and chapter 6 of this thesis is discussed in detail in three following sections here. The first section describes the calculation of time-dependent coefficients followed by the discussion about the generation of energy resolved $\boldsymbol{S}$-matrix elements in the second section. Finally, the procedure used for the calculation of probabilities and cross sections is discussed in the third section. But before going to the details of theory, let us first have the basic iterative equation(s) used for the propagation of the WP. It is noted here that the basic theory employed behind the algorithm used for the state-to-state study is the real wave packet methodology of Gray and Balint-Kurti [26].

Following equation 2.10, it can be written as

$$\chi(Q, t+\tau) = e^{-i\hat{H}_{nuc}\tau/\hbar}\chi(Q,t). \tag{2.40}$$

Here τ is discrete time step and $\chi(Q,t)$ represents the nuclear wave function. If its backward counterpart is considered and consequently τ is replaced by $-\tau$, equation 2.40 is reduced to

$$\chi(Q, t-\tau) = e^{i\hat{H}_{nuc}\tau/\hbar}\chi(Q,t). \tag{2.41}$$

The addition of equation 2.40 and 2.41 gives rise to

$$\begin{aligned}\chi(Q,t+\tau)+\chi(Q,t-\tau) &= \left[e^{-i\hat{H}_{nuc}\tau/\hbar}+e^{i\hat{H}_{nuc}\tau/\hbar}\right]\chi(Q,t)\\ &= 2cos\left(\frac{\hat{H}_{nuc}\tau}{\hbar}\right)\chi(Q,t). \qquad (2.42)\end{aligned}$$

Hence

$$\chi(Q,t+\tau) = -\chi(Q,t-\tau)+2cos(\frac{\hat{H}_{nuc}\tau}{\hbar})\chi(Q,t). \qquad (2.43)$$

Similarly, subtraction of equation 2.41 from equation 2.40 results

$$\chi(Q,t+\tau) = \chi(Q,t-\tau)-2isin(\frac{\hat{H}_{nuc}\tau}{\hbar})\chi(Q,t). \qquad (2.44)$$

Equation 2.43 and equation 2.44 are equivalent to the Schrödinger equation and each iteration requires the information of two previous time steps [27]. But equation 2.43 involving cosine iteration does not contain i and hence the real and imaginary part of χ can be propagated independently of each other. If q' and p' are real valued functions and they are defined as follows,

$$\begin{aligned}q'(Q,t) &= Re[\chi(Q,t)]\\ p'(Q,t) &= Im[\chi(Q,t)]\end{aligned}$$

then equation 2.43 can be rewritten as

$$\begin{aligned} q'(Q,t+\tau)+ip'(Q,t+\tau) &= -[q'(Q,t-\tau)+ip'(Q,t-\tau)] \\ &+ 2cos(\frac{\hat{H}_{nuc}\tau}{\hbar})[q'(Q,t)+ip'(Q,t)] \\ &= -q'(Q,t-\tau)+2cos(\frac{\hat{H}_{nuc}\tau}{\hbar})q'(Q,t) \\ &+ i[-p'(Q,t-\tau)+2cos(\frac{\hat{H}_{nuc}\tau}{\hbar})p'(Q,t)] \end{aligned} \quad (2.45)$$

Comparing real and imaginary parts on the right hand and left hand side of equation 2.45 we obtain

$$q'(Q,t+\tau) = -q'(Q,t-\tau)+2cos(\frac{\hat{H}_{nuc}\tau}{\hbar})q'(Q,t) \quad (2.46)$$

and

$$p'(Q,t+\tau) = -p'(Q,t-\tau)+2cos(\frac{\hat{H}_{nuc}\tau}{\hbar})p'(Q,t). \quad (2.47)$$

It is reiterated here that each iteration of equation 2.46 requires the wavefunction of two previous iteration steps and hence this equation can not evaluate the wave function at the initial step. The equation to obtain the wave function at the initial time step can be derived from equation 2.40 as follows

$$\begin{aligned} \chi(Q,\tau) &= [cos(\frac{\hat{H}_{nuc}\tau}{\hbar})-isin(\frac{\hat{H}_{nuc}\tau}{\hbar})]\chi(Q,0) \\ q'(Q,\tau)+ip'(Q,\tau) &= [cos(\frac{\hat{H}_{nuc}\tau}{\hbar})-isin(\frac{\hat{H}_{nuc}\tau}{\hbar})](q'(Q,0)+ip'(Q,0)) \\ &= cos(\frac{\hat{H}_{nuc}\tau}{\hbar})q'(Q,0)+icos(\frac{\hat{H}_{nuc}\tau}{\hbar})p'(Q,0) \\ &- isin(\frac{\hat{H}_{nuc}\tau}{\hbar})q'(Q,0)+sin(\frac{\hat{H}_{nuc}\tau}{\hbar})p'(Q,0) \end{aligned} \quad (2.48)$$

Once again by comparing the real parts on both sides of the equation, we get

$$q'(Q,\tau) = cos(\frac{\hat{H}_{nuc}\tau}{\hbar})q'(Q,0) + sin(\frac{\hat{H}_{nuc}\tau}{\hbar})p'(Q,0). \tag{2.49}$$

Hence, once the wavefunction at an initial time step is known by equation 2.49, further time evolution can be carried out by equation 2.46. At this point of discussion it is to be mentioned that the algorithm coded in the DIFFREALWAVE code of Hankel *et al.* [28,29] is adapted with structural modification in the present applications.

2.3.1 Calculation of time-dependent coefficients

Body-fixed product Jacobi coordinate system defined by R_c (the distance between C atom to the center of mass of AB diatom), r_c (AB diatom internuclear distance) and γ_c (the angle generated by C atom, center of mass of AB diatom and B atom) is used here and this is schematically shown in Figure 2.2. For the numerical solution of iterative equation, discrete grid points are generated along R_c, r_c and γ_c followed by the construction of potential energy matrix at these points. Each set of product Jacobi coordinate corresponds to an unique set of internal coordinate and the transformation between them is carried out by following three equations.

$$r_{bc} = \sqrt{R_c^2 + (\frac{w_A}{w_A + w_B})^2 r_c^2 - 2(\frac{w_A}{w_A + w_B}) r_c R_c cos\gamma_c},$$
$$r_{ac} = \sqrt{R_c^2 + (\frac{w_B}{w_A + w_B})^2 r_c^2 + 2(\frac{w_B}{w_A + w_B}) r_c R_c cos\gamma_c}$$

and

$$r_{ab} = r_c$$

In these equations r_{bc}, r_{ac} and r_{ab} are the internuclear distances (see Figure 2.2), whereas, w_A and w_B represent the masses of A and B atoms. Such transformation is required as the PES is constructed as a function of internal coordinates. The potential energy matrix is one of the four large matrices to be formed and stored in each processor during calculation. It is noted here that unlike the methodology followed for the state-selected study described in the previous section, a single calculation following present algorithm provides the state-to-state dynamical attributes of only one product channel (AB + C or AC + B) at a time out of the two possibilities and the channel is selected by the sequence of the nuclear masses. Thus, separate calculations are required for different product channels.

The ro-vibrational energies of the product diatom (AB) are calculated at the product asymptote by solving the eigenvalue equation,

$$\left[-\frac{1}{2\mu_r^{AB}}\frac{\partial^2}{\partial r_c^2} + V_{AB}(r_c) + \frac{j(j+1)}{2\mu_r^{AB} r_c^2}\right]\phi_{v'j'}^{AB}(r_c) = \epsilon_{v'j'}^{AB}\phi_{v'j'}^{AB}(r_c) \tag{2.50}$$

In the above equation μ_r^{AB}, $\phi_{v'j'}^{AB}$ and $\epsilon_{v'j'}^{AB}$ represent the reduced mass, ro-vibrational wavefunction and energy of the product diatom, respectively. The diatomic potential, $V_{AB}(r_c)$ is calculated at $R_c \to \infty$ and Colbert-Miller representation of kinetic energy matrix [2] is used for the solution of equation 2.50. Like all other dynamics calculations, the interaction potential is set to zero at the equilibrium minimum of reagent diatom and hence a knowledge about the endoergicity/exoergicity of the A + BC $\to$ AB + C reaction is obtained from $V_{AB}(r_c)$. Furthermore, a preliminary idea about the number of rotational and vibrational

levels of the product diatom required is gained from the solution of equation 2.50 as the dissociation energy of the diatom is known from $V_{AB}(r_c)$.

The ro-vibrational wave functions and energies of product diatom are calculated once again at the analysis line, $R_c = R_\infty$ by solving equation 2.50. The diatomic potential, $V_{AB}(r_c)$ is obtained by averaging the potential over the angular grid, γ_c calculated at $R_c = R_\infty$. The wave functions, $\phi^{AB}_{v'j'}$ are stored for the calculation of state-to-state time-dependent coefficients at a latter stage.

An analogous eigenvalue equation like equation 2.50 is solved to obtain ro-vibrational energies and wave functions of the reagent diatom, BC at $R_a \to \infty$ (at the reagent asymptote) and at $R_a = R_0$. Calculated energies and wave functions correspond to the initial state of the reagent diatom and R_a represents the scattering coordinate of reagent Jacobi coordinate system here. The ro-vibrational energy obtained at reagent asymptote is required to construct the energy grid during the calculation of energy resolved $\boldsymbol{S}$-matrix elements. On the other hand, the wave function, $\phi^{BC}_{vj}(r_a)$ calculated at $R_a = R_0$ is stored for the construction of initial WP. Here r_a is the internuclear distance of BC diatom and the reagent Jacobi coordinate system used is similar to Figure 2.1 except the Jacobi angle. Unlike Figure 2.1, the Jacobi angle, γ_a is considered to be the angle among A-atom, center of mass of BC diatom and C atom.

2.3.1.1 Construction of initial WP

Solution of the Schrödinger equation is an initial value problem and the initial WP bears the characteristic of reagent diatom. Hence the initial WP must be pertinent to reagent asymptote. Each set of product Jacobi coordinate (R_c, r_c and γ_c) corresponds to an unique set of reagent Jacobi coordinate (R_a, r_a and γ_a). The Cartesian coordinates of the three nuclei are initially found from product Jacobi

coordinates by setting the origin at the center-of-mass (CM) of AB diatom and A and B atoms at the negative and positive sides of the abscissa, respectively. The CM of BC diatom is further evaluated from the Cartesian coordinates of B and C atoms. The coordinates of the CM of BC diatom and A atom allow to calculate R_a, whereas r_a is evaluated from the coordinates of B and C atoms, respectively. Finally, the Jacobi angle, γ_a is calculated by using the parallelogram law. Furthermore, β (the angle between $\mathbf{R}_a$ and $\mathbf{R}_c$) is also calculated here. The initial WP is then formed at the reagent asymptote ($R_a = R_0$) by the relation [28],

$$\begin{aligned} q'^{j\Omega}(R_a, r_a, \gamma_a, t=0) &= \frac{sin[\alpha(R_a - R_0)]}{R_a - R_0} cos[(k_0)(R_a - R_0)] \\ &\times e^{-\beta_s (R_a - R_0)^2} \phi_{vj}^{BC}(r_a) P_j^{\Omega}(cos\gamma_a) \end{aligned} \tag{2.51}$$

In the above equation, $\frac{sin[\alpha(R_a - R_0)]}{R_a - R_0} cos[(k_0)(R_a - R_0)] e^{-\beta_s (R_a - R_0)^2}$ represents the real part of a sinc WP [30]. Here α and β_s are related to the width and smoothness of energy distribution of the WP, respectively, whereas, k_0 defines the initial momentum of the WP. $\phi_{vj}^{BC}(r_a)$ corresponds to the ro-vibrational wavefunction of reagent diatom at its j^{th} rotational and v^{th} vibrational level which is obtained by linear interpolation of the latter at r_a calculated earlier at different grid values. Finally, $P_j^{\Omega}(cos\gamma_a)$ is the normalized associated Legendre polynomial at γ_a in which Ω represents the projection of J on the body-fixed z-component of reagent Jacobi coordinate system. The WP involving the real valued imaginary part of the sinc WP is

$$\begin{aligned} p'^{j\Omega}(R_a, r_a, \gamma_a, t=0) &= -\frac{sin[\alpha(R_a - R_0)]}{R_a - R_0} sin[(k_0)(R_a - R_0)] \\ &\times e^{-\beta_s (R_a - R_0)^2} \phi_{vj}^{BC}(r_a) P_j^{\Omega}(cos\gamma_a) \end{aligned} \tag{2.52}$$

The wave packets generated at reagent Jacobi coordinate by equation 2.51 and equation 2.52 are immediately transformed into product Jacobi coordinates by the following relations [28] before the propagation starts.

$$\begin{aligned} q'^{J\Omega'}(R_c, r_c, \gamma_c, t=0) &= N\sqrt{w'_c}q'^{j\Omega}(R_a, r_a, \gamma_a, t=0) \\ &\times \frac{R_c r_c}{R_a r_a} d^J_{\Omega\Omega'}(\beta) \end{aligned} \tag{2.53}$$

and

$$\begin{aligned} p'^{J\Omega'}(R_c, r_c, \gamma_c, t=0) &= N\sqrt{w'_c}p'^{j\Omega}(R_a, r_a, \gamma_a, t=0) \\ &\times \frac{R_c r_c}{R_a r_a} d^J_{\Omega\Omega'}(\beta) \end{aligned} \tag{2.54}$$

In the above two equations, N and $d^J_{\Omega\Omega'}(\beta)$ represent the normalization constant and the reduced Wigner matrix [31,32]. Care must be taken regarding the choice of R_0 (center of the initial WP in reagent Jacobi coordinate) and the starting point of the absorption range along r_c (r_c^{abs}). The latter must be chosen to be sufficiently large so that after the transformation, the WP must not reside beyond r_c^{abs} [29].

2.3.1.2 Action of Hamiltonian operator on the WP

The action of the Hamiltonian operator ($\hat{H}_{nuc}$ expressed in atomic units here) on the real wave packet characterized by J and Ω' is given by [28, 33]

$$\begin{aligned}
\hat{H}_{nuc}q'^{J\Omega'}(Q_c,t) &= \left[-\frac{1}{2\mu_R^{ABC}}\frac{\partial^2}{\partial R_c^2}-\frac{1}{2\mu_r^{AB}}\frac{\partial^2}{\partial r_c^2}\right]q'^{J\Omega'}(Q_c,t)\\
&- \left(\frac{1}{2\mu_R^{ABC}R_c^2}+\frac{1}{2\mu_r^{AB}r_c^2}\right)\left[\frac{1}{sin\gamma_c}\frac{\partial}{\partial\gamma_c}sin\gamma_c\frac{\partial}{\partial\gamma_c}-\frac{\Omega'^2}{sin^2\gamma_c}\right]q'^{J\Omega'}(Q_c,t)\\
&+ \hat{V}(Q_c)q'^{J\Omega'}(Q_c,t)+\left(\frac{1}{2\mu_R^{ABC}R_c^2}\right)(J(J+1)-2\Omega'^2)q'^{J\Omega'}(Q_c,t)\\
&- \frac{C^+_{J\Omega'}}{2\mu_R^{ABC}R_c^2}\left[\frac{\partial}{\partial\gamma_c}-\Omega' cot\gamma_c\right]q'^{J(\Omega'+1)}(Q_c,t)\\
&- \frac{C^-_{J\Omega'}}{2\mu_R^{ABC}R_c^2}\left[-\frac{\partial}{\partial\gamma_c}-\Omega' cot\gamma_c\right]q'^{J(\Omega'-1)}(Q_c,t), \qquad (2.55)
\end{aligned}$$

where $C^{\pm}_{J\Omega'}=\sqrt{[J(J+1)-\Omega'(\Omega'\pm1)]}$. Here J represents the quantum number for total angular momentum, whereas, Ω' is the projection of J on the body-fixed z-axis of product Jacobi coordinate system. In equation 2.55, $\mu_R^{ABC}(=w_C(w_A+w_B)/(w_A+w_B+w_C))$ and $\mu_r^{AB}(=(w_Aw_B)/(w_A+w_B))$ represent the three body and product diatom reduced masses, respectively. Furthermore, Q_c collectively represents the product Jacobi coordinates for the nuclei.

From equation 2.55 it is seen that the action of Hamiltonian involves only a particular value of J and hence calculations can be done separately for each value of it. In contrast, the centrifugal or Coriolis coupling terms present in nuclear Hamiltonian (see the last two operators present on the R. H. S. of equation 2.55) lead to the mixing of the WP, $q'^{J\Omega'}$ with others corresponding to different Ω'. Thus, Ω' does not behave as a good quantum number from the calculation point of view. The calculation of cross sections requires the dynamics study of many J values and depending on the parity, for each J, either $(J+1)$ or J numbers of Ω'

must be involved. In the present approach, dynamics study for higher values of J are made possible by parallelizing the calculations over Ω' on different processors. Such approach of parallelization bears similarity with the procedure followed by Goldfield and Gray [34]. Calculations for each combination of J and Ω' are assigned to different processors and only neighboring processors are required to communicate among themselves.

It is worth mentioning here the basic technicalities followed to carry out the action of the Hamiltonian operator on the wave packet , $\hat{H}_{nuc}q'^{J\Omega'}$ (cf. Eq. 2.55), and hence they are outlined below [29].

a) **For radial kinetic energy operator along** R_c, $-\frac{1}{2\mu_R^{ABC}}\frac{\partial^2}{\partial R_c^2}$: The wave packet is transformed to the momentum space by Fourier transformation followed by its multiplication with kinetic energy ($\frac{k^2}{2\mu_R^{ABC}}$) in momentum space and finally it is back transformed to the coordinate space.

b) **For radial kinetic energy operator along** r_c, $-\frac{1}{2\mu_r^{AB}}\frac{\partial^2}{\partial r_c^2}$: Fourier transformation is done in r_c followed by the multiplication of the wave packet in momentum space by the kinetic energy ($\frac{k^2}{2\mu_r^{AB}}$). Finally the wave packet is transformed back to the coordinate space by inverse Fourier transformation.

c) **For potential energy operator**, $\hat{V}$: As the potential energy is local in coordinate space its effect on the wave packet in simply multiplicative, $\hat{V}(Q_c)q'^{J\Omega'}$.

d) **For the angular kinetic energy operator associated with** R_c,
$(-\frac{1}{2\mu_R^{ABC}R_c^2})\left[\frac{1}{sin\gamma_c}\frac{\partial}{\partial\gamma_c}sin\gamma_c\frac{\partial}{\partial\gamma_c}-\frac{\Omega'^2}{sin^2\gamma_c}\right]+(\frac{1}{2\mu_R^{ABC}R_c^2})(J(J+1)-2\Omega'^2)$:
Calculation of $(j'(j'+1)+(J(J+1)-2\Omega'^2))/(2\mu_R^{ABC}R_c^2)$ followed by the transformation to grid representation by the transformation matrix for Ω' and multiplication with the WP, $q'^{J\Omega'}$.

e) **For the angular kinetic energy operator associated with** r_c,
$-\frac{1}{2\mu_r^{AB}r_c^2}\left[\frac{1}{sin\gamma_c}\frac{\partial}{\partial\gamma_c}sin\gamma_c\frac{\partial}{\partial\gamma_c}-\frac{\Omega'^2}{sin^2\gamma_c}\right]$:

Calculation of $(j'(j'+1))/(2\mu_r^{AB}r_c^2)$ followed by the transformation to grid representation by the transformation matrix for Ω' and multiplication with the WP, $q'^{J\Omega'}$.

f) **For the Coriolis coupling term associated with** $(\Omega'+1)$ **quantum number**, $-\frac{C^+_{J\Omega'}}{2\mu_R^{ABC}R_c^2}\left[\frac{\partial}{\partial\gamma_c}-\Omega' cot\gamma_c\right]$:
Calculation of $[(\sqrt{J(J+1)-\Omega'(\Omega'+1)})(\sqrt{j(j+1)-\Omega'(\Omega'+1)})]/(2\mu_R^{ABC}R_c^2)$ followed by the transformation to the grid representation by using the transformation matrix for $(\Omega'+1)$ and multiplication with the WP, $q'^{J(\Omega'+1)}$.

g) **For the Coriolis coupling term associated with** $(\Omega'-1)$ **quantum number**, $-\frac{C^-_{J\Omega'}}{2\mu_R^{ABC}R_c^2}\left[-\frac{\partial}{\partial\gamma_c}-\Omega' cot\gamma_c\right]$:
Calculation of $[(\sqrt{J(J+1)-\Omega'(\Omega'-1)})(\sqrt{j(j+1)-\Omega'(\Omega'-1)})]/(2\mu_R^{ABC}R_c^2)$ followed by the transformation to the grid representation by using the transformation matrix for $(\Omega'-1)$ and multiplication with the WP, $q'^{J(\Omega'-1)}$.

For the evaluation of the angular kinetic energy operators and Coriolis coupling terms, the wave packet is expanded in a set of basis of associated Legendre polynomials, $P_{j'}^{\Omega'}(cos\gamma_c)$. Same grid points for γ_c are considered for wave packets of different Ω' value [16, 35] and these correspond to the associated Legendre quadrature points for Ω'=0. It is obvious from above discussion that for the evaluation of the action of angular kinetic energy operators and Coriolis interactions, transformation of the WP to the basis set representation is required. Furthermore, transformation matrices are different for each Ω' value and hence the processor following the evaluation of the WP, $q'^{J\Omega'}$ needs to store matrices for Ω', $\Omega'+1$ and $\Omega'-1$. It is worthwhile to mention here that limiting of Coriolis coupling potential is also taken care off [28] in present calculations.

2.3.1.3 Recursion relation for the propagation of the wave packet

Let us define a function of the Hamiltonian operator as [26]

$$f(\hat{H}_{nuc}) = -\frac{\hbar}{\tau} cos^{-1}(\hat{H}_{nuc,s}). \tag{2.56}$$

Here $\hat{H}_{nuc,s}(= a'_s \hat{H}_{nuc} + b'_s)$ represents a scaled and shifted Hamiltonian whose eigenvalues lie between -1 and +1. If E_{min} and E_{max} represent the lower and upper bound of $\hat{H}_{nuc}$ spectrum, a'_s and b'_s terms are defined as follows

$$a'_s = \frac{2}{(E_{max} - E_{min})}$$
$$b'_s = -1 - a'_s E_{min}.$$

$\hat{H}_{nuc,s}$ turns out to be the same scaled and shifted Hamiltonian as that is used in the Chebyshev polynomial scheme [20]. With the choice of this function (see equation 2.56) equation 2.46 can be rewritten as

$$q'^{J\Omega'}(Q_c, t+\tau) = -q'^{J\Omega'}(Q_c, t-\tau) + 2\hat{H}_{nuc,s} q'^{J\Omega'}(Q_c, t). \tag{2.57}$$

On the other hand, the equation to find the WP at the initial time step can be derived from equation 2.49 and 2.56 as

$$q'^{J\Omega'}(Q_c, \tau) = \hat{H}_{nuc,s} q'^{J\Omega'}(Q_c, 0) - \sqrt{1 - \hat{H}^2_{nuc,s}}\, p'^{J\Omega'}(Q_c, 0). \tag{2.58}$$

Thus, equation 2.57 and 2.58 are the two principal equations used for the propagation of the WP in the state-to-states dynamics study described in chapter 5 and 6. Furthermore, in equation 2.58, the evaluation of the square root operator

is carried out by expanding this by Chebyshev polynomials as

$$\sqrt{1-\hat{H}_{nuc,s}^2} = \sum_n \beta'_n T'_n(\hat{H}_{nuc,s}), \tag{2.59}$$

where β'_n and T'_n are the expansion coefficients and Chebyshev polynomials of order n, respectively. It is worth mentioning here that at each time step, the action of the scaled Hamiltonian, $\hat{H}_{nuc,s}$ on the WP is carried out by following the technicalities described previously in section 2.3.1.2 and the functional form of the absorption function used at grid boundaries to avoid spurious reflections from there is [28]

$$A(x') = exp[-c_{abs}exp(-2(x'_{max} - x'_{abs})/(x' - x'_{abs}))], \tag{2.60}$$

where c_{abs} and x'_{abs} are the strength and starting point of absorption, respectively. The absorption is effective for $x' > x'_{abs}$ and the value of the function, A=1 elsewhere. In the above equation x' represents either R_c or r_c here.

2.3.1.4 Analysis of the propagated WP and calculation of time-dependent coefficients

To analyze the propagated WP at every iteration step, an analysis line is placed at the product asymptote, $R_c = R_\infty$ which yields $q'^{J\Omega'}(R_c = R_\infty, r_c, \gamma_c, t)$. The latter is expanded in terms of the ro-vibrational eigenfunctions of the product diatom, $\phi^{AB}_{v'j'}(r_c, \gamma_c)$ with time-dependent coefficients $C^J_{v,j,\Omega\rightarrow v',j',\Omega'}(t)$ as [28]

$$q'^{J\Omega'}(R_c = R_\infty, r_c, \gamma_c, t) = \sum_{v',j'} C^J_{v,j,\Omega\rightarrow v',j',\Omega'}(t)\phi^{AB}_{v'j'}(r_c, \gamma_c) \tag{2.61}$$

In this equation, v and j are the vibrational and rotational states of reagent diatom, whereas, v' and j' represent the same for the product diatom. Hence, the expression for the coefficients can be written from equation 2.61 as

$$C^{J}_{v,j,\Omega\rightarrow v',j',\Omega'}(t) = \int \phi^{*AB}_{v'j'}(r_c,\gamma_c) q'^{J\Omega'}(R_c = R_\infty, r_c, \gamma_c, t) dr_c sin(\gamma_c) d\gamma_c. \quad (2.62)$$

It is mentioned here that in all results presented in chapter 5 and chapter 6, $j = \Omega = 0$ is considered. Finally, after every iteration step, the time-dependent coefficients calculated in different processors by employing equation 2.62 are stored inside a common file in a sequential way which is used latter to calculate energy resolved $\boldsymbol{S}$-matrix elements.

2.3.2 Calculation of energy resolved $\boldsymbol{S}$-matrix elements

The energy resolved $\boldsymbol{S}$-matrix is a fundamental quantity to be evaluated in a state-to-state scattering calculation. The elements of it represent the amplitudes for the beginning from some initial state, i and ending to a final state, f at a fixed energy [36]. The time-dependent coefficients calculated by equation 2.62 are Fourier transformed to obtain energy-dependent coefficients, $A^{J}_{v,j,\Omega\rightarrow v',j',\Omega'}(E)$ as [28]

$$A^{J}_{v,j,\Omega\rightarrow v',j',\Omega'}(E) = \frac{1}{2\pi}\int_0^\infty exp(\frac{iEt}{\hbar}) C^{J}_{v,j,\Omega\rightarrow v',j',\Omega'}(t) dt. \quad (2.63)$$

Though these coefficients are proportional to the BF $\boldsymbol{S}$-matrix elements [37–39], the latter are not directly calculated from $A^{J}_{v,j,\Omega\rightarrow v',j'\Omega'}(E)$. The long range Coriolis coupling terms present in a BF coordinate system prevent the calculation of $\boldsymbol{S}$-matrix elements correctly for $J >0$ and hence the latter should be initially calculated in a space-fixed (SF) reference frame [40]. To this effort, the energy-dependent coefficients calculated in equation 2.63 are transformed from BF to SF

reference frame by the relation [28],

$$A^J_{v,j,l\rightarrow v',j',l'}(E) = \sum_{\Omega'\Omega}^{min(j',J)} T^J_{l\Omega} A^J_{v,j,\Omega\rightarrow v',j',\Omega'}(E) T^J_{l'\Omega'}. \tag{2.64}$$

In this equation, $T^J_{l'\Omega'}$ and $T^J_{l\Omega}$ are the elements of $\mathbf{T}^c$ and $\mathbf{T}^a$ transformation matrices for products and reagents, respectively. It is worth mentioning here that for $j = \Omega = 0$ which is considered in the calculations presented in this thesis, the $\mathbf{T}^a$ can be excluded. The other transformation matrix, $\mathbf{T}^c$ with the elements $T^J_{l'\Omega'}$ diagonalizes the tri-diagonal Coriolis coupling matrix, $\mathbf{T}^{CC}$. The diagonal and off-diagonal elements of $\mathbf{T}^{CC}$ (expressed in atomic units) are $\left(\frac{1}{2\mu_R^{ABC}R_c^2}\right)$ $[J(J+1)+$ $j'(j'+1)-2\Omega^2]$ and $-\left(\frac{1}{2\mu_R^{ABC}R_c^2}\right)$ $[\sqrt{J(J+1)-\Omega'(\Omega'+1)}\sqrt{j(j+1)-\Omega'(\Omega'+1)}]$, respectively. Now the $\boldsymbol{S}$-matrix elements in a SF frame are calculated by using the energy-dependent coefficients obtained from equation 2.64 as

$$\begin{aligned} S^J_{v,j,l\rightarrow v',j',l'}(E) &= -\frac{\hbar^2 a'_s}{\sqrt{1-(a'_s E + b'_s)^2}} \sqrt{\frac{k^p_{v'j'} k^r_{vj}}{\mu_R^{ABC}\mu_R}} \\ &\times \frac{2A^J_{v,j,l\rightarrow v',j',l'}(E)}{\bar{g}(k^r_{vj})} e^{-i(k^p_{v'j'}R_\infty + \delta\eta'_{v'j'l'} + \delta\eta'_{vjl})}. \end{aligned} \tag{2.65}$$

In this equation, a'_s and b'_s are the parameters used to scale the Hamiltonian, whereas, $k^r_{vj}(=\sqrt{2\mu_R(E-\epsilon'_{vj})}/\hbar^2)$ and $k^p_{v'j'}(=\sqrt{2\mu_R^{ABC}(E-\epsilon^{AB}_{v'j'})}/\hbar^2)$ represent the wave vector components with the reagent and product channels, respectively. Furthermore, $\bar{g}(k^r_{vj})$ is the Fourier transformation of the initial WP in the momentum space and finally, $\delta\eta'_{v'j'l'}$ and $\delta\eta'_{vjl}$ are used for the phase adjustment of

$\boldsymbol{S}$-matrix and these are expressed as

$$\begin{aligned}\delta\eta'_{vjl} &= -\sqrt{2\mu_R(E-\epsilon'_{vj})R_0^2 - J(J+1)} \\ &+ \sqrt{J(J+1)}sin^{-1}\left(-\sqrt{\frac{J(J+1)}{2\mu_R(E-\epsilon'_{vj})R_0^2}}\right) \\ &+ \sqrt{2\mu_R(E-\epsilon'_{vj})}R_0 \end{aligned} \tag{2.66}$$

and

$$\begin{aligned}\delta\eta'_{v'j'l'} &= -\sqrt{2\mu_R^{ABC}(E-\epsilon^{AB}_{v'j'})R_\infty^2 - l'(l'+1)} \\ &+ \sqrt{l'(l'+1)}sin^{-1}\left(\sqrt{\frac{l'(l'+1)}{2\mu_R^{ABC}(E-\epsilon^{AB}_{v'j'})R_\infty^2}}\right) \\ &+ \sqrt{2\mu_R^{ABC}(E-\epsilon^{AB}_{v'j'})}R_\infty. \end{aligned} \tag{2.67}$$

On the R. H. S. of equation 2.66, l has been replaced by J as j=0 is considered. The other terms used in these two equations are defined previously in this chapter. Finally the $\boldsymbol{S}$-matrix elements calculated in the SF frame (see equation 2.65) are transformed back to the BF basis by an inverse transformation using the same matrices $\mathbf{T}^c$ and $\mathbf{T}^a$ as [28]

$$S^J_{v,j,\Omega\to v',j',\Omega'}(E) = \sum_{l'l} T^J_{\Omega l} S^J_{v,j,l\to v',j',l'}(E) T^J_{\Omega' l'}. \tag{2.68}$$

Here it is noted that $T^J_{\Omega' l'}$ and $T^J_{\Omega l}$ represent the elements of $(\mathbf{T}^c)^T$ and $(\mathbf{T}^a)^T$, respectively.

2.3.3 Calculation of probabilities and cross sections

The square of the modulus of state-to-state $\boldsymbol{S}$-matrix elements produces energy resolved state-to-state reaction probabilities as

$$P_{v,j,\Omega\rightarrow v',j',\Omega'}(E) = |S^J_{v,j,\Omega\rightarrow v',j',\Omega'}(E)|^2. \tag{2.69}$$

Total reaction probabilities are calculated by the relation

$$P^J_{v,j,\Omega}(E) = \sum_{v'j'\Omega'} P^J_{v,j,\Omega\rightarrow v',j',\Omega'}(E), \tag{2.70}$$

whereas, product vibrational level resolved reaction probabilities are obtained by a sum over j' and Ω' as

$$P^J_{v,j,\Omega\rightarrow v'}(E) = \sum_{j'\Omega'} P^J_{v,j,\Omega\rightarrow v',j',\Omega'}(E). \tag{2.71}$$

Furthermore, for a selected value of v', product rotational level resolved probabilities are obtained by summing the state-to-state probabilities, $P_{v,j,\Omega\rightarrow v',j',\Omega'}(E)$ over Ω'.

State-to-state DCSs, $\sigma'_{v,j\rightarrow v',j'}(E,\theta)$, are calculated from $\boldsymbol{S}$-matrix elements by considering all partial wave contributions of J as

$$\sigma'_{v,j\rightarrow v'j'}(E,\theta) = \frac{1}{2j+1}\sum_{\Omega\Omega'}\frac{1}{4(k^r_{vj})^2}|\sum_J (2J+1)S^J_{v,j,\Omega\rightarrow v',j',\Omega'}(E)d^J_{\Omega\Omega'}(\pi-\theta)|^2. \tag{2.72}$$

Here θ is the scattering angle and this equation is obtained by the usual replacement, $\theta \rightarrow \pi - \theta$ on the R. H. S. of the equation for DCS as shown by Zhang and Miller (cf. equation 2.22b of Ref. [41]). Scattering of the product at θ=180^0 and

θ=0^0 correspond to backward and forward scattering, respectively. State-to-state ICSs are further calculated by integrating corresponding DCSs over all angles as

$$\begin{aligned} \sigma_{v,j\rightarrow v',j'}(E) &= \int_0^{2\pi} d\phi \int_0^{\pi} \sigma'_{v,j\rightarrow v',j'}(E,\theta) sin(\theta) d\theta \\ &= 2\pi \int_0^{\pi} \sigma'_{v,j\rightarrow v',j'}(E,\theta) sin(\theta) d\theta. \end{aligned} \tag{2.73}$$

At this point, it is worthwhile to mention here that as only the real part of the WP is majorly involed in the calculation, the memory requirement is very less here which becomes advantageous for the dynamics study of insertion type of reactions where large number of grid points are needed. On the other hand, a huge number of processors are needed to work simultaneously for larger values of J as the calculations are parallelized over Ω'. For example, for the dynamics calculation of J=50, 51 processors are required simultaneously and this aspect of the method is a bottleneck at present.

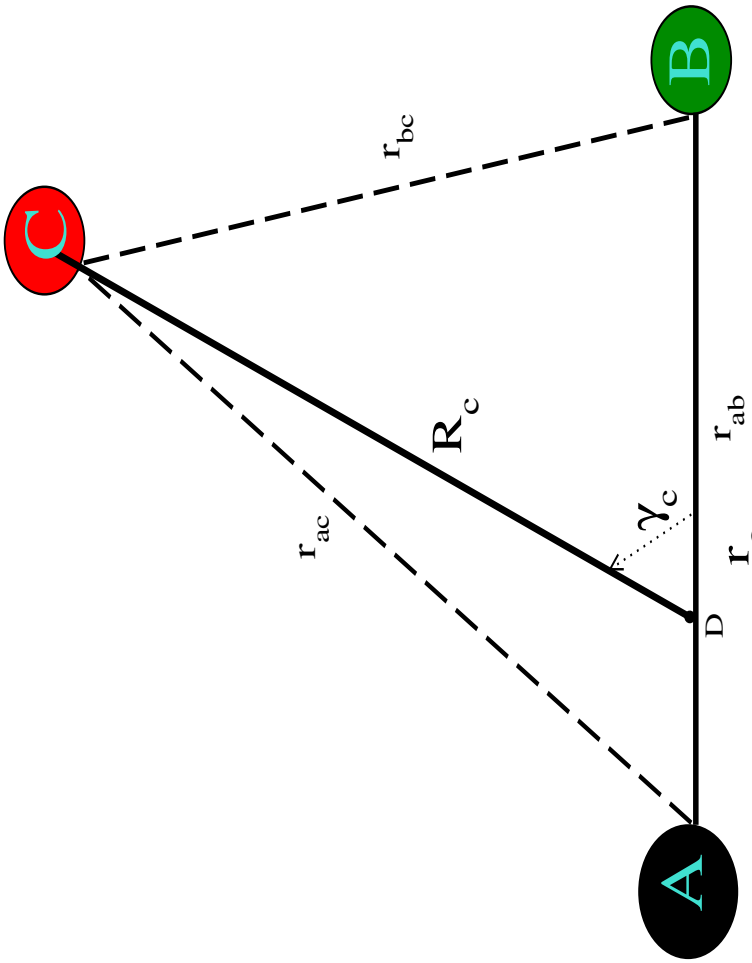

Figure 2.2: Schematic representation of the body-fixed product Jacobi coordinate system used for the state-to-state dynamics study. See text for details.

2.4 Procedure for the construction of MEP

The methodologies and mathematical details followed for the construction of minimum energy paths (MEPs) for the S + OH → SO + H and C + OH → CO + H reactions presented in chapter 3 and chapter 4 are outlined in this section. MEPs are generated for different approach angles of the attacking atom. Let us look back to Figure 2.1 and consider $r_{ab} = r_1$(bond distance correspond to product diatom), $r_{bc} = r_2$(bond distance correspond to reagent diatom), $r_{ac} = r_3$, $\angle DAB = \alpha$, $\angle ABD = \beta$. Moreover, $\gamma = \angle ADB$ represents the approach angle of the attacking atom. The calculation starts with the generation of identical grid points along r_1 and r_2. The potential energy of HCO and HSO reactive systems on second excited and electronic ground states, respectively, is function of internuclear distances and hence the value of r_3 is required to obtain the potential energy. The latter is calculated by the following relations.

$$r_{BD} = \frac{w_C}{(w_B + w_C)} r_2,$$

where r_{BD} is the distance between B atom and the center of mass of BC diatom, D (see Figure 2.1), whereas, w_B and w_C represent the masses of B and C atoms, respectively. By using the law of sines for ADB triangle, it can be written that

$$\alpha = sin^{-1}[\frac{r_{BD} sin\gamma}{r_1}].$$

Hence, the value of angle β is $\pi - (\alpha + \gamma)$ and by using the law of sines for ADB triangle once again it is obtained that

$$R = \frac{r_1 sin\beta}{sin\gamma}.$$

Hence the values of the set of Jacobi coordinate are known and r_3 is calculated by the relation,

$$r_3 = \sqrt{R^2 + (\frac{w_B}{w_B + w_C})^2 r_2^2 + 2(\frac{w_B}{w_B + w_C}) r_2 R cos\gamma}.$$

finally, by using all internuclear distances the potential energies for each set of r_1 and r_2 values are calculated and stored inside a two dimensional array. The reaction coordinate is chosen as r_1-r_2 and a particular value of the latter can be obtained by many combinations of $r_1(i) - r_2(j)$, where i and j represent the index for grid points. For n grid points along r_1 and r_2 coordinates, the minimum value of the potential energy is chosen from all such combinations of $2n$ number of r_1-r_2 arrangements and they are plotted against the latter. Furthermore, by definition $(r_1 - r_2) >> 0$ and $(r_1 - r_2) << 0$ represent the reagent and product channels, respectively.

References

[1] R. Kosloff, J. Phys. Chem. **92** 2087 (1988); Ann. Rev. Phys. Chem. **45**, 145 (1994). and references therein.

[2] D.T. Colbert and W. H Miller, J. Chem. Phys. **96**, 1982 (1992).

[3] R. T. Pack, J. Chem. Phys. **60**, 633 (1974).

[4] R. Kosloff, in C. Cerjan (NATO ASI Ser. C 412) (Eds.), Numerical Grid methods and Their applications to Schrödinger Equation, Kluwera Academic Publishers, Dordreht, The Netherlands, 1933, p. 175.

[5] R. Kosloff in Time Dependent Methods for Quantum dynamics, NATO ASI Ser. B229, Plenum Press, New York, 1992.

[6] D. Kosloff and R. Kosloff, J. Comput. Phys. **52**, 35 (1983); Comput. Phys. Commun. **30**, 333 (1983).

[7] J. A. Fleck, Jr., J. R. Morris, and M. D. Feit, Appl. Phys. **10**, 129 (1976).

[8] M. D. Feit, J. A. Fleck, Jr., A. Steiger, J. Comput. **47**, 412 (1982); M. D. Feit, J. A. Fleck, Jr. J. Chem. Phys. **78**, 301 (1983); J. Chem. Phys. **80**, 2578 (1984).

[9] S. Mahapatra and N. Sathyamurthy, J. Chem. Soc., Faraday Trans. **93**, 773 (1997).

[10] J. W. Cooley and J. W. Tuckey, Math. Computation **19**, 297 (1965).

[11] D. O. Harris, G. G. Engerholm, and W. D. Gwinn, J. Chem. Phys. **43**, 1515 (1965).

[12] A. S. Dickison and P. R. Certain, J. Chem. Phys. **49**, 4209 (1968).

[13] J. V. Lill, G. A. Parker and J. C. Light, Chem. Phys. Lett. **89**, 483 (1982); J. C. Light, I. P. Hamilton, and J. V. Lill, J. Chem. Phys. **82**, 1400 (1985); J. P. Hamilton and J. C. Light, J. Chem. Phys. **84**, 306 (1986).

[14] R. M. Whitnell and J. C. Light, J. Chem. Phys. **90**, 1774 (1989).

[15] Z. Bačić and J. C. Light, Ann. Rev. Phys. Chem. **40**, 469 (1989).

[16] C. Leforestier, J. Chem. Phys. **94**, 6388 (1991).

[17] P. McGuire and D. J. Kouri, J. Chem. Phys. **60**, 2488 (1974).

[18] A. Askar and A. S. Cakmak, J. Chem. Phys. **68**, 2794 (1978); D. Kosloff and R. Kosloff, Comput. Phys. Commun. **30**, 333 (1983); J. Chem. Phys. **52**, 35 (1983).

[19] M. D. Feit, J. A. Fleck Jr., and A. Steiger, J. Comput. Phys. **47**, 412 (1982).

[20] H. Tal-Ezer and R. Kosloff, J. Chem. Phys. **81**, 3967 (1984).

[21] T. J. Park and J. C. Light, J. Chem. Phys. **85**, 5870 (1986).

[22] D. Kosloff and R. Kosloff, Comput. Phys. Commun. **30**, 333 (1983); J. Comput. Phys. **52**, 35 (1983).

[23] D. Neuhauser, M. Baer, R. S. Judson, and D. J. Kouri, Comput. Phys. Com. **63**, 463 (1991).

[24] W. H. Miller, J. Chem. Phys. **102**, 793 (1998).

[25] N. Balakrishnan, C. Kalyanaraman and N. Sathyamurthy, Phys. Rep. **280**, 79 (1997).

[26] S. K. Gray and G. G. Balint-Kurti, J. Chem. Phys. **108**, 950 (1998).

[27] S. K. Gray, J. Chem. Phys. **96**, 6543 (1992).

[28] M. Hankel, S. C. Smith, R. J. Allan, S. K. Gray, and G. G. Balint-Kurti, J. Chem. Phys. **125**, 164303 (2006).

[29] M. Hankel, S. C. Smith, S. K. Gray, and G. G. Balint-Kurti, Comp. Phys. Commun. **179**, 569 (2008).

[30] M. Hankel, G. G. Balint-Kurt, and S. K. Gray, Int. J. Quant. Chem. **92**, 205 (2003).

[31] A. R. Edmonds, *Angular momentum in Quantum Mechanics*(Princeton University Press, Princeton, NJ, 1960).

[32] R. N. Zare, *Angular Momentum* (Willey, New York, 1988).

[33] A. R. Offer, and G. G. Balint-Kurti, J. Chem. Phys. **101**, 10416 (1994).

[34] E. M. Goldfield and S. K. Gray, Comput. Phys. Commun. **84**, 1 (1996).

[35] G. Corey and D. Lemoine, J. Chem. Phys. **97**, 4115 (1992).

[36] M. Brouard and C. Vallance (EDs.), *Tutorials in Molecular Reaction Dynamics*, RSC Publishing, 2010.

[37] W. L. Wang, C. Rosa, and J. Brandão, Chem. Phys. Lett. **418**, 250 (2006).

[38] G. G. Balint-Kurti, Adv. Chem. Phys. **128**, 249 (2003).

[39] G. G. Balint-Kurti, R. N. Dixon, and C. C. Marston, J. Chem. Soc. Faraday Trans, **86**, 1741 (1990).

[40] S. C. Althorpe, J. Chem. Phys. **114**, 1601 (2001).

[41] J. Z. H. Zhang and W. H. Miller, J. Chem. Phys. **91**, 1528 (1989).

Chapter 3

Time-dependent quantum wave packet dynamics of the S + OH reaction on its electronic ground potential energy surface

3.1 Introduction

Initial state-selected dynamics study of the exoergic, S(^{3}P) + OH ($X^2\Pi$, v=0-5, j=0-3) $\rightarrow$ SO ($X^3\Sigma^-, \Sigma v', \Sigma j'$) + H (^{2}S), reaction on the electronic ground PES ($\tilde{X}^2A''$) [1] of HSO reactive system, calculated by the methodology given in section 2.2 is presented and discussed in detail in this chapter. Findings on reaction probabilities, ICSs and rate constants are discussed. Reaction probabilities are calculated upto 0.5 eV collision energy within CS approximation [2, 3] for total angular momentum, J >0. Effect of rotational and vibrational excitations of reagent OH on the dynamics is also examined here. The other product channel,

SH + O is not considered here as it lies $\sim$ 0.84 eV (see Figure 1.1) above the S + OH reagent asymptote.

3.2 Theoretical and computational details

The theoretical formalism and computational details used for the calculation of initial state-selected and energy resolved total reaction probabilities and cross sections for the S + OH $\rightarrow$ SO + H reaction are discussed in section 2.2. In addition to the reaction probabilities and cross sections, rate constants are also reported in this chapter. The temperature dependent state-specific rate constant, $k_{vj}(T)$, for the S + OH reaction is calculated as [4]

$$k_{vj}(T) = \sqrt{\frac{8K_BT}{\pi\mu_R}}\frac{1}{(K_BT)^2}\int_0^\infty E\sigma_{vj}(E)e^{-E/K_BT}dE. \tag{3.1}$$

In this equation, σ_{vj}(E) is the reaction cross section corresponding to v^{th} vibrational and j^{th} rotational level of reagent OH, μ_R is the three-body reduced mass and K_B represents the Boltzmann constant. Moreover, the rate constant obtained by Equation 3.1 is further multiplied by a temperature-dependent function, f_e(T) [5], in order to consider the fine structures arising from spin-orbit coupling of the reactants. The latter function also corresponds to the probability of initiating the reaction on the electronic ground state of the HSO reactive system. Under the assumption of Maxwell-Boltzmann distribution of the initial population of the fine structure levels, the function assumes the following form.

$$f_e(T) = \frac{g^{HSO}}{[g_2^S + g_1^S exp(-\Delta E_1/T) + g_0^S exp(-\Delta E_2)/T]} \times \frac{1}{[g_{1/2}^{OH} + g_{3/2}^{OH} exp(-\Delta E_3/T)]} \tag{3.2}$$

In equation 3.2, ΔE_1=569 K and ΔE_2=825 K are the energy differences between the $^3P_2$ and $^3P_1$, and $^3P_2$ and $^3P_0$ fine structure levels, respectively. Whereas, ΔE_3=205 K corresponds to the energy splitting between the two doubly degenerate, $^2\Pi_{1/2}$ and $^2\Pi_{3/2}$ states of reagent OH. On the other hand, g_0^S=1, g_1^S=3 and g_2^S=5 correspond to the electronic degeneracies of the fine structure levels of the ground ^{3}P state of the sulfur atom. Finally, $g_{1/2}^{OH}$=$g_{3/2}^{OH}$=2 is considered as both these states are doubly degenerate and g^{HSO}=2 represents the degeneracy of the HSO molecule on its ground state.

Furthermore, the relative population of the j^{th} rotational levels of reagent OH at a given temperature is calculated by

$$p(j,T) = \frac{(2j+1)e^{Bhc(j+1)/K_BT}}{Q_{rot}}, \tag{3.3}$$

where

$$Q_{rot} = \sum_j (2j+1)e^{-Bhc(j+1)/K_BT} \tag{3.4}$$

is the rotational partition function of reagent OH. In equation 3.3 and equation 3.4, B corresponds to the rotational constant and the other three factors, K_B, h and c carry their usual meanings.

3.3 Results and discussion

3.3.1 Reaction probabilities

3.3.1.1 Probabilities for OH(v=0, j=0)

Initial state-selected and energy resolved total reaction probabilities for the, S (^{3}P) + OH (X$^2\Pi$, v=0, j=0) → SO (X$^3\Sigma^-$) + H (^{2}S), reaction and for J=0 are

plotted in panel (a) of Figure 3.1 as a function of collision energy. From Figure 3.1 (a) it can be clearly seen that the reaction does not have an energy threshold as it proceeds along a barrierless entrance channel [1]. Maximum reaction probability, ∼0.91, is found at ∼0.017 eV and it decreases afterwards until it reaches to ∼0.03 at ∼0.085 eV collision energy. The probabilities then remain almost constant and oscillate around an average value of ∼ 0.2 throughout the rest of the energies considered here. It is worth mentioning here that it is difficult to get converged reaction probabilities when scattering resonances are present in the reaction dynamics and particularly the difficulty appears to be more at low collision energies. Moreover, the choice of TIQM method is always better than a TDWP approach for a dynamics study in the limit of zero collision energy. In order to reduce errors in present calculation, the lowest value of energy is kept as $\sim 10^{-3}$ which is far above the collision energy range for which the TDWP results are not expected to be converged. Furthermore, all the parameters given in this chapter were subjected to rigorous convergence tests to achieve reasonable convergence in the total reaction probabilities for J=0 when the reagent OH was kept at its ground rovibrational level. The final converged values of all parameters are given in Table 3.1 and they were used in remaining calculations. During the calculation of probabilities for few $J > 0$ values, these parameters were inadequate to provide reasonably good results and they are altered within the limit of acceptable convergence.

Jorfi *et al.* have calculated initial state-selected total reaction probabilities for this reaction and for J=0 [6] by means of TIQM and QCT methods. TIQM results are reproduced from Ref. [6] and these are shown in panel (b) of Figure 3.1 in red colour line. It is seen from panel (a) and (b) that probabilities calculated in the present study and by TIQM method are not in agreement with each other.

In particular, the difference is severe in the intermediate collision energy range. Consequently, the convergence and the results of present TDWP approach were called into question. The convergence of the TDWP calculation was re-checked and no serious problem was found. To confirm further, Roncero calculated reaction probabilities for J=0 by using another TDWP method where reactant to product coordinate (Jacobi) transformation method was employed [7–9] and the results are shown in panel (c) of Figure 3.1. On comparison between the probabilities shown in panel (a) and panel (c), the results obtained by the two WP based methods were found to be in very good agreement with each other. On the other hand, after a detailed analysis of the TIQM results of Jorfi *et al.* [6], it turned out that these were not converged properly. Moreover, it was realized that the number of channels included in TIQM study was inadequate and it is very difficult to get convergence for this particular HSO reactive system by the hyperspherical coordinate based TIQM method. The system involves two heavy atoms, S and O, three different channels and it follows a large (∼0.8 eV) exoergic reaction path. Jorfi *et al.* could not achieve the convergence in their calculation even for J=0, as large number of open and closed channels are required in the basis set and also in the close coupling equations.

On the contrary, Jorfi *et al.* have investigated the dynamics of C + OH reaction on its first excited state successfully by the TIQM method [10] and the results were in good accord with the same calculated by a TDWP approach [11]. Hence the difficulty of getting the convergence for the S + OH reaction by the hyperspherical coordinated based TIQM method does not limit the capability of the method, rather, it is limited by the huge computational overhead to achieve convergence.

Reverting back to Figure 3.1, it can be seen that the probabilities calculated

by the QCT method (reproduced from Ref. [6] and presented in panel (b) of Figure 3.1 in black colour line) are in good accord with the same calculated by present TDWP method [cf. Figure 3.1 (a)].

The reaction probabilities calculated in the present study [see Figure 3.1 (a)] exhibit sharp and intense resonance oscillations. The intensity (measured in terms of the probability value) is more at the lower energy range, whereas, comparatively it is less at intermediate and higher energies. The resonances appear in the total reaction probability curve for J=0 due to the formation of intermediate collision complexes inside the two deep potential wells (cf., Figure 1.2 of chapter 1) present on the underlying PES [1]. The probabilities presented in Figure 3.1 (a) show similarities with those of C + OH → CO + H reaction on its first ($1^2A''$) and second ($1^4A''$) excited electronic states [10–12], whereas, these are in strong contrast with the probabilities calculated by using the electronic ground PES of COH reactive system [13]. In the latter, no resonance was found and the probability remained ∼1.0 throughout the whole energy range considered [13]. These observations can be correlated to the topographical features of the underlying PESs of these two reactive systems. Both the reactions are exoergic, barrierless at the entrance channel and they progress through deep potential wells on the underlying PESs [1, 14, 15]. The exoergicities of the C + OH → CO + H reaction are ∼6.4 eV, ∼0.41 eV, and ∼0.41 eV on its electronic ground (X^2A'), $1^2A''$ and $1^4A''$ states, respectively. All these three PESs comprise two potential wells on each of them corresponding to HCO and COH collision complexes, respectively, and the depths of these are ∼7.26 eV and ∼5.50 eV on X^2A', ∼6.16 eV and ∼4.63 eV on $1^2A''$, ∼2.25 eV and ∼1.85 eV on $1^4A''$ states, respectively [14, 15]. On the other hand the exoergicity of S + OH reaction is ∼0.80 eV and the well depths are ∼3.43 eV and ∼3.38 eV [1]. All these energy values are given here with re-

spect to the energy of the asymptotic reagent channels, C + OH and S + OH, respectively. From all these numerical values mentioned, it can be concluded that small exoergicity and larger well depths facilitate the formation of intermediate complexes, whereas, larger exoergicity and smaller well depths help the complex to dissociate into products as many channels are energetically available at the product asymptote and consequently the signature of resonance becomes weak in the probability curve. Furthermore, the late barrier (with respect to the product asymptote) present along the MEP of S + OH $\rightarrow$ SO + H reaction [1] make the dissociation of collision complexes even more difficult.

Initial state-selected total reaction probabilities for J >0 are also calculated within the CS [2, 3] approximation and few of them are shown in Figure 3.2. The value of J is shown in each panel. It can be seen from Figure 3.2 that it is very difficult to find a particular trend for the variation of probabilities with the increase of J value and the probabilities upto $\sim$ J=35 look similar to those for J=0 (cf. Figure 3.1 (a) and panel (a), (b) and (c) of Figure 3.2). The onset of the reaction shifts slowly with the increase of J value due to the appearance of centrifugal barrier along the reaction path and the latter introduces a threshold (e.g. $\sim$0.027, $\sim$0.08 and $\sim$0.36 eV for J=80, 100 and 127, respectively) to the reaction. As the centrifugal barrier height is inversely proportional to the reduced mass of the system, the shift is somewhat less compared to those reactions involving lighter nuclei [16–18] and consequently probabilities for a large value of J are required to calculate ICSs upto $\sim$0.5 eV collision energy for the S + OH reaction.

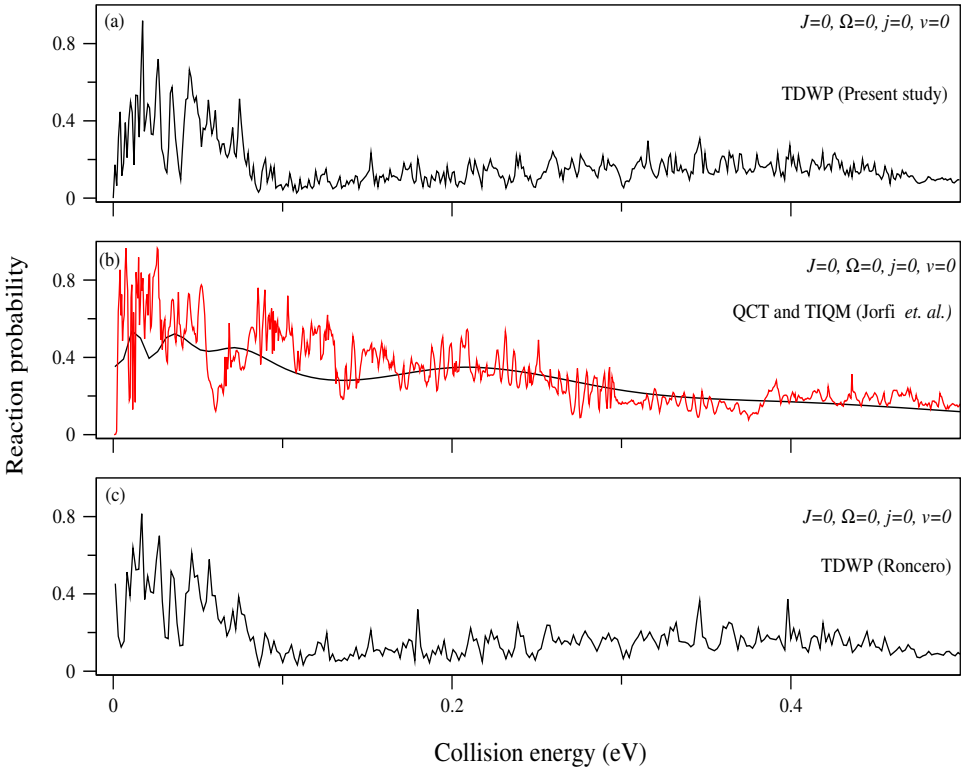

Figure 3.1: Initial state-selected and energy resolved total reaction probabilities calculated for the S (^{3}P) + OH (X$^2\Pi$, v=0, j=0, Ω=0) $\rightarrow$ SO (X$^3\Sigma^-$) + H (^{2}S) reaction on its electronic ground PES and for J=0 by different methods. The results calculated in the present TDWP study, by QCT and TIQM method and another TDWP approach by Roncero are shown in panel (a), (b) and (c), respectively.

Table 3.1: Description of coordinate grid parameters, properties of initial wave packet and the damping function used to obtain the dynamics results of S + OH → SO + H reaction on its electronic ground state.

Parameter	Numerical value	Description
$N_R/N_r/N_\gamma$	1024/128/45	Number of grid points along R, r and γ
R_{min}/R_{max} (a_0)	0.1/37.0	Extension of grid along R
r_{min}/r_{max} (a_0)	0.1/12.0	Extension of grid along r
$\Delta R/\Delta r$ (a_0)	0.0360/0.0937	Grid spacing along R and r
r_d (a_0)	6.565	Location of the dividing surface in the product channel
R_{mask}/r_{mask} (a_0)	26.2149/9.2826	Starting point of the damping function
$\Delta X_{mask}(R)$ (a_0)	10.785	Width of the damping region along R
$\Delta X_{mask}(r)$ (a_0)	2.717	Width of the damping region along r
R_0 (a_0)	14.5	Initial location of the center of the GWP in the coordinate space
E_{trans} (eV)	0.25	Initial translational kinetic energy
$\delta(a_0)$	0.04	Initial width parameter of the GWP
Δt(fs)	0.135	Length of the time step used in the WP propagation
T(fs)	4049.0	Total propagation time

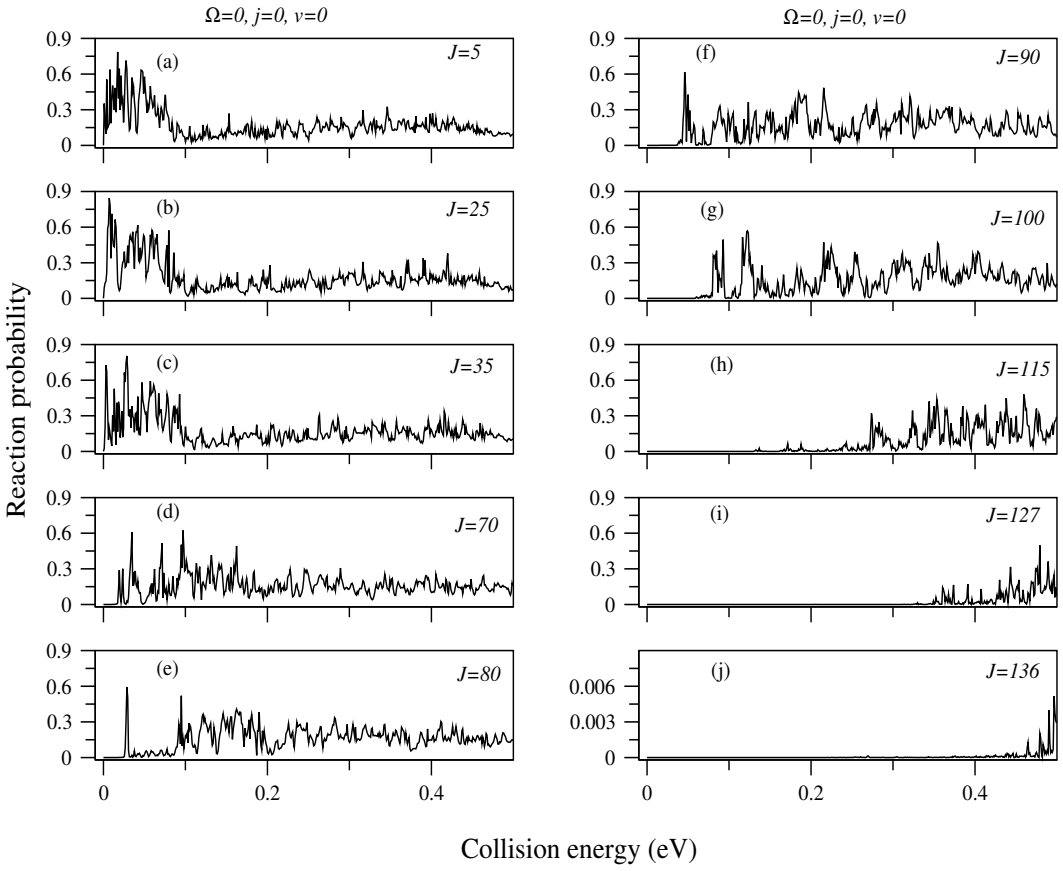

Figure 3.2: Same as Figure 3.1 but for total angular momentum, $J > 0$.

3.3.1.2 Effect of reagent rotational excitation on probability

Initial state-selected total reaction probabilities for OH($X^2\Pi$, v=0, j=0-3) and J=0 are plotted as a function of collision energy in panels (a)-(d) of Figure 3.3. It can be seen from Figure 3.3 that the maximum probability shifts towards higher collision energy for OH(v=0, j=1), whereas, it returns to low energy for OH(v=0, j=2). It seems very difficult to find a particular trend regarding the variation of the magnitude of probability with rotationally hot reagent OH, nonetheless, it can be inferred that probabilities for OH (v=0, j=3) is less compared to the others almost throughout the entire energy range considered here. This can be attributed to the loss of preferred orientation of OH diatom owing to its rotational excitation [19].

The effect of rotationally hot reagent OH on the probabilities for J >0 and Ω >0 are shown in Figure 3.4. In particular, probabilities for OH (v=0, j=1-3, Ω=1) are plotted in panel (a)-(c) and for OH (v=0, j=2-3, Ω=2) are plotted in panel (d) and (e) in Figure 3.4. From all these panels it can be seen that the probabilities at higher collision energies decrease with reagent rotational excitation.

3.3.1.3 Effect of Ω on probability

The effect of Ω [the quantum number for the projection of the rotational (j) and total angular momentum quantum number (J)] on reaction probabilities are shown and discussed in this section. The probabilities for OH (v=0, j=1 Ω=0-1) and for some selected values of J are plotted in Figure 3.5. Specifically, probabilities for OH (v=0, j=1, Ω=0) and OH (v=0, j=1, Ω=1) are plotted in panel (a)-(g) and in panel (h)-(n), respectively. It can be seen that the probabilities for Ω=1 are $\sim$2 times smaller in magnitude than those obtained for Ω=0. This

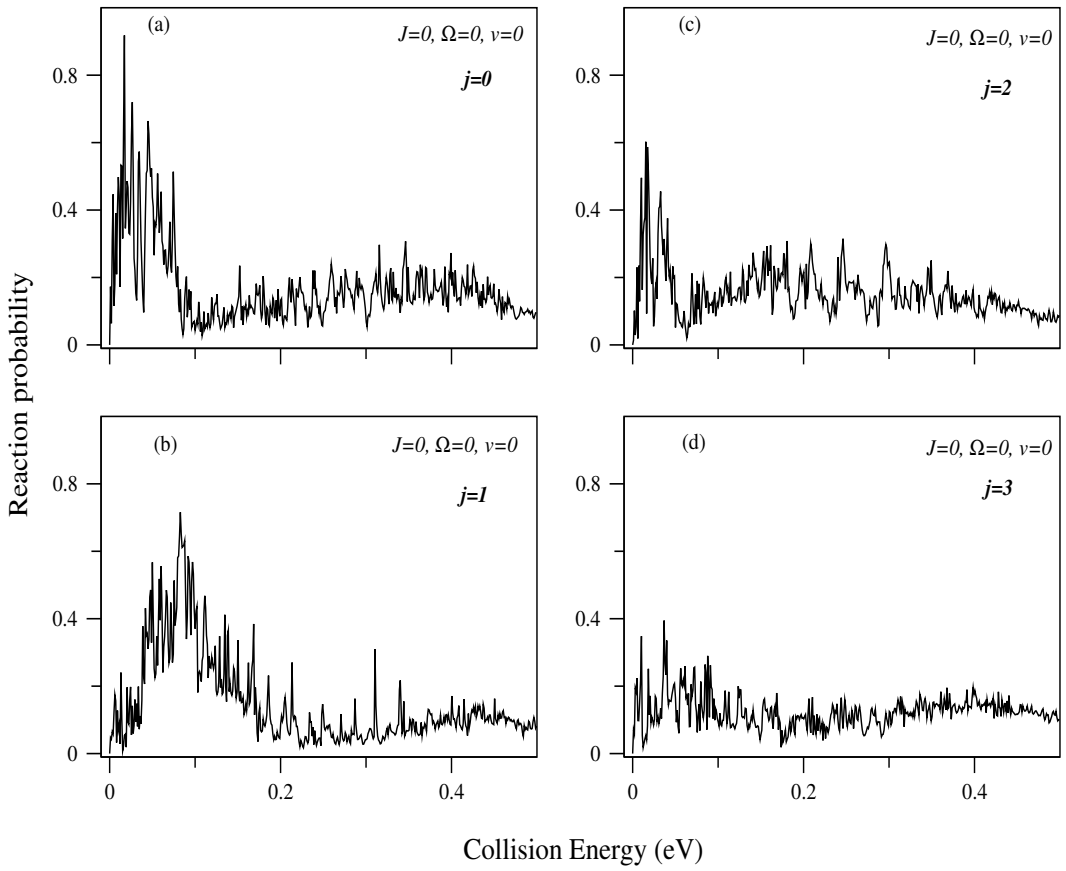

Figure 3.3: Same as Figure 3.1 but for OH(v=0, j=0-3, Ω=0). Different quantum numbers are given in each panel to show the excitation.

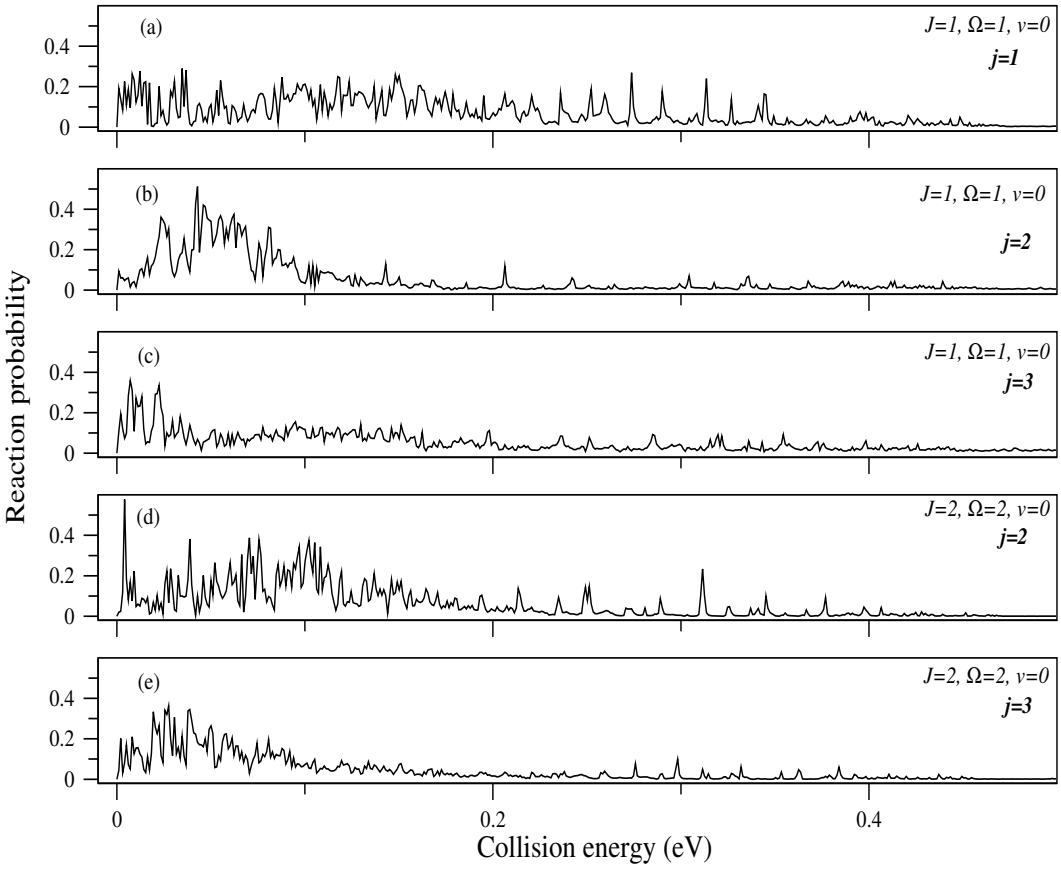

Figure 3.4: Initial state-selected total reaction probabilities for the S + OH (v=0, j=1-3, Ω=1-2) → SO + H reaction and for J=1-2 on its electronic ground DMBE PES as a function of collision energy. Values of different quantum numbers are shown in each panel to show the excitation.

is in strong contrast to those obtained for the C + OH → CO + H reaction on its first ($1^2A''$) and second ($1^4A''$) excited states. The probabilities for Ω=1 were ∼10 times smaller than those for Ω=0 on the $1^2A''$ state [11], whereas, they were comparable upto ∼ 0.1 eV followed by somewhat decrease at higher energies on $1^4A''$ state (cf. chapter 4) of HCO reactive system. From Figure 3.5 it can be found that probabilities for Ω=0 show a maximum which shifts towards higher collision energy with the increase of J, whereas, those for Ω=1 are uniform almost throughout the entire energy range. The appearance of threshold to the reaction is also evident here with the increase of J value due to the increase of centrifugal barrier.

The dependence of probability on Ω for OH (v=0, j=2) and for J=2 are presented in Figure 3.6. From panel (a) and (b) it is seen that the maximum shifts towards higher energies with increasing Ω, but the magnitude of probability decreases for Ω=1 than those obtained for Ω=0 throughout the entire range of energy except at around ∼0.05 eV. On the other hand probabilities for Ω=2 are higher than those for Ω=1 except at collision energies beyond ∼0.44 eV and at around ∼0.05 eV (cf. panel (b) and (c) of Figure 3.6). Moreover, the resonance oscillations are weakest for Ω=1 compared to the others. Hence, no general pattern for the variation of probabilities with the increase of Ω is found for the S + OH → SO + H reaction on its electronic ground state.

3.3.1.4 Effect of vibrationally hot OH on probability

Initial state-selected total reaction probabilities for the S + OH (v=0-5, j=0, Ω=0) → SO + H reaction on its electronic ground state are shown in panel (a)-(f) of Figure 3.7. Different quantum numbers are given in each panel to show the excitations. Primarily from Figure 3.7 it can be seen that reagent vibrational

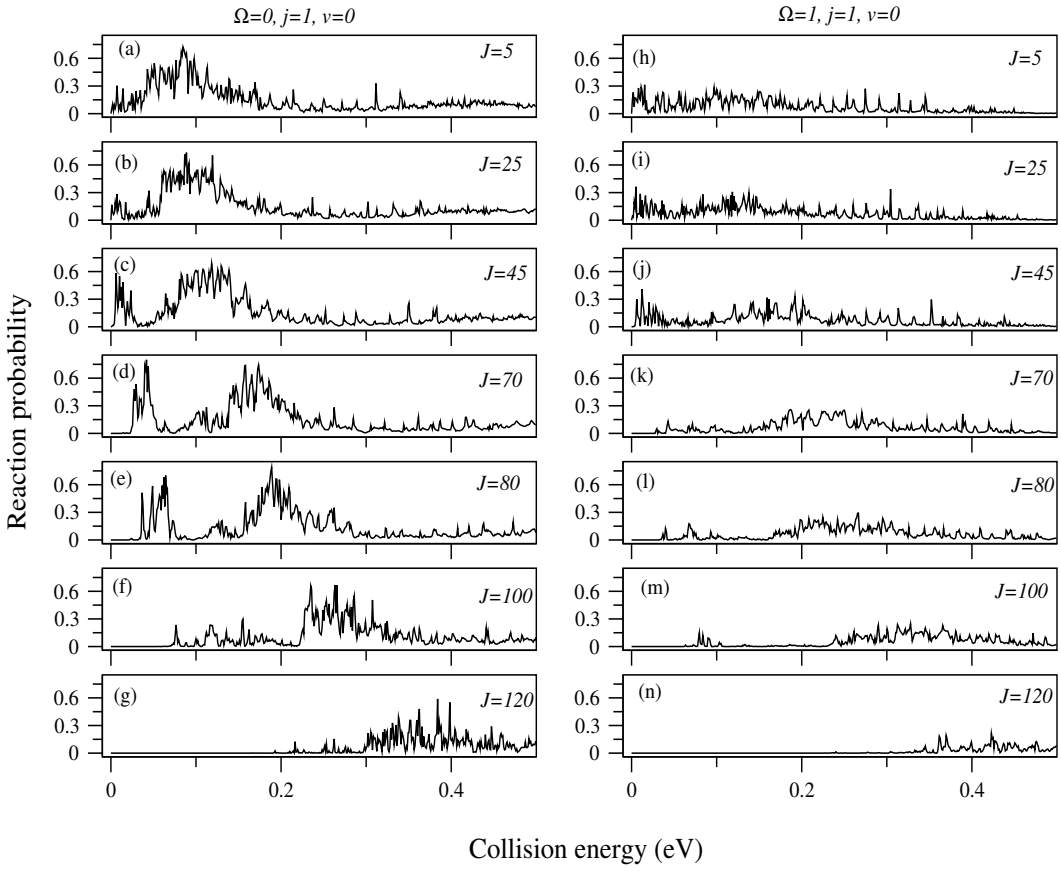

Figure 3.5: Same as Figure 3.2 but for reagent OH (v=0, j=1). See text for details.

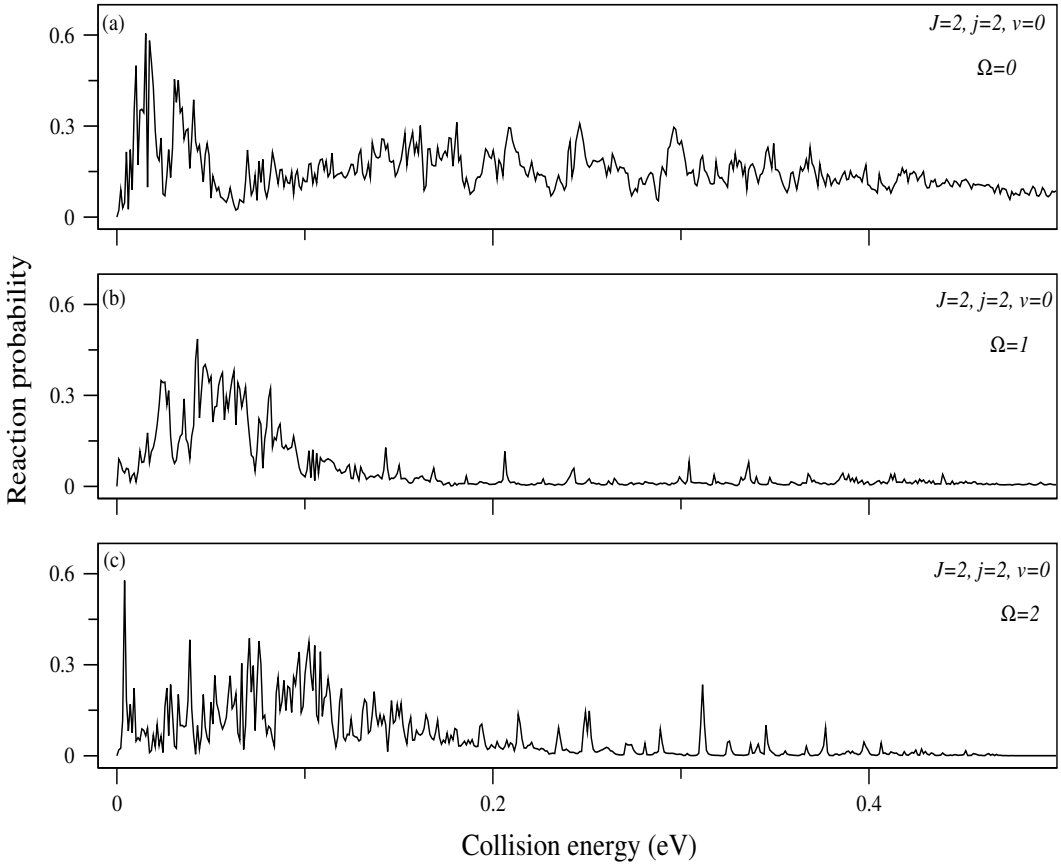

Figure 3.6: Initial state-selected total reaction probabilities for S + OH (v=0, j=2, Ω=0-2) $\rightarrow$ SO + H reaction on its electronic ground DMBE PES. Different quantum numbers are mentioned in each panel.

excitation has immense impact on both the magnitude and pattern of probabilities. The maximum probability is found at lower collision energies followed by a decrease of the same at intermediate and higher energies for reagent OH (v=0-2, j=0, Ω=0) [see panel (a)-(c)]. In contrast, uniform probabilities are found for OH (v=3-5, j=0, Ω=0) [see panel (d)-(f)]. The probabilities at higher collision energy range increase with reagent vibrational excitation, whereas, the resonance gets weaker. More specifically, oscillations become weak at the intermediate energy range for OH (v=2-3, j=0, Ω=0) [see panel (c) and (d)] and probability becomes almost a smooth function of collision energy for OH (v=3-4, j=0, Ω=0) [see panel (e) and (f)] except at very low collision energies. These observations are quite similar to those for the C + OH (v=0-5, j=0, Ω=0) $\rightarrow$ CO + H reaction occurring on its second excited state [cf. chapter 4].

The effect of vibrationally hot reagent OH (v=0-5, j=0, Ω=0) on probabilities for J=5, 70, 100 and 130 are shown in panel (a)-(x) of Figure 3.8. It is seen that the observations for J=0 (see Figure 3.7) are valid for J=5 and 70 (see Figure 3.8), whereas, differences are found for J=100 and 130. In particular, from panel (s), (t), (w) and (x) of Figure 3.8 it is found that significant resonance oscillations are present in the probabilities for OH (v=4-5, j=0, Ω=0) and these are not uniform throughout, rather almost monotonically increasing function of collision energy.

Hence, in sumary it can be infered that vibrational excitation of reagent OH has stronger impact on the reactivity as compared to its rotational excitation. It will be interesting to find the effect of reagent internal excitations on ICSs where all partial wave contributions for total angular momentum J >0 will be included.

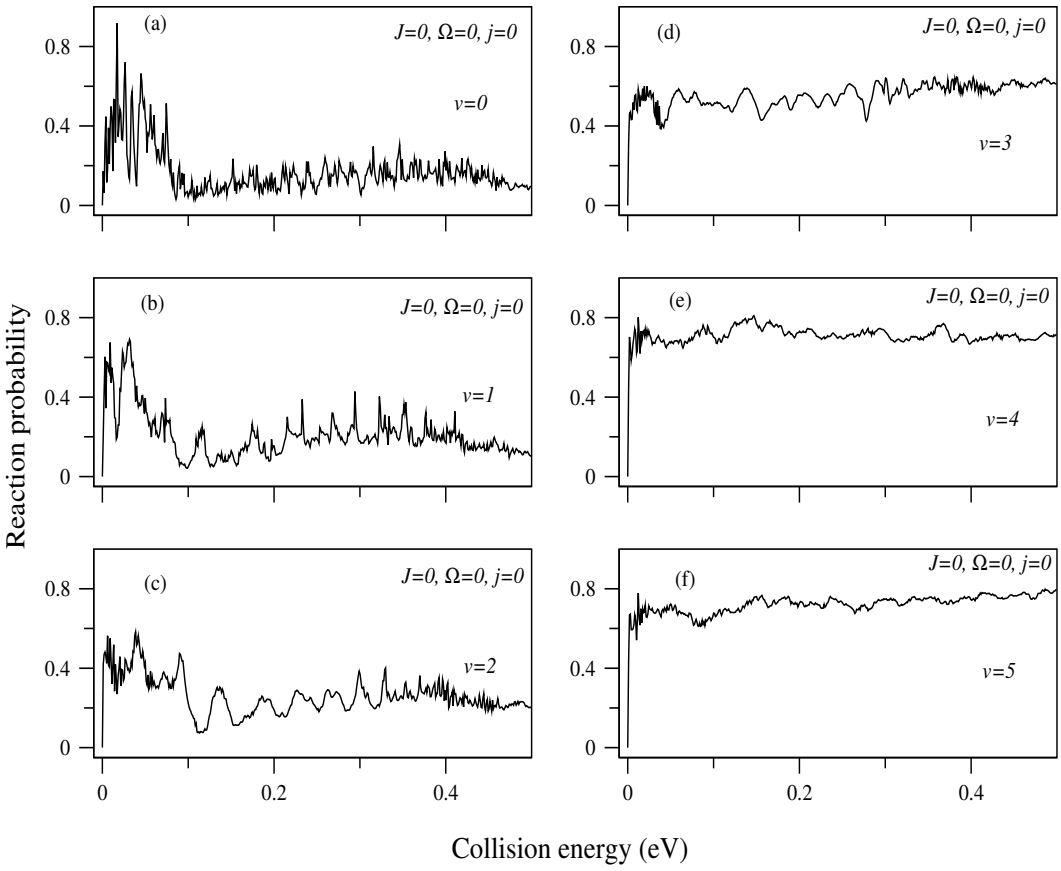

Figure 3.7: Same as Figure 3.1 but for OH (v=0-5, j=0, Ω=0). See text for details.

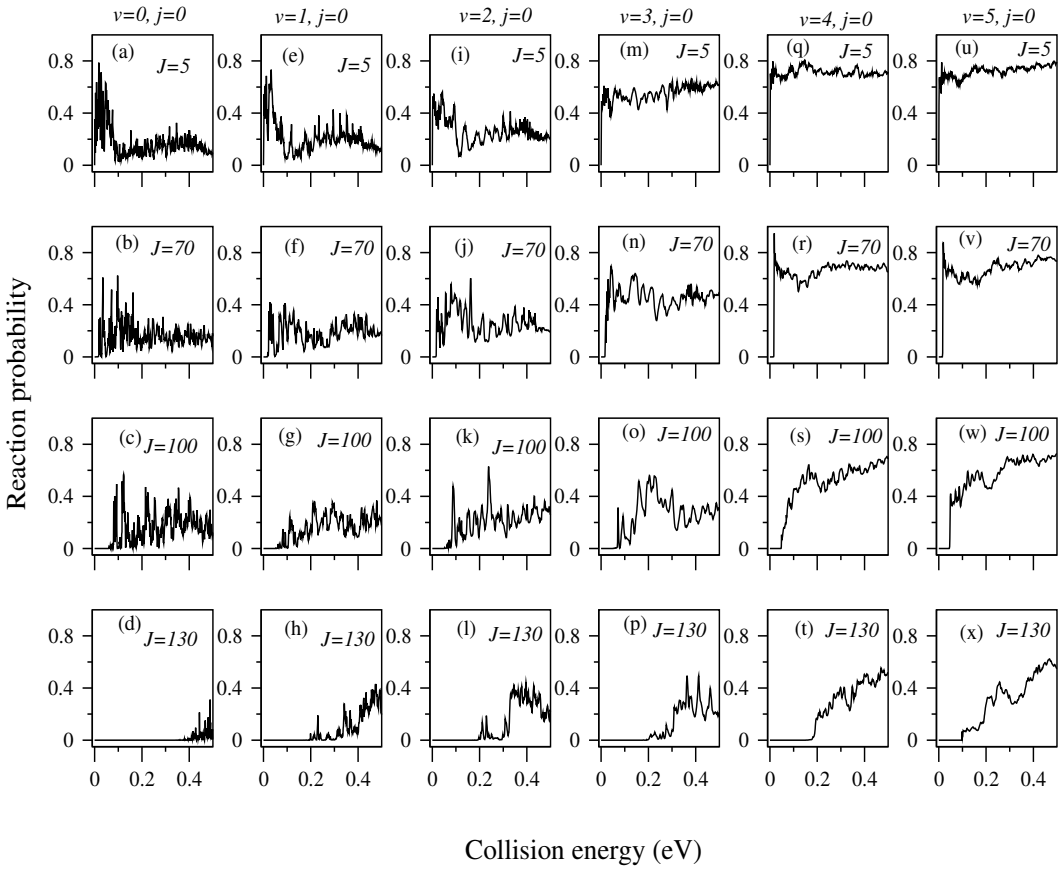

Figure 3.8: Same as Figure 3.2 but for OH (v=0-5, j=0, Ω=0). See text for details.

3.3.2 Initial state-selected integral cross section

Initial state-selected and energy resolved total integral cross sections for the S + OH (v=0-3, j=0-2) $\rightarrow$ SO + H reaction on its electronic ground state are shown in Figure 3.9. ICSs for OH (v=0, j=0), OH (v=0, j=1) and OH (v=0, j=2) are presented in panel (a) as a function of collision energy in different colours. To obtain converged cross sections for OH (v=0, j=0-2) upto $\sim$0.5 eV collision energy, partial wave contributions for total angular momentum upto J=138 are included in the calculation. Moreover, for rotationally hot reagent OH, the quantum number, Ω was restricted to $0 \leq \Omega \leq \min(j, J)$. It is seen in panel (a) of Figure 3.9 that ICSs corresponding to all three values of j look similar in pattern but they differ in magnitude. ICSs are very high at the onset and they fall very sharply to a value of $\sim$35 Å^2 (for j=0), $\sim$21 Å^2 (for j=1) and $\sim$17 Å^2 (for j=2), respectively, at $\sim$0.021 eV, $\sim$0.012 eV and $\sim$ 0.0101 eV collision energies. ICSs decrease smoothly and steadily afterwards upto certain energy and they remain almost constant at higher energies. Such behavior of ICSs against collision energy is typical for barrierless exothermic reactions and it is found for other reactions of similar type [11, 20]. The ICSs for OH (v=0, j=0) and OH (v=0, j=1) become equal in the $\sim$0.14-0.20 eV collision energy range [cf. inset (I) of panel (a)] and the former is more than the latter outside this energy range [cf. panel (a)]. On the other hand, from inset (II) of panel (a) it is found that $\sigma(v$=0, j=2) > $\sigma(v$=0, j=1) within $\sim$ 0.038-0.09 eV energy range and the opposite trend is followed at other energies [cf. panel (a)]. Here σ symbolizes ICS. Moreover, from the two insets of panel (a) it is seen that weak resonance oscillations survive in $\sigma(v$=0, j=0-2). The intensity of the resonances found in reaction probabilities gets decreased in ICSs due to the inclusion of the partial wave contributions of total angular momentum quantum number, J.

Jorfi *et al.* have calculated the ICSs [5] for this reaction by using QCT method. They found a smaller decrease of ICS for rotationally excited OH [see Figure 2 of Ref. [5]] compared to the observation of present study. These are reproduced from Ref. [5] and plotted in panel (a) and (b) of Figure 3.10 along with the TDWP results. TDWP and QCT results are shown by the black and red colour lines in both panels. From panel (a) it can be seen that QCT results for OH (v = 0, j=0) are in good accord with the present TDWP results and a magnified view of this comparison is also given in the inset. Understandably, no resonance is found in the QCT studies compared to the TDWP results [see the inset of panel (a)] as resonance is purely a quantum mechanical phenomena. From panel (b) it is seen that the QCT study overestimates the ICSs and the disagreement is severe at low collision energies for OH (v=0, j=1). Nevertheless, the variation of ICSs with collision energy is similar in both studies.

The effect of vibrationally hot reagent OH on state-selected ICSs is shown in panel (b) of Figure 3.9 in different colours. All partial wave contributions of the total angular momentum, upto J=0-138, J=0-158, J=0-175 and J=0-180 were included to obtain converged ICSs upto ∼0.5 eV for reagent OH prepared in its v=0, 1, 2 and 3 levels, respectively. The cross section for OH (v=0, j=0) is also presented in panel (b) for the sake of comparison. It can be noticed from Figure 3.9 (b) that ICSs with vibrationally hot OH behave in the same way of $\sigma(v$=0, j=0). They are high at the onset, fall sharply at low collision energies and remain almost constant at higher collision energies. Moreover, throughout the entire energy range considered here the ICSs follow the trend $\sigma(v$=0, j=0) $\simeq \sigma(v$=1, j=0) $< \sigma(v$=2, j=0) $< \sigma(v$=3, j=0), which is in strong contrast to those obtain for the C + OH → CO + H reaction on the $1^2A''$ state [11]. This is a remarkable finding as the reagent diatom is same in both these reactions and

the observations can be correlated to the topography of the underlying surfaces. In order to understand this, MEPs for different approach angles of the attacking S atom are computed by using the procedure discussed in section 2.4 and some of them are presented in Figure 3.11. From different panels of Figure 3.11 it can be seen that the approaches for $\gamma < 140^0$ are almost barrierless at the entrance channel. Panel (l)-(o) depict that MEPs are quite complicated within the angular range, $115^0 \leq \gamma \leq 140^0$. The approaches for γ ~0-110^0 follow a barrierless entrance channel and a barrier (with respect to the product asymptote) at the exit channel except for γ=50^0 and 60^0 [see panel (f and (g)]. Thus it appears that there is a high chance for the reactive system to cross a late barrier at the exit channel before reaching at the product valley. Indeed the MEP supports the formation of SOH collision complex inside the well of lower depth and a late barrier at the exit channel [see Figure 12 (b) of Ref. [1]]. Such a late barrier is absent on the $1^2A''$ state of the HCO reactive system [see Figure 1 of Ref. [11]]. On the other hand, the well depths are large on the $1^2A''$ PES (~6.16 and ~4.63 eV) [15] of HCO system, whereas, they are relatively smaller (~3.43 and ~3.38 eV) on the electronic ground PES of HSO reactive system [see Figure 1.2 and section 1.1.1]. Hence, the increase of the total energy via reagent vibrational excitation assists the decomposition of collision complex to products from a well of relatively lower depth. In addition to this, the barrier is of late type for the S + OH reaction and such a barrier causes the increase in reactivity with reagent vibrational excitation [21]. On the contrary, observations found in panel (b) of Figure 3.9 have resemblance with those obtained for the C + OH $\rightarrow$ CO + H reaction on its $1^4A''$ state [cf. chapter 4]. The wells are even less deeper and a high barrier is also found at the exit valley on the $1^4A''$ PES of HCO reactive system [15]. From the inset present in panel (b) of Figure 3.9, it can be seen that

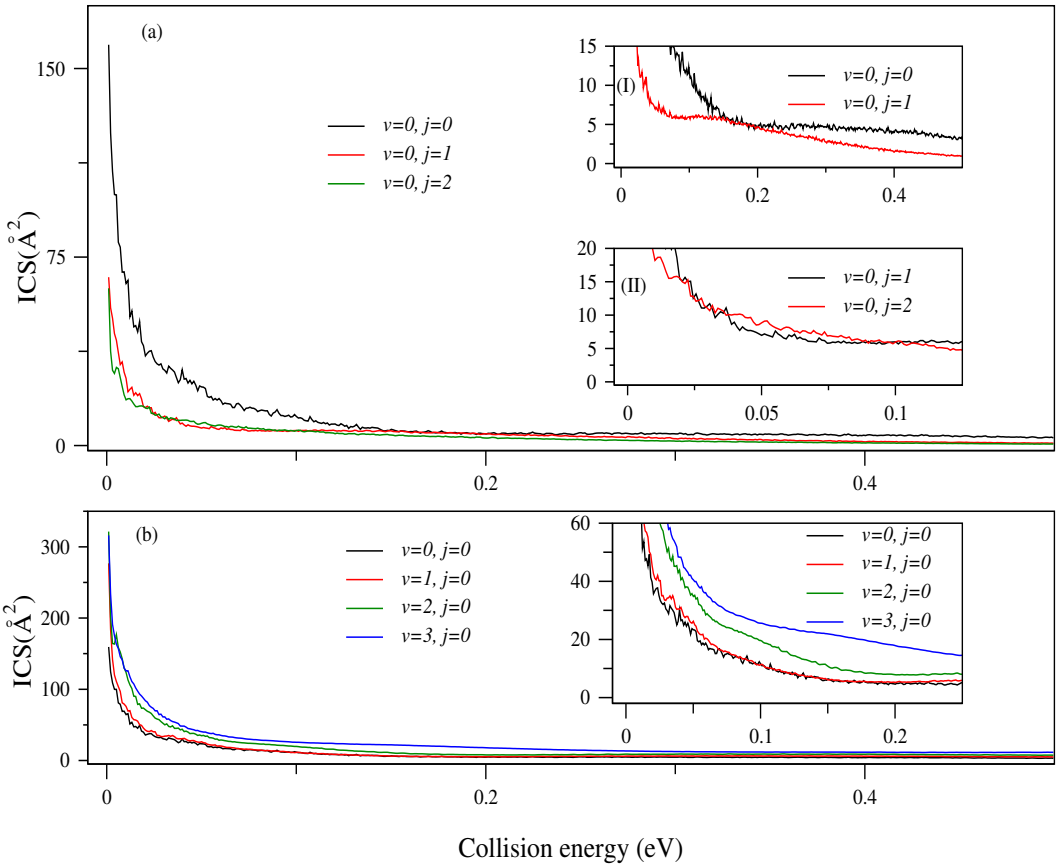

Figure 3.9: Initial state-selected ICSs for the S + OH (v=0-3, j=0-2)→ SO + H reaction as a function of collision energy. The effect of rotational and vibrational excitations of reagent diatom on ICSs are presented in panel (a) and (b), respectively.

ICSs become less structured with reagent vibrational excitation. This can be attributed to the fact that the resonance oscillations become broad and diffused for vibrationally hot reagent OH [see Figure 3.7, and Figure 3.8]. Finally, it can be concluded from Figure 3.9 that rotational excitation of reagent OH decreases the reactivity, whereas, its vibrational excitation enhances the same. More specifically, a significant enhancement in the reactivity is found when reagent OH is excited to its third vibrational level, v=2.

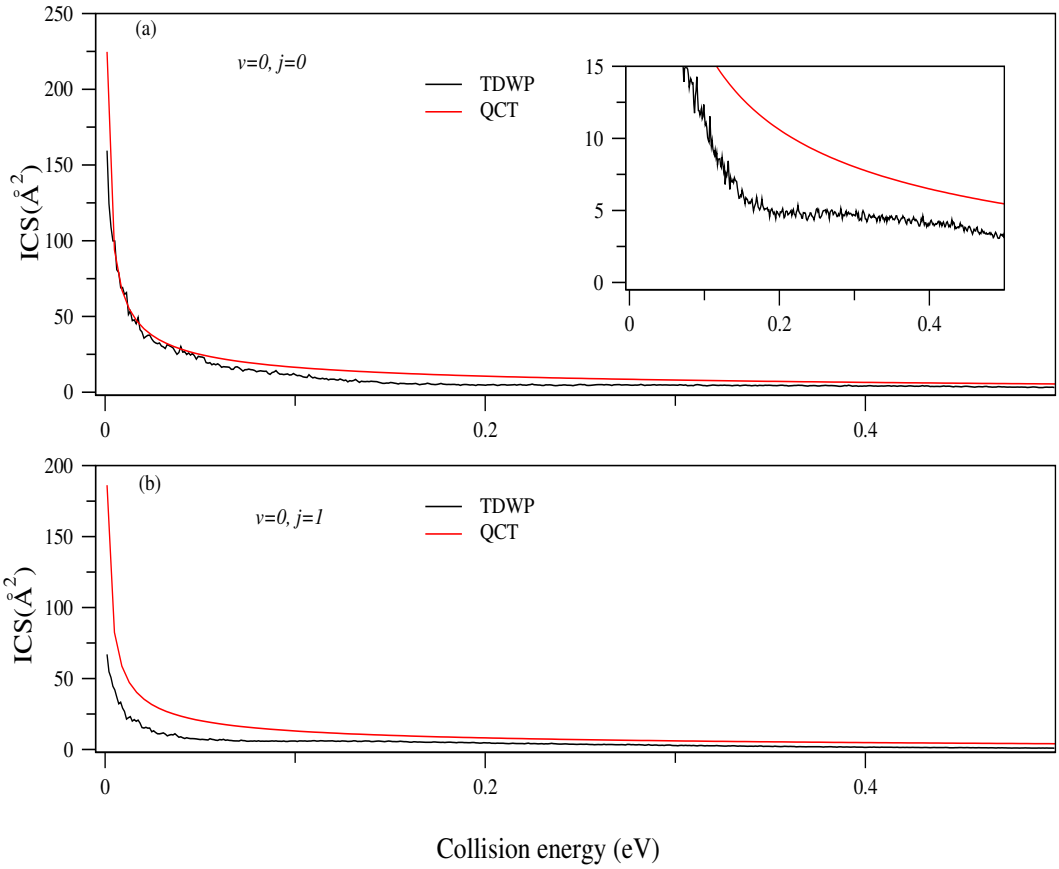

Figure 3.10: Comparison of ICSs calculated by QCT and TDWP approach for the S + OH → SO + H reaction on its electronic ground state. ICSs for OH (v=0, j=0) and OH (v=0, j=1) are compared in panel (a) and (b), respectively.

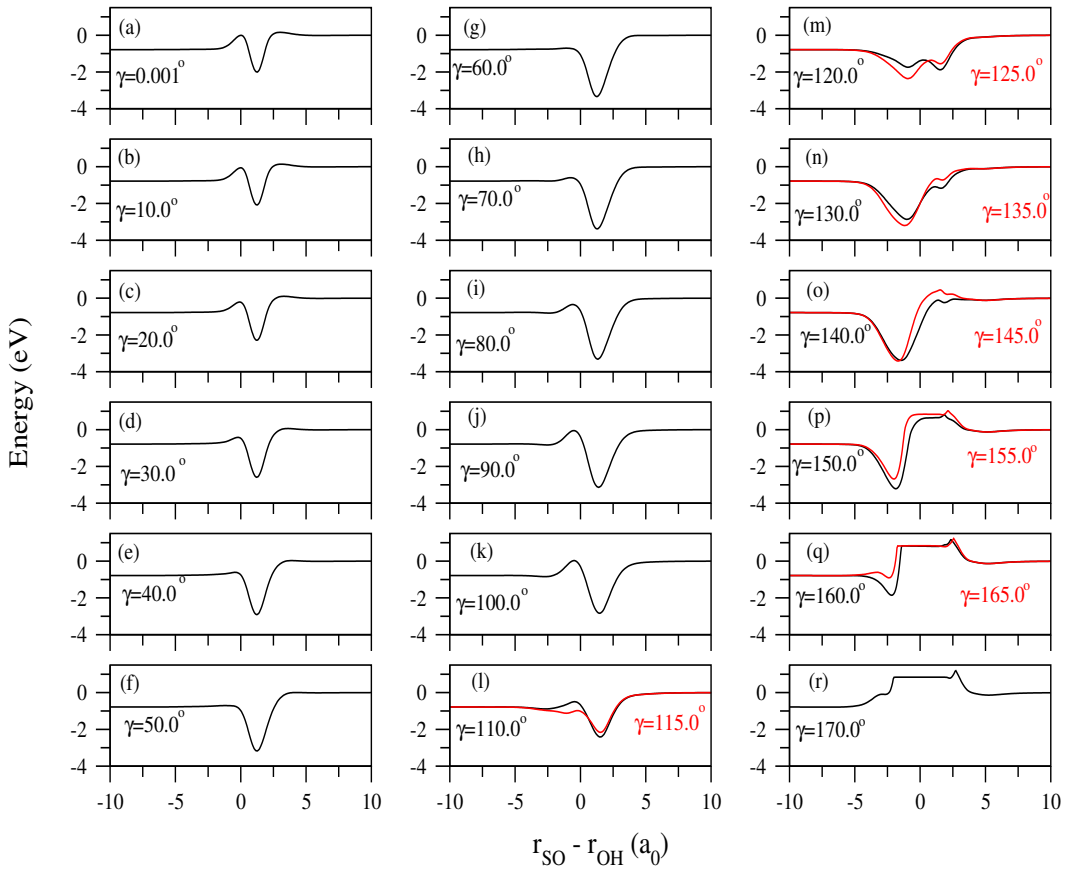

Figure 3.11: Minimum energy paths (MEPs) for different approach angles of attacking S atom towards reagent OH for the S + OH → SO + H reaction on its electronic ground state. r_{OH} and r_{SO} are the internuclear distances between the S and O atoms, and O and H atoms, respectively.

3.3.3 State-specific rate constant

State-specific thermal rate constants for the S + OH (v=0, j=0-2) → SO + H reaction calculated by using equation 3.1 and 3.2 are plotted in Figure 3.12 as a function of temperature. The calculation of rate constant is restricted for OH (v=0) only as this is the only channel that is open in the given temperature range. It is worth mentioning that the rate constant calculated without the electronic degeneracy factor, f_e(T), [see Eq. 3.2] increases rapidly at low temperatures and remains almost constant at higher temperatures. But with the inclusion of f_e(T) in the rate constant formula drastically changes the behaviour of rate constant with temperature. Such drastic changes for barrierless exothermic reactions are also found in the literature for O + OH → O_2 + H and C + OH → CO + H reactions [22, 23].

The rate constants shown in Figure 3.12 increase sharply at the onset, reaches to a maximum [∼4.9 × 10^{-11} cm^3 s^{-1} $molecule^{-1}$ at ∼48 K for OH (v=0, j=0), ∼2.1 × 10^{-11} cm^3 s^{-1} $molecule^{-1}$ at ∼45 K for OH (v=0, j=1) and ∼1.6 × 10^{-11} cm^3 s^{-1} $molecule^{-1}$ at ∼52 K for OH(v=0, j=2)] and finally decrease smoothly with the increase of temperature. Thus the rate constants show negative temperature dependence at $\sim T > 60$ K. This kind of unusual dependence of rate constant on temperature is found for many atom-radical reactions [10, 11, 20, 24] and this can be attributed to the temperature dependence of the function, f_e(T). From Figure 3.12 it can be seen that reagent rotational excitation decreases rate constants which is shown by the dashed lines in black (for j=0), red (for j=1) and blue (j=0) colours.

From Figure 3.9, it can be seen that the cross sections rise sharply at low collision energies and hence ICSs below 10^{-3} eV collision energy will have significant contribution over the rate constants particularly at low temperatures below

$\sim$50 K. We reiterate here that ICSs have been computed down to 10^{-3} eV in the present study as the TDWP approach is inappropriate to calculate converged ICS below 10^{-3} eV due to the difficulties in damping the outgoing wave packet with large de Broglie wavelength. In order to have approximate value of ICS below 10^{-3} eV, the low energy part of the ICSs of OH (v=0, j=0-2) is analytically fitted and extrapolated down to 10^{-6} eV. The analytical fitting and extrapolation are shown in Figure 3.13 with the quantum numbers and the functional form indicated in each panel. It is found that inclusion of ICSs down to 10^{-6} eV was adequate to obtain converged rate constants down to 10 K. Rate constants calculated by using the extrapolated ICSs are shown by the solid lines in Figure 3.12 with black [for OH (v=0, j=0)], red [for OH (v=0, j=1)] and blue [for OH (v=0, j=2)] colours, respectively. It is quite obvious from Figure 3.12 that the rate constants calculated with the extrapolated cross sections (in the 10^{-3} to 10^{-6} eV collision energy range) are larger than the same calculated by excluding the extrapolated cross section and the difference is severe at low temperatures. For example, at 15 K, the difference is found to be $\sim$12.9 %, $\sim$7.1 % and $\sim$ 12.5 % for OH (v=0, j=0), OH (v=0, j=1) and OH (v=0, j=2), respectively. Thus a dynamics study at cold and ultracold conditions is needed to be carried out by TIQM formalism to obtain more accurate behavior of ICSs and rate constants at low energies and temperatures, respectively.

At this point the observations of Figure 3.12 merit some explanations. As many factors control the reactivity of a chemical system, it is very difficult to find a general rule which can unambiguously explain and predict the outcomes of a bimolecular collision. In particular, the literature data mostly lacking of satisfactory explanation of the results of a bimolecular reaction occurring on a PES having deep potential wells. Nonetheless, it is believed that the features

of a bimolecular encounter on such a PES depend on the masses of the nuclei participating in the reaction, the exoergicity, long-range interaction and the well depth(s). The last two factors partly represent the topography of the underlying PES. In addition to these, the formation of collision complexes inside the wells and their dissociation into products play the key role in these reactions.

Furthermore, it is commonly believed that all reactions occur smoothly through a straightforward pathway when a preferred relative orientation of the reactants is gained and any factor which inhibits the reactants to achieve such orientation diminishes the reactivity. Rotational excitation of reagent OH (v=0, j=1-2) for the S + OH $\rightarrow$ SO + OH reaction is such an example and consequently it reduces the reactivity which is seen in panel (a) of Figure 3.9 and in Figure 3.12. Moreover, the reaction under discussion belongs to the category of H + HL (L, light; H, heavy) class of reactions and the decrease of reactivity with reagent rotational excitation for such reactions is predicted in the literature [19].

Sate-specific rate constants calculated by Jorfi *et al.* by means of QCT method are reproduced from Ref. [5] and plotted in Figure 3.14 along with present TDWP results for the ease of comparison. In both panels TDWP and QCT results are shown by black and red colour lines, respectively. From panel (a) it can be seen that rate constant for OH (v=0, j=0) obtained by both methods are in good accord with each other. Whereas, a substantial difference is found for the rate constant for rotationally excited OH (v=0, j=1) [cf. panel (b) of Figure 3.14]. Such disagreement can be attributed to the inherent shortcomings of QCT approach which ignores the inclusion of major quantum mechanical effects and also to the consideration of CS approximation in present time-dependent calculations. In literature it is found that the inclusion of Coriolis forces alter resonance widths for LiH_2 reactive system [25, 26] and also its importance for the H + O_2 $\rightarrow$ OH

+ O reaction has been shown by Guo *et al.* [27] and Meijer *et al.* [28]. Thus, we presume that the Coriolis forces may play an important role in the present reaction also as the reaction proceeds through the formation of metastable floppy intermediate complexes. But the investigation of the dynamics of S + OH → SO + H reaction including Coriolis coupling is quite challenging as it requires huge computational overheads.

Boltzmann distributions of reagent OH over its rotational levels at three different temperatures are shown in Figure 3.15. Temperatures are mentioned in each panel and populations are shown by both dashed lines and bar diagrams. From different panels of Figure 3.15, it can be seen that ICSs for j=3, 5 and 7 are required to obtain rotationally averaged thermal rate constant up to 100 K, 300 K and 500 K, respectively. The dynamical calculations for $j \geq 3$ are computationally very expensive as all Ω values within the restriction, $0 \leq \Omega \leq \min(j, J)$ must be included and consequently, no attempt was made to calculate thermally averaged rate constant.

The experimental rate constant value at 298 K, k=6.6 ($\pm$1.4) $\times$ 10^{-11} cm^3s^{-1} $molecule^{-1}$, measured by Jourdain *et al.* [29] is shown in Figure 3.12 with the error bars. It can be seen that the TDWP rate constant at 298 K is below the experimental value. Furthermore we mention here that both TDQM and QCT results are not in agreement with the experimental value at 298 K. Such disagreement may arise due to the inaccuracies of the DMBE PES, the inherent shortcomings of the QCT approach and the consideration of the CS approximation in the present TDWP study. On the other hand, the experimental value may contain some uncertainties and consequently more measurements in a wide temperature range are required to check the correctness of experimental data and to obtain its temperature dependence.

Stoecklin *et al.* has recently found an upper limit of rate constant for the S + OH reaction in 10-500 K temperature range [30] by using the adiabatic capture model in the centrifugal sudden approximation method (ACCSA). For the ease of a better comparison, this is shown in Figure 3.12 along with the TDWP and experimental results. It is found that the ACCSA rate constant is in good agreement with the experiment at 298 K but this accord may be fortuitous as the ACCSA approach is an approximate method and certainly it is less accurate than the QCT method in most cases [30] and the present TDWP approach. Indeed, it is found that the ACCSA rate constants for three reactive systems (C, N, S + OH) are overestimated by a factor of 2 than more accurate rate constants calculated by using quantum mechanical and QCT methods and global PESs [30]. Moreover, the ACCSA approach assumes the reaction probability is independent of energy for barrierless reactions which is in strong contrast to the probabilities found in the present study for the S + OH reaction. Specially low probabilities were found at high collision energies due to dominant back dissociation.

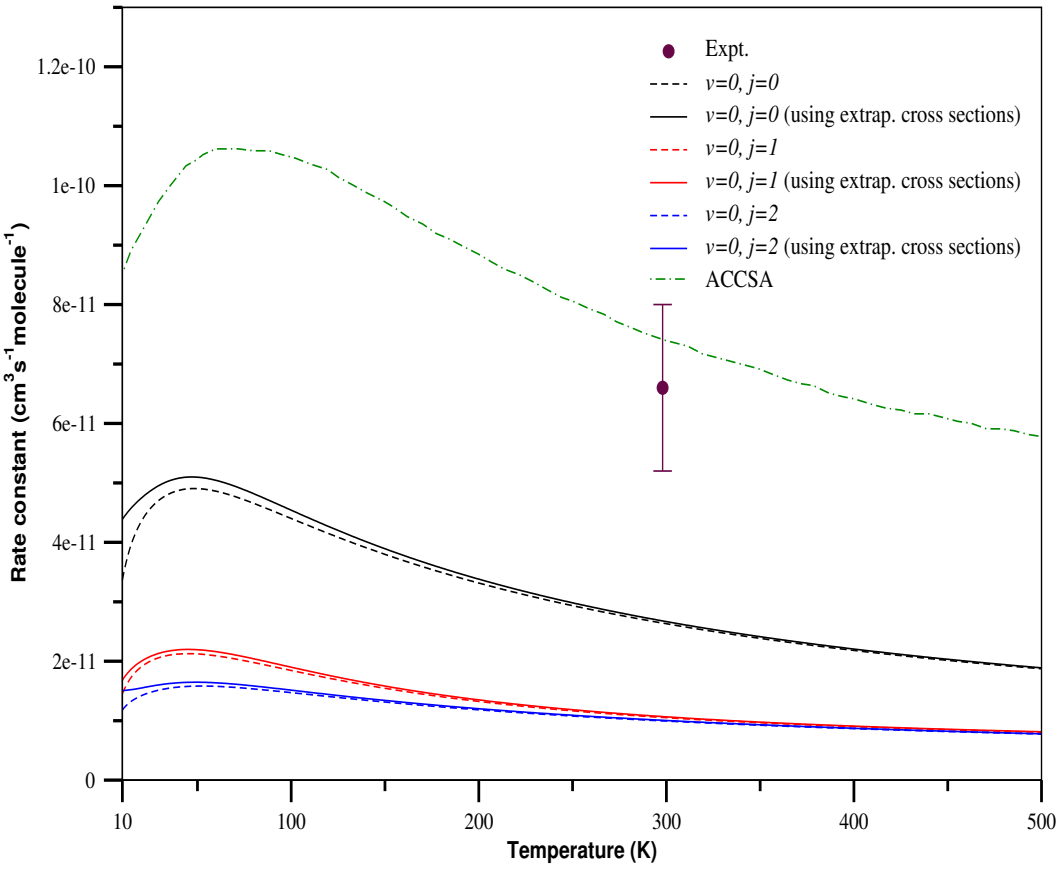

Figure 3.12: State-specific thermal rate constants for the S + OH (v=0, j=0-2) $\rightarrow$ SO + H reaction as a function of temperature are shown in different colours as indicated. Rate constants calculated with and without extrapolated cross sections are shown in solid and dotted lines, respectively. The experimental rate constant measured at 298 K is also presented here along with the same obtained by using the ACCSA approach.

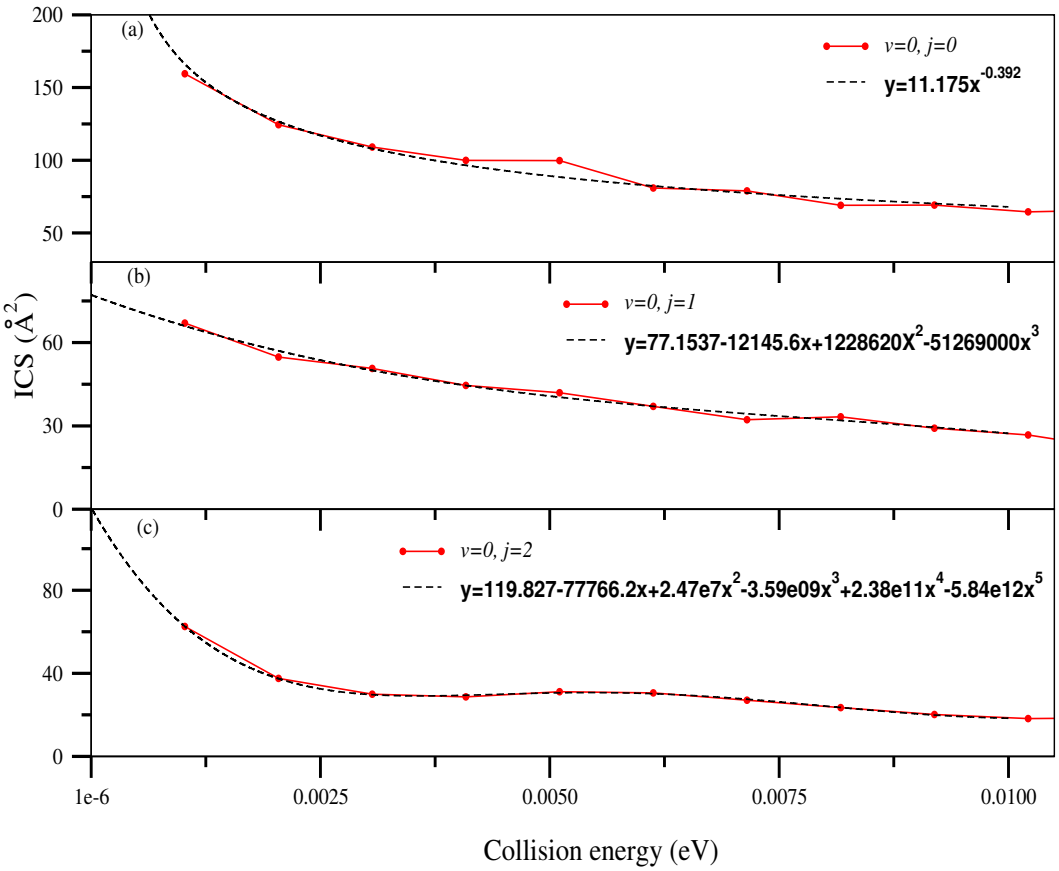

Figure 3.13: Analytical fit (dashed lines in black colour) of the low energy parts of the ICSs of S + OH (v=0, j) $\rightarrow$ SO + H reaction calculated in the present study (solid lines in red colour). Analytical fit functions and the vibrational and rotational quantum numbers of reagent OH are shown in each panel.

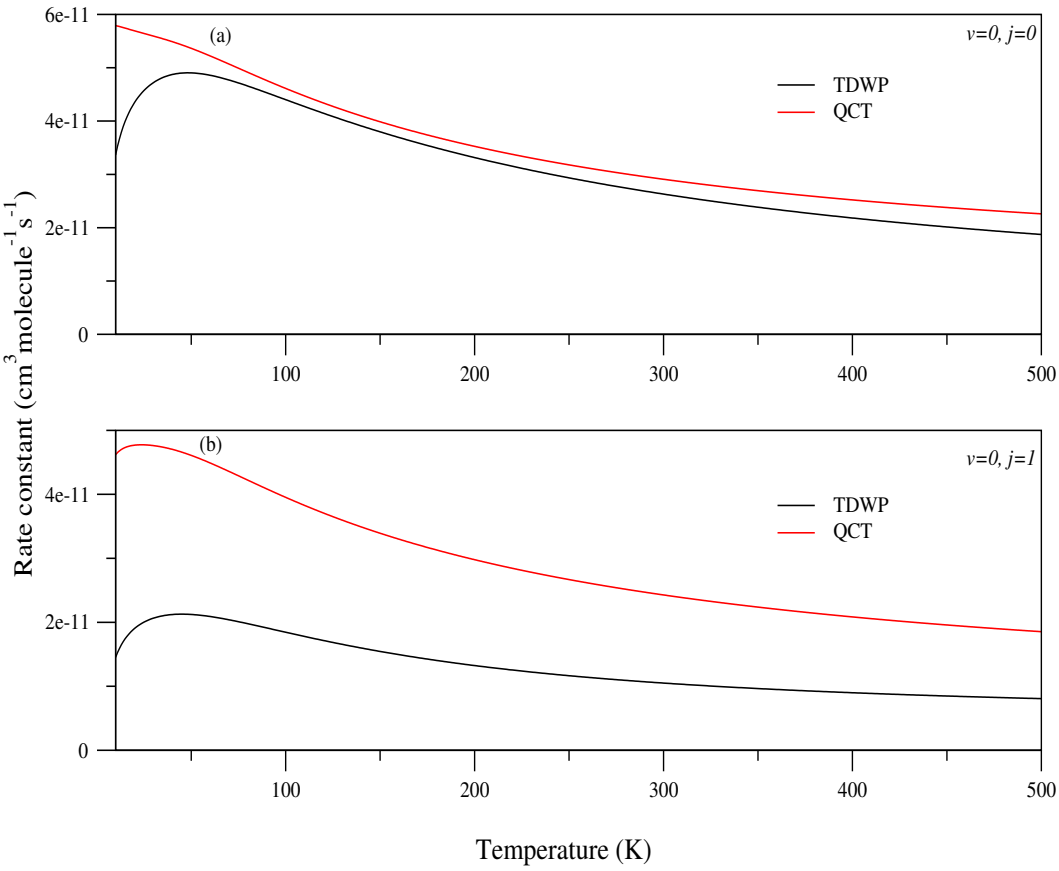

Figure 3.14: Comparison of state-specific rate constants for the S + OH (v=0, j=0-1) $\rightarrow$ SO + H reaction calculated in present TDWP study and QCT study of Jorfi *et al.* [5]. The results of the latter calculation are reproduced form Ref. [5] and presented by red colour lines

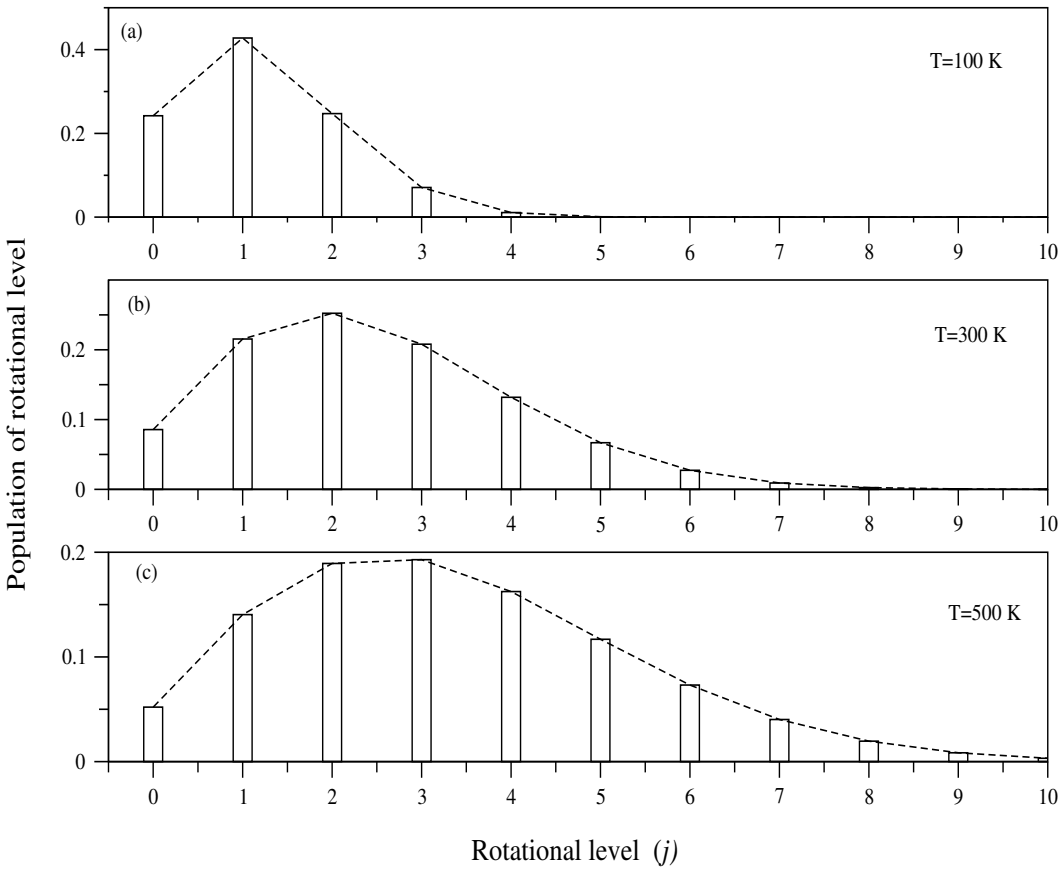

Figure 3.15: Population of reagent OH over its rotational levels at three temperatures. See text for the details.

3.4 Summary

A comprehensive theoretical account for the dynamics of S (^{3}P) + OH ($X^2\Pi$) $\rightarrow$ SO ($X^3\Sigma^-$) + H (^{2}S) reaction occurring on its electronic ground state ($\tilde{X}^2A''$) is presented in this chapter. Initial state-selected total reaction probabilities, ICSs and state-specific rate constants are calculated by means of a TDWP approach within the CS approximation as an accurate quantum mechanical study of this reaction requires huge computational overheads and currently out of the scope. Significant oscillations found in reaction probabilities and ICSs are attributed to the formation of intermediate complexes formed inside the deep potential wells on underlying PES [1]. Resonance oscillations become broader and diffused with reagent vibrational excitations. Effect of rotational and vibrational excitations of reagent OH on the dynamics is also reported here. Reagent rotational excitations is found to decrease the reactivity, while the vibrational excitation enhances the same. Present TDWP results are in fair agreement with those obtained by using QCT method [5].

References

[1] E. Martínez-Núñez and A. J. C. Varandas, J. Phys. Chem. A **105**, 5923 (2001).

[2] P. McGuire and D. J. Kouri, J. Chem. Phys. **60**, 2488 (1974).

[3] R. T. Pack, J. Chem. Phys. **60**, 633 (1974).

[4] F. J. Aoiz, L. Bañares, and J. F. Castillo, J. Chem. Phys. **111**, 4013 (1999).

[5] M. Jorfi and P. Honvault, Phys. Chem. Chem. Phys. **13**, 8414 (2011).

[6] M. Jorfi and P. Honvault, J. Chem. Phys. **133**, 144315 (2010).

[7] S. Gómez-Carrasco and O. Roncero, J. Chem. Phys. **125**, 054102 (2006).

[8] A. Zanchet, O. Roncero, T. González-Lezana, A. Rodriíguez-López, A. Aguado, C. Sanz-Sanz and S. Gómez-Carrasco, J. Phys. Chem. A **113**, 14488 (2009).

[9] T. González-Lezana, A. Aguado, M. Paniagua and O. Roncero, J. Chem. Phys. **123**, 194309 (2005).

[10] M. Jorfi and P. Honvault, J. Phys. Chem. A **114**, 4742 (2010).

[11] T. R. Rao, S. Goswami, S. Mahapatra, B. Bussery-Honvault, and P. Honvault, J. Chem. Phys. **138**, 094318 (2013).

[12] M. Jorfi and P. Honvault, J. Phys. Chem. A **115**, 8791 (2011).

[13] N. Bulut, A. Zanchet, P. Honvault, B. Bussery-Honvault, and L. Bañares, J. Chem. Phys. **130**, 194303 (2009).

[14] A. Zanchet, B. Bussery-Honvault, and P. Honvault, J. Phys. Chem. A **110**, 12017 (2006).

[15] A. Zanchet, B. Bussery-Honvault, M. Jorfi, and P. Honvault, Phys. Chem. Chem. Phys. **11**, 6182 (2009).

[16] T. Roy, T. R. Rao, and S. Mahapatra, Chem. Phys. Lett. **501**, 252 (2011).

[17] T. Roy and S. Mahapatra, J. Chem. Phys. **136**, 174313 (2012).

[18] R. Padmanaban and S. Mahapatra, J. Chem. Phys. **121**, 7681 (2004).

[19] N. Sathyamurthy, Chem. Rev. **83**, 601 (1983).

[20] N. Bulut, O. Roncero, M. Jorfi, and P. Honvault, J. Chem. Phys. **135**, 104307 (2011).

[21] J. C. Polanyi, Acc. Chem. Res. **5**, 161 (1972).

[22] M. Jorfi, P. Honvault, P. Halvick, S. Y. Lin, and H. Guo, Chem. Phys. Lett. **462**, 53 (2008).

[23] A. Zanchet, P. Halvick, J.-C. Rayez, B. Bussery-Honvault, and P. Honvault, J. Chem. Phys. **126**, 184308 (2007).

[24] F. Lique, M. Jorfi, P. Honvault, P. Halvick, S. Y. Lin, H. Guo, D. Xie, P. J. Dagdigian, J. Kios, and M. H. Alexander, J. Chem. Phys. **131**, 221104 (2009).

[25] R. Padmanaban and S. Mahapatra, J. Theor. Comput. Chem. **5**, 871 (2006).

[26] R. Padmanaban and S. Mahapatra, J. Phys. Chem. A **110**, 6039 (2006).

[27] S. Y. Lin, Z. Sun, H. Guo, D. H. Zang, P. Honvault, D. Xie and S.-Y. Lie, J. Phys. Chem. A **112**, 602 (2008).

[28] A. J. H. M. Meijer and E. M. Goldfield, J. Chem. Phys. **110**, 870 (1999).

[29] J. L. Jourdain, G. L. Bras, and J. Combourieu, Int. J. Chem. Kinet. **11**, 569 (1979).

[30] T. Stoecklin, B. Bussery-Honvault, P. Honvault, and F. Dayou, Comput. Theor. Chem. **990**, 39 (2012).

Chapter 4

Effect of internal excitations of reagent OH on initial state-selected dynamics of the C + OH → CO + H reaction on its second excited ($1^4A''$) state

4.1 Introduction

Initial state-selected total reaction probabilities and ICSs of C (^{3}P) + OH ($X^2\Pi$) → CO ($a^3\Pi$) + H (^{2}S) reaction occurring on its second excited electronic state ($1^4A''$) [1] are reported and discussed in detail in this chapter. Total reaction probabilities for OH (v=0-5, j=0-3) upto 0.50 eV collision energy and converged ICSs for OH (v=0-2, j=0-1) upto 0.25 eV collision energy are calculated by using the TDWP approach described in section 2.2. Probabilities for total angular

momentum, $J > 0$ are calculated within coupled states (CS) approximation [2, 3] and all partial wave contributions for J=0-48 are considered to obtain converged ICSs upto 0.25 eV collision energy for OH (v=0, j=0). Contributions from more partial waves and higher values of total angular momentum are required for rotationally and vibrationally hot reagent OH. The effect of rotational and vibrational excitations of reagent OH on the dynamics has also been studied and the findings are explained with respect to the topographical features of underlying PES. Finally, the results are compared with those [4, 5] obtained by other theoretical methods and the mechanistic details of the C + OH $\rightarrow$ CO + H reaction occurring on its first ($1^2A''$) and second ($1^4A''$) excited electronic states are discussed in detail by comparing the results of present study with those of one of our previous studies [6] in connection to the PES topographies. We mention here that due to higher endoergicity ($\sim$1.0 eV, see Figure 1.3) of the other product channel, CH + O, it is not included in present discussion.

4.2 Theoretical and computational details

Reagent Jacobi coordinate based time-dependent wave packet propagation approach for the dynamics study of bimolecular reactions is described in detail in section 2.2. Initial state-selected total reaction probabilities and ICSs are calculated by using this approach and hence the methodology is not reiterated here. Readers are referred to section 2.2 for a complete description of the theoretical and computational methods used in the present study.

4.3 Results and Discussions

4.3.1 Reaction probabilities

4.3.1.1 Probabilities for OH (v=0, j=0)

Initial state-selected and energy resolved total reaction probabilities for the C (^{3}P) + OH ($X^2\Pi$, v=0 j=0) $\rightarrow$ CO ($a^3\Pi$, $\Sigma v', \Sigma j'$) + H (^{2}S) reaction on its second excited electronic state ($1^4A''$) and for total angular momentum J=0 are presented in panel (a) of Figure 4.1 as a function of collision energy. At every collision energy, the probability represents a sum over all the open channel, v' and j' of the product diatom, CO. From Figure 4.1 (a), it can be seen that there are substantial probabilities at low collision energies and in fact there is no threshold for the reaction. This is due to the absence of a barrier in the entrance channel. Moreover, numerous sharp and intense resonance oscillations are found in total reaction probabilities which make it difficult to find a particular trend for the variation of probabilities with collision energy. Nonetheless, it can be noticed that maximum probability, $\sim$0.524 is found at $\sim$0.018 eV and it reaches to its minimum, $\sim 10^{-3}$ at $\sim$0.075 eV. After this drop the probability rises and gets an average value of $\sim$0.3 within $\sim$0.11-0.2 eV collision energy. The probabilities decrease further at higher energies and it oscillates around $\sim$0.2 upto $\sim$0.4 eV followed by a decrease in magnitude and resonance intensity at higher collision energies. Thus the magnitude of probability is not uniform throughout the energy range considered in the present study, rather it oscillates.

It is worthwhile to mention here that like in the case of S + OH $\rightarrow$ SO + H reaction on its electronic ground state (see chapter 3), difficulties were faced to obtain convergence in the total reaction probabilities for J=0 (see panel (a) of Figure 4.1) in present study also. Numerous test calculations are carried out

to achieve good convergence and after such a huge number of test calculations, convergence was achieved in the total reaction probabilities for OH (v=0, j=0) and for J=0. The converged parameters are listed in Table 4.1 and they are used in all remaining calculations. It is worthwhile to mention here that the convergence was so good that these parameters were required to alter a little for the probability calculation of only a few J >0 values. The dynamics calculations turn out to be computationally very expensive due to the complex topography of the underlying PES and the participation of heavier atoms. This is easily understandable from the number of grid points required along the three Jacobi coordinates and the total time for the propagation of the wave packet mentioned in Table 4.1. Indeed, the calculation of probabilities for every J value required ∼3.5 GB RAM and ∼ seven days in a Xeon processor of ∼2.6 GHz clock speed.

Jorfi *et al.* have also studied the dynamics of the C + OH → CO + H reaction on its $1^4A''$ state by TIQM method and they have reported total reaction probabilities for J=0 upto 0.9 eV collision energy [4]. The latter probabilities upto 0.5 eV are reproduced from Ref. [4] and are plotted in solid black colour line in panel (b) of Figure 4.1. Comparison between the results presented in solid black colour lines in panel (a) and (b) of Figure 4.1, reveals that the two sets of probabilities show qualitative similarities, but quantitatively they differ at few energies. Such quantitative differences were also found in the probabilities for this reaction occurring on its first excited ($1^2A''$) state [6, 7] and also for other reactions of similar types taking place on PESs having well(s) on them [8, 9]. These quantitative differences are attributed to the choice of different coordinate systems used to treat the dynamics. Moreover, the intensity and the positions of the resonance peaks in probabilities largely depend on the chosen energy grid. Nonetheless, the overall shape of the total reaction probability curves obtained

for J=0 by two different methods is comparable. On the other hand, an excellent agreement is found when the probabilities calculated for J=0 [see Figure 4.1(a)] in the present study are compared with those obtained by Zanchet *et al.* by another TDQM method. These results are reproduced from Ref. [5] and presented in dashed red colour line in panel (b) of Figure 4.1. The agreement gets better as the time-dependent formalism is followed in both the studies.

Numerous sharp and intense oscillations found in the probabilities for J=0 [see Figure 4.1] are attributed to the formation of intermediate collision complexes inside the two deep potential wells on the $1^4A''$ PES [see Figure 1.4 and Table 1.6]. The probabilities calculated for J=0 in the present study can be compared with those obtained for the C + OH reaction occurring on its electronic ground [10] and first excited ($1^2A''$) [1] states by various theoretical methods [6, 7, 11–13]. Sharp and intense resonance oscillations were also found in the probabilities obtained on the $1^2A''$ state [6, 7]. In particular, the resonance peaks are more intense in low collision energy range and hence they bear similarities with the probabilities calculated in the present study [see Figure 4.1 (a)]. In contrast, no such resonance oscillations are found in the probabilities calculated for the C + OH reaction on its electronic ground state [10–12]. The probabilities on the electronic ground PES were found to be independent of collision energy with a magnitude ∼1.0 throughout the entire energy range. These observation can be justified in terms of the topographical details of underlying PESs of the three lowest lying electronic states of the COH reactive system. Small exoergicity and wells of relatively larger depths along reaction paths make the formation of intermediate collision complexes easier [14] which further leave their signature in various dynamical observables. The depths of the two wells present on each of electronic ground, first excited ($1^2A''$) and second excited ($1^4A''$) PESs are ∼7.26 eV and ∼5.50

eV, ∼6.16 eV and ∼4.63 eV, ∼2.25 eV and ∼1.85 eV, respectively [see Table 1.2 , 1.4 and 1.6]. Thus the wells on the electronic ground PES are the deepest. Similarly, the exoergicity, ∼6.4 eV on the latter is more compared to the other two surfaces. Both $1^2A''$ and $1^4A''$ states have the same exoergicity of ∼0.41 eV [see Figure 1.3]. Hence, though deepest wells are present on the electronic ground PES the higher exoergicity makes the decomposition of the intermediate complexes into products faster. Moreover, the less deeper well corresponding to the formation of COH complex represents a metastable minima on the electronic ground state. On the other hand, less exoergicity on both excited states makes the dissociation of the intermediate complexes difficult even form relatively less deeper wells. Moreover, the barrier present at the exit channel on the $1^4A''$ PES makes the dissociation further more difficult [see Figure 1 of Ref. [4]]. Finally, it can be inferred that the wells are deep enough and the exoergicity is small enough on the $1^4A''$ PES to yield sharp and intense resonance oscillations in total reaction probability. Similar sharp and intense resonance oscillations are also found in the probabilities for S + OH → SO + H reaction on its electronic ground state [see Figure 3.1].

Total reaction probabilities for $J > 0$ are also calculated within CS approximation [2, 3] and few of them are shown in panel (a)-(j) of Figure 4.2. It can be seen from Figure 4.2 that the resonances obtained for $J=0$ also persist for $J > 0$. Probabilities increase at higher energies with the increase of J value and also the resonances become sharper and more intense. The increase of centrifugal barrier height with an increase of J makes the dissociation of intermediate collision complexes difficult even at higher energies. This results into an increase of the lifetime of the floppy intermediate complex inside the wells which yields sharp and intense peaks in the probability curve. The centrifugal barrier leads a

threshold for this barrierless reaction which is manifested by the slow shift of the onset of the reaction with increasing J value.

Zanchet *et al.* have also calculated reaction probabilities of the C + OH reaction on its $1^4A''$ state for J=0-50 [5] to obtain ICSs upto 0.1 eV collision energy. They followed a TDQM method and included the Coriolis coupling terms in the Hamiltonian. A comparison among the probabilities calculated in the present study and those of Zanchet *et al.* [5] gives an idea about the impact of Coriolis forces on the state-selected dynamics. For the sake of comparison, probabilities calculated by Zanchet *et al.* for J=10, 30 and 40 are reproduced for Ref. [5] and are presented in panel (b), (f) and (h) of Figure 4.2, respectively, in dashed red colour lines. From panel (b), the magnitude and pattern of probabilities for J=10 are found to be in good accord with each other. Whereas, the probabilities calculated for J=30 in the present study is less than those of Zanchet *et al.* at low collision energies but these are in fair agreement at higher energies [see panel (f)]. Finally, from panel (h), it can be seen that the onset of the reaction for J=40 shifts faster in the present study than the results of Zanchet *et al.* Similar observations were also found for the, $He + H_2^+ \rightarrow HeH^+ + H$, reaction where the reaction proceeds through the formation of long-lived intermediate complexes [15]. Thus it can be inferred that the effects of Coriolis force in not very significant for lower J values, rather it is noticeable for higher J. Lastly, from panel (j) it is obvious that the threshold for the reaction becomes $\sim$0.25 eV and hence inclusion of reaction probabilities upto J=48 is adequate to obtain ICSs upto 0.25 eV collision energy within the CS approximation.

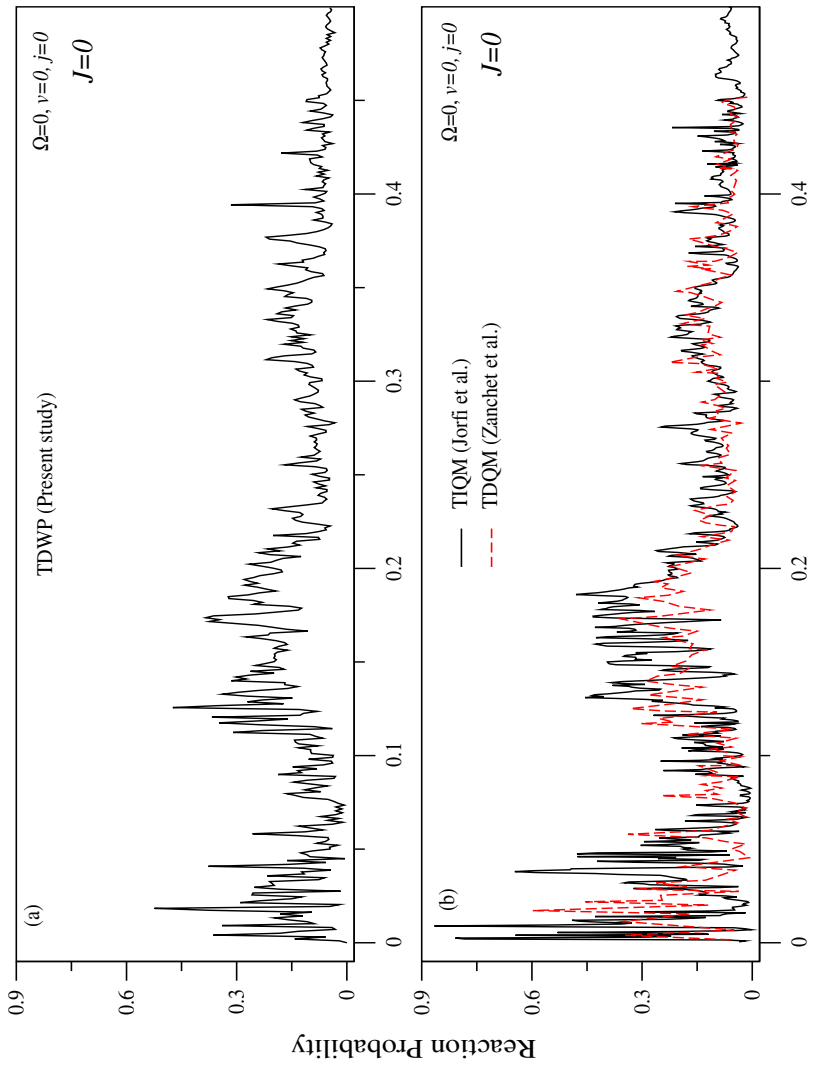

Figure 4.1: Initial state-selected and energy resolved total reaction probabilities calculated for the C (^{3}P) + OH ($X^2\Pi$, v=0, j=0, Ω=0) $\rightarrow$ CO ($a^3\Pi$, $\Sigma v'$, $\Sigma j'$) + H (^{2}S) reaction on its $1^4A''$ state and for J=0 as a function of collision energy. Present TDWP results and those calculated by TIQM methods by Jorfi *et al.* [4] are presented in solid black colour lines in panel (a) and (b), respectively. The results of Zanchet et at. are also reproduced from Ref. [5] and shown in dashed red colour lines in panel (b) for the ease of comparison.

Table 4.1: Description of coordinate grid parameters, properties of initial wave packet and the damping functions used to obtain the dynamics results of C + OH → CO + H reaction on its second excited ($1^4A''$) state.

Parameter	Numerical value	Description
$N_R/N_r/N_\gamma$	1024/128/85	Number of grid points along R, r and γ
R_{min}/R_{max} (a_0)	0.1/38.0	Extension of grid along R
r_{min}/r_{max} (a_0)	0.1/10.0	Extension of grid along r
$\Delta R/\Delta r$ (a_0)	0.037/0.0779	Grid spacing along R and r
r_d (a_0)	6.65	Location of the dividing surface in the product channel
R_{mask}/r_{mask} (a_0)	23.22/7.35	Starting point of the damping function
R_0 (a_0)	15.0	Initial location of the center of the GWP in the coordinate space
E_{trans} (eV)	0.25	Initial translational kinetic energy
$\delta(a_0)$	0.09	Initial width parameter of the GWP
Δt(fs)	0.135	Length of the time step used in the WP propagation
T(fs)	9448.0	Total propagation time

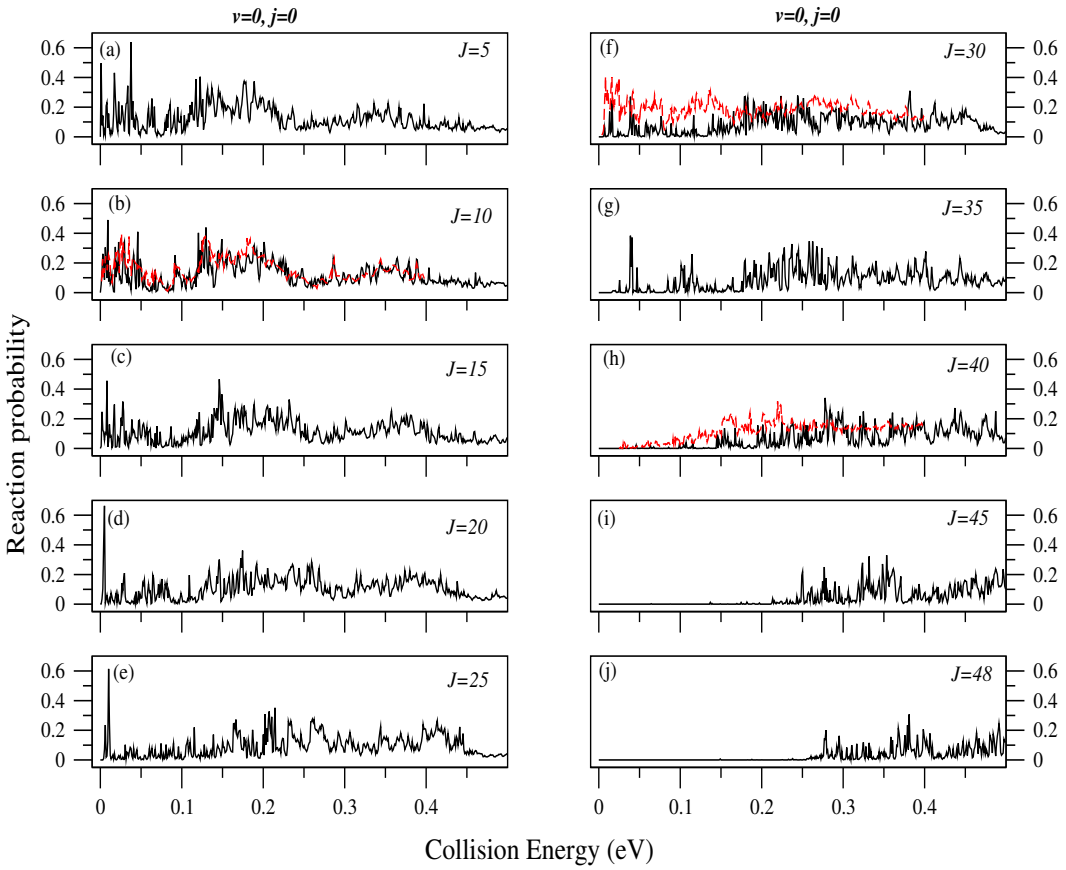

Figure 4.2: Same as Figure 4.1 but for total angular momentum $J > 0$. The value of J is shown in each panel . The probabilities for J=10, 30 and 40 are reproduced from Ref. [5] and shown in panel (b), (f) and (h) in dashed red colour lines, respectively, along with those of present study for the ease of comparison.

4.3.1.2 Effect of rotationally hot reagent OH on total reaction probability

The effect of rotationally hot reagent OH (v=0, j=0-3) on initial state-selected probabilities for total angular momentum $J \geq 0$ are shown and discussed in this section. Probabilities for the, C + OH (Ω=0, v=0, j=0-3) $\rightarrow$ CO + H, reaction and for J=0 are plotted in panels (a)-(d) of Figure 4.3. From panel (a) and (b) it is obvious that the magnitude and pattern of the probabilities alter when the reagent diatom is excited to its j=1 rotational level from j=0. In particular, the probability for OH (v=0, j=1) starts with a maximum at low collision energies, it decreases slowly with the increase of collision energy and finally oscillates around $\sim$0.15 at higher energies. Moreover, a careful look reveals that rotational excitation to j=1 enhances the probability compared to those for j=0 almost throughout the entire energy range considered here. On the other hand, a substantial decrease in probability occurs for OH (v=0, j=2) compared to that of OH (v=0, j=1) [cf., panel (b) and (c)]. This decrease is not so prominent compared to j=0 probabilities. From panel (d) of Figure 4.3 it can be seen that probability for OH (v=0, j=3) decreases noticeably compared to that shown in other panels. Hence, no general trend of variation of probabilities for J=0 with reagent rotational excitation can be established. The effect of rotational excitation of reagent OH on probabilities shown in different panels of Figure 4.3 can be partly attributed to the orientation effect [16]. The loss of preferred orientation for j=1 is compensated by the energy gained by the system through reagent rotational excitation and the latter enhances the reactivity [see panel (b)]. On the contrary, huge disruption of the orientation for j=3 is not compensated by the excess rotational energy and it results a substantial decrease in reactivity [see panel (d)]. Finally, it can be seen that sharp and intense oscillations found for

OH (v=0, j=0) are also present in the probability curves for OH (v=0, j=1-3).

The effect of rotationally hot reagent OH on initial state-selected reaction probabilities for $\Omega > 0$ and $J > 0$ is also studied. Probabilities for, C + OH (Ω=1, v=0, j=1-3) $\rightarrow$ CO + H, reaction and for J=1 are plotted in panels (a)-(c) of Figure 4.4. From panel (a) it can be seen that maximum probability for OH (Ω=1, v=0, j=1) is found below $\sim$0.06 eV collision energy and except a few peaks of magnitude $\sim$0.35 in the $\sim$0.094-0.12 eV range, the probability oscillates around $\sim$0.1 throughout the rest of the energies. The probabilities for OH (Ω=1, v=0, j=2) consistently oscillate around $\sim$0.5 from the onset to 0.15 eV collision energy [see panel (b)]. Finally, form panel (c) it can be found that probability for OH (Ω=1, v=0, j=3) is maximum within $\sim$0.13-0.2 eV collision energy range except a sharp peak present at $\sim$0.003 eV. Hence all these observations take us to the conclusion that the probabilities at low collision energies decrease, while they increase at intermediate energies with reagent rotational excitation. In addition to this, it is also seen that oscillations in the probabilities persist at higher collision energies for rotationally excited reagent diatom. Total reaction probabilities for reagent OH (Ω=2, v=0, j=2-3) and J=2 are shown in panel (d) and (e) of Figure 4.4 as a function of collision energy. The results show that the probabilities increase with reagent rotational excitation except at very low collision energies and at $\sim$0.44 eV. Once again the increase of internal energy of the reactive system through reagent rotational excitation enhances the reactivity, while the disruption of the preferred orientation is not too much due to the rapid rotation of the reagent excited to its j=3 level.

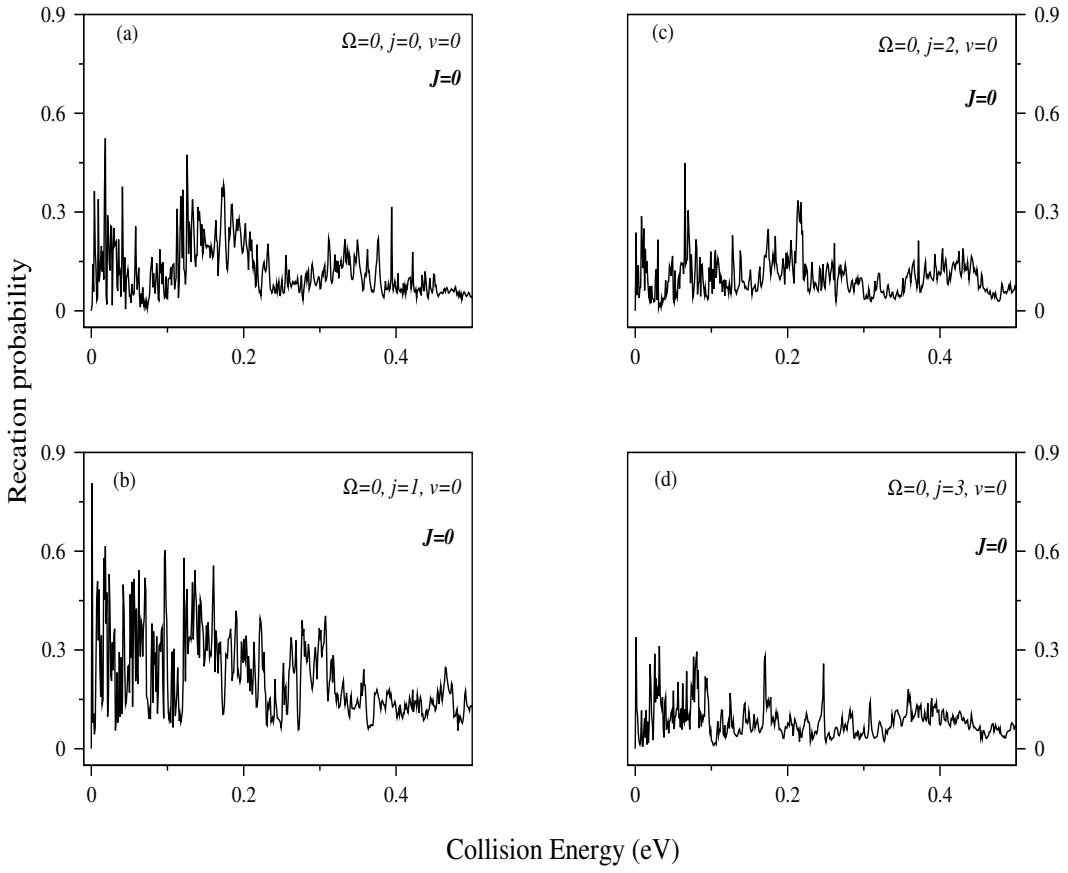

Figure 4.3: Same as Figure 4.1 but for OH (Ω=0, v=0, j=0-3). All quantum numbers are given in each panel to show the excitation.

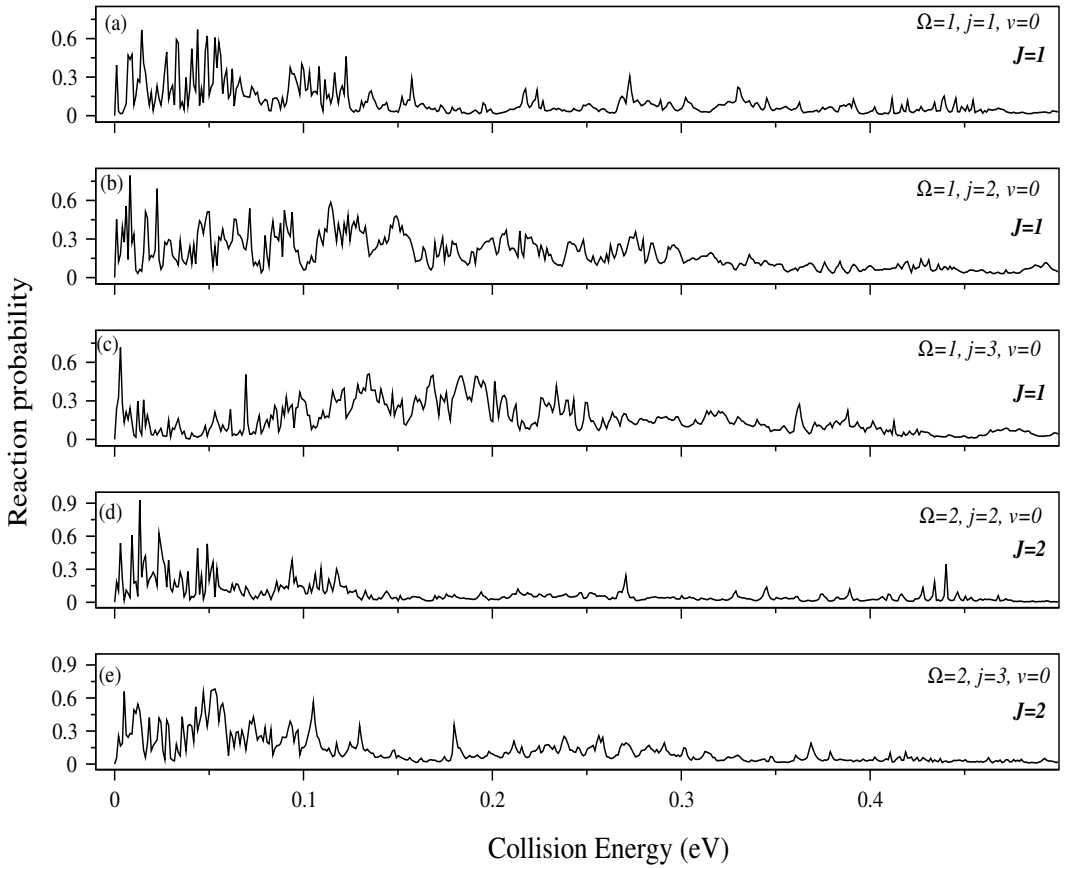

Figure 4.4: Initial state-selected total reaction probabilities for the C + OH (Ω=1-2, v=0, j=1-3) → CO + H reaction as a function of collision energy. Different quantum numbers are given in each panel to show the excitation.

4.3.1.3 Effect of Ω on probability

The effect of Ω, the quantum number for the projection of J and j, on the total reaction probabilities for a few values of J and for OH (v=0, j=1) is shown in Figure 4.5. More specifically, probabilities for OH (Ω=0, v=0, j=1) and OH (Ω=1, v=0, j=1) are shown in panels (a)-(f) and (g)-(l), respectively, as a function of collision energy. From different panels of Figure 4.5 it can be seen that probabilities for Ω=1 are comparable with those of Ω=0 upto ∼0.1 eV collision energy, whereas the former are somewhat less at higher energies. This observation is in strong contrast to the finding of, C + OH → CO + H, reaction on its $1^2A''$ state. The probabilities for OH (Ω=1, v=0, j=1) were found to be ∼10 times less than those for OH (Ω=0, v=0, j=1) in the latter [6]. Furthermore, the effect of Ω on the probability for OH (v=0, j=1) is also in contrast to the findings for the, S + OH → SO + H, reaction on its electronic ground state [cf., Figure 3.5].

The effect of Ω on the dynamics is further examined by plotting initial state-selected probabilities for OH (Ω=0-2, v=0, j=2) and for J=2 in panel (a)-(c) of Figure 4.6. From panel (a) and (b) it can be seen that probabilities for Ω=1 are higher than those for Ω=0 except within ∼0.37-0.48 eV collision energy range. On the contrary, except a few sharp peaks at lower and relatively higher collision energies, probabilities decrease for Ω=2 compared to those of Ω=1 [cf., panel (b) and (c)]. The trend of variation of probabilities with Ω found for OH (j=2) and for J=2 is opposite compared to the finding for the, S + OH → SO + H, reaction on its electronic ground state [cf., Figure 3.6].

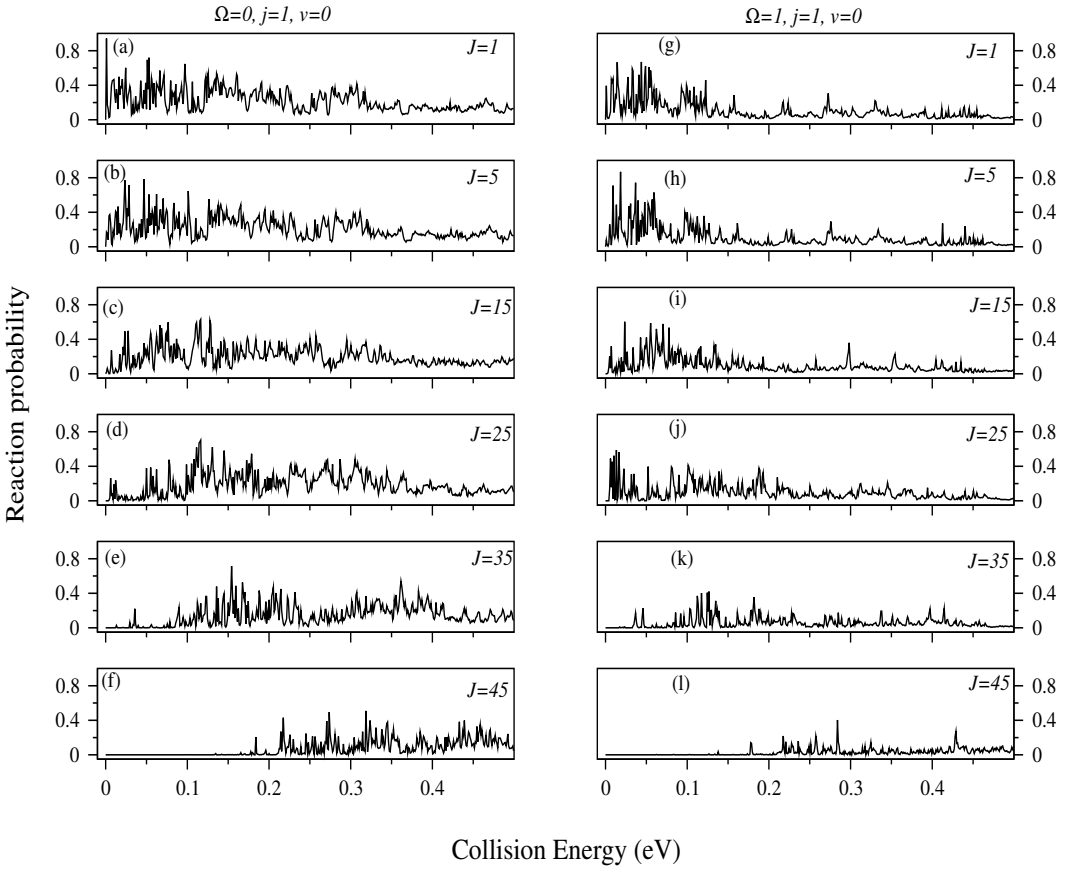

Figure 4.5: Same as Figure 4.2 but for reagent OH (v=0, j=1). Probabilities for OH (Ω=0, v=0, j=1) and OH (Ω=1, v=0, j=1) are shown in panel (a)-(f) and (g)-(l), respectively. The value of J is shown in each panel.

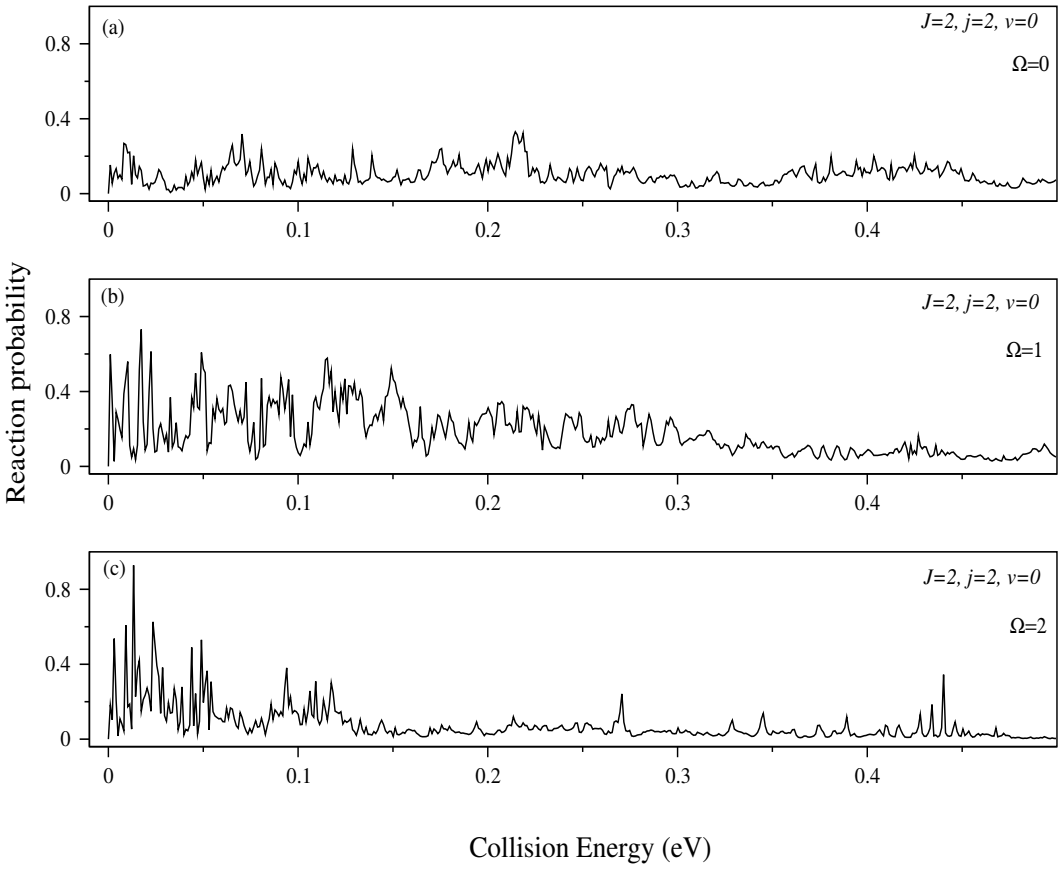

Figure 4.6: Initial state-selected total reaction probabilities for OH (Ω=0-2, v=0, j=2) and for J=2 as a function of collision energy. Different quantum numbers are shown in each panel.

4.3.1.4 Effect of vibrationally hot reagent OH on total reaction probability

Initial state-selected total reaction probabilities for OH (v=0-5, j=0) and for J=0 are shown in panels (a)-(f) of Figure 4.7 as a function of collision energy. Different quantum numbers are given in each panel to indicate the level of excitation. It can be seen from Figure 4.7 that reagent vibrational excitation significantly affects the probabilities. Both the magnitude and pattern of probabilities change dramatically with vibrationally hot reagent OH. In particular, there is a steady increase of probability in the ∼0.4-0.5 eV collision energy range with reagent vibrational excitations. The increase is more prominent for v=0-3 compared to that for v=3-5. The intensity of oscillations gets decreased in the intermediate collision energies for OH (v=1, j=0) compared to the intensity for OH (v=0, j=0) [cf., panel (a) and (b)]. On the contrary, resonances are more dense at higher energies for OH (v=1, j=0). From panel (c) it is quiet obvious that sharp oscillations completely disappear for OH (v=2, j=0) at both intermediate and higher collision energies. Finally, weak oscillations survive only at low collision energies for OH (v=3-5, j=0) and they are almost washed out completely at higher energies [see panels (d)-(f) of Figure 4.7]. The energy available to the system through reagent vibrational excitations and in the form of translational energy open up more product channels for the dissociation of the intermediate collision complexes into products and consequently the lifetime of these floppy intermediates is shortened which is manifested in the smooth probability curves for vibrationally excited reagent OH. Similar findings are also obtained for the, S + OH (v=0-5, j=0) → SO + H, reaction on its electronic ground state [see panels (a)-(f) of Figure 3.7].

The effect of vibrationally hot reagent OH on reactivity is further discussed

by plotting probabilities for OH (v=1-5, j=0) and for J=20, 40, 60 and 80 in panels (a)-(t) of Figure 4.8. From panels (a)-(d) it is seen that oscillations are present for all four J values mentioned here and for OH (v=1, j=0). On the other hand, oscillations are less dense for J=40 and 60 compared to that of J=20 when reagent OH is excited to its v=2 level, but dense resonances are seen at high collision energies for J=80 [cf., panel (e)-(h)]. The centrifugal barrier height becomes very high for J=80 and a large part of the collision energy is spent by the reactive system to overcome this barrier. As a result, the collision complex stays inside the well for longer time and produces oscillations in probabilities. On the contrary, from panels (i)-(t) it can be seen that resonances become less dense with the increase of J value for OH (v=3-5, j=0). More precisely, probabilities for J=60 and 80 seem to be smooth functions of collision energy for OH (v=4-5, j=0) [see panel (o), (p), (s) and (t)]. Finally, it can be seen from Figure 4.8 that for every J value, reagent vibrational excitation increases probability at high collision energies and makes resonance oscillations less intense. These findings are more prominent for J=60 and 80.

Thus, the probabilities for different values of J and different levels of vibrational excitations of reagent OH presented in Figure 4.7 and 4.8 reveal that the magnitude and the pattern of probabilities strongly depend on the value of the vibrational quantum number, v, of reagent diatom. In summary, vibrationally hot reagent OH affects initial state-selected probabilities noticeably and it will be interesting to find how these excitations affect ICSs.

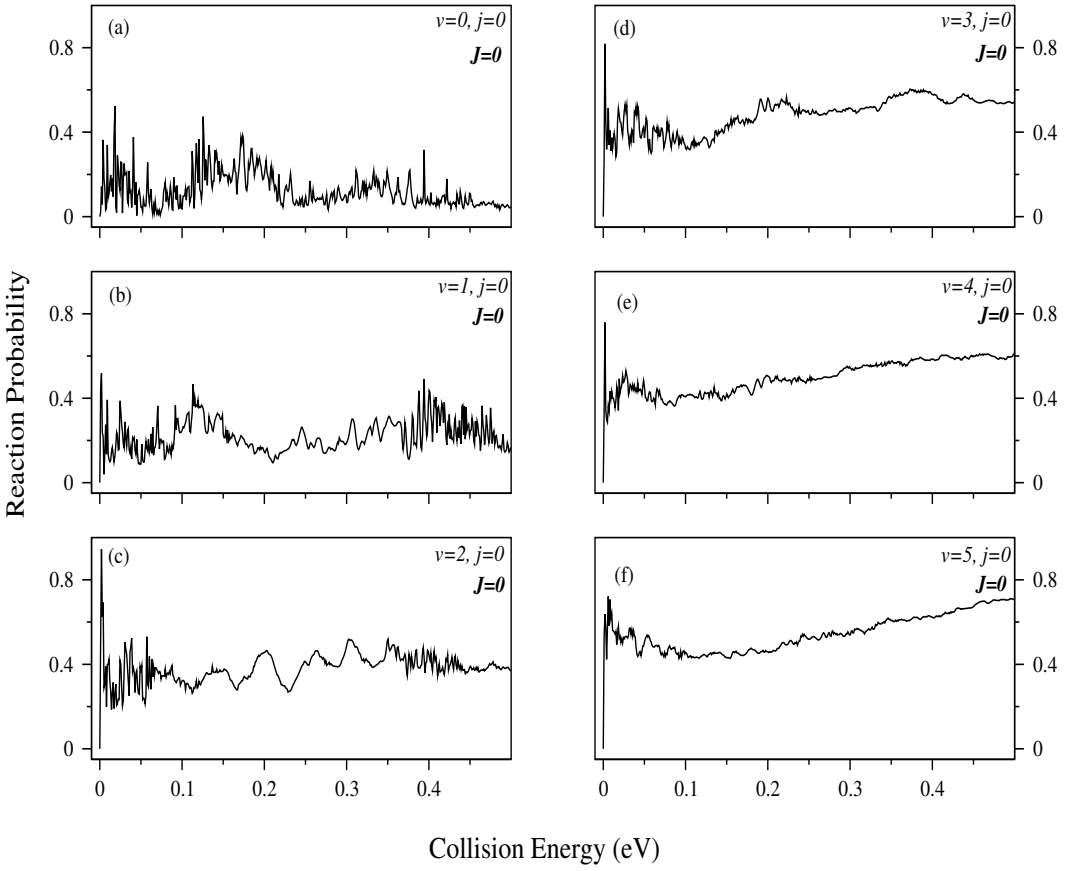

Figure 4.7: Same as Figure 4.1 but for reagent OH (v=0-5, j=0). Different quantum numbers are given in each panel to show the level of excitation.

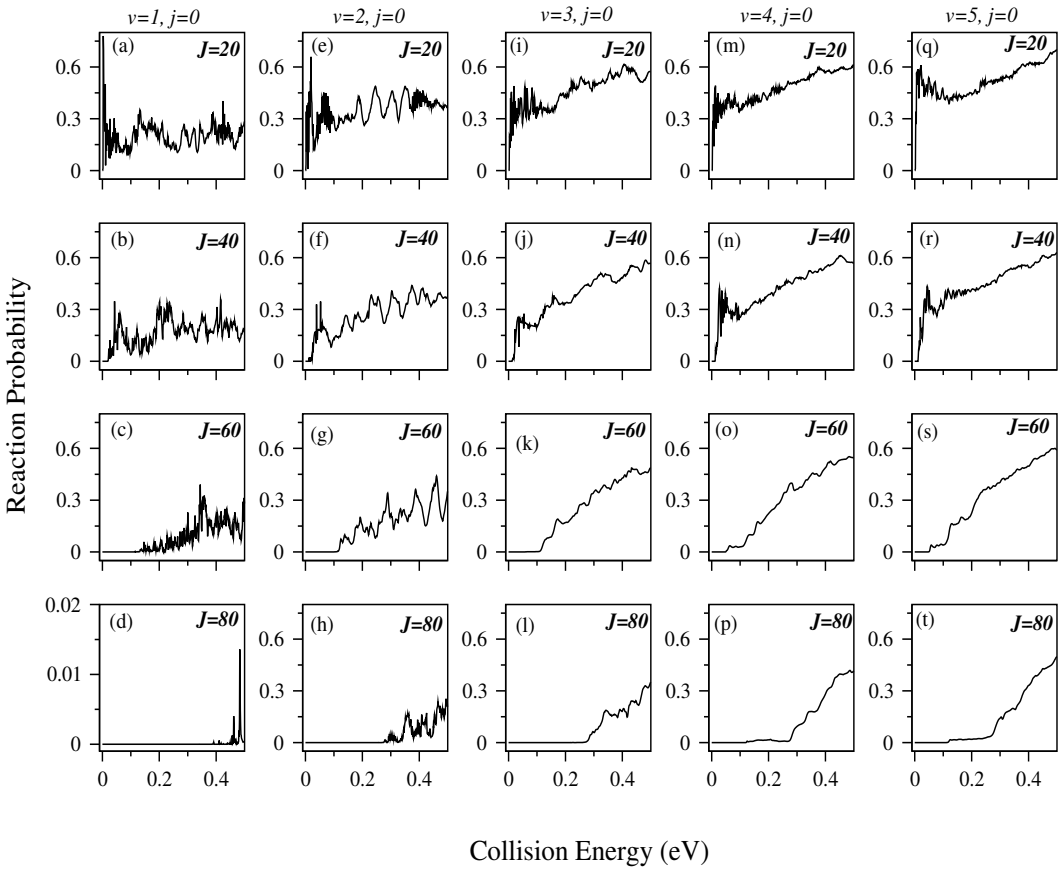

Figure 4.8: Same as Figure 4.2 but for reagent OH (v=1-5, j=0) and for few selected values of J. See text for details.

4.3.2 Initial state-selected and energy resolved ICSs

The findings on the initial state-selected and energy resolved ICSs for the, C + OH (v=0-2, j=0-1) $\rightarrow$ CO + H, reaction on its second excited ($1^4A''$) state are discussed in detail in this section. All partial wave contributions for J=48, 51, 69 and 78 are included for OH (v=0, j=0), OH (v=0, j=1), OH (v=1, j=0) and OH (v=2, j=0), respectively, to calculated converged cross sections upto 0.25 eV collision energy. The ICSs calculated in the present study are compared with those obtained on the first excited ($1^2A''$) PES [1,6] in each panel of Figure 4.9. Different quantum numbers are given in each panel to show different levels of rotational and vibrational excitations of reagent OH. ICSs calculated on the second ($1^4A''$) and first ($1^2A''$) excited PESs are presented in solid black and red colour lines (dashed), respectively, in different panels of Figure 4.9. The variation of ICSs with collision energy is found to be similar on both the PESs [cf., panels (a)-(d)]. Maximum ICS is found at the onset followed by its rapid decrease within a very short energy range. Thereafter, smooth decrease of ICSs with collision energy is seen in all panels of Figure 4.9. Moreover, it is seen that ICSs are larger on the $1^2A''$ state compared to those of $1^4A''$ state and the difference is quite large at low collision energies. Maximum difference in reactivity on the $1^2A''$ and $1^4A''$ states is found for OH (v=0, j=0), whereas, it decreases with reagent vibrational excitations and becomes least for OH (v=2, j=0). The less reactivity of the C + OH reaction on its $1^4A^{''}$ state was anticipated in section 1.1.2 and it is due to the barrierless approach of the C atom along a very narrow angular range and the presence of a barrier at the exit channel. It can also be seen from Figure 4.9 that resonance oscillations present in the ICSs of present study is more sharp and intense than the ICSs obtained on the $1^2A''$ PES [6]. Bulut *et al.* have calculated ICSs [12] for the C + OH reaction on its electronic ground PES. A

careful comparison among all ICSs calculated on the three lowest lying electronic states of C + OH reaction [cf., Figure 4.9 and Ref. [12]] reveals that the variation of ICSs with collision energy is similar everywhere but maximum ICS is found on the electronic ground state due to the highest exoergicity of the reaction on the latter surface [10].

The effect of Ω, reagent rotational and vibrational excitations on ICSs is shown in panel (a), (b) and (c) of Figure 4.10, respectively, in different colours and line types. In particular, the ICSs for OH (Ω=0, v=0, j=1) and OH (Ω=1, v=0, j=1) are presented by black (solid) and red (dashed) colour lines in panel (a). It can be seen here that ICS for Ω=1 is larger than for Ω=0 upto ∼0.1 eV collision energy, whereas they are nearly equal throughout the rest of the energy range. The probabilities for Ω=0 and Ω=1 of OH (v=0, j=1) are found to be equal upto ∼0.1 eV, whereas, at higher energies probabilities for Ω=0 are higher [see Figure 4.5]. Hence, the value of the degeneracy factor, g_k(=1 for Ω=0 and 2 for Ω >0) [see equation 2.39 in chapter 2] contributes to the larger ICS for Ω=1 upto ∼0.1 eV and nearly equal ICS for both Ω=0 and 1 beyond 0.1 eV collision energy.

The dependence of ICSs on rotational excitations of reagent OH is shown in panel (b) of Figure 4.10 by plotting the cross sections for OH (v=0 j=0) and OH (v=0, j=1) as a function of collision energy in black (solid) and red (dashed) colour lines, respectively. ICSs for OH (v=0, j=1) are obtained by summing up the contributions from OH (Ω=0) and OH (Ω=1). It is seen in panel (b) that ICSs increase with reagent rotational excitation within ∼0.018-0.18 eV collision energy range, whereas, the ICSs correspond to j=0 and 1 are closer to each other at higher energies. The variations of ICSs for j=0 and j=1 at the onset is little different from each other. ICSs for OH (v=0, j=0) rises sharply at ∼0.004 eV prior to a steep fall, whereas, a sharp decrease with a few oscillations is found

for OH (v=0, j=1). The different behavior of ICSs for rotationally excited and ground reagent OH results in a cross over at ∼0.008 eV. These observations are in strong contrast to those found on the electronic ground and first excited PESs of HCO reactive system. The ICSs are insensitive to reagent rotational excitation on the electronic ground state [12, 17], whereas, reactivity decreases upon excitation of reagent OH to its j=1 level [6, 13] on its $1^2A''$ state.

The effect of vibrational excitations of reagent OH on the ICSs is shown in panel (c) of Figure 4.10. Cross sections for OH (v=0, j=0), OH (v=1, j=0) and OH (v=2, j=0) are shown in panel (c) as a function of collision energy by black (solid), red (dashed) and green (dot-dashed) colours, respectively. It is obvious from panel (c) that reagent vibrational excitation enhances the reactivity and the enhancement is more prominent when the reagent is excited to its v=1 level. The effect of reagent vibrational excitation on ICSs for the, C + OH → CO + H, reaction on its electronic ground state is also studied by real wave packet (RWP) and QCT methods [12, 17]. The RWP study predicted a decrease of ICSs at low collision energies (see left-bottom panel of Figure 6 of Ref. [12]), whereas, no such decrease in ICSs with reagent vibrational excitations is found in QCT results (cf. Figure 1 and right-bottom panel of Figure 6 of Ref. [17] and Ref. [12], respectively). ICSs for the, C + OH (v=0-2, j=0) → CO + H, reaction on its $1^2A''$ state are calculated by Rao *et al.* [6] by using a TDWP approach. In the latter study, it is found that ICSs decrease with reagent vibrational excitations at collision energy less than ∼0.05 eV, while an opposite trend is noticed at higher energies (>0.1 eV) [cf. Figure 6 of Ref. [6]]. Thus the dependence of ICSs on vibrationally hot reagent OH found on the second excited state is in contrast to those found on the electronic ground and first excited states. Moreover, such enhancement of ICSs with reagent vibrational excitations is also found for the S

+ OH reaction on its electronic ground state [cf. Figure 3.9 of Chapter 3]

The effect of reagent vibrational excitation on ICSs on the $1^4A''$ state is found to be more prominent than on the $1^2A''$ state [cf. panel (b) of Figure 6 of Ref. [6] and panel (c) of Figure 4.10]. This observation needs an explanation. The differences found in the dynamics observables of the C + OH reaction on its first ($1^2A''$) and second $1^4A''$ excited states can be attributed to a difference in the topographies of the underlying surface as the mass combination and the exoergicity are same on both these excited states. A QCT study of Jorfi *et al.* reveals that the reactive system on the $1^2A''$ PES meets both the wells during its journey from reagent to product channels and the sole effect of either of these on the dynamics is minor [cf. Figure 2 of Ref. [13]]. The reactive system glides into the less deeper COH well at the beginning of the collisions and moves to the deepest HCO well by crossing the isomerization barrier followed by its dissociation into products. The HCO complex formed inside the deepest well need not overcome any barrier to reach at the product valley [see schematic energy diagram of the $1^2A''$ PES in Ref. [6]] and hence the topography lacking of any late barrier along the reaction path hardly brings any noticeable effect on the ICSs. On the other hand, though the reactive system on the $1^4A''$ PES proceeds through a similar trajectory via both the wells, the sole impact of the less deeper COH well on the dynamics is more significant than the HCO well [5,13]. Moreover, unlike $1^2A''$ state, the $1^4A''$ state comprises a late barrier at the exit channel [4]. MEPs constructed by the method stated in section 2.4 of chapter 2 for few approaches of attacking C atom at different angles on the $1^4A''$ PES are shown in panels (a)-(r) of Figure 4.11 to facilitate the discussion. It can be seen from panels (e)-(k) that all favorable approaches encounter a late barrier of energy more than the reagent channel. Late barriers are also found on the electronic ground PES of COH system but

these are energetically lower than reagents. Hence, the topography of the second excited ($1^4A''$) PES is unique for a barrierless (in the entrance channel) exoergic reaction where a late barrier exists in the product channel. The presence of this late barrier on the $1^4A''$ PES causes the enhancement of reactivity with reagent vibrational excitations and such observations are also found for many other reactions [18].

Recently, Zanchet *et al.* have calculated the ICSs for the, C + OH (v=0, j=0) $\rightarrow$ CO + H, reaction on its $1^4A''$ state by means of a time-dependent method upto 0.1 eV collision energy. Partial wave contributions for the total angular momentum, J=0-50, including the Coriolis coupling were considered in their study [5]. The ICS calculated for OH (v=0, j=0) in the present study within the CS approximation is found to be little less at lower collision energies compared to that of Zanchet *et al.* This difference is expected to be present as the C + OH reaction takes place on its $1^4A''$ state via an indirect mechanism where intermediate collision complexes are formed and similar observations are also recorded for many other reactions [15, 19–21]. Moreover, the oscillations present in ICSs for OH (v=0, j=0) [see Figure 4.10] are more intense in the present study which includes CS approximation than that of Zanchet *et al.* [5]. Resonance oscillations are absent in the latter study as Coriolis coupling assists the intermediate complexes to dissociate into products and it has a strong influence over reactive resonances [22, 23].

It is to be noted here that the results presented here for the C + OH reaction are qualitatively in good accord to the observations of reactions between OH and other open shell atoms (e.g. O, N, S) [8, 14, 24–28]. Dense resonance oscillations in reaction probabilities and maximum value of ICS at the onset followed by its decrease at higher energies are also found for the latter reactions. Finally, to the

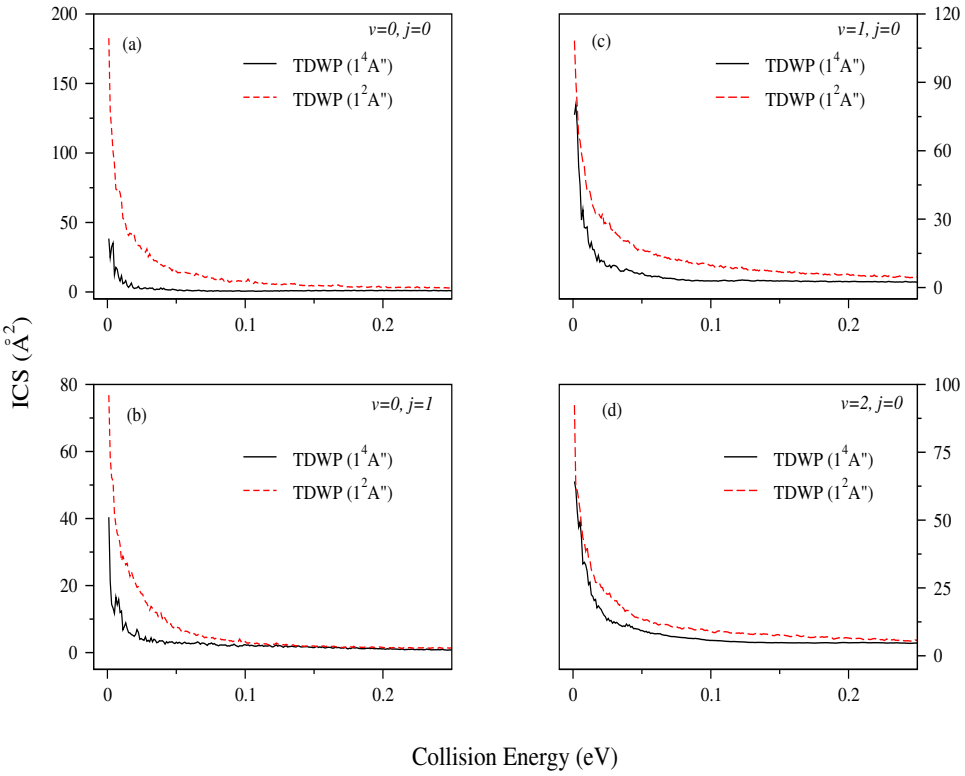

Figure 4.9: Initial state-selected and energy resolved total ICSs for the C + OH (v=0-2, j=0-1) $\rightarrow$ CO + H reaction calculated in the present study are compared with those calculated by using the $1^2A''$ PES in each panel. ICSs obtained on the $1^4A''$ and $1^2A''$ PESs of HCO reactive system are shown in solid black and dashed red line types, respectively.

best of my knowledge, the present discussion provides the most comprehensive account on the mechanistic details of the, C + OH $\rightarrow$ CO + H, reaction on its three lowest lying electronic states.

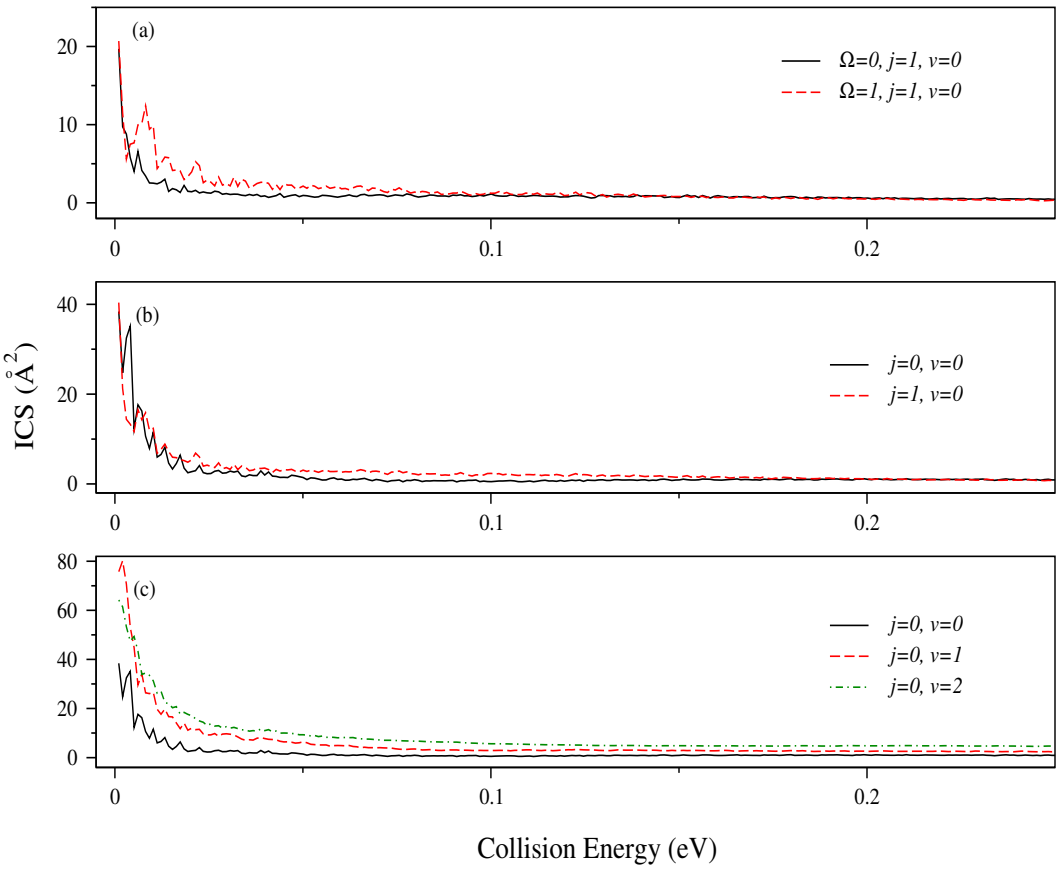

Figure 4.10: Same as in Figure 4.9 but only for the second excited ($1^4A''$) state of the HCO reactive system. Probabilities for OH (Ω=0-1, v=0, j=1), OH (v=0, j=0-1) and OH (v=0-2, j=0) are presented in panel (a), (b) and (c) respectively, in different colours and line types.

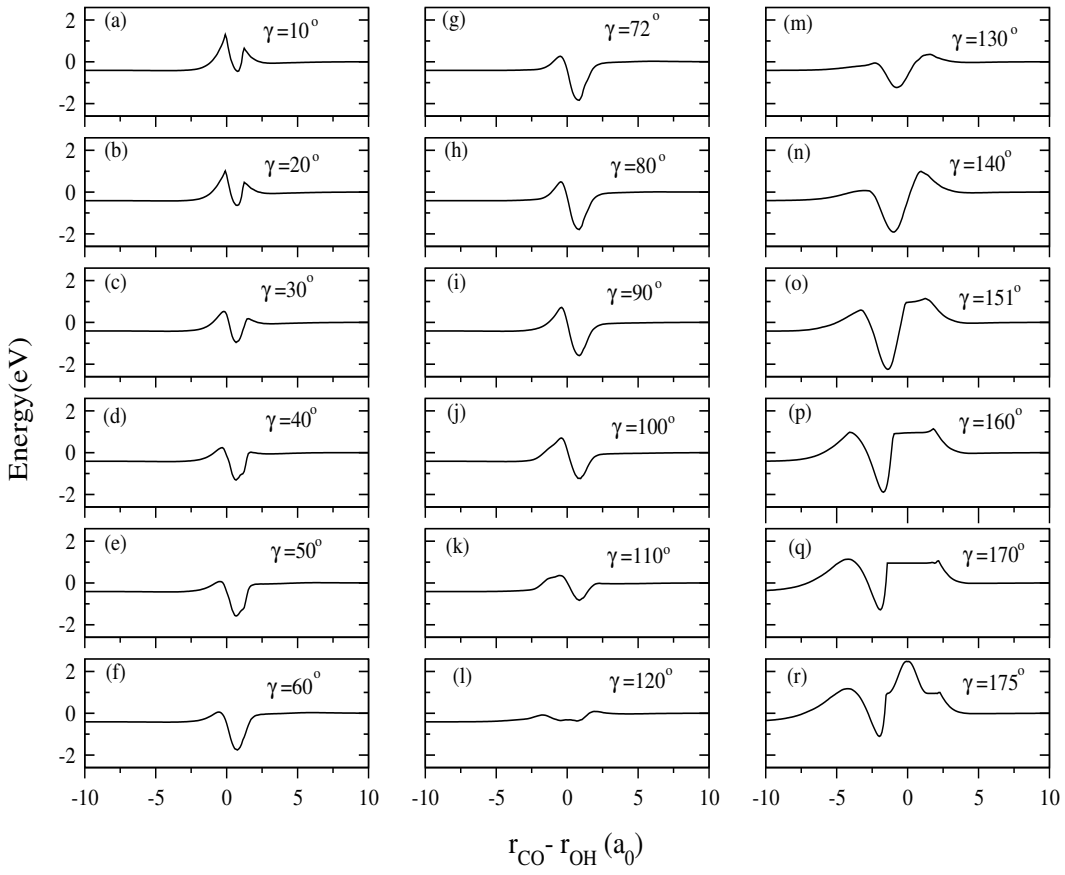

Figure 4.11: Minimum energy paths for few approach angles of attacking C atom towards reagent OH on the $1^4A''$ PES of HCO reactive system. See text for details.

4.4 Summary

A comprehensive theoretical account regarding the effect of internal excitations of reagent diatom on the initial state-selected dynamics of, C (^{3}P) + OH ($X^2\Pi$, v=0-5, j=0-3) $\rightarrow$ CO ($a^3\Pi$) + H (^{2}S), reaction occurring on its second excited ($1^4A''$) state is presented in this chapter. A TDWP approach considering CS approximation is employed to calculate probabilities for OH (v=0-5, j=0-3) upto 0.5 eV collision energy and ICSs for OH (v=0-2, j=0-1) upto 0.25 eV collision energy. Dense oscillations are found in total reaction probabilities due to the formation of intermediate collision complexes inside the deep potential wells on the underlying surface. Less exoergicity also makes the dissociation of the intermediate complexes into products difficult due to an increase of their lifetime. A dramatic change in the pattern of these resonances is found due to reagent vibrational excitations. The resonances survive in ICSs at low collision energies and these are more intense for OH (v=0, j=0). Rotational and vibrational excitations of reagent OH affect ICSs differently. ICS decreases at very low collision energies, it increases at intermediate collision energies with the increase of j value of reagent OH. On the other hand, except at very low collision energies and for OH (v=2, j=0), vibrational excitation increases the reactivity. The enhancement of ICSs with vibrationally hot reagent OH is attributed to the presence of a barrier along the reaction path at the exit channel. This barrier at the exit channel makes the surface topography unique for this particular insertion type reaction. Finally, it is found that the total reaction probabilities for J=0 and OH (v=0, j=0) reported here are in good agreement with those obtained by TIQM and another time-dependent quantum mechanical studies [4, 5].

References

[1] A. Zanchet, B. Bussery-Honvault, M. Jorfi, and P. Honvault, Phys. Chem. Chem. Phys. **11**, 6182 (2009).

[2] R. T. Pack, J. Chem. Phys. **60**, 633 (1974).

[3] P. McGuire and D. J. Kouri, J. Chem. Phys. **60**, 2488 (1974).

[4] M. Jorfi and P. Honvault, J. Phys. Chem. A **115**, 8791 (2011).

[5] A. Zanchet, T. González-Lezana, O. Roncero, M. Jorfi, P. Honvault, and M. Hankel, J. Chem. Phys. **136**, 164309 (2012).

[6] T. R. Rao, S. Goswami, S. Mahapatra, B. Bussery-Honvault, and P. Honvault, J. Chem. Phys. **138**, 094318 (2013).

[7] M. Jorfi and P. Honvault, J. Phys. Chem. A **114**, 4742 (2010).

[8] N Bulut, O. Roncero, M. Jorfi, and P. Honvault, J. Chem. Phys. **135**, 104307 (2011).

[9] E. Carmona-Novilo, T. González-Lezana, O. Roncero, P. Honvault, J.-M. Launay, N. Bulut, F. J. Aoiz, L. Banãres, A. Trottier, and E. Wrede, J. Chem. Phys. **128**, 014304 (2008).

[10] A. Zanchet, B. Bussery-Honvault, and P. Honvault, J. Phys. Chem. A **110**, 12017 (2006).

[11] S. Ying Lin, H. Guo, and P. Honvault, Chem. Phys. Lett. **453**, 140 (2008).

[12] N. Bulut, A. Zanchet, P. Honvault, B. Bussery-Honvault, and L. Bañares, J. Chem. Phys. **130**, 194303 (2009).

[13] M. Jorfi, T. González-Lezana, A. Zanchet, P. Honvault, and B. Bussery-Honvault, J. Phys. Chem. A **117**, 1872 (2013).

[14] S. Goswami, T. R. Rao, S. Mahapatra, B. Bussery-Honvaul, and P. Honvault, J. Phys. Chem. A **118**, 5915 (2014).

[15] T.-S. Chu and K.-L. Han, Phys. Chem. Chem. Phys. **10**, 2431 (2008).

[16] N. Sathyamurthy, Chem. Rev. **83**, 601 (1983).

[17] A. Zanchet, P. Halvick, J.-C. Rayez, B. Bussery-Honvault, and P. Honvault, J. Chem. Phys. **126**, 184308 (2007).

[18] J. C. Polanyi, Acc. Chem. Res. **5**, 161 (1972).

[19] S. Y. Lin and H. Guo, J. Phys. Chem. A **108**, 2141 (2004).

[20] H. Zhai, W. Li, and Y. Liu, Bull. Korean Chem Soc. **35**, 151 (2014).

[21] T. Chu, D. Liang, J. Xu, and S. Dong, Int. J. Quant. Chem. **115**, 803 (2015).

[22] R. Padmanaban and S. Mahapatra, J. Phys. Chem. A **110**, 6039 (2006).

[23] R. Padmanaban and S. Mahapatra, J. Theor. Comput. Chem. **5**, 871 (2006).

[24] C. Xu, D. Xie, P. Honvault, S. Y. Lin, and H. Guo, J. Chem. Phys. **127**, 024304 (2007).

[25] M. Jorfi, P. Honvault, P. Halvick, S. Y. Lin, and H. Guo, Chem. Phys. Lett, **462**, 53 (2008).

[26] S. Y. Lin, H. Guo, P. Honvault, C. Xu, and D. Xie, J. Chem. Phys. **128**, 014303 (2008).

[27] M. Jorfi, P. Honvault, and P. Halvick, Chem. Phys. Lett. **471**, 65 (2009).

[28] M. Jorfi and P. Honvault, Phys. Chem. Chem. Phys. **13**, 8414 (2011).

Chapter 5

State-to-state dynamics of C + OH (v, j=0) reaction on its excited states

5.1 Introduction

The comparison of the initial state-selected dynamics results of the, C (^{3}P) + OH ($X^2\Pi$) → CO ($a^3\Pi$) + H (^{2}S), reaction on its excited ($1^2A''$ and $1^4A''$) states [1] and relevant discussions made in chapter 4 motivated us to extend the investigation at the state-to-state level in order to find the mechanistic details of this reaction in more detail. An attempt is made here towards this direction. Total and state-to-state reaction probabilities upto 0.5 eV collision energy of the, C + OH (v, j=0) → CO + H, reaction and for J=0 are calculated on the first ($1^2A''$) and second ($1^4A''$) excited states. The effect of vibrationally hot reagent OH on reaction probabilities and product vibrational level distributions at five different collision energies are also reported here. The results are compared with those

available in the literature.

5.2 Theoretical and computational details

Product Jacobi coordinate based TDQM method where only the real part of an WP is propagated is adopted here. The methodology is discussed in detail in section 2.3.

5.3 Results and discussions

5.3.1 Dynamics results on the second excited ($1^4A''$) state of HCO reactive system

5.3.1.1 Total reaction Probabilities for OH (v=0-2, j=0) and for J=0

Energy resolved total reaction probabilities for the, C + OH (v=0, j=0) $\rightarrow$ CO ($\sum v', \sum j'$) + H, reaction on its $1^4A''$ state and for J=0 are plotted in panel (a) of Figure 5.1 as a function of collision energy. Numerous resonance oscillations are found in total reaction probabilities due to the formation of intermediate collision complexes inside the wells present on the underlying PES [1] (see also Figure 1.4). Total reaction probabilities for the C + OH reaction occurring on its $1^4A''$ state are reproduced from Ref. [2] and [3] and presented in panel (b) and (c) of Figure 5.1 for comparison. The probabilities shown in Figure 5.1 [(b) and (c)] are also shown in panel (a) and (b) of Figure 4.1, respectively. It can be seen from panel (a)-(c) of Figure 5.1 that the probabilities calculated in different studies are in excellent agreement among themselves. Probability is maximum at low collision energies followed by a drop at $\sim$ 0.075 eV. The latter gets an average value of $\sim$0.3

within ∼0.11-0.2 eV collision energy range and afterwards it oscillates around ∼0.2 upto ∼0.4 eV collision energy. The magnitude of probability decreases at higher collision energies.

Energy resolved total reaction probabilities calculated in the present study for OH (v=1, j=0) and OH (v=2, j=0) are presented in panel (a) and (c) of Figure 5.2, respectively. Total reaction probabilities calculated by Goswami *et al.* by employing a TDWP propagation approach are reproduced from Ref. [2] and presented here in panel (b) and (d) of Figure 5.2 in order to compare with present results. The latter are also shown in panel (b) and (c) of Figure 4.7. It can be seen from Figure 5.2 that the present results are in good agreement with those of Goswami *et al.*. Such good agreements found here between the results of present study and those available in literature presented in Figure 5.1 and Figure 5.2 confirms the correctness of the results of the present study. Numerous test calculations are carried out separately for reagent OH (v=0, j=0), OH (v=1, j=0) and OH (v=2, j=0) to achieve good convergence. The converged parameters are listed in Table 5.1, Table 5.2 and Table 5.3 for OH (v=0, j=0), OH (v=1, j=0) and OH (v=2, j=0), respectively. From the number of grid points along the three product Jacobi coordinates and the number of iteration steps required for the dynamics study, it is easily understandable that the calculations are computationally very expensive. Moreover, it is worthwhile to mention here that adequate number of product rotational level were to be included to assure all open product channels are accounted for at a given energy in each calculation. Resonance oscillations decrease at intermediate collision energy range for OH (v=1, j=0) compared to those of OH (v=0, j=0) [cf. Figure 5.1(a) and 5.2(a)]. Furthermore, from panel (c) of Figure 5.2, it can be seen that sharp oscillations are almost washed out at intermediate and higher collision energies for OH (v=2, j=0).

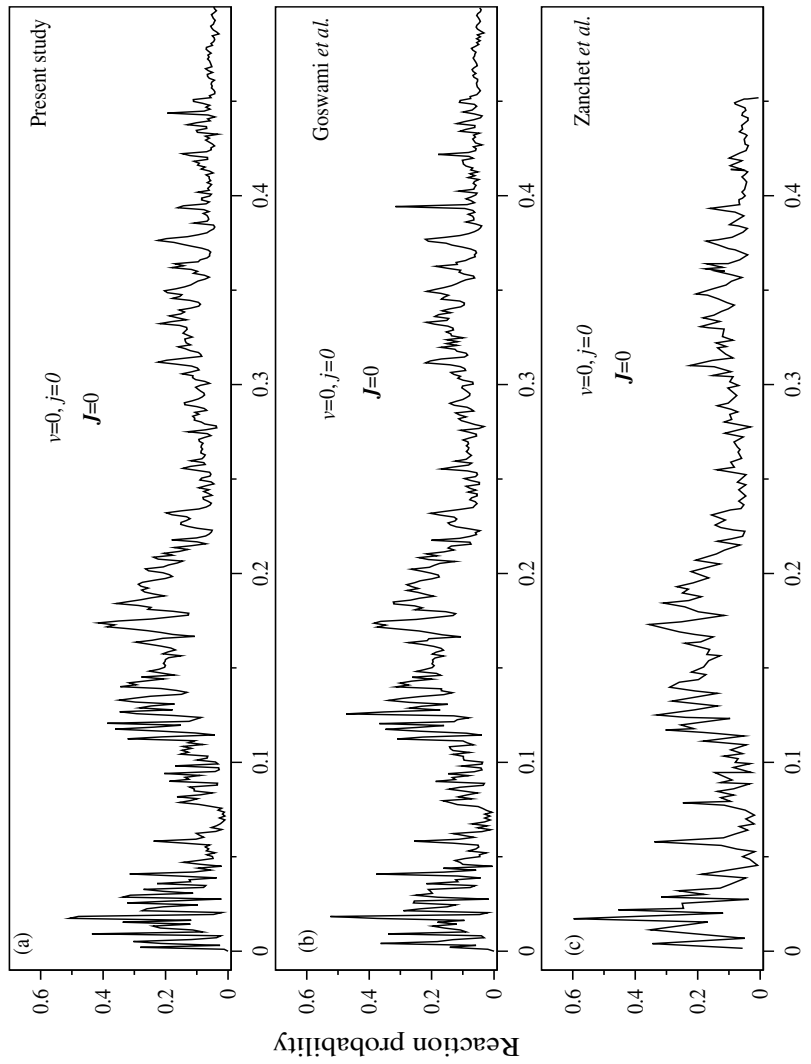

Figure 5.1: Energy resolved total reaction probabilities calculated for the C (^{3}P) + OH ($X^2\Pi$, v=0, j=0) → CO ($a^3\Pi$, $\sum v'$, $\sum j'$) + H (^{2}S) reaction occurring on its second excited ($1^4A''$) state and for the total angular momentum quantum number, J=0, as a function of collision energy. Reaction probabilities calculated in present study are shown in panel (a). Whereas, those calculated by Goswami *et al.* [2] and Zanchet *et al.* [3] are shown in panel (b) and (c), respectively, for the ease of comparison.

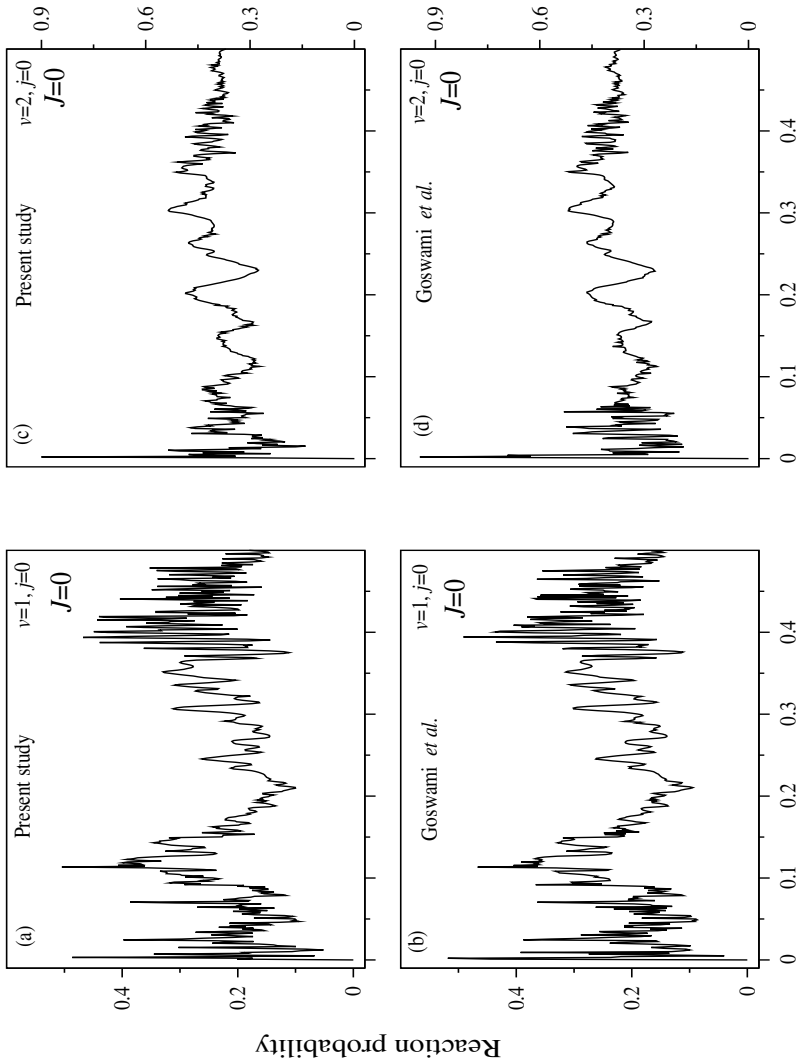

Figure 5.2: Energy resolved total reaction probabilities calculated for the C (^{3}P) + OH ($X^2\Pi$, v=1-2, j=0) $\rightarrow$ CO ($a^3\Pi$, $\sum v'$, $\sum j'$) + H (^{2}S) reaction occurring on its second excited ($1^4A''$) state and for J=0. See text for details.

Table 5.1: Details of grid parameters, properties of initial WP and the absorption function used to obtain the dynamics results for the, C + OH (v=0, j=0)→ CO + H, reaction on its second excited ($1^4A''$) state.

Parameter	Value	Description
$N_R/N_r/N_\gamma$	239/359/100	Number of grid points along the three product Jacobi coordinates, R_c, r_c and γ_c, respectively.
R_{min}/R_{max} (a_0)	0.094/28.0	Extension of the grid along R_c
r_{min}/r_{max} (a_0)	0.094/17.9902	Extension of the grid along r_c
R_∞ (a_0)	12.00	Location of the dividing surface in the product channel
R_{abs}/r_{abs} (a_0)	15.0 /14.00	Starting point of the absorption function along R_c and r_c
C_{abs}/c_{abs}	0.5/0.5	Strength of absorption along R_c and r_c
R_0 (a_0)	11.5	Center of initial wave packet in reagent Jacobi coordinate
E_{trans} (eV)	0.135	Initial translational energy in eV
α	11.00	Width of initial wave packet
β_s	0.5	Smoothing of initial wave packet
nstep	120000	Number of iteration steps
nvab	6	Number of vibrational levels of product diatom

Table 5.2: Details of grid parameters, properties of initial WP and the absorption function used to obtain the dynamics results for the, C + OH (v=1, j=0)→ CO + H, reaction on its second excited ($1^4A''$) state.

Parameter	Value	Description
$N_R/N_r/N_\gamma$	239/383/100	Number of grid points along the three product Jacobi coordinates, R_c, r_c and γ_c, respectively.
R_{min}/R_{max} (a_0)	0.094/28.0	Extension of the grid along R_c
r_{min}/r_{max} (a_0)	0.094/17.9902	Extension of the grid along r_c
R_∞ (a_0)	12.00	Location of the dividing surface in the product channel
R_{abs}/r_{abs} (a_0)	15.0 /13.50	Starting point of the absorption function along R_c and r_c
C_{abs}/c_{abs}	0.5/0.5	Strength of absorption along R_c and r_c
R_0 (a_0)	12.5	Center of initial wave packet in reagent Jacobi coordinate
E_{trans} (eV)	0.135	Initial translational energy in eV
α	11.00	Width of initial wave packet
β_s	0.5	Smoothing of initial wave packet
nstep	150000	Number of iteration steps
nvab	8	Number of vibrational levels of product diatom

Table 5.3: Details of grid parameters, properties of initial WP and the absorption function used to obtain the dynamics results for the, C + OH (v=2, j=0)→ CO + H, reaction on its second excited ($1^4A''$) state.

Parameter	Value	Description
$N_R/N_r/N_\gamma$	239/439/130	Number of grid points along the three product Jacobi coordinates, R_c, r_c and γ_c, respectively.
R_{min}/R_{max} (a_0)	0.094/28.0	Extension of the grid along R_c
r_{min}/r_{max} (a_0)	0.094/22.0	Extension of the grid along r_c
R_∞ (a_0)	12.00	Location of the dividing surface in the product channel
R_{abs}/r_{abs} (a_0)	15.0 /13.50	Starting point of the absorption function along R_c and r_c
C_{abs}/c_{abs}	0.5/0.7	Strength of absorption along R_c and r_c
R_0 (a_0)	12.5	Center of initial wave packet in reagent Jacobi coordinate
E_{trans} (eV)	0.135	Initial translational energy in eV
α	15.00	Width of initial wave packet
β_s	0.5	Smoothing of initial wave packet
nstep	150000	Number of iteration steps
nvab	10	Number of vibrational levels of product diatom

5.3.1.2 Product vibrational level resolved probabilities for OH (v=0-2, j=0) and for J=0

Product vibrational level resolved reaction probabilities of the, C + OH (v, j=0) $\rightarrow$ CO (v', $\sum j'$) + H (^{2}S) reaction on its second excited ($1^4A''$) state and for J=0 are shown in Figure 5.3, Figure 5.4 and Figure 5.5 for reagent OH (v=0), OH (v=1) and OH (v=2), respectively.

From panel (a)-(f) of Figure 5.3 it can be seen that v'=0 and 1 mainly contribute to the total reaction probabilities for J=0 and for OH (v=0, j=0). Resonance oscillations are found in the probabilities for all v' of product diatom. Jorfi *et al.* [4] have also studied the dynamics of the, C + OH (v=0, j=0), reaction on its $1^4A''$ state by employing TIQM method. Product vibrational level resolved reaction probabilities for CO (v'=0-3) reproduced from Ref. [4] are shown by dashed (red) lines in panel (a)-(d) of Figure 5.3. On comparison with the results of present study [shown by solid (black) lines, cf. panel (a)-(d)] of Figure 5.3, it can be seen that despite some quantitative difference, qualitatively they are in good agreement among themselves. From Figure 5.3(d) it can be seen that a threshold for the reaction appears for CO (v'=3). The threshold appears as the ro-vibrational energy of product CO (v'=3, j'=0) ($\sim$0.31 eV) is higher than the ro-vibrational energy of reagent OH (v=0, j=0) ($\sim$0.23 eV). The energy threshold further increases for higher v' of product CO diatom.

Product vibrational level resolved reaction probabilities for OH (v=1, j=0) and OH (v=2, j=0) are shown in Figure 5.4 [(a)-(h)] and Figure 5.5 [(a)-(j)], respectively. It can be seen from these two figures that more product channels open up with reagent vibrational excitation. Thus, a part of reagent vibrational energy is used to produce products in excited vibrational levels. The major contribution comes from the v'=0-2 [cf. Figure 5.4 ((a)-(c))] and v'=0-4 [cf. Figure

5.5 ((a)-(e))] levels of product CO diatom to the total reaction probabilities for OH (v=1, j=0) and OH (v=2, j=0), respectively. Moreover, an energy threshold is found from v'=5 (see panel (f) of Figure 5.4) and v'=8, (see panel (i) of Figure 5.5).

5.3.1.3 Product vibrational level distribution at five different collision energies

Product vibrational level distribution of the, C + OH (v=0-2, j=0) → CO + H, reaction on the $1^4A''$ state at five different collision energies (0.01 eV, 0.05 eV, 0.1 eV, 0.3 eV and 0.5 eV) and for J=0 are shown in Figure 5.6 in different colours and line types. In particular, distributions for OH (v=0, j=0), OH (v=1, j=0) and OH (v=2, j=0) are presented in panel (a), (b) and (c) of Figure 5.6 as a function of v' (quantum number for product vibrational level). The distribution is found to be statistical at all five different collision energies for OH (v=0, j=0) (cf. panel (a) of Figure 5.6). Jorfi *et al.* also calculated product vibrational level distributions by using a TIQM method [4] for reagent OH (v=0, j=0). Despite quantitative differences, qualitatively the distributions reported in the present study are fairly in good agreement with those of Jorfi *et al.* (cf. Figure 5 of Ref. [4] and panel (a) of Figure 5.6 here) except at ∼0.5 eV. At 0.5 eV collision energy, Jorfi *et al.* obtained little more probability for v'=2 compared to v'=1 [4]. The quantitative difference found in the distribution between the results of Jorfi *et al.* and present study is attributed to the different theoretical techniques employed in these studies.

From panel (b) of Figure 5.6 it can be seen that except at 0.01 eV and 0.50 eV collision energies, the distributions are statistical for OH (v=1, j=0). On the contrary, except at 0.05 eV collision energy, product vibrational level dis-

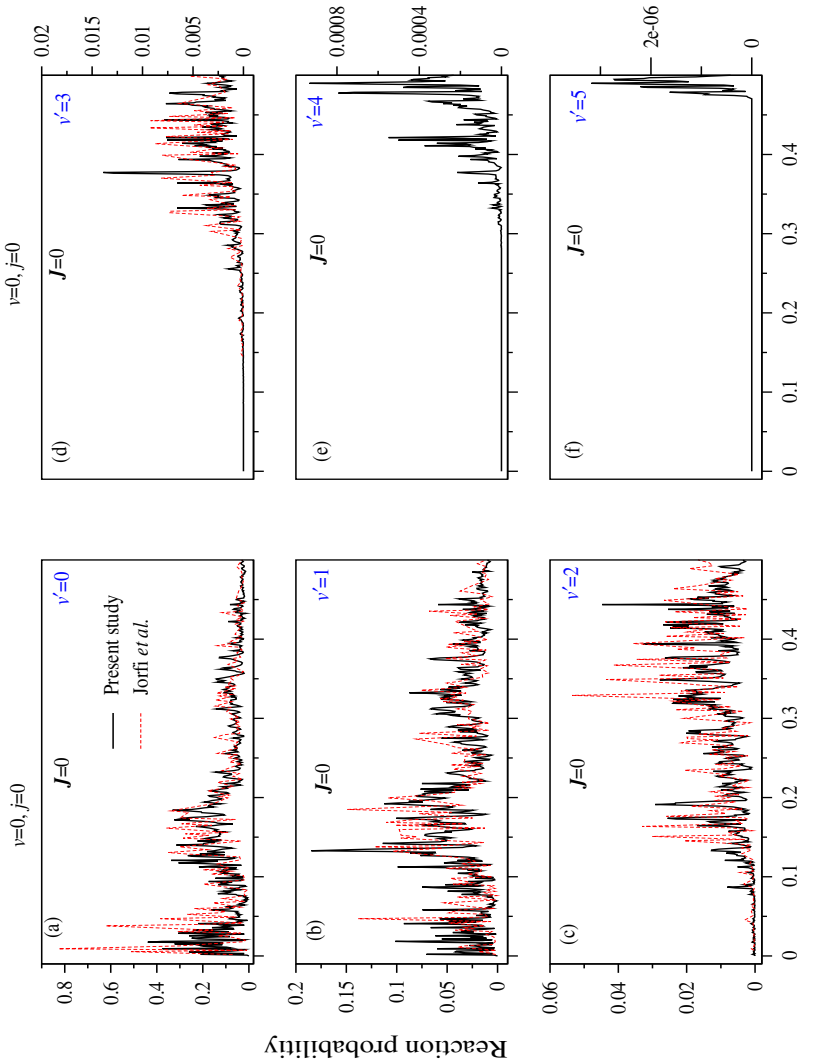

Figure 5.3: Product vibrational level resolved reaction probabilities of the, C + OH (v=0, j=0) → CO (v', $\sum j'$) + H, reaction on its $1^4A''$ state and for J=0 are shown as a function of collision energy. Quantum number for the vibrational level of the product diatom is shown in each panel. See text for further details.

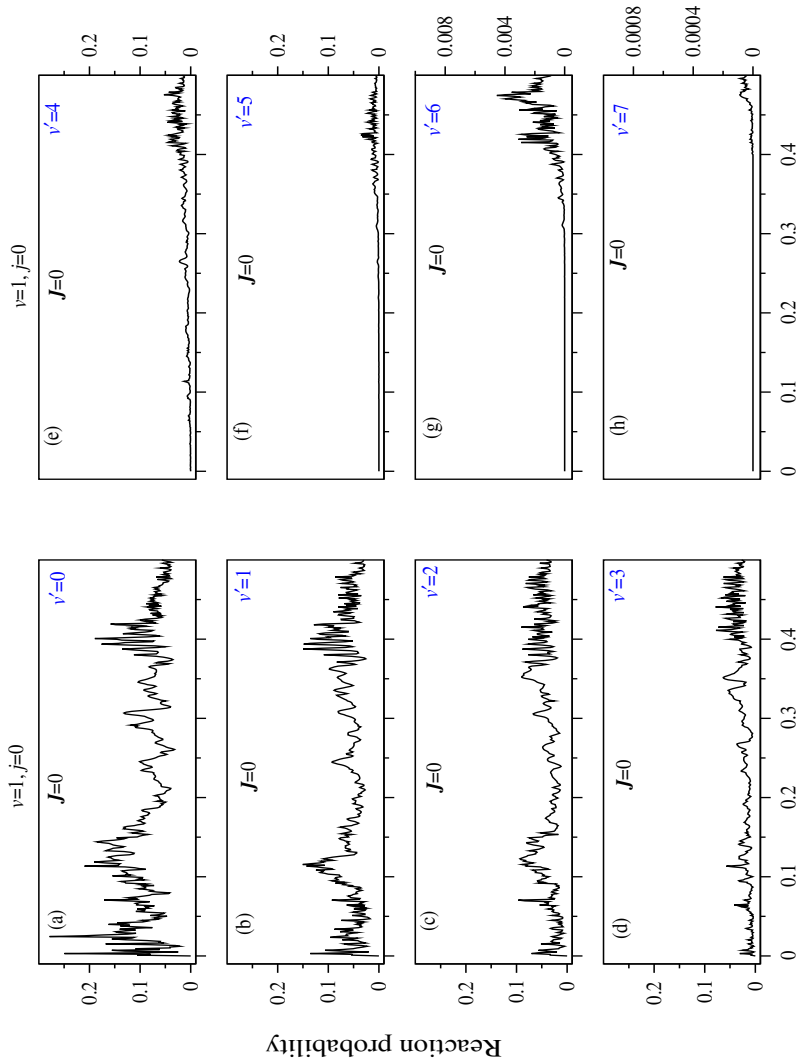

Figure 5.4: Same as Figure 5.3 but for reagent OH (v=1, j=0).

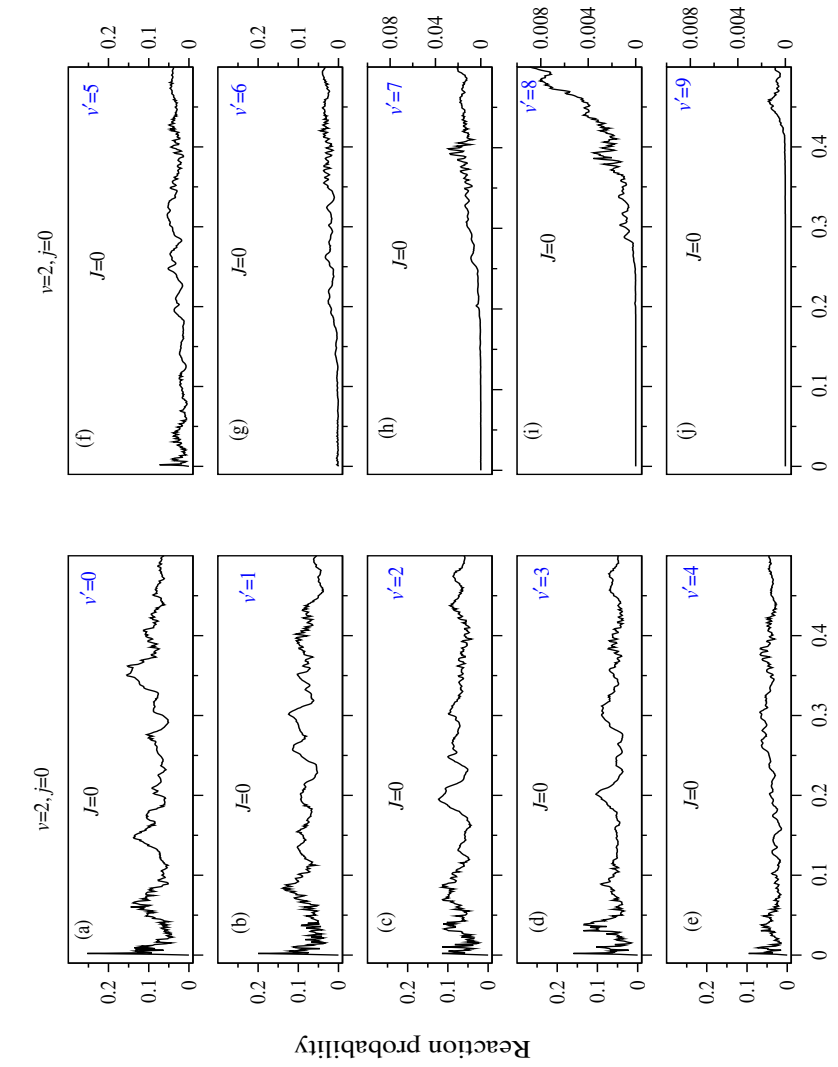

Figure 5.5: Same as Figure 5.3 but for reagent OH (v=2, j=0).

tributions are found to be inverted for OH (v=2, j=0) (cf. panel (c) of Figure 5.6). Thus, from different panels of Figure 5.6, it can be seen that with reagent vibrational excitation, product vibrational level distributions become more non-statistical and hence the reaction mechanism becomes more direct in nature. The broadening and the decrease of the intensity of resonance oscillations with reagent vibrational excitation (cf. Figure 5.2) is also a manifestations of the fact that the mechanism becomes more direct with reagent vibrational excitation.

5.3.1.4 Product rotational level resolved probabilities for OH (v=0-2, j=0) and for J=0

State-to-state reaction probabilities of the, C + OH (v=0-2, j=0) $\rightarrow$ CO (v'=0, j'=5, 15, 25) + H, reaction on its $1^4A''$ states are shown in different panels of Figure 5.7 as a function of collision energy. It can be seen from Figure 5.7 that probabilities decrease with the increase of product diatom rotational excitation for reagent OH (v=0-2, j=0). It is worthwhile to mention here that despite a difference in the magnitude, similar findings are also observed for CO (v'=1). Jorfi *et al.* have also reported the product rotational level resolved probabilities for the C + OH (v=0, j=0) $\rightarrow$ CO (v'=0, j') + H reaction (see Figure 4 of Ref. [4]). The probabilities for CO (v'=0, j'=5, 15) calculated in the present study is found to be in fair agreement with those of Jorfi *et al.* [cf. panel (a) and (b) of Figure 5.7 and Figure 4 of Ref. [4]].

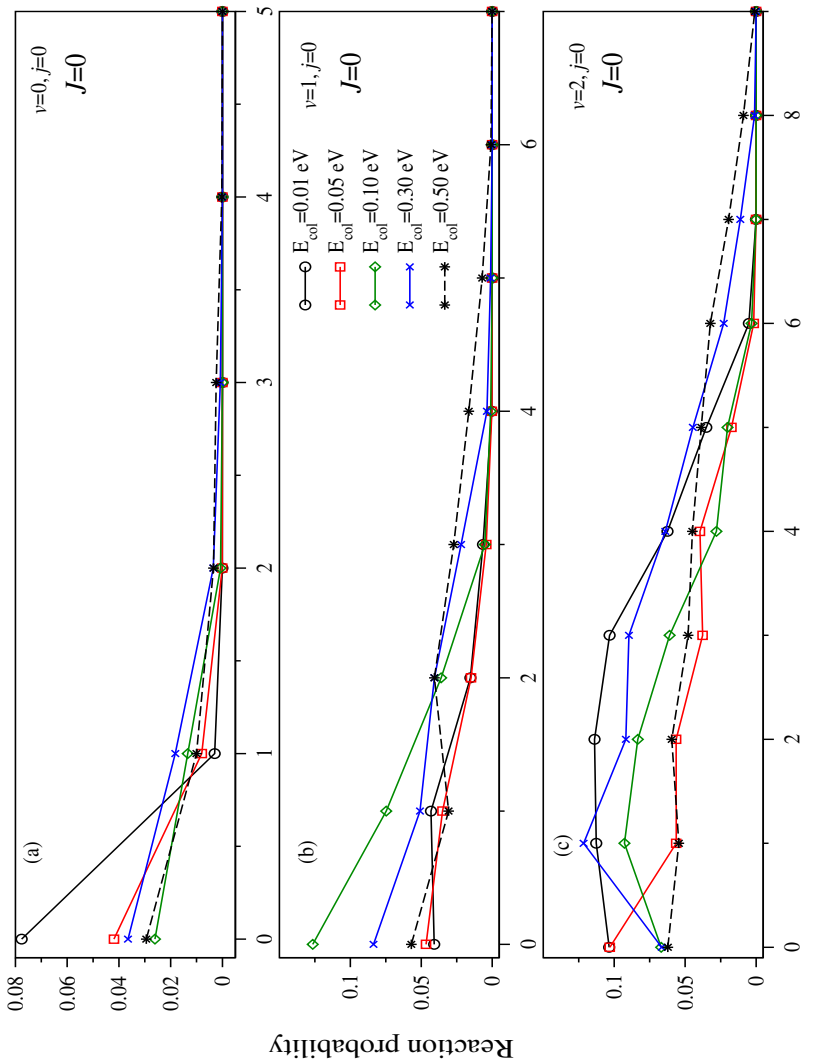

Figure 5.6: Product vibrational level distributions of the, C + OH (v=0-2, j=0) → CO + H, reaction on the second excited ($1^4A''$) state and for J=0 at 0.01 eV, 0.05 eV, 0.1 eV, 0.3 eV and 0.5 eV collision energies (E_{col}). Distributions for OH (v=0, j=0), OH (v=1, j=0) and OH (v=2, j=0) are shown in different colours and line types in panel (a), (b) and (c), respectively.

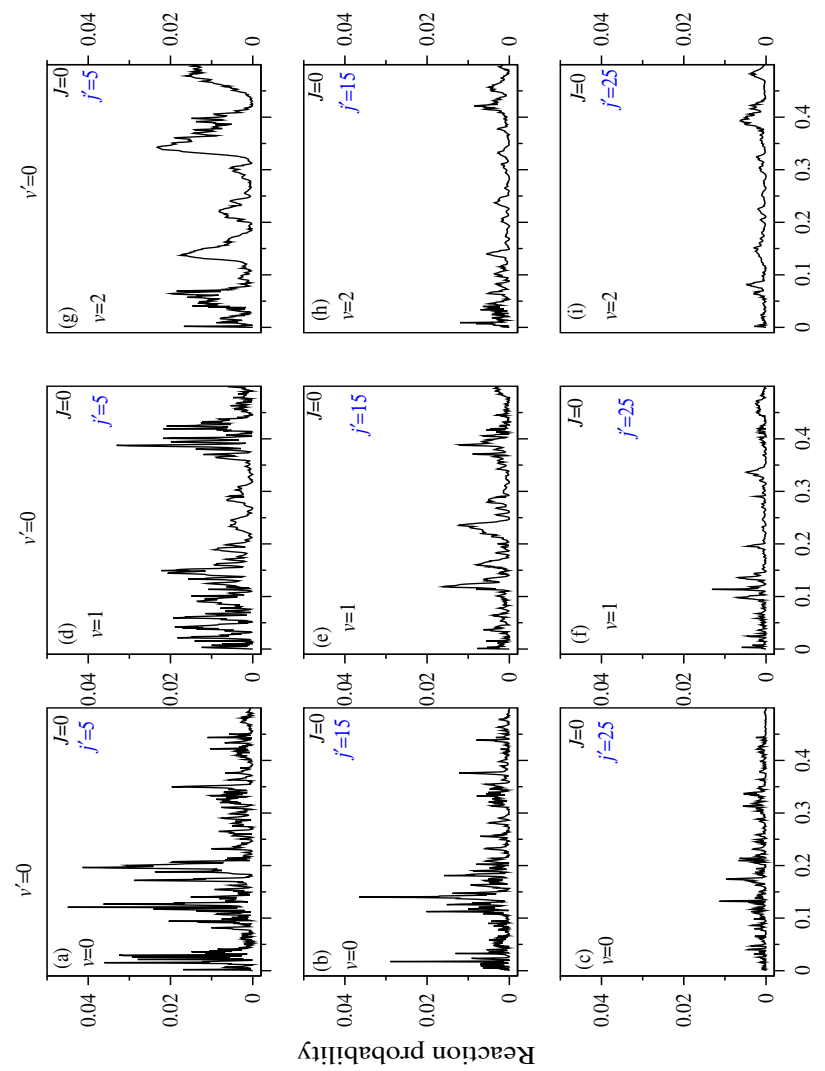

Figure 5.7: Product rotational level resolved state-to-state reaction probabilities of the, C + OH (v=0-2, j=0) → CO (v'=0, j'=5, 15, 25) + H, reaction on the second excited ($1^4A''$) state as a function of collision energy.

5.3.2 Dynamics results on the first excited ($1^2A''$) state of HCO reactive system

5.3.2.1 Total reaction Probabilities for OH (v=0-1, j=0) and for J=0

Energy resolved total reaction probabilities for the C + OH (v=0-1, j=0) $\rightarrow$ CO ($\sum v'$, $\sum j'$) + H reaction on the first excited ($1^2A''$) state [1] of HCO reactive system and for J=0 are shown in Figure 5.8. In particular, probabilities for OH (v=0, j=0) and for OH (v=1, j=0) calculated in the present study are shown in panel (a) and (c) of Figure 5.8. Intense resonance oscillations are found in total reaction probabilities due to the formation of collision complexes inside the wells present on the underlying PES [1] (see also Table 1.4). From panel (a) it can be seen that maximum reaction probabilities for OH (v=0, j=0) are found at low collision energies and it oscillates around $\sim$0.2 within $\sim$0.1-0.2 eV collision energy. At higher energies the latter increases and it oscillates around $\sim$0.25. Rao *et al.* [5] has investigated the initial state-selected dynamics of the C + OH reaction on its first excited state by using a TDWP propagation approach . Total reaction probabilities for OH (v=0, j=0) are reproduced from Ref. [5] and are presented in panel (b) of Figure 5.8 for the ease of comparison. From panel (a) and (b) it can be seen that the probabilities calculated in present study are in good agreement with those obtained by Rao *et al.* except at very low collision energies. This discrepancy can be attributed to the use of two different kinds of initial wave packet. In the present study, a sinc WP [6] is used, whereas, Rao *et al.* used a GWP in their calculation. Nonetheless attempts are being made presently to remove this little discrepancy. Such a good agreement confirms the correctness of the results of present study. Numerous test calculations are carried out to achieve a good convergence for the C + OH reaction on the first excited

Table 5.4: Details of grid parameters, properties of initial WP and the absorption function used to obtain the dynamics results for the, C + OH (v=0, j=0)→ CO + H, reaction on its first excited ($1^2A''$) state.

Parameter	Value	Description
$N_R/N_r/N_\gamma$	299/539/125	Number of grid points along the three product Jacobi coordinates, R_c, r_c and γ_c, respectively.
R_{min}/R_{max} (a_0)	0.1/28.0	Extension of the grid along R_c
r_{min}/r_{max} (a_0)	0.1/18.0	Extension of the grid along r_c
R_∞ (a_0)	17.00	Location of the dividing surface in the product channel
R_{abs}/r_{abs} (a_0)	18.5 /14.00	Starting point of the absorption function along R_c and r_c
C_{abs}/c_{abs}	0.5/0.5	Strength of absorption along R_c and r_c
R_0 (a_0)	10.5	Center of initial wave packet in reagent Jacobi coordinate
E_{trans} (eV)	0.145	Initial translational energy in eV
α	12.5	Width of initial wave packet
β_s	0.5	Smoothing of initial wave packet
nstep	180000	Number of iteration steps
nvab	6	Number of vibrational levels of product diatom

state. Furthermore, convergence is checked separately for OH (v=0, j=0) and OH (v=1, j=0) and the parameters used in the present study are listed in Table 5.4 and Table 5.5. From the grid parameters and the number of time steps for the propagation of the WP present in these two tables, it is easily understandable that the calculation are computationally very expensive like the dynamics study on the $1^4A''$ state mentioned previously. A comparison between the probabilities shown in panel (a) and (c) of Figure 5.8 reveals that the total reaction probability decreases with reagent vibrational excitation. Unlike the probabilities for OH (v=1, j=0) on the $1^4A''$ state, oscillations persist throughout the energy range on the $1^2A''$ state (cf. panel (a) of Figure 5.2 and panel (c) of Figure 5.8).

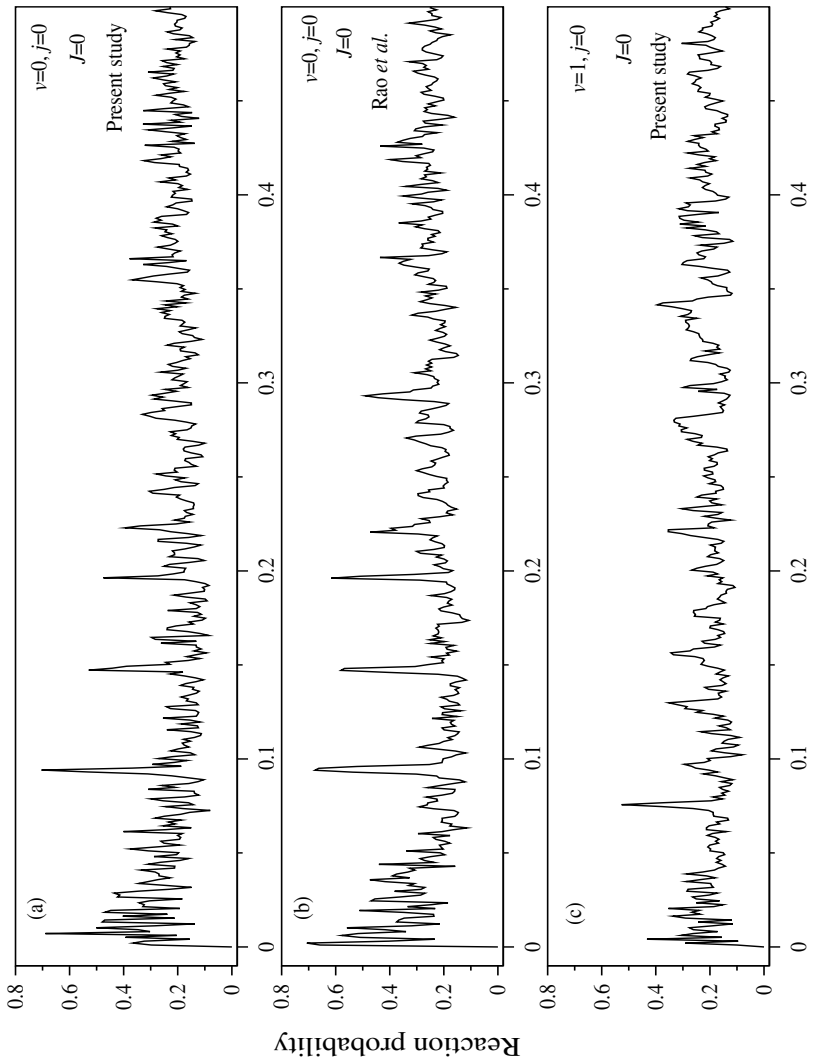

Figure 5.8: Total reaction probabilities of the, C + OH (v=0-1, j=0) → CO ($\sum v'$, $\sum j'$) + H reaction on the first excited ($1^2A''$) state of HCO reactive system as a function of collision energy. Probabilities calculated in the present study for OH (v=0) and OH (v=1) are shown in panel (a) and (c), respectively, whereas, those calculated by Rao *et al.* for OH (v=0, j=0) are reproduced form Ref. [5] and presented in panel (b).

Table 5.5: Details of grid parameters, properties of initial WP and the absorption function used to obtain the dynamics results for the, C + OH (v=1, j=0)→ CO + H, reaction on its first excited ($1^2A''$) state.

Parameter	Value	Description
$N_R/N_r/N_\gamma$	299/539/125	Number of grid points along the three product Jacobi coordinates, R_c, r_c and γ_c, respectively.
R_{min}/R_{max} (a_0)	0.1/28.0	Extension of the grid along R_c
r_{min}/r_{max} (a_0)	0.1/18.0	Extension of the grid along r_c
R_∞ (a_0)	18.00	Location of the dividing surface in the product channel
R_{abs}/r_{abs} (a_0)	19.5 /13.00	Starting point of the absorption function along R_c and r_c
C_{abs}/c_{abs}	0.5/0.5	Strength of absorption along R_c and r_c
R_0 (a_0)	10.5	Center of initial wave packet in reagent Jacobi coordinate
E_{trans} (eV)	0.145	Initial translational energy in eV
α	12.5	Width of initial wave packet
β_s	0.5	Smoothing of initial wave packet
nstep	180000	Number of iteration steps
nvab	8	Number of vibrational levels of product diatom

5.3.2.2 Product vibrational level resolved probabilities for OH (v=0-1, j=0) and for J=0

Product vibrational level resolved reaction probabilities for the C + OH (v=0, j=0) → CO (v', $\sum j'$) + H reaction on its $1^2A''$ state are presented in Figure 5.9. It can be seen from this figure that v'=0-2 levels mainly contribute to the total reaction probabilities for J=0. Moreover, an energy threshold starts to appear for v'=3 onwards. It is to be noted here that Rao made an attempt to calculate state-to-state dynamical attributes for this reaction on the $1^2A''$ state and preliminary results are reported in his Ph. D thesis [7]. But it was mentioned that the used parameters were not converged properly and hence no attempt is made here to compare present results with those given in Ref. [7]. On the other hand, Jorfi *et al.* [8] studied the state-to-state dynamics of the C + OH (v=0, j=0) reaction on the first excited state by employing a TIQM method . Reaction probabilities for CO (v'=3) is reproduced from Figure 2 of Ref. [8] and are compared with present results in panel (d) of Figure 5.9. A fair agreement is found here between the results of these two studies.

Product vibrational level resolved probabilities for OH (v=1, j=0) are presented in different panels of Figure 5.10. Quantum number of the vibrational level of product diatom is given in each panel. It can be seen from this figure that resonance oscillations are present for all v' and v'=0-5 contribute almost equally to the total reaction probabilities for J=0. This is in sharp contrast to those obtained for the C + OH reaction on its $1^4A''$ state. Vibrationally hot product diatoms are found to contribute more towards the total reaction probabilities on the first excited ($1^2A''$) state compared to that on the second excited ($1^4A''$) state [cf. Figures 5.3, 5.4, 5.9, and 5.10]. But like $1^4A''$ state, more product channels also open up with reagent vibrational excitation on the first excited ($1^2A''$) state

[cf. Figure 5.9 and Figure 5.10].

5.3.2.3 Product vibrational level distribution at five different collision energies

Product vibrational level distributions at five different collision energies (0.01 eV, 0.05 eV, 0.1 eV, 0.3 eV and 0.5 eV collision energies) are presented in panel (a) and (b) of Figure 5.11 for OH (v=0, j=0) and OH (v=1, j=0), respectively. From panel (a) it can be seen that except at 0.3 eV collision energy, the distributions are non-statistical. This is in contrast to those obtained on the second excited ($1^4A''$) state (cf. panel (a) of Figure 5.6). On the other hand, distributions are found to be inverted at all five collision energies considered here for OH (v=1, j=0) on the $1^2A''$ state (see panel (b) of Figure 5.11). On the contrary, from panel (b) of Figure 5.6 it can be seen that at 0.01 eV and 0.50 eV collision energies the distributions are inverted on the $1^4A''$ state. The difference in the product vibrational level distributions for J=0 reaction probabilities on the $1^2A''$ and $1^4A''$ states of HCO reactive system primarily suggests different mechanism for the C + OH reaction on these two states.

Finally, it is worthwhile to mention here that Jorfi *et al.* have also reported the product vibrational level distribution for the C + OH (v=0, j=0) reaction on the $1^2A''$ state (see Figure 4 of Ref. [8]). But the agreement with the present results (cf. panel (a) of Figure 5.11) is not as good as it is found for the $1^4A''$ state.

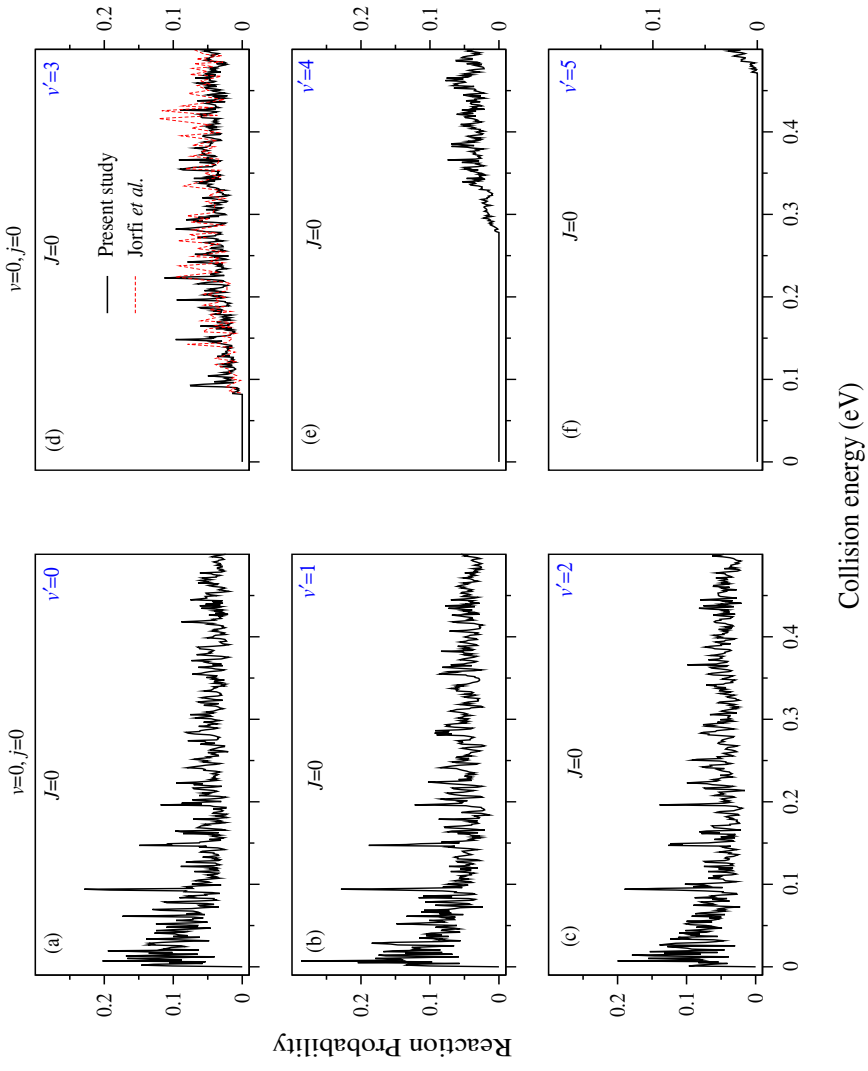

Figure 5.9: Product vibrational level resolved reaction probabilities of the, C + OH (v=0, j=0) → CO (v', $\sum j'$) + H, reaction on the $1^2A''$ state and for J=0 are shown as a function of collision energy. Quantum number for the vibrational level of the product diatom is shown in each panel. See text for further details.

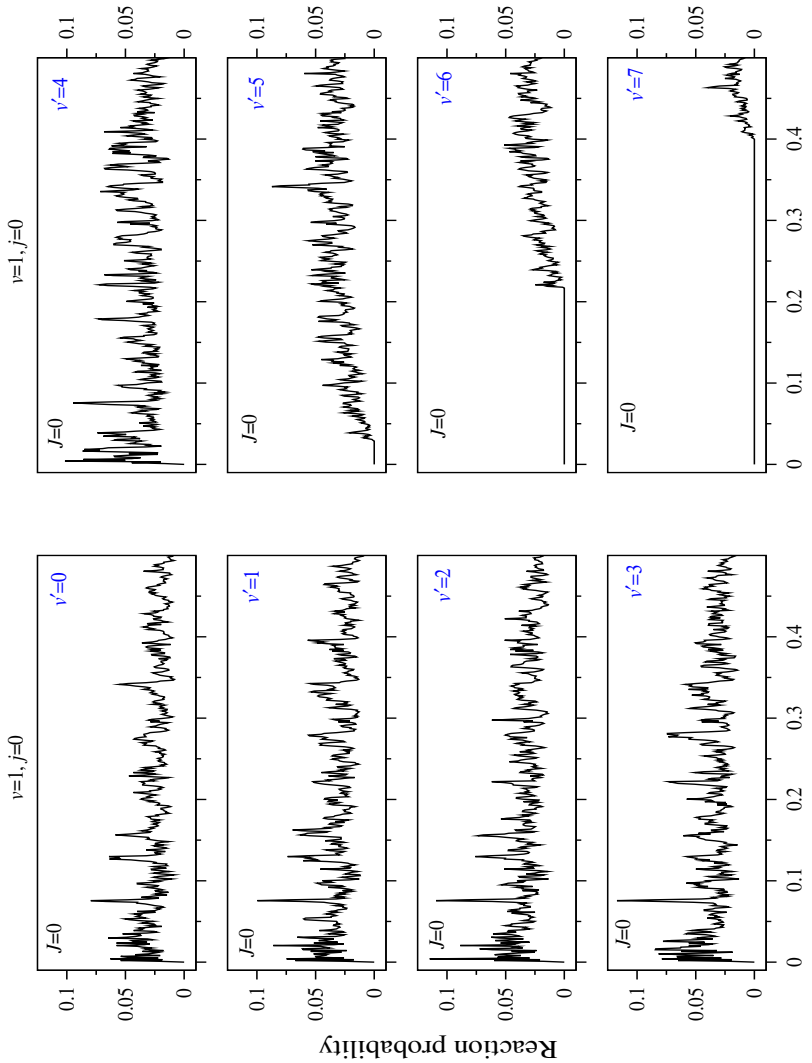

Figure 5.10: Same as Figure 5.9 but for reagent OH (v=1, j=0).

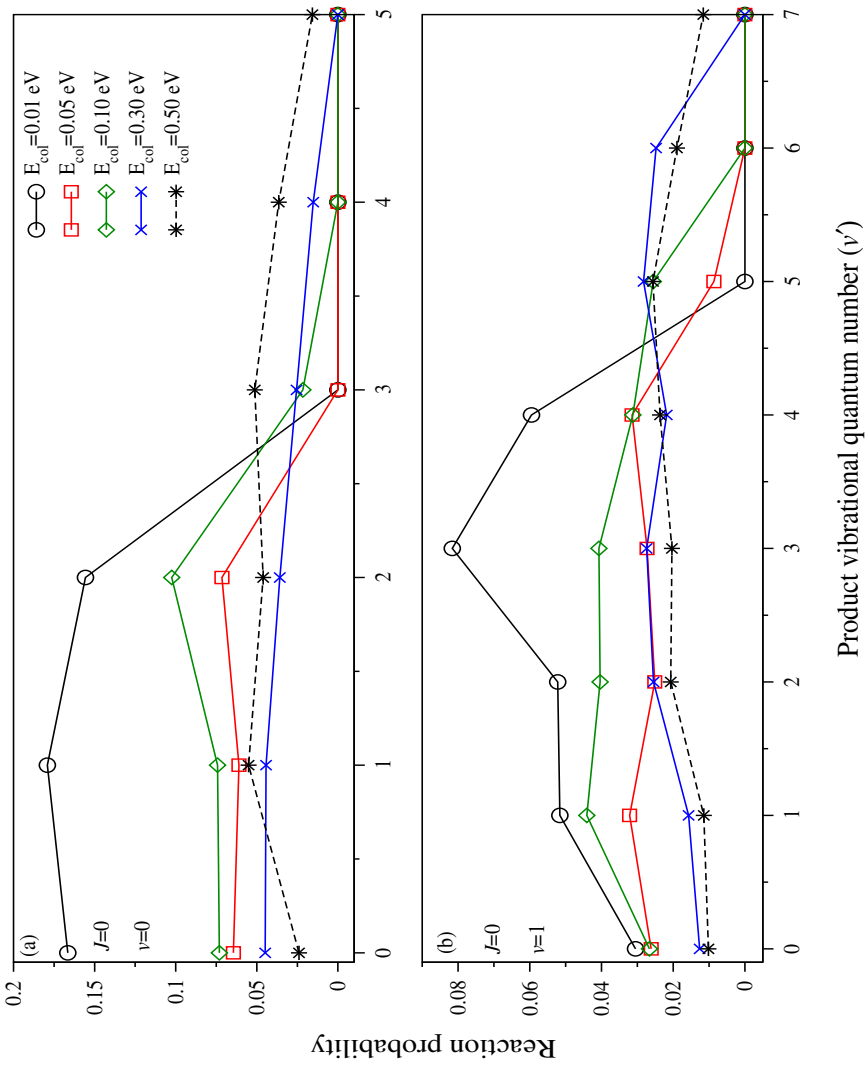

Figure 5.11: Product vibrational level distributions of the, C + OH (v=0-1, j=0) → CO + H, reaction on the first excited ($1^2A''$) state and for J=0 at 0.01 eV, 0.05 eV, 0.1 eV, 0.3 eV and 0.5 eV collision energies (E_{col}). Distributions for OH (v=0, j=0) and OH (v=1, j=0) are shown in different colours and line types in panel (a) and (b), respectively.

5.4 Summary

A preliminary theoretical account addressing the effects of reagent vibrational excitations on the state-to-state reaction probabilities and product vibrational level distributions for the total angular momentum quantum number, J=0 at five different collision energies is given in this chapter. Predominant inverted distribution is found on first excited ($1^2A''$) PES, whereas, it is obvious only for OH (v=2, j=0) on the second excited ($1^4A''$) PES. Furthermore, unlike $1^4A''$ PES, where only lower vibrational levels of product CO contribute noticeably, vibrationally hot product diatoms are found to contribute significantly to the total reaction probabilities on the $1^2A''$ PES. All these findings together suggest different mechanisms to govern the dynamics of the, C + OH $\rightarrow$ CO + H, reaction on the first ($1^2A''$) and second ($1^4A''$) excited states.

References

[1] A. Zanchet, B. Bussery-Honvault, M. Jorfi, and P. Honvault, Phys. Chem. Chem. Phys. **11**, 6182 (2009).

[2] S. Goswami, B. Bussery-Honvault, P. Honvault, and S. Mahapatra, Mol. Phys. (in press) DOI : 10.1080/00268976.2017.1296195

[3] A. Zanchet, T. González-Lezana, O. Roncero, M. Jorfi, P. Honvault, and M. Hankel, J. Chem. Phys. **136**, 164309 (2012).

[4] M. Jorfi and P. Honvault, J. Phys. Chem. A **115**, 8791 (2011).

[5] T. R. Rao, S. Goswami, S. Mahapatra, B. Bussery-Honvault, and P. Honvault, J. Chem. Phys. **138**, 094318 (2013).

[6] M. Hankel, G. G. Balint-Kurt, and S. K. Gray, Int. J. Quant. Chem. **92**, 205 (2003).

[7] T. R. Rao, *Reactive Chemical Dynamics : Born-Oppenheimer And Beyond* (Ph. D Thesis).

[8] M. Jorfi and P. Honvault, J. Phys. Chem. A **114**, 4742 (2010).

Chapter 6

The H + H_2 → H_2 + H reaction with vibrationally excited reagent H_2

6.1 Introduction

The effect of vibrational excitation of reagent H_2 on the state-to-state dynamics of the benchmark, H + H_2 → H_2 + H, reaction is presented in this chapter. The BKMP2 PES [1] describing the electronic ground state of H_3 reactive system is used in the present study. Total and product vibrational level resolved reaction probabilities as a function of collision energy, ICSs, product vibrational level distributions and DCSs as a function of scattering angle at few collision energies are calculated by using a TDQM method. In particular, the real wave packet methodology of Gray *et al.* [2] is employed here.

6.2 Theoretical and computational details

Product Jacobi coordinate based TDQM method to calculate state-to-state dynamical attributes is followed here and in this approach only the real part of the WP is propagated. The methodology is discussed in detail in section 2.3 and hence it is not reiterated here.

6.3 Results and discussions

6.3.1 Reaction probabilities

6.3.1.1 Total reaction probabilities for J=0

Energy resolved total reaction probabilities of the, H + H_2(v=0-5, j=0) $\rightarrow$ H_2($\sum v'$, $\sum j'$) + H, reaction for the total angular momentum quantum number, J=0, are plotted as a function of collision energy in Figure 6.1. Converged reaction probabilities are calculated upto 1.25 eV collision energy. Probabilities for reagent H_2 prepared in different vibrational levels (v) are shown in different colours in Figure 6.1. It can be seen from Figure 6.1 that with reagent vibrational excitations, the onset of the reaction shifts towards lower collision energies. Finally, the reaction becomes barrierless when the regent diatom is excited to its 5^{th} and 6^{th} (v=4 and 5, respectively) vibrational levels. Hence, a reaction with a classical barrier of $\sim$0.42 eV [3] becomes barrierless upon excitation of the reagent diatom to its higher vibrational levels. Furthermore, it can be seen from Figure 6.1 that except for a few energies, vibrational excitation enhances the reactivity and dense resonance structure appears at low collision energies for v=3, 4 and 5.

It is worthwhile to mention here that numerous test calculations are carried out to achieve good convergence of probabilities for J=0 and for every vibrational

level of reagent H_2. The converged parameters obtained for J=0 are used in all remaining calculations for J >0. Converged parameters for reagent H_2 prepared at v=0, 4 and 5 levels are given in Table 6.1, Table 6.2 and Table 6.3, respectively. It can be seen form these tables that the number of grid points along R_c, r_c and γ_c and the propagation time increase with reagent vibrational excitations. Therefore, calculations become computationally very expensive for vibrationally hot reagent H_2. It is to be noted here adequate number of rotational levels of product diatom are considered in each calculation to account for all possible product channels. Furthermore, the reagent diatom is kept in its ground rotational level in the present study.

6.3.1.2 Product vibrational level resolved reaction probabilities for J=0

Product vibrational level resolved reaction probabilities for the, H + H_2(v=0-5, j=0) $\rightarrow$ H_2(v', $\sum j'$) + H, reaction are presented in panel (a)-(f) of Figure 6.2 as a function of collision energy. Vibrational quantum number, v of reagent H_2 is shown in each panel and the probabilities for different v' are shown in different colours and line types. From different panels of Figure 6.2 it can be seen that more vibrational levels of product diatom are populated with reagent vibrational excitation. This can be attributed to the enhancement of the total reaction probabilities with reagent vibrational excitation (cf. Figure 6.1). Hence, the additional energy supplied to the vibrational degrees of freedom of the reagent is utilized by the reactive system to open up more product channels. From panel (e) and (f) of Figure 6.2 it can be seen that the H-exchange reaction becomes barrierless (it is also seen in Figure 6.1) but obvious threshold is present for the formation of the product at higher vibrational levels. Moreover, dense resonance

oscillations are found (cf. panel (d), (e) and (f)) at low collision energies and for low v' values. The most interesting observation that can be made form Figure 6.2 that except at high collision energies for reagent H_2 (v=5), the formation of the product diatom at the same vibrational level as of reagent is most probable. It will be very interesting to see whether the same trend is followed in product vibrational level resolved ICSs as contributions from total angular momentum quantum number J >0 will also be present there.

6.3.1.3 Total reaction probabilities for J >0

Energy resolved total reaction probabilities for $J > 0$ are also calculated by including Coriolis coupling in the present study. Total reaction probabilities for few J values and for reagent H_2(v=0-5, j=0) are presented in panel (a)-(f) of Figure 6.3. The vibrational quantum number of reagent H_2 and the value of every J are given in each panel of Figure 6.3. Probabilities for J=15 and for H_2(v=0, j=0) are in excellent agreement with those obtained by Zhao *et al.* (cf. Figure 1 of Ref. [4] and panel (a) of Figure 6.3). The onset of the reaction shifts towards higher collision energies with the increase of J due to the increase of the height of teh centrifugal barrier. Moreover, it is found from Figure 6.3 that the energy supplied to the vibrational degrees of freedom of the reagent diatom helps the system to overcome the centrifugal barrier and consequently substantial reaction occurs at higher J values also.

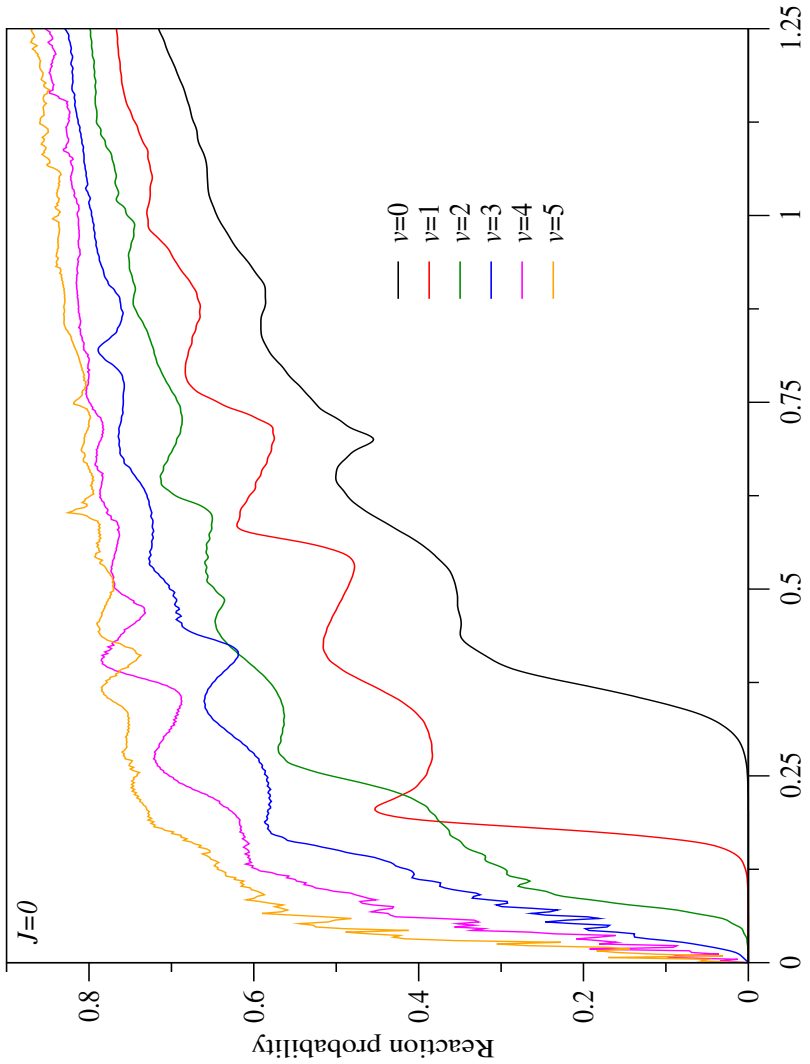

Figure 6.1: Energy resolved total reaction probabilities of the, H + H_2(v=0-5, j=0) → H_2 ($\sum v'$, $\sum j'$) + H, reaction for J=0 on the electronic ground BKMP2 [1] PES as a function of collision energy.

Table 6.1: Details of grids, initial WP parameters and the absorption function used in the dynamics calculations of the, H + $H_2(v = 0, j = 0) \rightarrow H_2$ + H, reaction.

Parameter	Value	Description
$N_R/N_r/N_\gamma$	143/139/60	Number of grid points along the three product Jacobi coordinates, R_c, r_c and γ_c, respectively.
R_{min}/R_{max} (a_0)	0.2/15.0	Extension of the grid along R_c
r_{min}/r_{max} (a_0)	0.5/14.5	Extension of the grid along r_c
R_d (a_0)	8.00	Location of the dividing surface in the product channel
R_{abs}/r_{abs} (a_0)	8.50 /8.00	Starting point of the absorption along R_c and r_c
C_{abs}/c_{abs}	20.00/20.00	Strength of absorption along R_c and r_c
R_0 (a_0)	7.0	Center of initial wave packet in reactant Jacobi coordinate
E_{trans} (eV)	0.7	Initial translational energy in eV
α	8.00	Width of initial wave packet
β_s	0.5	Smoothing of initial wave packet
nstep	3000	Number of iteration steps
nvab	3	number of vibrational levels of product diatom

Table 6.2: Same as in Figure 6.1, for the, H + $H_2(v = 4, j = 0) \rightarrow H_2$ + H, reaction.

Parameter	Value	Description
$N_R/N_r/N_\gamma$	263/179/130	Number of grid points along the three product Jacobi coordinates, R_c, r_c and γ_c, respectively.
R_{min}/R_{max} (a_0)	0.2/30.0	Extension of the grid along R_c
r_{min}/r_{max} (a_0)	0.5/30.0	Extension of the grid along r_c
R_d (a_0)	12.00	Location of the dividing surface in the product channel
R_{abs}/r_{abs} (a_0)	12.50 /11.50	Starting point of the absorption along R_c and r_c
C_{abs}/c_{abs}	20.00/12.00	Strength of absorption along R_c and r_c
R_0 (a_0)	10.0	Center of initial wave packet in reactant Jacobi coordinate
E_{trans} (eV)	0.7	Initial translational energy in eV
α	12.00	Width of initial wave packet
β_s	0.5	Smoothing of initial wave packet
nstep	16000	Number of iteration steps
nvab	8	number of vibrational levels of product diatom

Table 6.3: Same as in Figure 6.1, for the, H + $H_2(v = 5, j = 0) \rightarrow H_2$ + H, reaction.

Parameter	Value	Description
$N_R/N_r/N_\gamma$	263/219/145	Number of grid points along the three product Jacobi coordinates, R_c, r_c and γ_c, respectively.
R_{min}/R_{max} (a_0)	0.2/35.0	Extension of the grid along R_c
r_{min}/r_{max} (a_0)	0.5/35.0	Extension of the grid along r_c
R_d (a_0)	12.00	Location of the dividing surface in the product channel
R_{abs}/r_{abs} (a_0)	13.50 /11.00	Starting point of the absorption along R_c and r_c
C_{abs}/c_{abs}	20.00/20.00	Strength of absorption along R_c and r_c
R_0 (a_0)	9.5	Center of initial wave packet in reactant Jacobi coordinate
E_{trans} (eV)	0.7	Initial translational energy in eV
α	12.00	Width of initial wave packet
β_s	0.5	Smoothing of initial wave packet
nstep	18000	Number of iteration steps
nvab	9	number of vibrational levels of product diatom

6.3.2 Opacity functions

Opacity functions, $(2J + 1)P_J(E)$, as a function of the total angular momentum quantum number, J at a fixed collision energy are shown in panel (a)-(f) of Figure 6.4. The opacity functions are calculated at 1.25 eV collision energy for reagent H_2 (v=0-4), whereas, for reagent H_2 (v=5, j=0), it is calculated at 0.25 eV. It can be seen from each panel of Figure 6.4 that the opacity function increases monotonically with the increase of J from a value close to 0 and reaches to a maximum at an intermediate value of J before falling down to zero at higher J values. It is revealed by these opacity functions that calculation of energy resolved $\boldsymbol{S}$-matrix elements upto J=29, 35, 40, 45 and 49 are enough to achieve converged cross sections upto 1.25 eV collision energy for v=0-4 levels of reagent H_2. Whereas, contribution of the total angular momentum upto J=26 is adequate

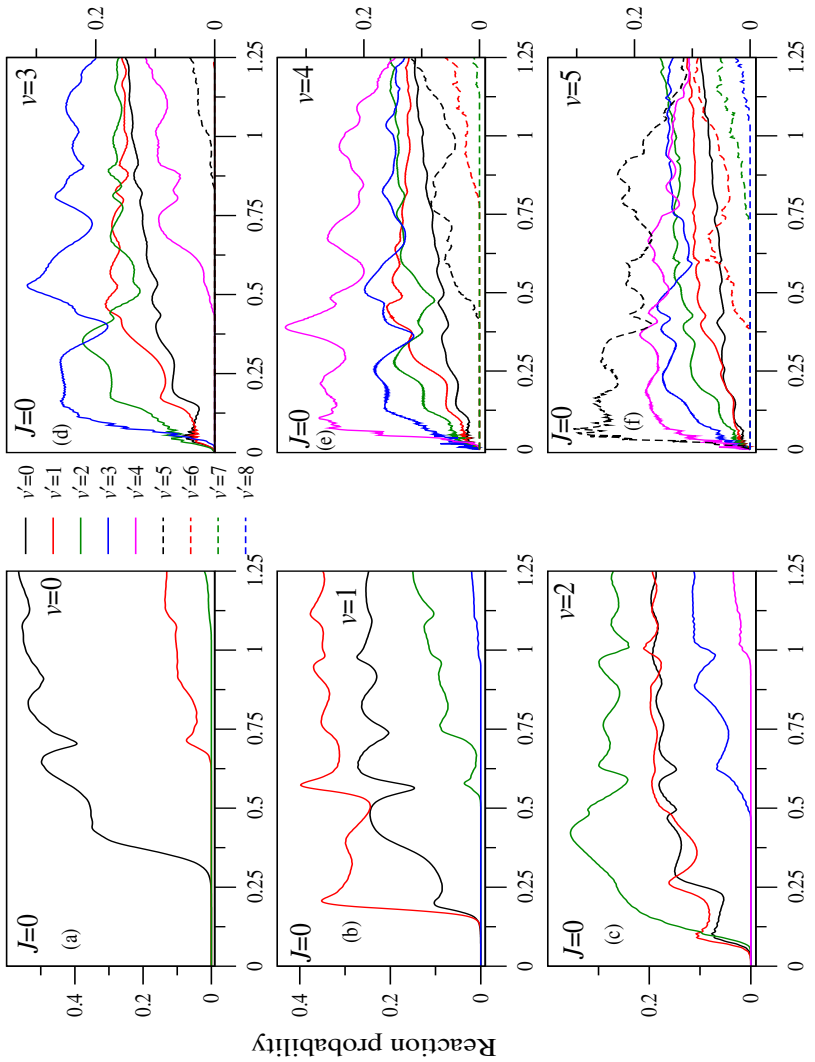

Figure 6.2: Product vibrational level resolved reaction probabilities for the, H + H_2(v=0-5, j=0) → H_2 (v', $\sum j'$) + H, reaction and for J=0 as a function of collision energy. See text for details.

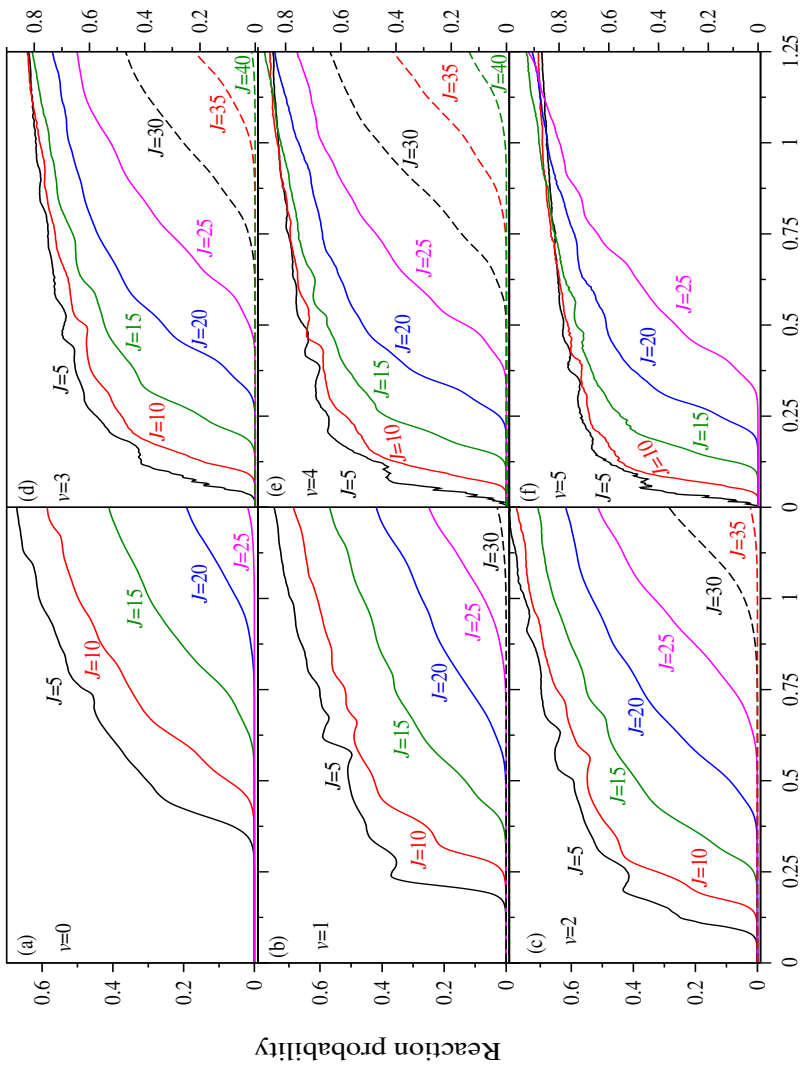

Figure 6.3: Same as Figure 6.1, but for $J > 0$.

to calculate converged cross section upto 0.25 eV collision energy for reagent H_2 (v=5, j=0)(see panel (f) of Figure 6.4).

6.3.3 Integral reaction cross sections

6.3.3.1 Total integral reaction cross sections

Total ICSs of the, H + H_2 (v=0-4, j=0)→ $H_2(\sum v', \sum j')$ + H, reaction on its electronic ground state are shown in Figure 6.5 as a function of collision energy in different colours. It can be seen from this figure that similar to total reaction probabilities (cf. Figure 6.1), reactivity is enhanced with reagent vibrational excitations and the reaction with a threshold for H_2(v=0, j=0) becomes barrierless for H_2(v=4, j=0). Moreover, it can be seen here that from the onset of the reaction, the ICSs rise smoothly with the increase of collision energy for H_2(v=0-3, j=0). Similar behavior of ICSs is also found earlier for H_2(v=0-2, j=0) by Barg *et al.* [5]. In the latter study, QCT method and the LSTH PES [6, 7] are employed. On the contrary, the variation of total ICSs for H_2(v=4, j=0) is somewhat different from the others (cf. Figure 6.5). The latter rises sharply at low collision energies with dense resonance structures followed by a smooth variation with the increase of collision energy. Thus, the resonance structures found in the total reaction probabilities for J=0 (see Figure 6.1) survive for H_2 (v=4, j=0) but washed out for H_2(v=3, j=0). It is worthwhile to mention here that the pattern and the magnitude of the total ICSs for H_2(v=0-1, j=0) are in good agreement with those calculated by Jiang *et al.* (cf. Figure 2 of Ref. [8]). In the latter study of Jiang *et al.*, the excitation functions are presented as a function of total energy.

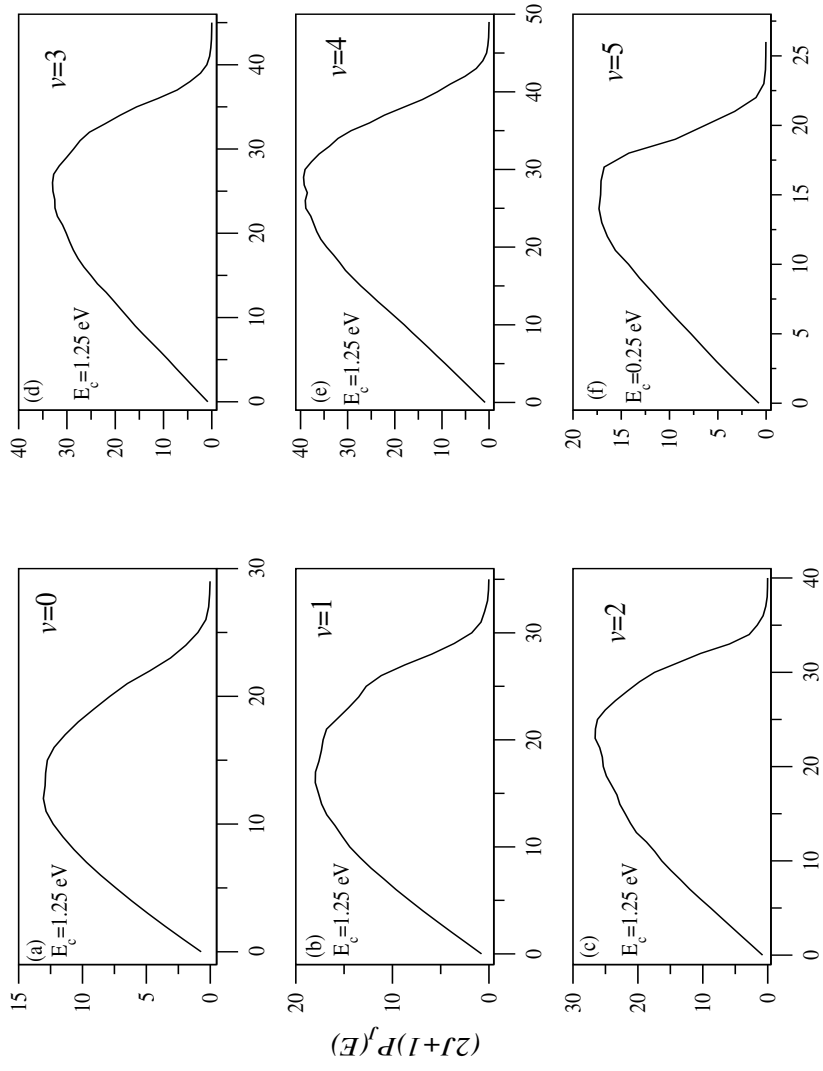

Figure 6.4: Opacity functions, $(2J+1)P_J(E)$ are shown at 1.25 eV collision energy for reagent H_2(v=0-4, j=0) and at 0.25 eV for reagent H_2 (v=5, j=0). Vibrational quantum number of reagent H_2 is shown in each panel.

6.3.3.2 Product vibrational level resolved integral reaction cross sections

Product vibrational level resolved ICSs for the H + H_2(v=0-5, j=0) $\rightarrow$ H_2(v', $\sum j'$) reaction are shown in panel (a)-(f) of Figure 6.6 in different colour lines as a function of collision energy. In particular, ICSs for reagent H_2(v=0-4, j=0) are shown upto 1.25 eV collision energy [see panel (a)-(e)], whereas, for reagent H_2 (v=5, j=0) are shown upto 0.25 eV [cf. panel (f)]. It can be seen from Figure 6.6 that resonance oscillations are present at low collision energies for reagent H_2(v=4-5, j=0). Such oscillations are not found in the product vibrational level resolved ICSs when the reagent diatom is prepared at lower vibrational levels, v=0-3. Furthermore, the preference for the formation of the product diatom at the same vibrational level of the reagent diatom found in Figure 6.2 is not followed here in the state-to-state ICSs (cf. Figure 6.6) except for reagent H_2 (v=0, j=0).

6.3.3.3 Product vibrational level distributions at different collision energies

Product diatom vibrational level distributions of the, H + $H_2(v = 1-4, j = 0) \rightarrow$ $H_2(v^{'}, \Sigma j^{'})$ + H, reaction at five different collision energies, 0.25 eV, 0.50 eV, 0.75 eV, 1.00 eV and 1.25 eV are shown in panel (a)-(t) of FIG. 6.7. It can be seen from FIG. 6.7 that with an increase of collision energy, the maximum of the distribution shifts towards lower vibrational quantum number, $v^{'}$, irrespective of the vibrational level of reagent H_2. Specifically, for $H_2(v = 1, j = 0)$, the distribution becomes completely statistical at 1.00 eV and 1.25 eV collision energy. On the other hand, at a fixed collision energy, distribution becomes wider and the maximum shifts towards higher vibrational levels with vibrational excitation of reagent H_2. For example, from panel (e) and (t) of FIG. 6.7 it can be seen that a

statistical distribution for $H_2(v = 1, j = 0)$ gets inverted showing the maximum at v'=2 for $H_2(v = 4, j = 0)$ at 1.25 eV collision energy. Hence, the two kinds of energies, the collision energy and the energy supplied to the vibrational degrees of freedom of reagent diatom affect product vibrational level distribution in opposite ways.

6.3.4 Differential cross sections

6.3.4.1 Total differential cross sections

The effects of vibrationally hot reagent H_2 and collision energy on the total DCSs are shown in panel (a)-(j) of Figure 6.8 at five different collision energies (0.25 eV, 0.50 eV, 0.75 eV, 1.00 eV and 1.25 eV). In particular, the effect of collision energy on the DCSs for reagent H_2(v=0-4, j=0) are shown in panel (a)-(e). It can be seen from panel (a)-(e) that forward scattering increases with an increase of collision energy. On the other hand, the effects of reagent vibrational excitation on the total DCSs are shown in panel (f)-(j), shows forward scattering is preferred with reagent vibrational excitations at each collision energy. Hence, unlike product vibrational level distribution shown in Figure 6.7, the two different kinds of energy available to the reagent system affect total DCSs in the same way.

6.3.4.2 State-to-state differential cross sections

The effect of reagent vibrational excitations on the state-to-state DCSs of the, H + H_2(v=0-4, j=0) $\rightarrow$ H_2(v'=0, j'=0-6) + H, reaction at 1.25 eV collision energy is shown in Figure 6.9. From the panels of the first column of Figure 6.9 it can be seen that forward scattering decreases for rotationally hot product diatom and sideways scattering seems to be preferred for the reagent H_2(v=0, j=0). In

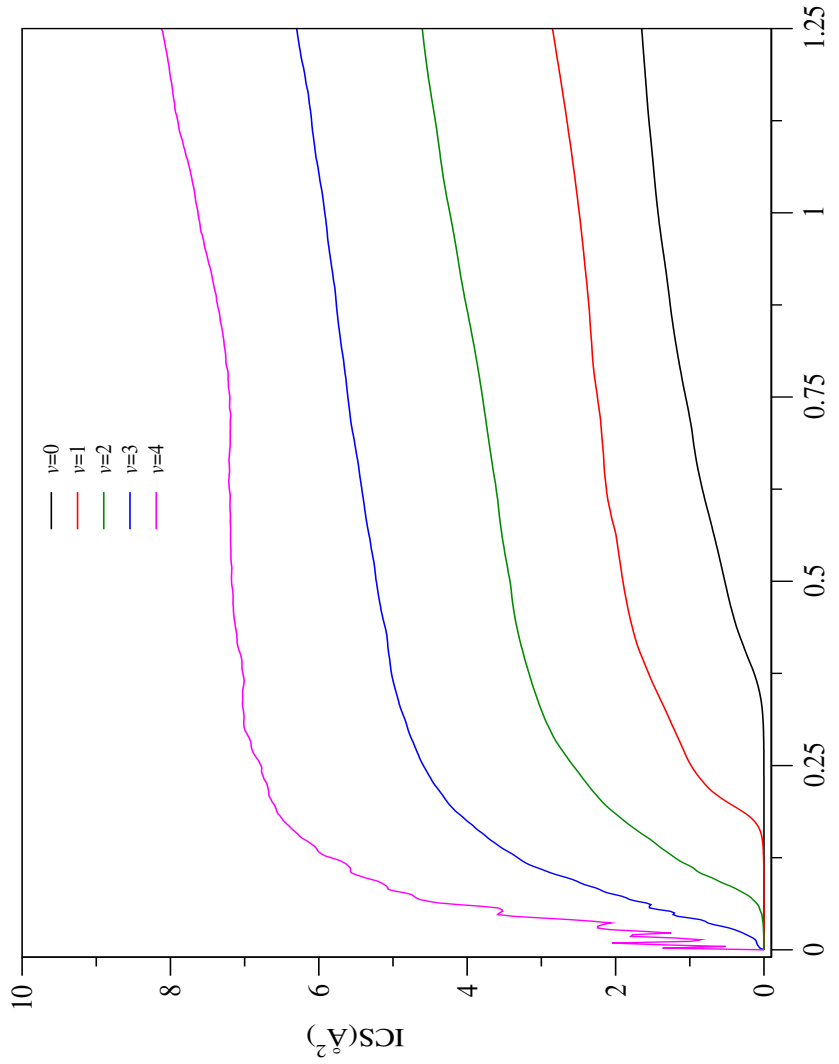

Figure 6.5: Energy resolved total integral reaction cross sections of the, H + H_2(v=0-4, j=0) → H_2 ($\sum v'$, $\sum j'$) + H, reaction as a function of collision energy. See text for details.

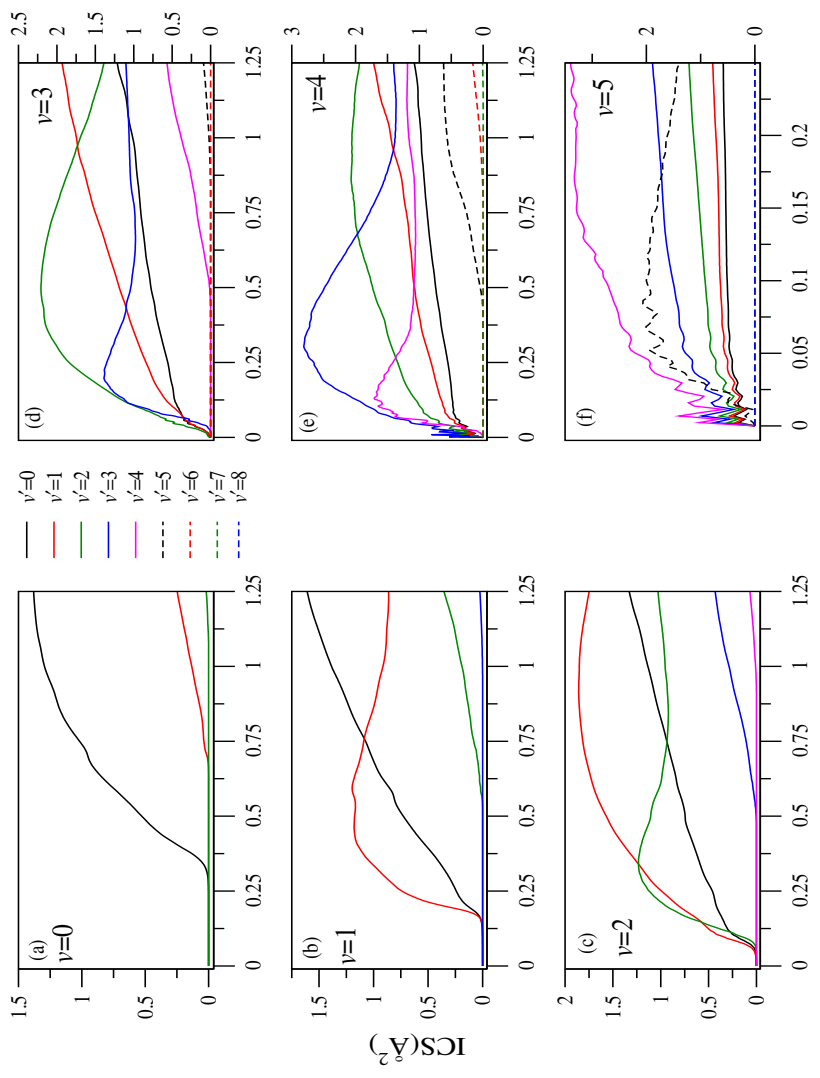

Figure 6.6: Product vibrational level resolved ICSs of the, H + H_2(v=0-5, j=0) → H_2 (v', $\sum j'$) + H, reaction as a function of collision energy. Quantum number for the vibrational level of reagent diatom is given in each panel.

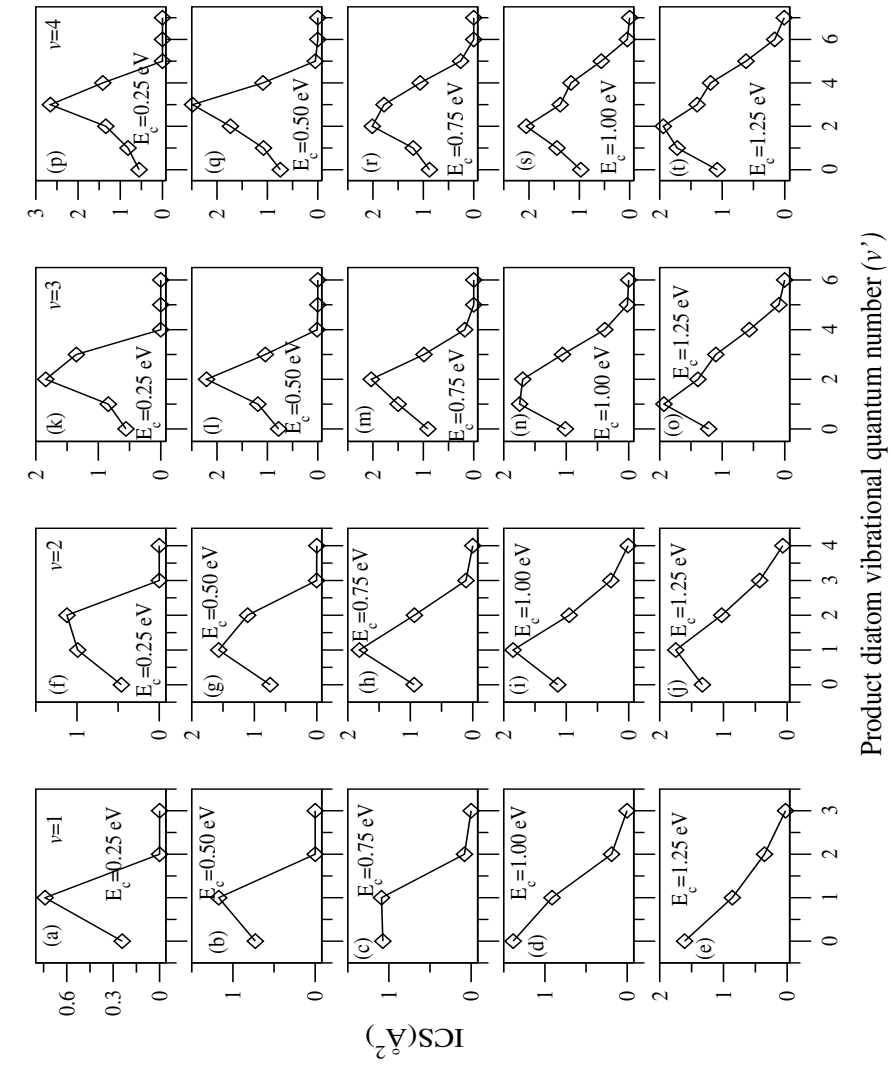

Figure 6.7: Product diatom vibrational level distributions of the, H + $H_2(v = 1-4, j = 0) \rightarrow H_2(v^{'}, \sum j^{'})$ + H, reaction at five different collision energies. Collision energy is expressed as E_c and it is mentioned in each panel.

contrary, the forward scattering occurs for j'=0-6 for reagent H_2(v=3-4, j=0) (cf. see the panels of the last two columns of Figure 6.9). Thus, it can be inferred that the reaction dynamics follows different mechanistic path depending on the vibrational level of reagent H_2.

The DCSs for the, H + H_2(v=2-4, j=0) → H_2(v'=1, j'=0-6) + H, reaction at 1.25 eV collision energy is presented in Figure 6.10 as a function of the scattering angle, θ. Whereas, DCSs for product H_2(v'=4, j'=0-5) are presented in Figure 6.11. From panel (a)-(f) of Figure 6.10 and Figure 6.11, it can be seen that the pattern of the DCSs of product H_2 (v'=1, j'=0-5) and H_2 (v'=4, j'=0-5) does not change significantly for the reagent H_2(v=2, j=0). Similar observations are made for reagent H_2(v=3-4, j=0) (cf. panels in second and third columns of Figures 6.10 and Figure 6.11, respectively.). Hence, unlike the observations of Jankunas *et al.* [3] for the H + D_2(v=0) reaction, the mechanism for the formation of product H_2(v'=1 and 4) at 1.25 eV collision energy remains similar for the H + H_2(v=2-4, j=0) reaction for j'=0-5 of product H_2. Furthermore, sharp resonance oscillations are found in case of forward scattering only (cf. Figure 6.10 and Figure 6.11).

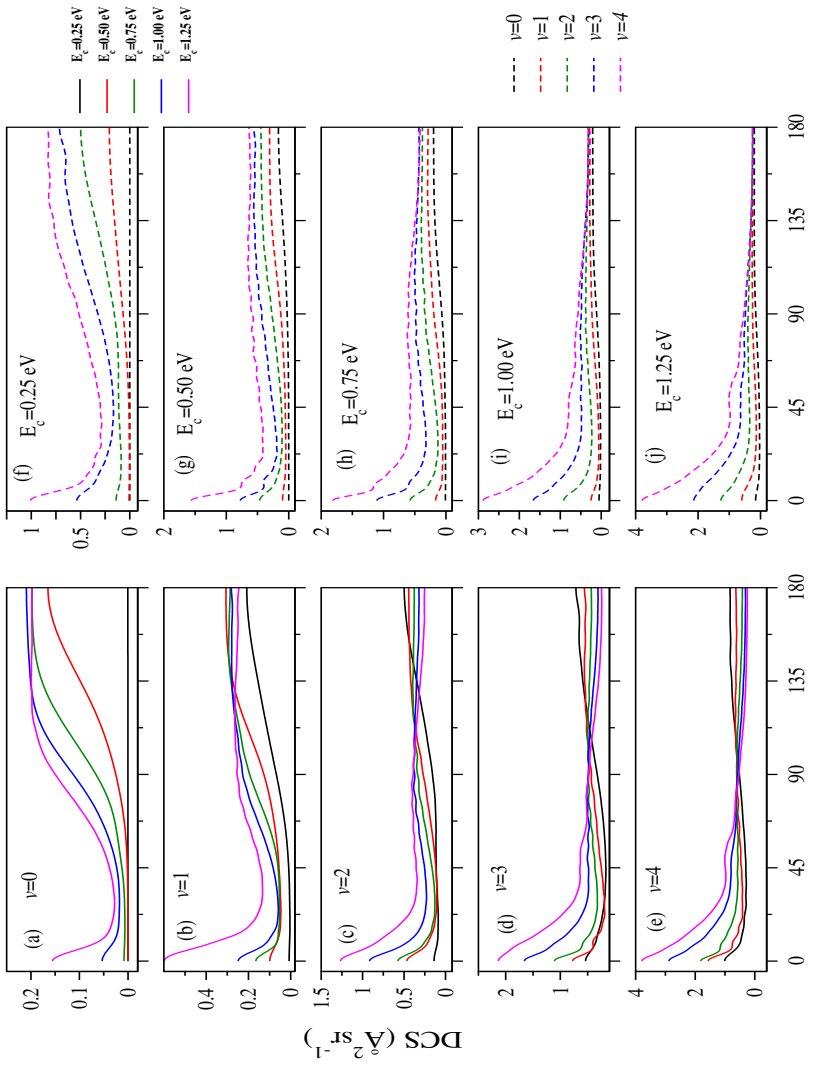

Figure 6.8: Total differential cross sections of the, H + H_2 (v=0-4, j=0) → H_2 + H, reaction at five different collision energies as a function of the scattering angle, θ.

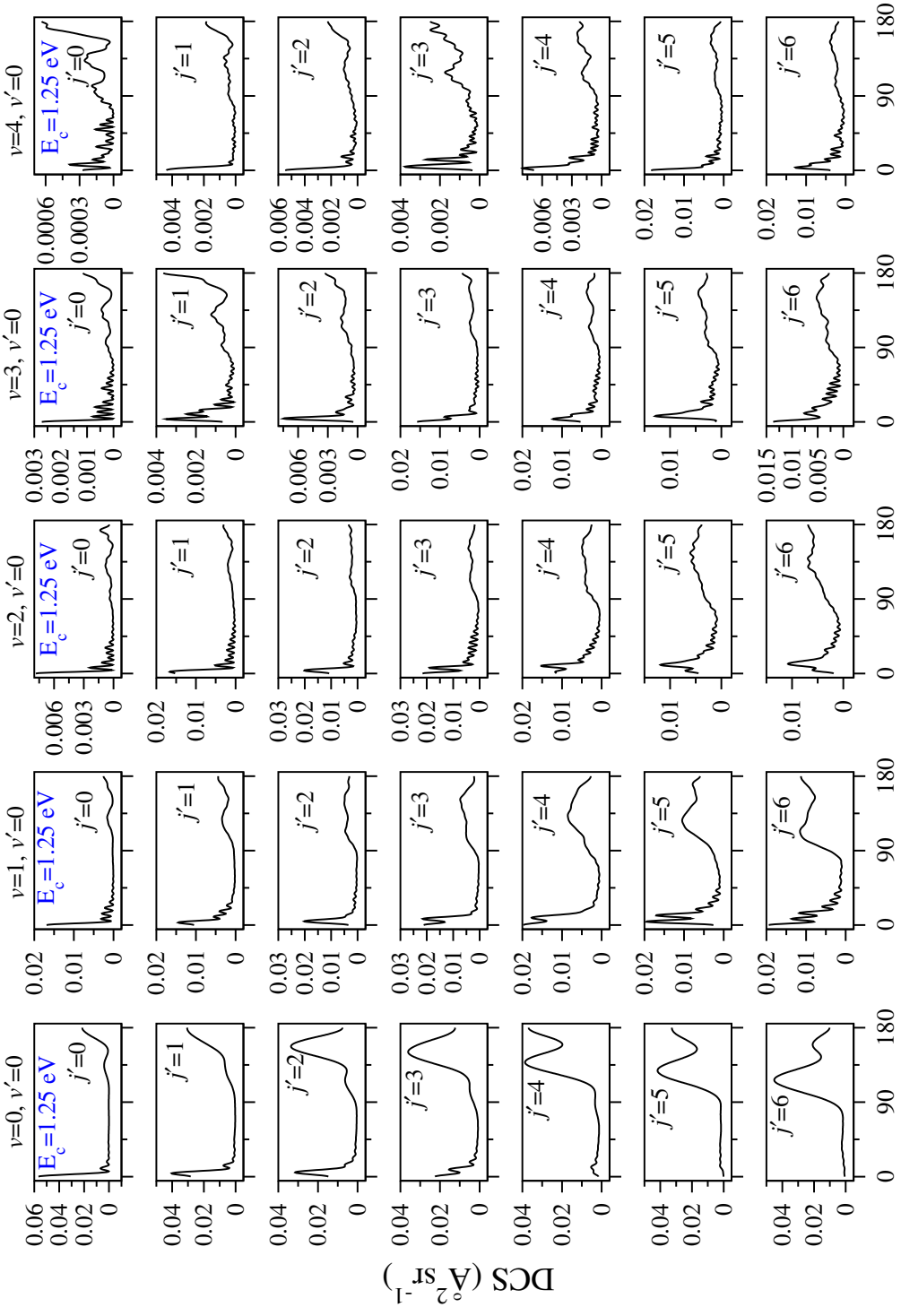

Figure 6.9: State-to-state DCSs for the H + $H_2(v{=}0\text{-}4,\ j{=}0) \rightarrow H_2(v'{=}0,\ j'{=}0\text{-}6)$ + H reaction at 1.25 eV collision energy.

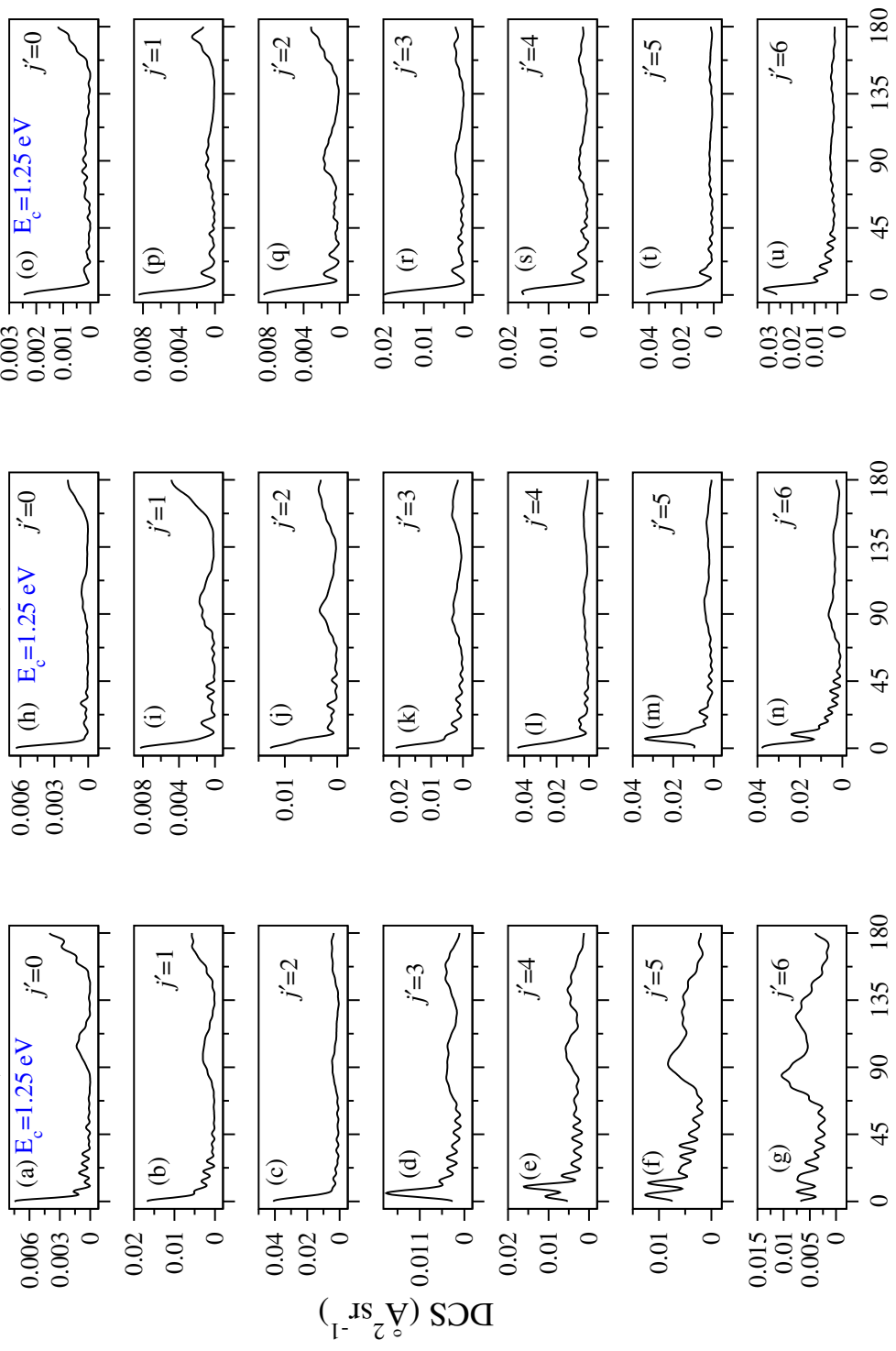

Figure 6.10: State-to-state DCSs for the H + $H_2(v=2\text{-}4,\ j=0) \rightarrow H_2(v'=1,\ j'=0\text{-}6)$ + H reaction at 1.25 eV collision energy.

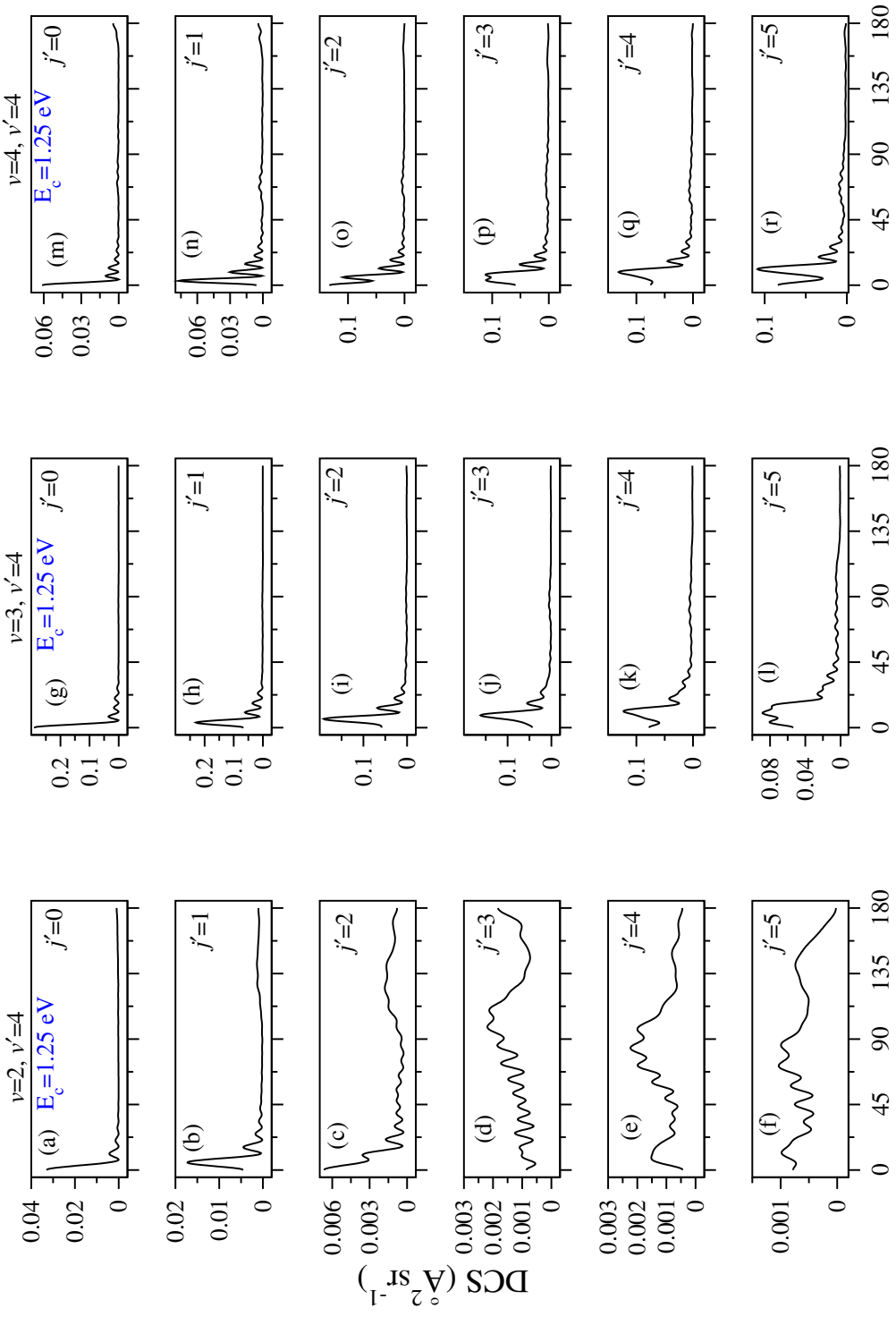

Figure 6.11: Same as Figure 6.10 but for product $H_2(v'=4, j'=0\text{-}5)$

6.4 Summary

A comprehensive account of the effects of reagent vibrational excitations on the dynamics of the benchmark, $H + H_2 \rightarrow H_2 + H$, reaction on its electronic ground BKMP2 [1] PES is carried out by employing a TDQM method (see section 2.3). State-selected and state-to-state dynamical attributes are calculated for reagent $H_2(v{=}0\text{-}5,\ j{=}0)$. Reactivity increases with reagent vibrational excitation. The collision energy and the internal energy of the reagent diatom through its vibrational excitation affect the product vibrational level distribution in a reverse way, *i. e.* the maximum of the distribution shifts towards lower vibrational quantum number with an increase of collision energy and the maximum shifts towards higher vibrational level with reagent vibrational excitation. Whereas, these two types of energy affect the total DCSs similarly. Forward scattering increases with reagent vibrational excitations and with the increase of collision energy. Different mechanisms govern the dynamics when the reagent H_2 is prepared in different vibrational levels.

References

[1] A. I. Boothroyd, W. J. Keogh, P. G. Martin, and M. R. Peterson, J. Phys. Chem. **104**, 7139 (1996).

[2] S. K. Gray and G. G. Balint-Kurti, J. Chem. Phys. **108**, 950 (1998).

[3] J. Jankunas, M. Sneha, R. N. Zare, F. Bouakline, S. C. Althorpe, D. Herráze-Aguilar, an d F. J. Aoiz, PNAS **111**, 15 (2014).

[4] B. Zhao, D.-H. Zhang, S-Y. Lee, and Z. Sun, J. Chem. Phys. **140**, 164108 (2014).

[5] G.-D. Barg, H. R. Mayne, and J. P. Toennies, J. Chem. Phys. **74**, 1017 (1981).

[6] D. G. Trauhler and C. J. Horowitz, J. Chem. Phys. **68**, 2466 (1978).

[7] D. G. Trauhler and C. J. Horowitz, J. Chem. Phys. **71**, 1514 (1979).

[8] B. Jiang, and H. Guo, J. Chem. Phys. **138**, 234104 (2013).

Chapter 7

Summary and outlook

A study of quantum reactive scattering dynamics is undertaken in this thesis. The investigations are carried out by time-dependent wave packet propagation approaches using the state-of-the-art electronic potential energy surfaces available in the literature. The results are compared with experiment whatever available in the literature. The findings on the dynamics of the, S + OH $\rightarrow$ SO + H, reaction on its electronic ground ($\tilde{X}^2A''$) state [1], C + OH $\rightarrow$ CO + H reaction, on its first ($1^2A''$) and second ($1^4A''$) states [2], and H + H_2 $\rightarrow$ H_2 + H, reaction on its electronic ground state [3] are presented and discussed. The dynamics of the S + OH reaction is studied at the initial state-selected level, whereas, state-to-state investigation is done for the C + OH and H + H_2 reactions. Grid based time-dependent quantum mechanical techniques are employed in these studies. Energy resolved reaction probabilities, integral reaction cross sections, differential cross sections, product vibrational level distributions and state-specific thermal rate constants are calculated. The effect of internal excitations of reagent diatom on the dynamical attributes of these reactive systems is also examined.

Dense resonance oscillations are found in the total reaction probabilities for

J=0 for the, S + OH reaction on its electronic ground state, and C + OH reaction on the excited states. This is attributed to the formation of intermediate collision complexes inside the wells present on the underlying PESs. These resonances become broader and diffuse with reagent vibrational excitation. Rotational excitations of the reagent diatom decrease the reactivity of the, S + OH, reaction, whereas, reactivity increases with reagent vibrational excitation. On the other hand, the effect of rotationally hot reagent on the ICSs of the, C + OH, reaction on its second excited ($1^4A''$) state depends on the collision energy and except at very low collision energies for reagent OH (v=2, j=0), ICSs increase with reagent vibrational excitations.

Product vibrational level distributions at some selected collision energies are found to be different for the, C + OH, reaction on the first ($1^2A''$) and second ($1^4A''$) excited states. Predominant inverted distribution is found for reagent OH (v=0-1, j=0) on the first excited state. On the contrary, predominant non statistical distribution is found only for reagent OH (v=2, j=0) on the second excited state of HCO reactive system. Moreover, it is found that only lower vibrational levels of the product diatom mainly contribute to the total reaction probabilities for J=0 on the $1^4A''$ PES. Whereas, vibrationally hot product CO also contribute noticeably on the first excited ($1^2A''$) PES. These observations primarily suggest different mechanisms for the, C + OH $\rightarrow$ CO + H, reaction on the first ($1^2A''$) and second excited ($1^4A^{''}$) states of HCO reactive system.

The reactivity of the H + H_2 $\rightarrow$ H_2 + H reaction on the electronic ground state also increases with vibrational excitation of reagent H_2. The H-exchange reaction with a barrier of $\sim$0.42 eV becomes barrierless for the reagent H_2 excited to higher vibrational levels. The collision energy and the vibrational energy of reagent H_2 affect the product vibrational level distribution in an opposite way.

Forward scattering becomes more prominent with reagent vibrational excitations and with the increase of collision energy. From the pattern of the DCSs shown in this thesis it can be realized that different mechanisms govern the dynamics when the reagent H_2 is prepared in different vibrational levels.

The observations reported in this thesis raised some interesting points which can be studied in the future. Investigation of the state-to-state dynamics of the, S + OH $\rightarrow$ SO + H, reaction on the electronic ground state of HSO reactive system is required to reveal the mechanistic details of this reaction rigorously. On the other hand, the effect of internal excitations of the reagent diatom on the state-to-state ICSs and DCSs of the, C + OH $\rightarrow$ CO + H, reaction on its first ($1^2A''$) and second ($1^4A''$) excited states can reveal the mechanistic details more precisely in relation to the topographical features of the underlying PESs. Finally, we hope that the effect of reagent rotational excitation with the inclusion of non adiabatic coupling on the state-to-state dynamics of the benchmark H-exchange reaction will be more interesting. It is worthwhile to mention here that the effect of non adiabatic coupling on the state-to-state reaction dynamics of the latter reaction in presently underway. As the preliminary results are not convincing enough, they are not presented in the thesis.

References

[1] E. Martínez-Nunez and A. J. C. Varandas, J. Phys. Chem. A **105**, 5923 (2001).

[2] A. Zanchet, B. Bussery-Honvault, M. Jorfi, and P. Honvault, Phys. Chem. Chem. Phys. **11**, 6182 (2009).

[3] A. I. Boothroyd, W. J. Keogh, P. G. Martin, and M. R. Peterson, J. Phys. Chem. **104**, (7139) (1996).

Publications:

1. T. Rajagopala Rao, **Sugata Goswami**, S. Mahapatra, B. Bussery-Honvault, and P. Honvault, "*Time-dependent quantum wave packet dynamics of the C + OH reaction on the excited electronic state*". J. Chem. Phys. **138**, 094318 (2013).

2. **Sugata Goswami**, T. Rajagopala Rao, S. Mahapatra, B. Bussery-Honvault, and P. Honvault, "*Time-dependent quantum wave packet dynamics of S + OH reaction on its electronic ground state*". J. Phys. Chem. A, **118**, 5915 (2014).

3. **Sugata Goswami**, B. Bussery-Honvault, P. Honvault, and S. Mahapatra, "*Effect of internal excitations of reagent diatom on initial state-selected dynamics of C + OH reaction on its second excited ($1^4A''$) electronic state*". Mol. Phys., (in press), DOI : 10.1080/00268976.2017.1296195

4. **Sugata Goswami**, T. Rajagopala Rao, Suranjan Kumar Paul, and S. Mahapatra, "*Effect of reagent vibrational excitation on the state-to-state reaction probabilities and integral reaction cross sections of hydrogen exchange reaction*, $H + H_2 \rightarrow H_2 + H$". (Manuscript under preparation).

5. **Sugata Goswami**, T. Rajagopala Rao, Suranjan Kumar Paul, and S. Mahapatra, "*Effect of reagent vibrational excitation on the state-to-state differential cross sections of hydrogen exchange reaction*, $H + H_2 \rightarrow H_2 + H$".

(Manuscript under preparation).

Presentations in Conferences and Symposiums:

1. Poster presentation in "*DAE BRNS Symposium on Current Trends in Theoretical Chemistry (CTTC-2013)*", 26-28 September, 2013, Bhabha Atomic Research Center, Mumbai, India.

2. Poster presentation in "*The First Indo-Taiwan Symposium on Recent Trends in Chemical Science (RTCS-2014)*", 17-18 November, 2014, University of Hyderabad, Hyderabad, India.

3. Poster Presentation in "*Theoretical Chemistry Symposium 2014*", 18-21 December, 2014, CSIR - National Chemical Laboratory, Pune in association with Indian Institute of Science Education and Research, Pune, India.

4. Oral Presentation in "*Chemfest-2016 (13^{th} Annual In-house Symposium)*", 18-19 March, 2016, School of Chemistry, University of Hyderabad, Hyderabad, India.

5. Poster Presentation in "*A Tributary Symposium on 100 years of Chemical Bonding-2016*", 4-5 August, 2016, CSIR-Indian Institute of Chemical Technology, Hyderabad, India.

6. Poster Presentation in "*15th Indian Theoretical Chemical Symposium (TCS 2016)*", 14-17 December, 2016, University of Hyderabad, Hyderabad, India.